DEVEOPMENT OF NANOSCALE METAL-ORGANIC FRAMEWORKS AND HYBRID SILICA NANOPARTICLES FOR BIOMEDICAL APPLICATIONS

Kathryn Michelle Louise Taylor

A dissertation submitted to the faculty of the University of North Carolina at Chapel Hill in partial fulfillment of the requirements for the degree of Doctor of Philosophy in the Department of Chemistry.

Chapel Hill

2009

Approved by

Professor Wenbin Lin

Professor Cynthia Schauer

Professor Michel Gagné

Professor Sergei Sheiko

Professor Wei You

ABSTRACT

Kathryn Michelle Louise Taylor: Development of Nanoscale Metal-Organic Frameworks
and Hybrid Silica Nanoparticles for Biomedical Applications
(Under the direction of Wenbin Lin)

This dissertation describes the use of several different types of nanoparticles for
biomedical applications including imaging, drug delivery, and sensing. Several novel
contrast agents for magnetic resonance imaging have been developed using different
nanoparticle platforms. First, highly efficient T_1-weighted contrast agents were developed
using mesoporous silica nanoparticles. This system was also extended to form a
biodegradable contrast agent based on the same mesoporous silica nanoparticle platform. By
incorporating paramagnetic metal ions Gd^{3+} and Mn^{2+} into nanoscale metal-organic
frameworks, new contrast agents for magnetic resonance imaging have also been developed.
All of these systems can also be modified to include either an organic fluorophore or
luminescent lanthanide ion, forming multimodal contrast agents that can be used for both
optical and magnetic resonance imaging.

The use of nanoscale metal-organic frameworks for drug delivery will also be
presented. Highly porous nanoscale metal-organic frameworks were synthesized using Fe^{3+}
and an organic bridging ligand. After the nanoparticles were synthesized, a platinum based
anticancer drug was covalently attached to the porous framework. These nanoparticles have
also been functionalized with organic fluorophores to create optical contrast agents.

Finally, the use of a nanoparticle sensor for the detection of dipicolinic acid, a
chemical marker for bacterial endospores (such as Anthrax), is demonstrated. Several

iii

different nanoparticle sensors were developed, and they are advantageous over the molecular

complexes because they allow for the incorporation of an internal standard, which eliminates

the need for instrument specific calibration curves.

ACKNOWLEGEMENTS

standing beside me through this long journey, and I'm looking forward to starting our new

married life together.

TABLE OF CONTENTS

LIST OF TABLES

LIST OF FIGURES

LIST OF ABBREVIATIONS AND SYMBOLS

Ala   *L*-alanine

APTES   aminopropyltriethoxysilane

BDC   benzenedicarboxylate

BHC   benzenehexacarboxylate

BJH   Barret-Joiner-Halenda

BODIPY   boron-dipyrromethene

bpy   bipyridine

BSA   bovine serum albumin

BTC   1,3,5-benzenetricarboxylate

CDI   1,1-carbonyldiimidazole

CLIO   cross-linked iron oxide

c(RGDfK)   cyclic(arginine-glycine-aspartic acid-phenylalanine-lysine)

CTAB   cetyltrimethylammonium bromide

DCP   direct current plasma spectroscopy

DIC   differential interference contrast microscopy

DMEM   Dulbecco's Modified Eagle's Medium

DMF   dimethylformamide

DMSA   2,3-dimercaptosuccinic acid

DMSO   dimethylsulfoxide

DOTA   1,4,7,10- tetraazacyclododecane-1,4,7,10-tetraacetic acid

DPA   dipicolinic acid

DPDP   N,N'-dipyridoxylethylenediamine-N,N'-diacetate-5,5'-bis(phosphate)

DSCP	disuccinatocisplatin
DTPA	diethylenetriaminepentaacetic acid
DTTA	diethylenetriaminetetraacetic acid
EDTA	ethylenediaminetetraacetic acid
EPR	enhance permeability and retention
ESI	electrospray ionization
FBS	fetal bovine serum
FDA	U. S. Food and Drug Administration
FITC	fluorescein isothiocyanate
GRAS	generally regarded as safe
HK	Horvath-Kawazoe
HT-29	human colon cancer cells
ICP-MS	inductively coupled plasma-mass spectrometry
IGROV-1	human ovarian adenocarcinoma cell line
i.v.	intravenous injection
K	lysine
LD_{50}	median lethal dose
LbL	layer-by-layer
MOF	metal-organic framework
MRI	magnetic resonance imaging
MS	mass spectrometry
MSN	mesoporous silica nanoparticles
MTS	3-(4,5-dimethylthiazol-2-yl)-5-(3-carboxymethoxyphenyl)-2-(4-sulfophenyl)-2H-tetrazolium

MW	molecular weight
MWCO	molecular weight cut-off
NMR	nuclear magnetic resonance
NMOF	nanoscale metal-organic framework
NSF	nephrogenic systemic fibrosis
NCP	nanoscale coordination polymer
PBS	phosphate buffered saline
PEG	poly(ethylene glycol)
PET	positron emission tomography
ppm	parts per million
PVP	poly(vinyl pyrrolidone)
PXRD	powder X-ray diffraction
QD	quantum dots
r_1	longitudinal relaxivity
r_2	transverse relaxivity
RES	reticuloendothelial system
RGD	arginine-glycine-aspartate peptide
RITC	rhodamine B isothiocyanate
rpm	revolutions per minute
SEM	scanning electron microscopy
Si_2-DTPA	bis(3-aminopropyl triethoxysilyl)diethylenetriamine pentaacetic acid
Si-DTTA	3-aminopropyl(trimethoxysilyl)diethylenetriamine tetraacetic acid
Si-S-S-DTPA	diethylenetriaminepenta(acetic acid)-ethyldisufanylpropyltriethoxysilane

SPECT	single photon emission computed tomography
SPIO	superparamagnetic iron oxide
T	Tesla
T_1	spin-lattice (longitudinal) relaxation time
T_2	spin-spin (transverse) relaxation time
$t_{1/2}$	half-life
θ	theta
TEM	transmission electron microscopy
TEOS	tetraethylorthosilicate
TGA	thermogravimetric analysis
THF	tetrahydrofuran
USPIO	ultrasmall superparamagnetic iron oxide
uv	ultraviolet
VCAM-1	Vascular cell adhesion molecule 1
W	water to surfactant molar ratio
wt%	weight percent

CHAPTER 1

Hybrid Nanoparticles for Biomedical Applications

1.1 Introduction

Purely inorganic or organic nanomaterials have been used extensively for a variety of biomedical applications. Semiconductor nanoparticles, or quantum dots (QDs), are nanomaterials generally composed of II-VI and III-V elements.[1-5] These nanoparticles show some unique optical properties, including sharp and symmetrical emission spectra, high quantum yields, broad absorption spectra, good chemical and photo-stability and size dependent emission wavelength tunability.[3] As a result, they have been evaluated extensively for use as optical imaging probes both *in vitro* and *in vivo*. Another class of inorganic nanoparticles that have been evaluated for biomedical imaging applications are metal oxides, including superparamaganetic iron oxide nanoparticles along with Gd_2O_3 and MnO nanoparticles. These materials have been used as contrast agents for magnetic resonance imaging, and one formulation of iron oxide nanoparticles has received FDA approval for clinical use.

Organic polymer nanoparticles have also found use in biomedical applications. There have been many reports on the use of polymeric hydrogel nanoparticles as delivery vehicles for a variety of drugs and other therapeutics.[6-15] Dendrimers and other organic polymers have also been extensively evaluated for their potential in drug delivery applicatons.[16-21]

Hybrid nanoparticles incorporate some of the advantages of both inorganic and organic nanomaterials, while also possessing some unique advantages over the other two

types. The main advantage provided by hybrid nanomaterials is the modular nature that allows for systematic tuning of the properties of the resultant material by careful selection of the different components. This chapter will give a brief overview of current hybrid nanomaterials used for biomedical applications, mainly as magnetic resonance imaging contrast agents and drug delivery platforms.

1.2 Magnetic Resonance Imaging

1.2.1 Introduction

Magnetic resonance imaging (MRI) is a non-invasive imaging technique whereby images are generated based on the nuclear magnetic resonance (NMR) signals of the water proton (^{1}H) nuclei in the specimen.[22] The spin-lattice (longitudinal) relaxation time (T_1) and the spin-spin (transverse) relaxation time (T_2) of the proton spins along with the proton density determine the MR signal intensity from a particular tissue. T_1-weighted MR images are generated based on the rate of longitudinal relaxation ($\propto 1/T_1$) of the water ^{1}H nuclei. When the protons resonating at an equilibrium frequency are excited with a radiofrequency pulse, a change in their net magnetization will occur as a result of the over-population of the higher energy states of the nuclear spins. Protons having more rapid longitudinal relaxation (i.e., shorter T_1) will relax back to their equilibrium state faster, yielding higher net electromagnetic signals to afford more intense signals in the MR image. T_2-weighted MR images, on the other hand, are generated based on the rate of transverse relaxation ($\propto 1/T_2$) of the water ^{1}H nuclei. A faster transverse relaxation leads to more rapid dephasing of individual spins, resulting in reduced signal intensity in the MR image. Owing to its

incredibly high spatial resolution, excellent soft tissue contrast, and large penetration depth, MRI has become a very powerful diagnostic tool in medicine.

1.2.2 MRI Contrast Agents

The main drawback of MRI, however, is its intrinsically low sensitivity. As a result, large doses of contrast agents are typically administered to alter the water ^{1}H relaxation times in order to enhance image contrast of specific tissues. Approximately half of clinical MR scans are performed with the aid of contrast agents.[23] Most of the current MR contrast agents are highly paramagnetic gadolinium (Gd) chelates which can reduce water proton T_1 values to result in increased (hyper-intense) signal intensity. The efficiency of a contrast agent to increase the rate of relaxation is expressed by the relaxivity value (r_1) which is defined as the slope of a plot of $1/T_1$ vs. concentration in the units of $mM^{-1} \cdot s^{-1}$. Gd chelates typically have modest r_1 values of ~4-5 $mM^{-1} \cdot s^{-1}$ and discernible contrast in the MR image can be achieved with sub mM concentrations of Gd chelates in the tissue.[24] Alternatively, superparamagnetic iron oxide nanoparticles are clinically used to enhance water transverse relaxation (r_2 relaxivity), leading to reduced (hypo-intense) MR signals, or so-called negative enhancement.

A straightforward strategy for disease diagnosis is to selectively and specifically deliver imaging contrast agents by conjugation to affinity molecules that target the biomarkers over-expressed by diseased cells. Such an approach has been successfully used to design target-specific positron emission tomography (PET) and single photon emission computed tomography (SPECT) contrast agents by tagging radionuclides or their complexes with antibodies or other cell-targeting molecules.[25,26]

Because of the need for high concentrations of paramagnetic Gd chelates, it remains a great challenge to develop T_1-contrast agents that specifically target diseased tissues and overcome the drawbacks of negative contrast enhancement afforded by iron oxide nanoparticles. Sufficient T_1-weighted MR image contrasts are typically achieved in the presence of sub mM concentrations of the Gd(III)-chelates, which is several orders of magnitude higher than that of over-expressed biomarkers.[24] There is thus an urgent need for synthetic strategies that allow for the delivery of a very large payload of Gd chelates with each cell-targeting molecule. Nanometer-scale materials offer one possible solution. They have several desirable characteristics for use as MR contrast agents, including, large payloads of the paramagnetic metal ions; decreased tumbling rates, which result in increased relaxivities; and the ability to alter the pharmacokinetics by modifying the surface of the particles to make them longer circulating or target specific. For T_1-weighted MRI contrast enhancement, these materials continue to require paramagnetic metals ions such as Gd^{3+} and Mn^{2+}, necessitating the development of hybrid cargo platforms.

1.2.3 Nanoparticle MRI Contrast Agents – T_2-Weighted

Superparamagnetic iron oxide (SPIO) nanoparticles were initially shown to improve the detection of focal liver lesions over Gd diethethylenetriaminepentaacetic acid (Gd-DTPA) enhanced MRI scans, leading to their FDA approval for clinical use in 1996.[27,28] SPIOs are composed of either maghemite (γ-Fe_2O_3) or magnetite (Fe_3O_4) phases that can be prepared by a variety of methods, most commonly by a co-precipitation reaction of a mixture of ferrous and ferric salts in aqueous media in the presence of stabilizers such as hydrophilic polymers.[29] They have extraordinary ability to shorten T_2 relaxation times due to their large

magnetization and result in large negative enhancements (darkening of images). The early clinical targets of SPIOs were liver diseases because of their selective uptake by the liver Kupffer cells.[30,31] If the normal liver architecture is destructed by a hepatic disease, such as hepatocellular carcinoma or liver metastasis, the region will have a reduced density of Kupffer cells. Due to the low uptake by the abnormal liver, the SPIO provides a strong contrast between normal and abnormal tissue, thereby enabling the detection of focal liver lesions.

As pioneered by Weissleder and co-workers, recent efforts have been focused on developing SPIO/biomolecule conjugates for target-specific MR imaging of cancers and other diseases. In one formulation, SPIOs were coated with cross-linked dextran, a naturally occurring glucose-based polysaccharide capable of complexing iron. Several variations of the formulation exist and are called cross-linked iron oxide (CLIO) and ultrasmall superparamagnetic iron oxide (USPIO, <50 nm). CLIO is composed of materials on the generally regarded as safe (GRAS) list and has been approved by the FDA. CLIO has been extensively used to image diseases in animals and humans, such as cancers, as well as to delineate biological processes *in vivo*.

Surface modification with dextran that is crosslinked with epichlorohydrin is of key importance to achieve longer blood circulation times (Scheme 1.1). The dextran can be chemically modified to allow for conjugation of targeting molecules,[32] however, dextran-coated iron oxide nanoparticles can also be used without any further functionalization to show image enhancement of disease states. Due to dextran's ability to evade the reticuloendothelial system (RES), signal void in circulation can be detected due to the T_2 relaxation of the water protons. Upon capture, the CLIO contrast enhancement allows the

delineation of RES abnormalities. Weissleder *et al.* showed such imaging capabilities in a clinical study of eighty prostate cancer patients[33] as well as other cancers[34,35]. The CLIO was shown to be lymphtrophic and could be effectively used to image nodal abnormalities that were otherwise undetectable.
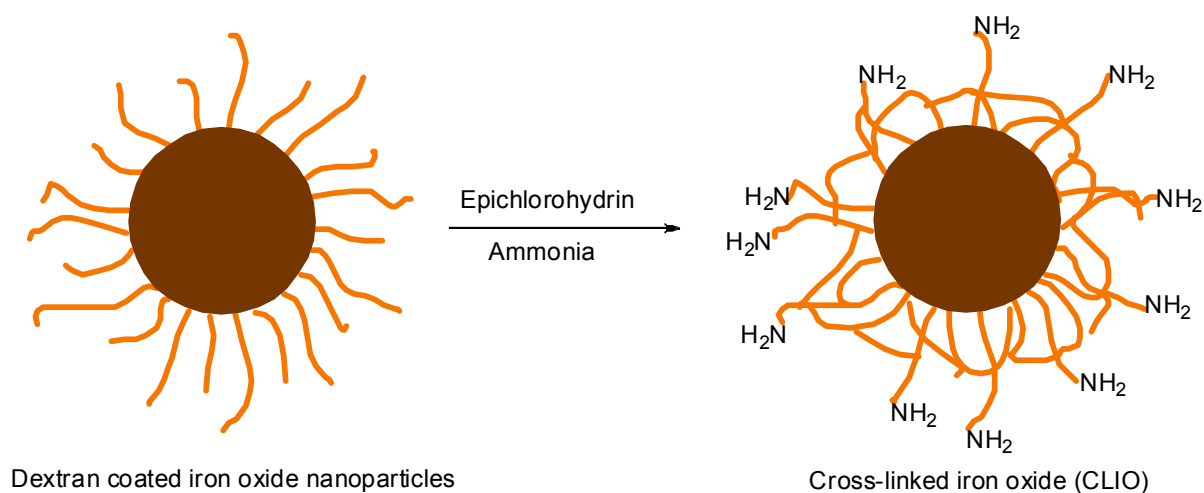
Scheme 1.1. Preparation of iron oxide nanoparticles with cross-linked dextran surface coating and amino functional groups for bioconjugation.

The dextran coating can be chemically modified to allow the conjugation of affinity molecules to endow the SPIOs target-specificity. Peptides and proteins have been used as functional conjugates with these nanoparticles to image prostate, hepatic, splenic, pancreatic, and glial neoplasia (Fig. 1.1).[33,35-37] When conjugated to E-selectin or VCAM-1, CLIO was used to detect endothelium specific proteins to monitor tumor angiogenesis.[38] Apoptotic cells can also be detected when the CLIO particles are functionalized with Annexin V, a calcium dependent protein that has high affinity for the phosphatidylserine apoptosis marker in the cell membrane.[39] Though extensively studied and considered relatively mature, the SPIO contrast agents continue to be at the forefront of biomedical imaging research.
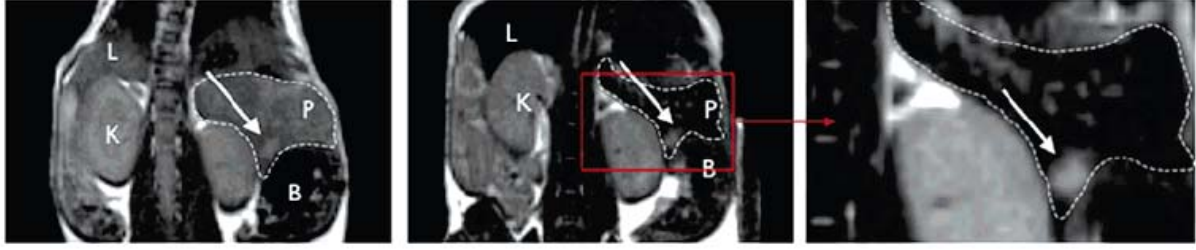
Figure 1.1. Cross-linked iron oxide nanoparticles for T_2-weighted images in rodent pancreatic cancer: preinjection of CLIO (left), postinjection of CLIO (center), and higher magnification of postinjection image (right) with the arrow indicating tumor.[37]

As shown in the model developed by Koenig and Keller, spin-spin relaxation is dependent on the magnetic moment of the nanoparticles (μ) according to Equation 1:[40]

$$R_2 = \frac{1}{T_2} = \frac{a}{d_{NP}D}\gamma^2\mu^2 C_{NP}J(\omega,\tau_D)$$ (Eq 1)

Where a is a constant, d_{NP} the diameter of the nanoparticle, D the diffusion coefficient, μ the magnetic moment of the nanoparticles, γ the gyromagnetic ratio of the water proton, C_{NP} the concentration of the nanoparticles, and $J(\omega, \tau_D)$ the spectral density function.

Eq 1 shows the quadratic dependence of r_2 on the magnetization of the nanoparticle. It is also established that the magnetic properties of nanoparticles are strongly dependent on their size, shape, and surface property. The magnetization of a nanoparticle can be significantly reduced as a result of the surface defects as described by Eq 2:[41]

$$m_S = M_S[(r-d)/r]^3$$ (Eq 2)

Where m_S is the saturation magnetization of the nanoparticle, M_S the saturation magnetization of the bulk material, r the size of the nanoparticle, and d the thickness of the disordered surface layer.

The r_2 relaxivities of SPIO and related ferrite nanoparticles can be optimized by enhancing their magnetic properties via 1) the intrinsic material properties such as material composition and crystal structure, and 2) extrinsic factors such as crystallinity, size, and

shape.   Over the past decade, many synthetic protocols have been developed for monodisperse and highly crystalline iron oxide and related ferrite nanoparticles, most notably via thermal decomposition of metal precursors in organic surfactant solutions at high temperatures of > 300 $^\circ$C.[42] The resulting hydrophobic nanoparticles had uniform sizes (σ < 10%), and their sizes (from 4 to 25 nm) could be finely controlled by modifying synthetic parameters. In particular, Hyeon *et al*. reported the large-scale production of various metal oxide nanoparticles from the thermal decomposition of metal-surfactant complexes.[43] Cheon and coworkers systematically studied the relationships among size, magnetism, and relaxivity of uniform-sized iron oxide nanoparticles (Fig. 1.2).[44] Larger iron oxide nanoparticles have larger magnetizations and high r_2 relaxivities, which makes it possible to increase the contrast in T_2-weighted images. Various bimetallic ferrite nanoparticles including $CoFe_2O_4$, $MnFe_2O_4$, and $NiFe_2O_4$ have also been tested as T_2 contrast agents. The $MnFe_2O_4$ nanoparticles (MnMEIO) have been found to have a very high magnetization and large relaxivity (Fig. 1.3).[45]
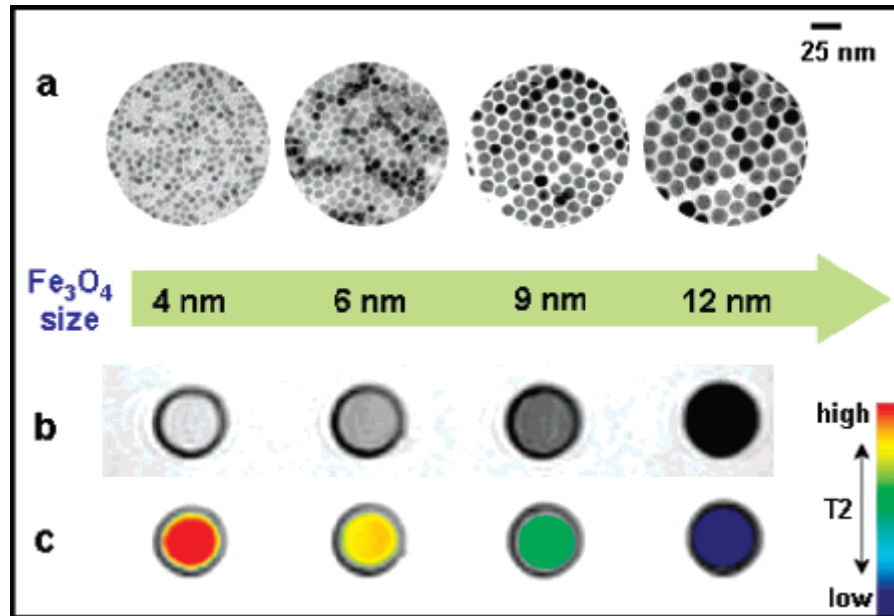
Figure 1.2. Effect of Fe_3O_4 nanoparticle size on relaxivity. (a) TEM images of Fe_3O_4 nanocrystals of 4, 6, 9, and 12 nm. (b) Size-dependent T_2-weighted MR images of Fe_3O_4 nanocrystals in aqueous solution at 1.5 T. (c) Size-dependent changes from red to blue in color-coded MR images based on T_2 values.[44]
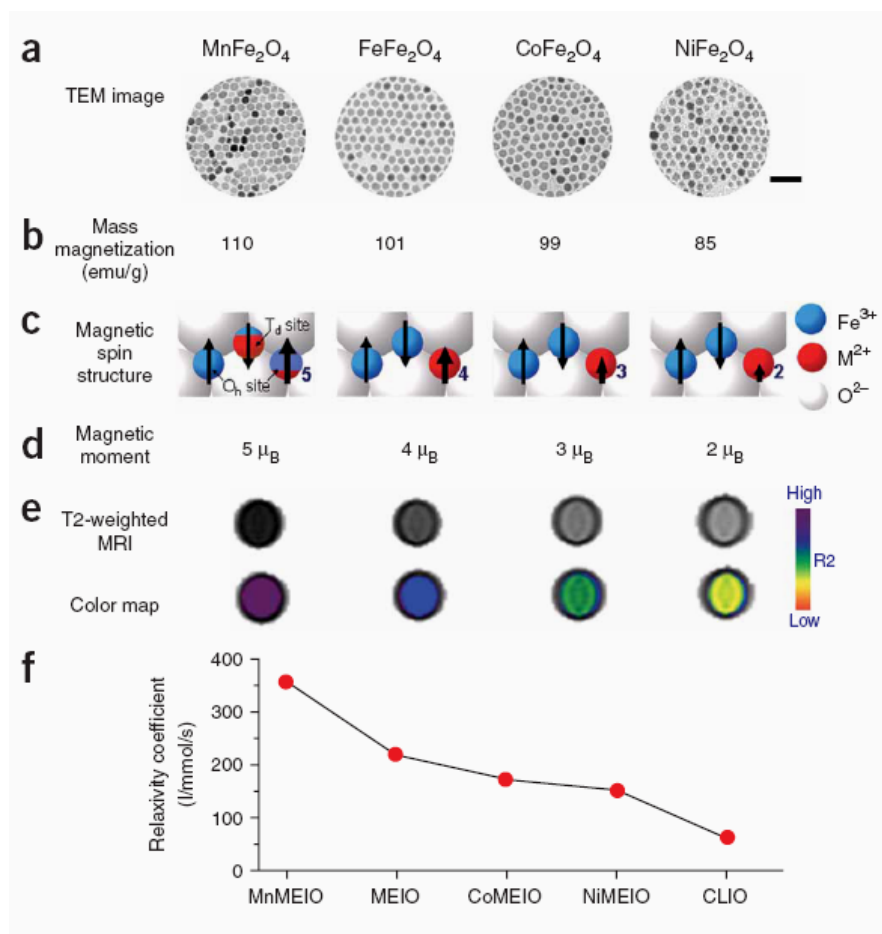
Figure 1.3. Magnetism-engineered iron oxide (MEIO) nanoparticles and effects of their magnetic spin on MRI. (a) TEM images of $MnFe_2O_4$ (MnMEIO), Fe_3O_4 (MEIO), $CoFe_2O_4$ (CoMEIO) and $NiFe_2O_4$ (NiMEIO). All nanoparticles were synthesized to be ~12 nm. Scale bar, 50 nm. (b) Mass magnetization values of MFe_2O_4. (c,d) Schematics of spin alignments of magnetic ions in spinel structures under external magnetic field, and magnetic spin moment of MFe_2O_4 nanoparticles. (e,f) T_2-weighted spin echo MR images, their color maps and relaxivity (r_2) of a series of MEIO nanoparticles at 1.5 T. In (f), the r_2 of CLIO is also presented, for comparison.[45]

Since the above uniform and crystalline superparamagnetic nanoparticles were synthesized in organic media, their hydrophobic surfaces have to be modified with hydrophilic coatings to ensure their aqueous dispersibility and biocompatibility as well as to allow for their reactivity with targeting molecules (such as antibodies). Several new coating strategies have recently been developed for metal oxide nanoparticles, in particular, iron oxide nanoparticles. For example, several functional groups were immobilized on iron oxide

nanoparticles via dopamine,[46,47] hydroxamic acid,[48] and 2,3-dimercaptosuccinic acid (DMSA).[45] The DMSA-coated iron oxide nanoparticles were dispersible in water and used for *in vivo* MRI.[45] Several strategies have also been developed to coat SPIOs with biocompatible polymers such as poly(ethylene glycol) (PEG).[49]

Superparamagnetic nanoparticles with suitable surface coatings were conjugated with affinity molecules such as antibodies, peptides, and oligonucleotides to afford target-specific contrast agents for efficient lesion detection. Cheon *et al.*, for example, demonstrated that Herceptin-conjugated $MnFe_2O_4$ nanoparticles showed more sensitive *in vivo* cancer imaging with large r_2 relaxivity (Fig. 1.4).[45] The shells of the nanoparticles can also provide novel functions in addition to MR imaging. For example, Hyeon synthesized discrete and monodisperse core-shell nanostructures with a magnetite nanocrystal core and a mesoporous silica shell loaded with a fluorescent dye and an anticancer drug.[50] The resulting composite core/shell nanoparticles were applied to simultaneous MR and optical imaging and drug delivery (Fig. 1.5).
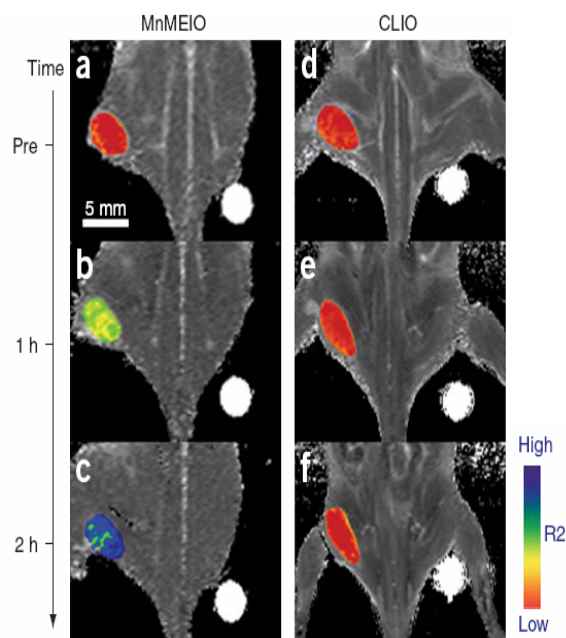
Figure 1.4. *In vivo* MR detection of cancer after administration of magnetic nanoparticles-Herceptin conjugates. $MnFe_2O_4$ nanoparticles (a-c) show higher signal enhancement than crosslinked iron oxide (CLIO) (d-f).[45]
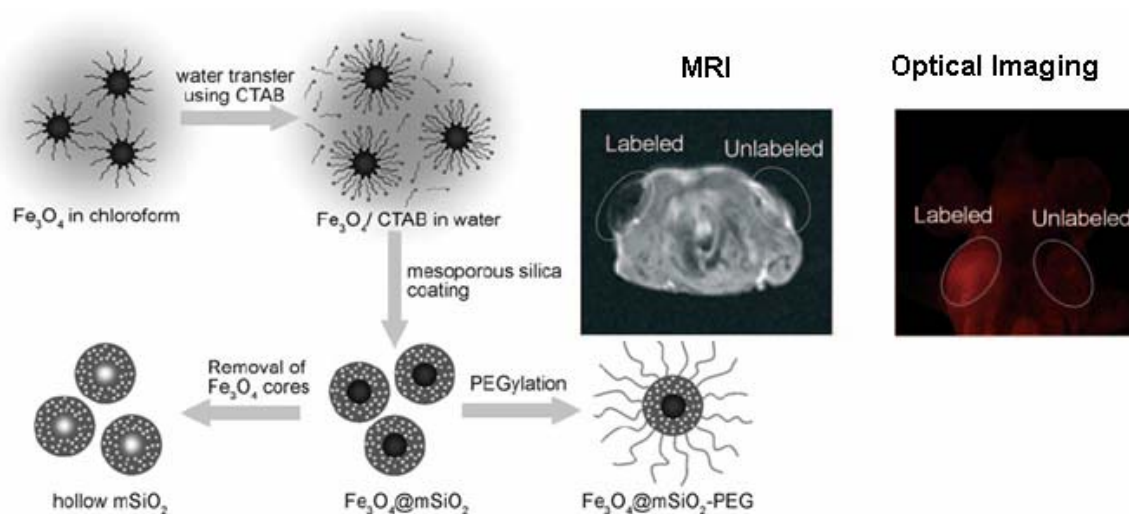
Figure 1.5. The synthesis of magnetite nanoparticle/mesoporous silica core–shell nanostructures and their *in vivo* dual modal imaging (MRI and optical imaging).[50]

1.2.4 Nanoparticle MRI Contrast Agents – T_1-Weighted

Superparamagnetic nanoparticles typically act as negative contrast agents which decrease the proton MR signal from the tissue. The resulting dark signal can be confused with other pathogenic conditions and cause undesired false positives. Moreover, the high

susceptibility of the T_2 contrast agents induces distortion of the magnetic field on neighboring normal tissues. This distortion of the background is called the susceptibility artifact or 'blooming effect', which generates obscure images and distorts the background around the lesions.[51]   There is thus a very strong interest in creating nanoparticles for efficient T_1-weighted MR imaging.

Wickline and Lanza have developed perfluorocarbon-based microemulsion contrast agents and extensively examined their utility in target-specific MR imaging *in vivo*.[52]   The nanoparticles of ~250 nm in diameter are composed of a perfluorocarbon core and a monolayer lipid shell.   The particles can be synthesized by emulsification of perfluorooctylbromide, surfactants, and glycerin to form a stable nanoparticle with a few hundred homing ligands and extraordinarily high payloads of paramagnetic metal centers, about 100,000 or more Gd chelates per nanoparticle.   These Gd-containing nanoparticles possess extremely large MR relaxivities on per particle basis.[53]

Targeting molecules can be incorporated into the stabilizing surface lipids to allow for their selective delivery to specific sites. Ligands for over-expressed disease biomarkers that have been used for this material include small molecules, integrins, fibrin, and antibodies.   The targeted derivatives of the perfluorocarbon-lipid nanoparticles were used extensively to image tumors and angiogenesis[54,55] as well as neovascularization in atherosclerosis.[56]

The perfluorocarbon core also allows for the unique capability of an additional MRI probe using the ^{19}F signal. [19]F MRI is an advantageous imaging tool because the magnetic resonance sensitivity is nearly as high as [1]H (83%), there is a low abundance of endogenous ^{19}F in biological systems, and the natural abundance of the ^{19}F isotope is 100%.

Perfluorocarbon emulsions encapsulated by lipid-surfactant monolayers have been used to prepare MRI contrast agents with high ^{19}F payloads. Perfluorocarbon-based microemulsion nanoparticles are thus multimodal and prove to be versatile in the early detection of cancers.

Oil-in-water microemulsions have been used as templates to engineer stable wax nanoparticles containing Gd chelates for potential use as MRI contrast agents.[57] Gd was incorporated into the lipid layer by forming chelates with dimyristoyl phosphoethanolamine diethylenetriamine pentaacetate. The wax nanoparticles have a payload of approximately 10^5 Gd(III) per nanoparticle, as determined by inductively coupled plasma atomic emission spectroscopy. In a 4.7 T MR scanner, relaxivities were determined to be $r_1 = 7.1$ and $r_2 = 13.0$ s^{-1} per mM Gd. These nanoparticles were also pegylated to increase blood circulation times, and the pegylated wax nanoparticles were used in MR imaging of nude mice bearing A549 lung carcinoma xenografts by taking advantage of the enhanced permeability and retention (EPR) effect.[58]

Liposomes are lipid vesicles consisting of an aqueous core enclosed in a lipid bilayer membrane. Gd-labeled liposomes have been prepared and extensively examined for *in vivo* MR imaging.[59-61] The first Gd(III)-containing liposomes were confirmed to be viable as MRI contrast agents for imaging the liver and spleen of normal Balb/c mice.[59-61] Later formulations were reported to show contrast enhancement of hepatic metastases in rats.[62-64] Liposomes can also be rendered target-specific by adding cell-targeting moieties to the bilayer surface. A number of target-specific liposome-based contrast agents have already been explored for imaging IGROV-1 xenograft tumors and hepatic metastases in rodents (Fig. 1.6).[54,65]
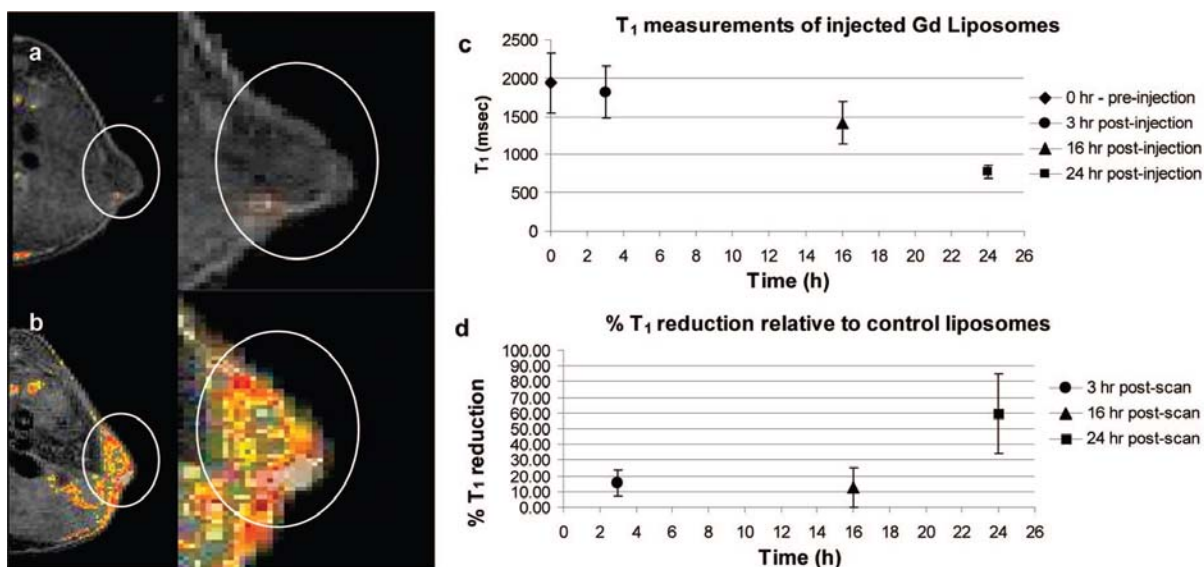
Figure 1.6. (a) Preinjection MR images of induced IGROV-1 tumors under the right flanks of nude Balb/c mice: large white circle represents zoomed image of tumor area marked with small circle. (b) MR images 24 h post i.v. injection of Gd-liposomes; the color map shows enhancement of tumor area: large white circle is zoomed image of tumor area marked with small circle. (c) T_1 measurements were obtained from tumor slices. (d) Image enhancement is supported by a 60% measured reduction in tumor T_1 values 24 h post i.v. injection relative to control liposomes (no Gd complexed).[65]

Inorganic nanoparticles composed of highly paramagnetic metal ions such as Gd^{3+} and Mn^{2+} have also been developed as new T_1 contrast agents. Large surface-to-volume ratios of such ultrasmall nanoparticles should allow facile interactions between the metal ions at or near the surface with surrounding water molecules, leading to fast longitudinal relaxation of the water protons. Nanoparticles of Gd_2O_3,[66] GdF_3,[67] and $GdPO_4$[68] have been investigated as MRI contrast agents. They exhibited signal enhancing contrast in T_1-weighted images. The Gd_2O_3 nanoparticle-based agents are composed of small cores of < 5 nm and stabilizing shells of dextran, PEG and silica.[66] Water dispersible GdF_3 nanoparticles were prepared with either a positively charged surface by conjugation with 2-aminoethyl phosphate groups or a negatively charged surface by coating with citrate groups.[67] Dextran-coated $GdPO_4$ nanoparticles were synthesized by a hydrothermal process in the presence of

dextran.[68] The clinical utility of such Gd-based nanoparticles is however uncertain because of the potential leaching of free Gd^{3+} ions which are the culprit of the recently discovered nephrogenic systemic fibrosis (NSF) syndrome.

MnO nanoparticles were recently examined as T_1 contrast agents for *in vivo* MR imaging.[69,70] MnO nanoparticles conjugated with a tumor-specific antibody were used for the selective imaging of breast cancer cells in a metastatic brain tumor (Fig. 1.7).[70] Metallic nanoparticles have also recently been shown to be promising T_1 contrast agents. Dai and coworkers synthesized FeCo nanoparticles stabilized with single graphitic carbon shell (FeCo/GC).[71] After non-covalent functionalization with phospholipid–poly(ethylene glycol) (PL-PEG) molecules, the FeCo/GC nanoparticles were long-circulating and provided positive contrast enhancement in depicting the artery in a rabbit model. Despite their promise as T_1 contrast agents, the detailed contrast enhancement mechanisms in both MnO and FeCo/GC nanoparticles have yet to be elucidated.
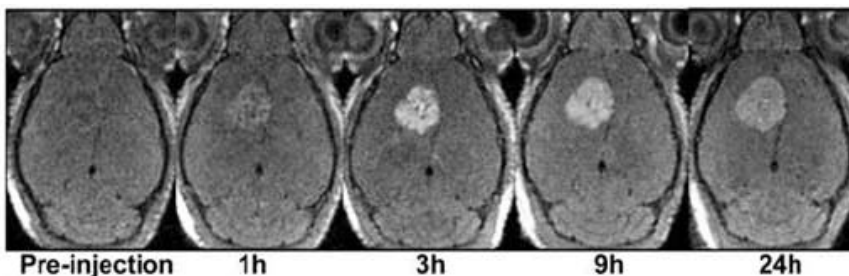
Figure 1.7. Breast cancer cells were selectively enhanced in T_1-weighted MRI by the Herceptin-functionalized MnO nanoparticles.[70]

Inspired by the microemulsion and liposomal contrast agents, our group prepared 37 nm hybrid silica nanoparticles containing embedded $[Ru(bpy)_3]Cl_2$ luminophore and a shell of Gd chelates.[72] Unlike the microemulsion and liposomal systems, the hybrid silica particles have a tunable size from 20-100 nm. The large Stokes shift of the $[Ru(bpy)_3]Cl_2$ fluorophore (Excitation: 525 nm; emission: 610 nm) in the core significantly reduces the

background signal from biological systems. Furthermore, $[Ru(bpy)_3]Cl_2$ is much more photostable than organic fluorophores such as fluorescein. The luminescence of the hybrid silica nanoparticles is thus highly compatible with biological imaging applications.

The Gd chelates were immobilized onto the surface of the silica nanoparticles in either a monolayer or multilayer fashion. The surface-immobilized Gd chelates effectively relax water protons. The resulting nanoparticle has relaxivities five orders of magnitude higher than the constituent Gd chelate due not only to the greatly increased Gd payload but also to the much enhanced per Gd relaxivity as a result of the reduced tumbling rates. Notably, the particles with multilayers of Gd chelates had reduced relaxivities compared to those with the monolayer coating, likely due to the reduced water accessibility of the Gd-chelates. Murine monocyte cells were successfully labeled with the hybrid silica nanoparticles and T_1-weighted signal enhancement of the cell pellet was observed in a 3 T MR scanner.[72] The efficacy of the hybrid silica nanoparticles as a dual optical and MR contrast agent was also demonstrated in a collagen-induced arthritis mouse model.

One strategy developed in our group in order to circumvent the reduced relaxivities found in the solid silica particles with multilayer coatings involved the use of a polyelectrolyte layer-by-layer (LbL) self-assembly approach to increase the Gd payload while maintaining the relaxivity on per Gd basis.[73] Positively charged MR-enhancing Gd-chelate oligomers were deposited onto negatively charged silica nanoparticles possessing a Gd-DTTA monolayer via electrostatic interactions. The resulting positively charged particle was further treated with negatively charged polystyrenesulfonate to provide a net negative charged layer. These steps were repeated to form the multilayer architecture as shown in Scheme 1.2. TEM and fluorescence studies indicated the consecutive deposition of

polymeric electrolytes onto the particle, whereas MR phantom studies demonstrated that nanoparticles with more layers of the Gd-DOTA polymers had the expected higher relaxivities on per particle basis. The relaxivities on a per Gd basis remained constant, regardless of the number of layers deposited. The LbL self-assembly thus increases the Gd payload without deleteriously affecting the MR relaxivity on per Gd basis, presumably as a result of the flexible and disordered nature of the polyelectrolyte LbL assembly which allows ready water access to the Gd(III) centers.
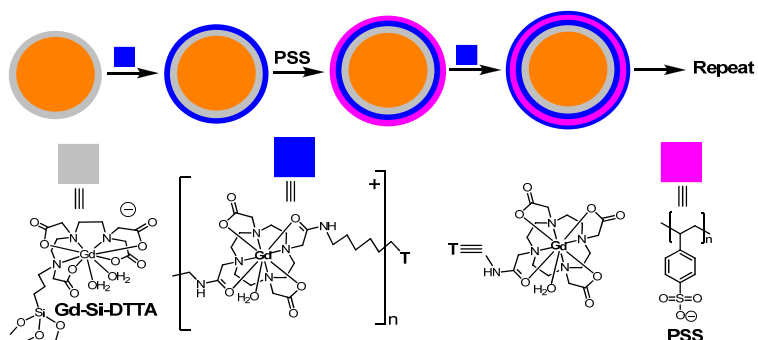
Scheme 1.2. Layer-by-layer self-assembly of multifunctional hybrid nanoparticles for an increased Gd payload.

A peptide sequence containing arginine-glycine-aspartate (RGD) and seven consecutive lysine (K) residues (K$_7$RGD) was adsorbed onto the particles terminated with negatively charged PSS layer via electrostatic interactions. The RGD peptide is known to bind strongly to the integrin cell surface receptors that are upregulated in angiogenic cancer cells. The RGD-terminated nanoparticles allowed target-specific optical and MR imaging of HT-29 human colon cancer cells (Figure 1.8).
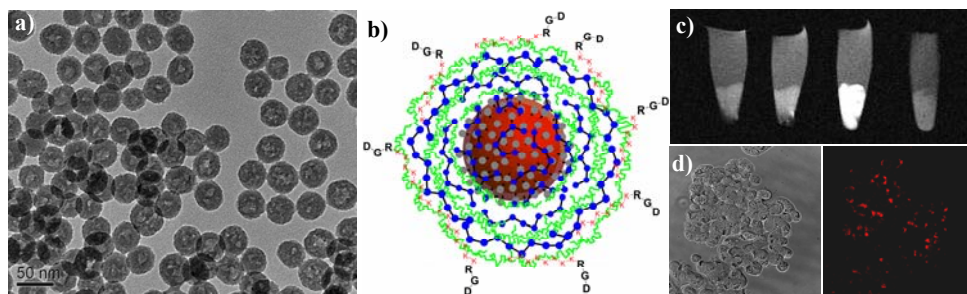
Figure 1.8. (a) TEM images and (b) schematic representation of LbL self-assembled nanoparticles decorated with RGD-peptides for integrin targeting. (c) T_1-weighted MR images of HT-29 cells that have been incubated with various nanoparticles. From left to right: control cells without any nanoparticle, cells with LbL nanoparticles, cells with LbL nanoparticles that were functionalized with RGD peptide, and cells with LbL nanoparticles that were functionalized with GRD peptide. (d) Phase contrast optical (left) and confocal fluorescence (right) images of HT-29 cells incubated with LbL nanoparticles that were functionalized with RGD peptide.

Another approach that was taken to increase the payload of Gd without sacrificing the per Gd relaxivity was to use mesoporous silica nanoparticles (MSN) as a platform.[74] The extremely high surface area of MSN allows for a high payload of Gd chelates with enhanced water accessibility which is the key to high r_1 relaxivity. MSNs were first prepared by a surfactant-templated, base-catalyzed condensation of tetraethylorthosilicate. Subsequently, a monolayer of Gd-chelates was grafted by refluxing in toluene. The resulting MSNs exhibited exceptionally high relaxivities both on a per Gd and per particle basis. The detailed synthesis and characterization of this contrast agent, as well as *in vitro* and *in vivo* MR imaging results will be described in Chapter 2. Chapter 3 describes the synthesis and characterization of biodegradable version of this MSN based contrast agent.

1.3 Nanoscale Metal-Organic Frameworks (NMOFs)

1.3.1 Introduction to NMOFs

Coordination polymers or metal-organic frameworks are built from metal ions or metal ion clusters that have two or more vacant coordination sites and polydentate bridging ligands. Prussian blue and mixed-metal cyanometallates are the classic examples of coordination polymers.[75] Numerous reports on the syntheses and characterization of cyanometallate nanoparticles have been published over the last decade,[76-82] and they exhibit unique size-dependent properties such as superparamagnetism,[76] photo-induced superparamagnetism,[77] and spin-glass-like behavior.[78] Coordination polymers however are not limited to the cyanometallates, and can be synthesized from a wide range of metal and organic building blocks. The tunable nature of coordination polymers has allowed them to be engineered for a number of bulk-scale applications, including gas storage,[83] catalysis,[84] and nonlinear optics.[85] By scaling them down to the nanometer-regime, the scope of coordination polymer nanoparticles can be vastly expanded. Recent reports on nanoscale coordination polymers have shown their application in a variety of areas, ranging from heterogeneous catalysis to anticancer drug delivery.

1.3.2 Use of NMOFs for Biomedical Imaging

By including paramagnetic metal ions such as Gd^{3+} and Mn^{2+}, NMOFs can be synthesized as efficient contrast agents for MR imaging. Our group has previously demonstrated the use of Gd^{3+} containing NMOFs as MR contrast agents. Nanorods of $Gd_2(BDC)_3(H_2O)_4$ (BDC is 1,4-benzenedicarboxylate) were synthesized using water-in-oil microemulsions (Fig. 1.9).[86] The morphology and size of the crystalline Gd NMOFs could

be controlled by the water to surfactant molar ratio (i.e., *W*-value). Using 1,2,4-benzenetricarboxylate as the bridging ligand afforded NMOFs with a plate-like morphology rather than nanorods.
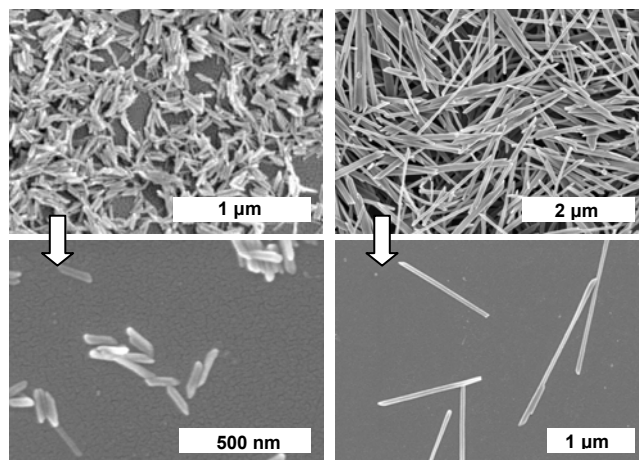
Figure 1.9. SEM images of Gd(BDC)$_{1.5}$(H$_2$O)$_2$ nanorods synthesized using a microemulsion with $W = 5$ (left) and $W = 10$ (right). BDC is 1,4-benzenedicarboxylate.

The Gd NMOFs display a longitudinal relaxivity (r_1) of 35.8 mM^{-1}s^{-1}, a value almost an order of magnitude higher than that of a commercially available T_1 contrast agent. The Gd NMOFs contain a large number of Gd metal centers and thus exhibit an r_1 of 2.5 x 10^7 s^{-1} per mM nanorod. The Gd centers at or near the surface of the NMOF are likely responsible for the observed relaxivities. By doping the Gd NMOFs with 5% of Eu or Tb, the nanorods exhibited characteristic red or green luminescence, respectively. The Gd NMOFs however leached μM concentrations of Gd^{3+} ions in water, which precludes their *in vivo* applications as MRI contrast agents due to the toxicity of Gd^{3+} ions. Attempts were made to stabilize the NMOFs by coating them with a silica shell.[87] The release of Gd^{3+} ions from the NMOF-silica core-shell nanostructures was significantly retarded but not entirely eliminated.

By varying the bridging ligand, and synthesis conditions, the size and morphology of the resulting NMOF can be changed. Chapter 4 describes the synthesis and characterization

of four new Gd^{3+} containing NMOFs synthesized using two different techniques. Because Mn^{2+} ions are much less toxic than Gd^{3+} ions, several NMOFs were synthesized using Mn^{2+} and two different bridging ligands. Chapter 5 describes the synthesis, characterization, and *in vitro* and *in vivo* imaging of two Mn^{2+} containing NMOFs.

1.3.3 Use of NMOFs for Drug Delivery

Our group has recently demonstrated the use of amorphous nanoscale coordination polymers (NCPs) as drug delivery vehicles.[88] NCPs based on a Pt containing anticancer drug were synthesized using a precipitation method whereby a poor solvent was added to an aqueous solution of the precursors, disuccinatocisplatin (DSCP) and Tb^{III}, inducing the formation of the nanoparticles (Scheme 1.3). In order to stabilize the particles against rapid dissolution they were coated with a silica shell. The half-life ($t_{1/2}$) for the release of DSCP, an analog of the anticancer drug cisplatin, from NCPs of the composition $Tb_2(DSCP)_3$-$(H_2O)_{12}$ could be tuned from approximately 5.5 hours to 9 hours by increasing the shell thickness from approximately 2 nm to 7 nm. In comparison, the as-synthesized NCPs had a $t_{1/2}$ for dissolution of only 1 hour. *In vitro* cytotoxicity assays showed that the Pt-based NCP particles displayed anticancer efficacies superior to the cisplatin standards. These results were significant because they clearly demonstrated the feasibility of using NCPs as delivery vehicles for clinically relevant cargos.

Scheme 1.3. Synthesis of NCPs based on the anticancer drug disuccinatocisplatin (DSCP).

Another approach to using NMOFs as drug delivery vehicles is to covalently graft an anticancer drug into the channels of a porous NMOF. Chapter 6 describes the synthesis and characterization of several Fe(III) NMOFs. These NMOFs were then loaded with various cargoes, including organic fluorophores and Pt based anticancer drugs, using post-synthetic modification.

1.4 Use of Nanoparticles for Biological Sensing Applications

A major concern in the event of biological warfare is the rapid detection of *Bacillus anthracis* endospores, which have been used in previous anthrax attacks. There are several techniques currently used for the detection of bacterial endospores, including immunoassays,[89-90] polymerase chain reaction (PCR),[91-93] surface-enhanced Raman spectroscopy,[94-96] and Tb(III) luminescence.[87,97-101] Tb(III) luminescence detection has been shown to be a rapid, sensitive, and inexpensive method for endospore detection. The luminescence detection is based on the sensing of dipicolinic acid (DPA) which can account for up to 15% of the dry mass of endospores. By combining the Tb(III) luminescence detection of DPA with a nanoparticle platform, a useful sensor can be created. The use of a nanoparticle platform allows for the incorporation of an internal standard, which eliminates the need for instrument specific calibration curves for quantifying amounts of DPA present in

an unknown sample. Chapter 7 describes the synthesis, characterization, and evaluation of several nanoparticle based sensors, which can detect DPA at nanomolar concentrations.

1.5 Conclusions

This chapter has introduced the use of nanomaterials for several biological applications, including imaging, drug delivery, and sensing. The use of nanomaterials for biomedical applications, especially MR imaging, offers several advantages including increased payload and the ability to modify the surface of the particles to increase circulation time *in vivo* or to impart target specificity. While much of the research done in this area has focused on the use of purely inorganic or organic nanomaterials, hybrid nanomaterials have begun to emerge as a useful platform. The combination of inorganic and organic components allows for an almost unlimited tunability, giving way to the design of materials for a variety of applications.

1.6 References

1. Smith, A. M.; Duan, H.; Mohs, A. M.; Nie, S., Bioconjugated quantum dots for in vivo molecular and cellular imaging. *Advanced Drug Delivery Reviews*. **2008**, *60* (11) 1226–1240.

2. Yu, W. W.; Chang, E.; Drezek, R.; Colvin, V. L., Water-soluble quantum dots for biomedical applications. *Biochemical and Biophysical Research Communications*. **2006**, *348* (3), 781–786.

3. Weng, J.; Ren, J., Luminescent quantum dots: a very attractive and promising tool in biomedicine. *Current Medicinal Chemistry*. **2006**, *13* (8)*,* 897-909.

4. Zhang, H.; Yee, D.; Wang, C., Quantum dots for cancer diagnosis and therapy: biological and clinical perspectives. *Nanomedicine*. **2008**, *3* (1), 83-91.

5. Biju, V.; Itoh, T.; Anas, A.; Sujith, A.; Ishikawa, M., Semiconductor quantum dots and metal nanoparticles: syntheses, optical properties, and biological applications. *Anal. Bioanal. Chem.* **2008**, *391* (7), 2469–2495.

6. Nayak, S.; Lyon, L. A., Soft Nanotechnology with Soft Nanoparticles. *Angew. Chem. Int. Ed.* **2005**, *44* (47), 7686 – 7708.

7. Hidaka, M.; Kanematsu, T.; Ushio, K.; Sunamoto, J., Selective and effective cytotoxicity of folic acid conjugated cholesteryl pullulan hydrogel nanoparticles complexed with doxorubicin in *in vitro* and *in vivo* studies. *Journal of Bioactive and Compatible Polymers*. **2006**, *21* (6), 591-602.

8. Gao, D.; Xu, H.; Philbert, M. A.; Kopelman, R., Ultrafine hydrogel nanoparticles: synthetic approach and therapeutic application in living cells. *Angew. Chem. Int. Ed.* **2007**, *46* (13), 2224 –2227.

9. Zeng, Y.; Pitt, W. G., Poly(ethylene oxide)-b-poly(N-isopropylacrylamide) nanoparticles with cross-linked cores as drug carriers. *J. Biomater. Sci. Polymer Edn*, **2005**, *16* (3), 371–380.

10. McAllister, K.; Sazani, P.; Adam, M.; Cho, M. J.; Rubinstein, M.; Samulski, R. J.; DeSimone, J. M., Polymeric nanogels produced via inverse microemulsion polymerization as potential gene and antisense delivery agents. *J. Am. Chem. Soc.* **2002**, *124* (51), 15198-15207.

11. Dai, H.; Chen, Q.; Qin, H.; Guan, Y.; Shen, D.; Hua, Y.; Tang, Y.; Xu, J., A temperature-responsive copolymer hydrogel in controlled drug delivery. *Macromolecules* **2006**, *39* (19)*,* 6584-6589.

12. Sahiner, N.; Alb, A. M.; Graves, R.; Mandal, T.; McPherson, G. L.; Reed, W. F.; John, V. T., Core-shell nanohydrogel structures as tunable delivery systems. *Polymer*. **2007**, *48* (3), 704-711.

13. Missirlis, D.; Kawamurab, R.; Tirelli, N.; Hubbell, J. A., Doxorubicin encapsulation and diffusional release from stable, polymeric, hydrogel nanoparticles. *European Journal of Pharmaceutical Sciences*. **2006**, *29* (2), 120–129.

14. Hamidi, M.; Azadi, A.; Rafiei, P., Hydrogel nanoparticles in drug delivery. *Advanced Drug Delivery Reviews*. **2008**, *60* (15), 1638–1649.

15. Chiellini, F.; Bartoli, C.; Dinucci, D.; Piras, A. M.; Anderson, R.; Croucher, T., Bioeliminable polymeric nanoparticles for proteic drug delivery. *Int. J. Pharmaceutics* **2007**, *343* (1-2), 90–97.

16. Lee, C. C.; MacKay, J. A.; Frechet, J. M.; Szoka, F. C., Designing dendrimers for biological applications. *Nat. Biotechnol*. **2005**, *23* (12), 1517-1526.

17. Gupta, U.; Agashe, H. B.; Asthana, A.; Jain, N. K., A review of in vitro–in vivo investigations on dendrimers: the novel nanoscopic drug carriers. *Nanomedicine: Nanotech., Biol, and Med*. **2006**, *2* (2), 66-73.

18. Yang, H.; Lopina, S. T.; DiPersio, L. P.; Schmidt, S. P., Stealth dendrimers for drug delivery: correlation between PEGylation, cytocompatibility, and drug payload. *J. Mater. Sci.: Mater. Med.* **2008**, *19* (5), 1991–1997.

19. Kunii, R.; Onishi, H.; Machida, Y., Preparation and antitumor characteristics of PLA/(PEG-PPG-PEG) nanoparticles loaded with camptothecin. *European Journal of Pharmaceutics and Biopharmaceutics*. **2007**, *67* (1), 9–17.

20. Yang, A.; Yang, L.; Liu, W.; Li, Z.; Xua, H.; Yang, X., Tumor necrosis factor alpha blocking peptide loaded PEG-PLGA nanoparticles: preparation and *in vitro* evaluation. *Int. J. Pharmaceutics*. **2007**, *331* (1), 123–132.

21. Cheng, J.; Teply B. A.; Sherifi, I.; Sung, J.; Luther, G.; Gu, F. X.; Levy-Nissenbaum, E.; Radovic-Moreno, A. F.; Langer, R.; Farokhzad, O. C., Formulation of functionalized PLGA–PEG nanoparticles for in vivo targeted drug delivery. *Biomaterials* **2007**, *28* (5), 869–876.

22. Stark, D. D.; Bradley Jr., W.G. *Magnetic Resonance Imaging*. Mosby: St. Louis, 1999.

23. Aime, S.; Botta, M.; Fasano, M.; Terreno, E., Lanthanide(III) chelates for NMR biomedical applications. *Chem. Soc. Rev.* **1998**, *27* (1), 19-29.

24. Caravan, P.; Ellison, J. J.; McMurry, T. J.; Lauffer, R. B., Gadolinium(III) chelates as MRI contrast agents: structure, dynamics, and applications. *Chem. Rev.* **1999**, *99* (9), 2293-2352.

25. Larson, S. M., Radioimmunology. Imaging and therapy. *Cancer.* **1991,** *67* (S4), 1253-1260.

26. Yang, D. J.; Kim, E. E.; Inoue, T., Targeted molecular imaging in oncology. *Ann. Nucl. Med.* **2006**, *20* (1), 1-11.

27. Gupta, H.; Weissleder, R., Targeted contrast agents in MR imaging. *Magn. Reson. Imaging Clin. N. Am.* **1996**, *4* (1), 171-184.

28. Petersein, J.; Saini, S.; Weissleder, R., Liver. II: Iron oxide-based reticuloendothelial contrast agents for MR imaging. Clinical review. *Magn. Reson. Imaging Clin. N. Am.* **1996**, *4* (1), 53-60.

29. Corot, C.; Robert, P.; Idée, J-M.; Port, M., Recent advances in iron oxide nanocrystal technology for medical imaging. *Adv. Drug Deliv. Rev.* **2006**, *58* (14), 1471-1504.

30. Dias, M. H. M.; Lauterbur, P. C., Ferromagnetic particles as contrast agents for magnetic resonance imaging of liver and spleen. *Magn. Reson. Med.* **1986**, *3* (2), 328-330.

31. Semelka, R. C.; Helmberger, T. K., Contrast agents for MR imaging of the liver. *Radiology*, **2001**, *218* (1), 27-38.

32. Kang, H. W.; Josephson, L.; Petrovsky, A.; Weissleder, R.; Bogdanov, Jr., A., Magnetic resonance imaging of inducible E-selectin expression in human endothelial cell culture. *Bioconjug. Chem.* **2002**, *13* (1), 122-127.

33. Harisinghani, M. G.; Barentsz, J.; Hahn, P. F.; Deserno, W. M.; Tabatabaei, S.; van de Kaa, C. H.; de la Rosette, J.; Weissleder, R., Noninvasive detection of clinically occult lymph-node metastases in prostate cancer. *N. Engl. J. Med.* **2003**, *348* (25), 2491-2499.

34. Harisinghani, M. G.; Jhaveri, K. S.; Weissleder, R.; Schima, W.; Saini, S.; Hahn, P. F.; Mueller, P. R., MRI contrast agents for evaluating focal hepatic lesions. *Clin. Radiol.* **2001**, *56* (9), 714-725.

35. Harisinghani, M. G.; Saini, S.; Weissleder, R.; Halpern, E. F.; Schima, W.; Rubin, D. L.; Stillman, A. E.; Sica, G. T.; Small, W. C.; Hahn, P. F., Differentiation of liver hemangiomas from metastases and hepatocellular carcinoma at MR imaging enhanced with blood-pool contrast agent code-7227. *Radiology* **1997**, *202* (3), 687-691.

36. Weissleder, R.; Elizondo, G.; Stark, D. D.; Hahn, P. F.; Marfil, J.; Gonzalez, J. F.; Saini, S.; Todd, L. E.; Ferrucci, J. T., The diagnosis of splenic lymphoma by MR imaging: value of superparamagnetic iron oxide. *AJR Am. J. Roentgenol.* **1989**, *152* (1), 175-180.

37. Montet, X.; Weissleder, R.; Josephson, L., Imaging pancreatic cancer with a peptide-nanoparticle conjugate targeted to normal pancreas. *Bioconjug. Chem.* **2006**, *17* (4), 905-911.

38. Kelly, K. A.; Allport, J. R.; Tsourkas, A.; Shinde-Patil, V. R.; Josephson, L.; Weissleder, R., Detection of vascular adhesion molecule-1 expression using a novel multimodal nanoparticle. *Circ. Res.* **2005**, *96* (3), 327-336.

39. Schellenberger, E. A.; Hogemann, D.; Josephson, L.; Weissleder, R., Annexin V-CLIO: a nanoparticle for detecting apoptosis by MRI. *Acad. Radiol.* **2002**, *9* (2, Suppl 1), S310-S311.

40. Koenig, S. H.; Keller, K. E., Theory of l/T_1 and 1/T_2 NMRD profiles of solutions of magnetic nanoparticles. *Magn. Reson. Med.* **1995**, *34* (2), 227-233.

41. Morales, M. P.; Veintemillas-Verdaguer, S.; Montero, M. I.; Serna, C. J., Surface and internal spin canting in γ-Fe_2O_3 nanoparticles. *Chem. Mater.* **1999**, *11* (11), 3058-3064.

42. Jeong, U.; Teng, X.; Wang, Y.; Yang, H.; Xia, Y., Superparamagnetic colloids: controlled synthesis and niche applications. *Adv. Mater.* **2007**, *19* (1), 33-60.

43. Park, J.; An, K.; Hwang, Y.; Park, J-G.; Noh, H-J.; Kim, J-Y.; Park, J-H.; Hwang, N-M.; Hyeon, T., Ultra-large-scale syntheses of monodisperse nanocrystals. *Nat. Mater.* **2004**, *3* (12), 891-895.

44. Jun, Y-w.; Huh, Y-M.; Choi, J-s.; Lee, J-H.; Song, H-T.; Kim, S.; Yoon, S.; Kim, K-S.; Shin, J-S.; Suh, J-S.; Cheon, J., Nanoscale size effect of magnetic nanocrystals and their utilization for cancer diagnosis via magnetic resonance imaging. *J. Am. Chem. Soc.* **2005**, *127* (16), 5732-5733.

45. Lee, J-H.; Huh, Y-M.; Jun, Y-w.; Seo, J-w.; Jang, J-t.; Song, H-T.; Kim, S.; Cho, E-J.; Yoon, H-G.; Suh, J-S.; Cheon, J., Artificially engineered magnetic nanoparticles for ultra-sensitive molecular imaging. *Nat. Med.* **2007**, *13* (1), 95-99.

46. Xu, C.; Xu, K.; Gu, H.; Zheng, R.; Liu, H.; Zhang, X.; Guo, Z.; Xu, B., Dopamine as a robust anchor to immobilize functional molecules on the iron oxide shell of magnetic nanoparticles. *J. Am. Chem. Soc.* **2004**, *126* (32), 9938-9939.

47. Kim, J. S.; Valencia, C. A.; Liu, R.; Lin, W., Highly-efficient purification of native polyhistidine-tagged proteins by multivalent NTA-modified magnetic nanoparticles. *Bioconjug. Chem.* **2007**, *18* (2), 333-341.

48. Kim, M.; Chen, Y.; Liu, Y.; Peng, X., Super-stable, high-quality Fe_3O_4 dendron-nanocrystals dispersible in both organic and aqueous solutions. *Adv. Mater.* **2005**, *17* (11), 1429-1432.

49. Kohler, N.; Fryxell, G. E.; Zhang, M., A bifunctional poly(ethylene glycol) silane immobilized on metallic oxide-based nanoparticles for conjugation with cell targeting agents. *J. Am. Chem. Soc.* **2004**, *126* (23), 7206-7211.

50. Kim, J.; Kim, H. S.; Lee, N.; Kim, T.; Kim, H.; Yu, T.; Song, I. C.; Moon, W. K.; Hyeon, T., Multifunctional uniform nanoparticles composed of a magnetite nanocrystal core and a mesoporous silica shell for magnetic resonance and fluorescence imaging and for drug delivery. *Angew. Chem. Int. Ed.* **2008**, *47* (44), 8438-8441.

51. Bulte, J. W. M.; Kraitchman, D. L., Iron oxide MR contrast agents for molecular and cellular imaging. *NMR Biomed.* **2004**, *17* (7), 484-499.

52. Lanza, G. M.; Winter, P. M.; Caruthers, S. D.; Hughes, M. S.; Cyrus, T.; Marsh, J. N.; Neubauer, A. M.; Partlow, K. C.; Wickline, S. A., Nanomedicine opportunities for cardiovascular diseases with perfluorocarbon nanoparticles. *Nanomed.* **2006**, *1* (3), 321-329.

53. Morawski, A. W.; Winter, P. M.; Crowder, K. C.; Caruthers, S. D.; Fuhrhop, R. W.; Scott, M. J.; Robertson, J. D.; Abendschein, D. R.; Lanza, G. M.; Wickline, S. A., Targeted nanoparticles for quantitative imaging of sparse molecular epitopes with MRI. *Magn. Reson. Med.* **2004**, *51* (3), 480-486.

54. Caruthers, S. D.; Wickline, S. A.; Lanza, G. M., Nanotechnological applications in medicine. *Curr. Opin. Biotechnol.* **2007**, *18* (1), 26-30.

55. Winter, P. M.; Caruthers, S. D.; Kassner, A.; Harris, T. D.; Chinen, L. K.; Allen, J. S.; Lacy, E. K.; Zhang, H.; Robertson, J. D.; Wickline, S. A.; Lanza, G. M., Molecular imaging of angiogenesis in nascent Vx-2 rabbit tumors using a novel $\alpha_v\beta_3$-targeted nanoparticle and 1.5 Tesla magnetic resonance imaging. *Cancer Res.* **2003**, *63* (18), 5838-5843.

56. Winter, P. M.; Morawski, A. M.; Caruthers, S. D.; Fuhrhop, R. W.; Zhang, H.; Williams, T. A.; Allen, J. S.; Lacy, E. K.; Robertson, J. D.; Lanza, G. M.; Wickline, S. A., Molecular imaging of angiogenesis in early-stage atherosclerosis with $\alpha_v\beta_3$-integrin–targeted nanoparticles. *Circulation* **2003**, *108* (18), 2270-2274.

57. Zhu, D.; White, R. D.; Hardy, P. A.; Weerapreeyakul, N.; Sutthanut, K.; Jay, M., Biocompatible nanotemplate-engineered nanoparticles containing gadolinium: stability and relaxivity of a potential MRI contrast agent. *J. Nanosci. Nanotechnol.* **2006**, *6* (4), 996-1003.

58. Zhu, D.; Lu, X.; Hardy, P. A.; Leggas, M.; Jay, M., Nanotemplate-engineered nanoparticles containing gadolinium for magnetic resonance imaging of tumors. *Invest. Radiol.* **2008**, *43* (2), 129-140.

59. Kabalka, G.; Buonocore, E.; Hubner, K.; Moss, T.; Norley, N.; Huang, L., Gadolinium-labeled liposomes: targeted MR contrast agents for the liver and spleen. *Radiology* **1987**, *163* (1), 255-258.

60. Kabalka, G. W.; Buonocore, E.; Hubner, K.; Davis, M.; Huang, L., Gadolinium-labeled liposomes containing paramagnetic amphipathic agents: targeted MRI contrast agents for the liver. *Magn. Reson. Med.* **1988**, *8* (1), 89-95.

61. Kabalka, G. W.; Davis, M. A.; Moss, T. H.; Buonocore, E.; Hubner, K.; Holmberg, E.; Maruyama, K.; Huang, L., Gadolinium-labeled liposomes containing various amphiphilic Gd-DTPA derivatives: targeted MRI contrast enhancement agents for the liver. *Magn. Reson. Med.* **1991**, *19* (2), 406-415.

62. Unger, E. C.; MacDougall, P.; Cullis, P.; Tilcock, C., Liposomal Gd-DTPA: effect of encapsulation on enhancement of hepatoma model by MRI. *Magn. Reson. Imaging.* **1989**, *7* (4), 417-23.

63. Unger, E. C.; Winokur, T.; MacDougall, P.; Rosenblum, J.; Clair, M.; Gatenby, R.; Tilcock, C., Hepatic metastases: liposomal Gd-DTPA – enhanced MR imgaging. *Radiology* **1989,** *171* (1), 81-85.

64. Sipkins, D. A.; Cheresh, D. A.; Kazemi, M. R.; Nevin, L. M.; Bednarski, M. D.; Li, K. C., Detection of tumor angiogenesis *in vivo* by $\alpha_v\beta_3$-targeted magnetic resonance imaging. *Nat. Med.* **1998**, *4* (5), 623-626.

65. Kamaly, N.; Kalber, T.; Ahmad, A.; Oliver, M. H.; So, P. W.; Herlihy, A. H.; Bell, J. D.; Jorgensen, M. R.; Miller, A. D., Bimodal paramagnetic and fluorescent liposomes for cellular and tumor magnetic resonance imaging. *Bioconjug. Chem.* **2008**, *19* (1), 118-129.

66. Bridot, J-L.; Faure, A-C.; Laurent, S.; Rivière, C.; Billotey, C.; Hiba, B.; Janier, M.; Josserand, V.; Coll, J-L.; Elst, L. V.; Muller, R.; Roux, S.; Perriat, P.; Tillement, O., Hybrid gadolinium oxide nanoparticles: multimodal contrast agents for in vivo imaging. *J. Am. Chem. Soc.* **2007**, *129* (16), 5076-5084.

67. Evanics, F.; Diamente, P. R.; van Veggel, F. C. J. M.; Stanisz, G. J.; Prosser, R. S., Water-soluble GdF_3 and GdF_3/LaF_3 nanoparticles – physical characterization and NMR relaxation properties. *Chem. Mater.* **2006**, *18* (10), 2499-2505.

68. Hifumi, H.; Yamaoka, S.; Tanimoto, A.; Citterio, D.; Suzuki, K., Gadolinium-based hybrid nanoparticles as a positive MR contrast agent. *J. Am. Chem. Soc.* **2006**, *128* (47), 15090-15091.

69. Gilad, A. A.; Walczak, P.; McMahon, M. T.; Na, H. B.; Lee, J. H.; An, K.; Hyeon, T.; van Zijl, P. C. M.; Bulte, J. W. M., MR tracking of transplanted cells with "positive contrast" using manganese oxide nanoparticles. *Magn. Reson. Med.* **2008**, *60* (1), 1-7.

70. Na, H. B.; Lee, J. H.; An, K.; Park, Y. I.; Park, M.; Lee, I. S.; Nam, D-H.; Kim, S. T.; Kim, S-H.; Kim, S-W.; Lim, K-H.; Kim, K-S.; Kim, S-O.; Hyeon, T., Development of a T_1 contrast agent for magnetic resonance imaging using MnO nanoparticles. *Angew. Chem. Int. Ed.* **2007**, *46* (28), 5397-5401.

71. Seo, W. S.; Lee, J. H.; Sun, X.; Suzuki, Y.; Mann, D.; Liu, Z.; Terashima, M.; Yang, P. C.; Mcconnell, M. V.; Nishimura, D. G.; Dai, H., FeCo/graphitic-shell nanocrystals as

advanced magnetic-resonance-imaging and near-infrared agents. *Nat. Mater.* **2006**, *5* (12), 971-976.

72. Rieter, W.J.; Kim, J.S.; Taylor, K.M.L.; An, H.; Lin, W.; Tarrant, T.; Lin, W., Hybrid silica nanoparticles for multimodal imaging. *Angew. Chem. Int. Ed*. **2007**, *46* (20), 3680-3682.

73. Kim, J.S.; Rieter, W.J.; Taylor, K.M.L.; An, H.; Lin, W.; Lin, W., Self-assembled hybrid nanoparticles for cancer-specific multimodal imaging. *J. Am. Chem. Soc*. **2007**, *129* (29), 8962-8963.

74. Taylor, K. M. L.; Kim, J. S.; Rieter, W. J.; An, H.; Lin, W.; Lin, W., Mesoporous silica nanospheres as highly efficient MRI contrast agents. *J. Am. Chem. Soc*. **2008**, *130* (7), 2154-2155.

75. Entley, W. R.; Girolami, G. S., High-temperature molecular magnets based on cyanovanadate building blocks: spontaneous magnetization at 230 K. *Science*. **1995**, *268* (5209), 397-400.

76. Vaucher, S.; Li, M.; Mann, S., Synthesis of prussian blue nanoparticles and nanocrystal superlattices in reverse microemulsions. *Angew. Chem. Int. Ed.* **2000**, *39* (10), 1793-1796.

77. Vaucher, S.; Fielden, J.; Li, M.; Dujardin, E.; Mann, S., Molecule-based magnetic nanoparticles: synthesis of cobalt hexacyanoferrate, cobalt pentacyanonitrosylferrate, and chromium hexacyanochromate coordination polymers in water-in-oil microemulsions. *Nano Lett.* **2002**, *2* (3), 225-229.

78. Catala, L.; Gacoin, T.; Boilot, J. P.; Riviere, E.; Paulsen, C.; Lhotel, E.; Mallah, T., Cyanide-bridged Cr^{III}-Ni^{II} superparamagnetic nanoparticles. *Adv. Mater*. **2003**, *15* (10), 826-829.

79. Uemura, T.; Kitagawa, S., Prussian blue nanoparticles protected by poly(vinyl-pyrrolidone). *J. Am. Chem. Soc.* **2003**, *125* (26), 7814-7815.

80. Fiorito, P. A.; Goncales, V. R.; Ponzio, E. A.; de Torresi, S. I. C., Synthesis, characterization and immobilization of Prussian blue nanoparticles. A potential tool for biosensing devices. *Chem. Commun.* **2005** (3), 366-368.

81. Taguchi, M.; Yamada, K.; Suzuki, K.; Sato, O.; Einaga, Y., Photoswitchable magnetic nanoparticles of prussian blue with amphiphilic azobenzene. *Chem. Mater.* **2005**, *17* (17), 4554-4559.

82. Uemura, T.; Kitagawa, S., Nanocrystals of coordination polymers. *Chem. Lett.* **2005**, *34* (2), 132-137.

83. Kitagawa, S.; Kitaura, R.; Noro, S., Functional porous coordination polymers. *Angew. Chem. Int. Ed.* **2004**, *43* (18), 2334-2375.

84. Wu, C-D.; Lin, W., Heterogeneous asymmetric catalysis with homochiral metal-organic frameworks: network-structure-dependent catalytic activity. *Angew. Chem. Int. Ed.* **2007**, *46* (7), 1075-1078.

85. Evans, O. R.; Lin, W., Crystal engineering of NLO materials based on metal-organic coordination networks. *Acc. Chem. Res.* **2002**, *35* (7), 511-522.

86. Rieter, W. J.; Taylor, K. M. L.; An, H.; Lin, W.; Lin, W., Nanoscale metal-organic frameworks as potential multimodal contrast enhancing agents. *J. Am. Chem. Soc.* **2006**, *128* (28), 9024-9025.

87. Rieter, W. J.; Taylor, K. M. L.; Lin, W., Surface modification and functionalization of nanoscale metal-organic frameworks for controlled release and luminescence sensing. *J. Am. Chem. Soc*. **2007**, *129* (32), 9852-9853.

88. Rieter, W. J.; Pott, K. M.; Taylor, K. M. L.; Lin, W., Nanoscale coordination polymers for platinum-based anticancer drug delivery. *J. Am. Chem. Soc.* **2008**, *130* (35), 11584-11585.

89. Yolken, R. H. and Wee, S-B., Enzyme immunoassays in which biotinillated β-lactamase is used for the detection of microbial antigens. *J. Clin. Microbiol.* **1984**, *19* (3), 356-360.

90. King, D.; Luna, V.; Cannons, A.; Cattani, J.; and Amuso, P., Performance assessment of three commercial assays for direct detection of *Bacillus anthracis* spores. *J. Clin. Microbiol.* **2003**, *41* (7), 3454-3455.

91. De Wit, M. Y.; Faber, W. R.; Krieg, S. R.; Douglas, J. T.; Lucas, S. B.; and Hartskeerl, R. A., Application of a polymerase chain reaction for the detection of mycobacterium leprae in skin tissues. *J. Clin. Microbiol.* **1991**, *29* (5), 906-910.

92. Hurtle, W.; Bode, E.; Kulesh, D. A.; Kaplan, R. S.; Garrison, J.; Bridge, D.; House, M.; Frye, M. S.; Loveless, B.; Norwood, D., Detection of the *Bacillus anthracis gyrA* gene by using a minor groove binder probe. *J. Clin. Microbiol.* **2004**, *42* (1), 179-185.

93. Fasanella, A.; Losito, S.; Adone, R.; Ciuchini, F.; Trotta, T.; Altamura, S. A.; Chiocco, D.; Ippolito, G., PCR assay to detect *Bacillus anthracis* spores in heat-treated specimens. *J. Clin. Microbiol*. **2003**, *41* (2), 896-899.

94. Farquharson, S.; Gift, A. D.; Maksymiuk, P.; and Inscore, F. E., Rapid dipicolinic acid extraction from Bacillus spores detected by surface-enhanced Raman spectroscopy. *Appl. Spectrosc.* **2004**, *58* (3), 351-354.

95. Zhang, X.; Young, M. A.; Lyandres, O.; and Van Duyne, R. P., Rapid detection of an anthrax biomarker by surface-enhanced Raman spectroscopy *J. Am. Chem. Soc.* **2005**, *127* (12), 4484-4489.

96. Bell, S. E. J.; Mackle, J. N.; and Sirimuthu, N. M. S., Quantitative surface-enhanced Raman spectroscopy of dipicolinic acid—towards rapid anthrax endospore detection. *Analyst* **2005**, *130* (4), 545-549.

97. Pellegrino, P. M.; Fell Jr., N. F.; and Gillespie, J. B., Enhanced spore detection using dipicolinate extraction techniques. *Analytica Chimica Acta*, **2002**, *455* (2), 167-177.

98. Rosen, D. L.; Sharpless, C.; and McGown, L. B., Bacterial spore detection and determination by use of terbium dipicolinate photoluminescence. *Anal. Chem.* **1997**, *69* (6), 1082-1085.

99. Pellegrino, P. M.; Fell, Jr., N. F.; Rosen, D. L.; and Gillespie, J. B., Bacterial endospore detection using terbium dipicolinate photoluminescence in the presence of chemical and biological materials. *Anal. Chem.* **1998**, *70* (9), 1755-1760.

100. Hindle, A. A. and Hall, E. A. H., Dipicolinic acid (DPA) assay revisited and appraised for spore detection. *Analyst* **1999**, *124* (11), 1599-1604.

101. Cable, M. L.; Kirby, J. P.; Sorasaenee, K.; Gray, H. B.; and Ponce, A., Bacterial spore detection by [Tb^{3+}(macrocycle)(dipicolinate)] luminescence. *J. Am.Chem. Soc.* **2007**, *129* (6), 1474-1475.

CHAPTER 2

Mesoporous Silica Nanoparticles as Contrast Agents for Magnetic Resonance Imaging

2.1 Introduction

Contrast enhanced magnetic resonance imaging (MRI) is a noninvasive diagnostic tool that cannot only provide high resolution anatomical images of soft tissue, but also quantitatively assess disease pathogenesis by measuring up-regulated biomarkers. However, currently used MRI contrast agents are mainly small molecule gadolinium chelates that lack sensitivity and often cannot provide sufficient image contrast enhancement in early disease stages. Nanoparticulate MR contrast agents are much more sensitive owing to the enhanced relaxivity (on per magnetic center basis) as a result of reduced tumbling rates and large payloads of active magnetic centers. For example, Weissleder *et al.* and others have used iron oxide nanoparticles as T_2 contrast agents to image tumor angiogenesis, inflammation, and gene expression.[1] Lanza, Wickline, and co-workers have developed Gd^{3+}-containing microemulsions as efficient T_1-contrast agents for intravascular MR imaging.[2] Several other Gd^{3+}-containing solid nanoparticles have also been recently evaluated as potential MRI contrast agents.[3-6]

Our recent results indicate that the accessibility of the magnetic center to water molecules is key to designing highly efficient nanoparticulate MR contrast agents,[5-6] underscoring the need of developing new strategies for the synthesis of nanoparticles that can allow ready access of water molecules to the magnetic centers. Our group has previously developed a solid silica nanoparticle based MRI contrast agent, which consists of 37 nm particles coated with either a monolayer coating or a polymeric multilayer coating of Gd^{3+} chelates. The results from these two systems revealed that the particles with a multilayer coating had reduced efficiency, or lower relaxivities, on a per Gd^{3+} basis. This was due to

the fact that the Gd chelates on the inner layers were not as accessible to the surrounding water molecules.[5]

In order to address the problem of reduced efficiency, while still increasing the number of metal centers per particle, an alternative method for forming the nanoparticle based contrast agents was developed. This method involved the use of a layer-by-layer electrostatic assembly of the particle coating. Using this method up to 7 bilayers of alternating negatively charged polystyrenesulfonate and a cationic Gd(III)-DOTA oligomer were assembled. Results from this nanoparticle system showed the relaxivity on a per Gd basis remained constant, independent of the number of layers assembled. The relaxivity on a per particle basis increased linearly with the increasing number of layers deposited. These results indicated that the disordered structure of the layer-by-layer assembly allows for efficient interaction of all the Gd(III) centers with the surrounding water.[6]

Another approach to designing a system that can incorporate a large number of Gd chelates while keeping them all accessible to the surrounding water is to use a porous platform. Mesoporous materials can provide an ideal platform for the development of MR-enhancing hybrid materials due to their high surface areas and tunable pore structures. MCM-41 type materials, for example, possess a hexagonal array of one dimensional channels with diameters that can be tuned from 2–10 nm.[7-8] More recently, synthetic procedures have been developed for controlling the morphologies of MCM-41 materials,[9-10] leading to mesoporous silica nanospheres (MSNs) with diameters ranging from 60 to 1100 nm that have been utilized in a variety of applications including catalysis[11] and drug delivery.[12-13] Victor Lin has also reported a co-condensation method used to incorporate various organic functional groups into the pores of MSN.[14-15] We surmised that grafting or incorporating of

Gd chelates onto MSNs can provide an ideal platform for designing highly efficient MR contrast agents because of the ability to carry a large payload of Gd centers and the enhanced water accessibility of the Gd chelates. We have synthesized and characterized several highly efficient MSN-based MR contrast agents and evaluated their application in *in vitro* and *in vivo* MR imaging.

2.2 Results and Discussion

2.2.1 Ligand and Gd Complex Synthesis

Two different DTPA based ligands were synthesized for this work. First, 3-aminopropyl(trimethoxysilyl)diethylenetriamine tetraacetic acid (Si-DTTA), was synthesized by reacting 3-(trimethoxysilylpropyl)diethylene triamine with 4 equivalents of bromo acetic acid under basic conditions. This formed a Gd chelating ligand containing one trialkoxy silane functional group for attachment to the silica based particles. The second, bis(3-aminopropyl triethoxysilyl)diethylenetriamine pentaacetic acid (Si_2-DTPA) was synthesized by reacting 2 equivalents of 3-aminopropyltriethoxysilane with DTPA dianhydride in anhydrous pyridine. This provided a Gd chelating ligand with two trialkoxysilane functional groups to allow for incorporation into the mesoporous silica. The corresponding Gd(III) complexes for each ligand were formed by reacting 1 equivalent of $GdCl_3$ with the deprotonated form of the ligand.

2.2.2 Synthesis of MSN-Gd Using Grafting Method (2-1)

The MSN nanoparticles (**2-0**) were first synthesized using a surfactant templated, base-catalyzed condensation procedure.[16] Briefly, cetyltrimethylammonium bromide

(CTAB) (0.100 g, 0.274 mmol) was dissolved in 48 mL of distilled water along with 0.35 mL of 2 M NaOH.   The solution was heated to 80 °C before the addition of 0.5 mL of tetraethylorthosilicate (TEOS). The reaction mixture was stirred for an additional 2 hours at 80 °C. The particles were isolated by centrifuging and washed with water and ethanol. The surfactant template was then extracted with either a 1 wt% solution of NaCl in methanol or a 1 volume% solution of HCl in methanol.

The Si-DTTA-Gd complex was grafted onto the MSN particles through the siloxane linkages by adding an aqueous solution of the complex to a suspension of extracted MSN particles in toluene (Scheme 2.1-2.2). The reaction was then heated to reflux for 18 hours. After cooling, the particles (**2-1**) were isolated by centrifuging, washed with water, ethanol, and a pH 3 solution. Finally, the particles were dialyzed against distilled water to remove any free chelates adsorbed into the channels.

Gd-Si-DTTA

Scheme 2.1. Schematic showing the Si-DTTA-Gd complexes residing in the hexagonally ordered nanochannels of **2-1** MSN**.**

Scheme 2.2. Schematic presentation of the Si-DTTA-Gd chelates that have been grafted onto the interior walls of the MSN nanoparticles **2-1** via the siloxane linkage.

Fluorescently labeled particles (**2-1a**) were also synthesized by immobilizing a rhodamine B derivative onto the particles. Rhodamine B isothiocyanate (RITC) was reacted with 3-aminopropyltriethoxysilane to give a rhodamine B derivative with a triethoxysilane group that can be used for covalent attachment to the silica particles. To synthesize the fluorescently labeled particles, 4 mol% of the rhodamine B-aminopropyltriethoxysilane (relative to Si-DTTA-Gd) was added along with the Gd complex during the coating reaction.

2.2.3 Synthesis of MSN-Gd Using the Co-Condensation Method

Several MSN-Gd contrast agents were also synthesized by incorporating varying amounts of the Si-DTTA-Gd or Si_2-DTPA-Gd complexes into the particles using a co-condensation method. Particles were synthesized using 10 wt% Si-DTTA-Gd (**2-2**) and 10, 20, 30, and 40 wt% Si_2-DTPA-Gd complexes (**2-3** through **2-6**) (relative to the amount of TEOS added), using a similar procedure as was used to synthesize the bare MSN particles.

For example, particles **2-3** (10 wt% Si$_2$-DTPA-Gd) were synthesized as follows. 0.200 g (0.549 mmol) of CTAB was dissolved in 240 mL of water containing 0.7 mL of 2 M NaOH (1.40 mmol). This solution was heated at 80 °C for 30 minutes before adding 1.0 mL (0.93 g, 4.48 mmol) of TEOS and 0.79 mL of a 0.17 M aqueous solution of the Si$_2$-DTPA-Gd complex. The reaction was then stirred at 80 °C for 2 hours. The particles were isolated by centrifuging and washed with water and ethanol. The surfactant template was then extracted with a 1 wt% solution of NaCl in methanol at room temperature. In order to ensure the removal of any free Gd^{3+} ions the particles were also washed with a pH 3 solution.

2.2.4 Characterization

Scanning electron and transmission electron microscopies (SEM and TEM) were used to evaluate the particle size and morphology. For MSN-Gd **2-1** the as-synthesized particles were fairly uniform spherical particles with a mean diameter of 75 nm (Fig. 2.1). No change in the particle size or morphology was seen after extraction of the solvent or grafting of the Si-DTTA-Gd chelate (Figs. 2.2-2.5). Particles **2-2** through **2-6** were more polydisperse compared to the bare MSN particles. The particle size also generally increased with increasing wt% of the Gd complex (Fig. 2.6-2.14). The SEM and TEM images also showed some evidence of aggregation and fusing of particles prepared using the co-condensation method.
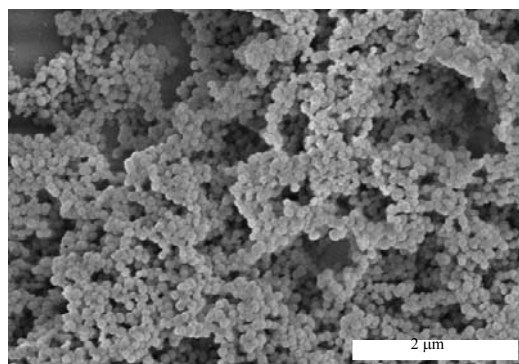
Figure 2.1. SEM image of as-synthesized bare MSN nanoparticles (**2-0**).
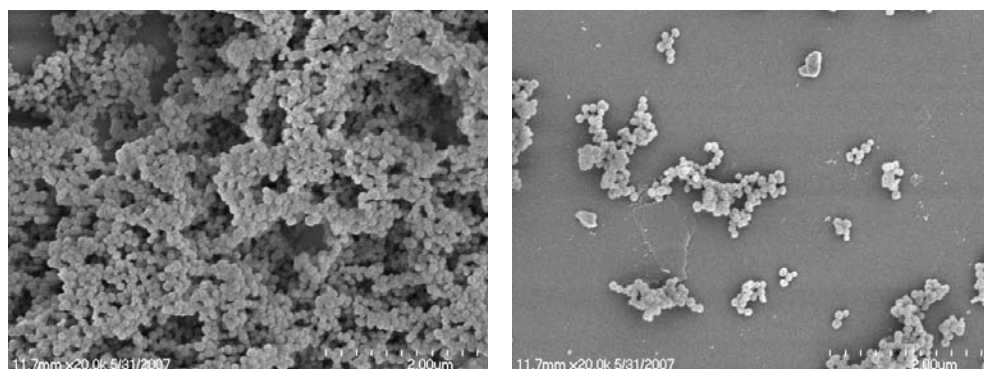
Figure 2.2. SEM images of surfactant-extracted bare MSN nanoparticles (**2-0**).
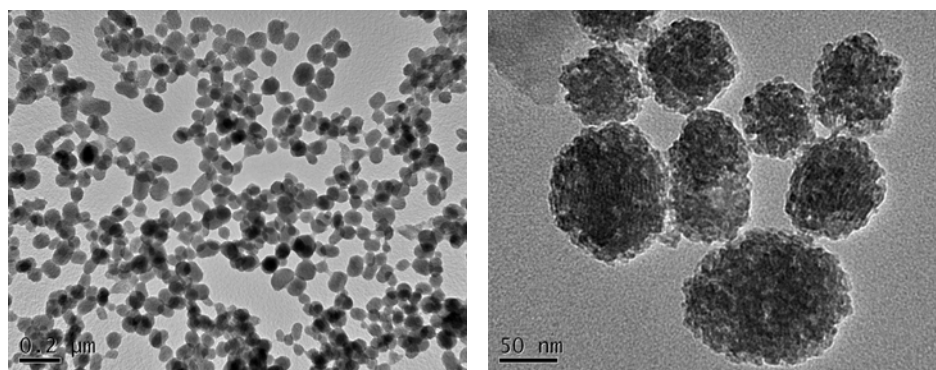
Figure 2.3. TEM images of surfactant-extracted bare MSN nanoparticles (**2-0**).
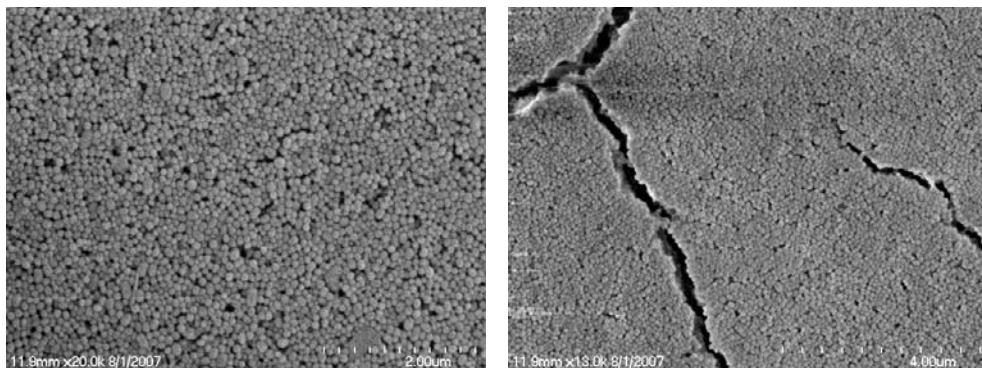
Figure 2.4. SEM images of MSN-Gd (**2-1**) particles.
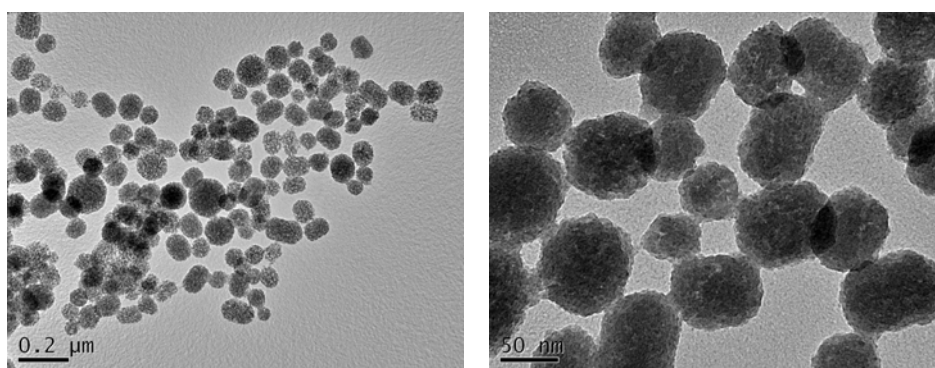
Figure 2.5. TEM images of MSN-Gd (**2-1**) particles.
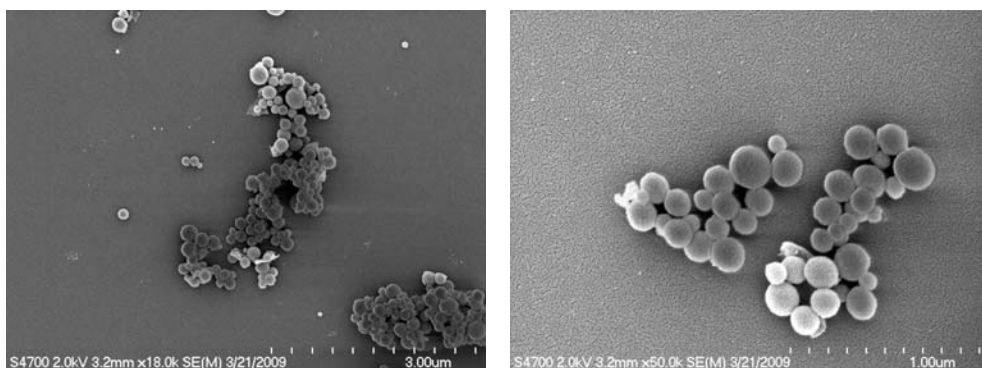
Figure 2.6. SEM images of **2-2** particles.
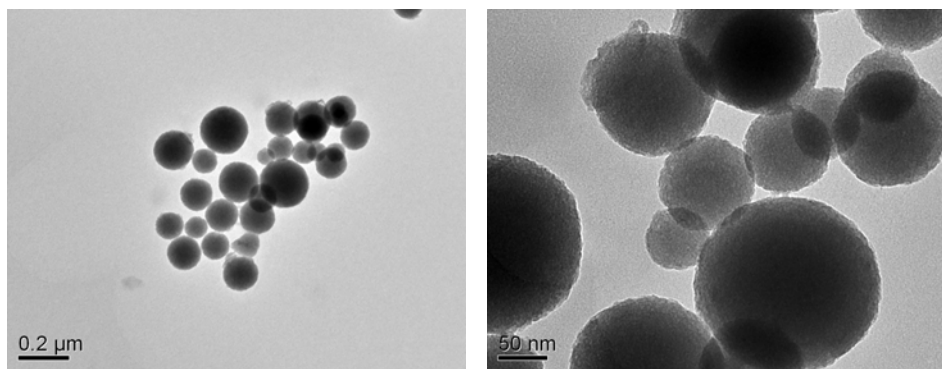
Figure 2.7. TEM images of **2-2** particles.
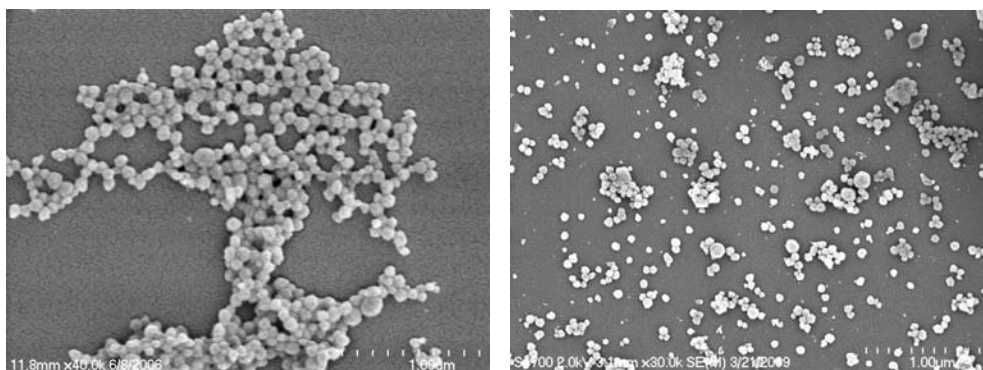
Figure 2.8. SEM images of **2-3** particles.
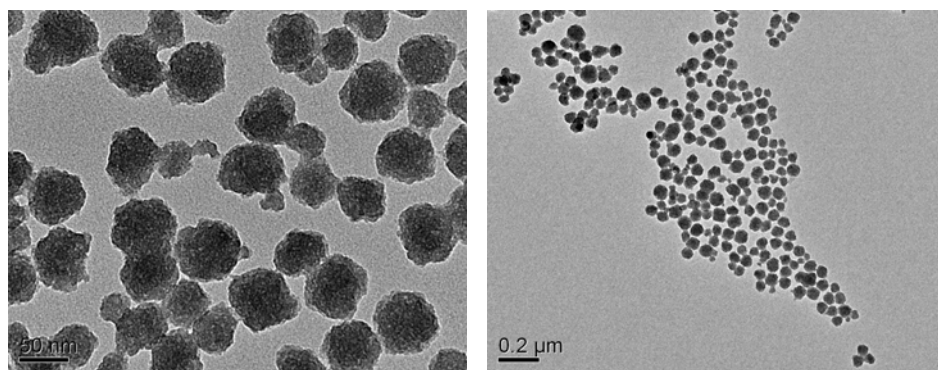
Figure 2.9. TEM images of **2-3** particles.
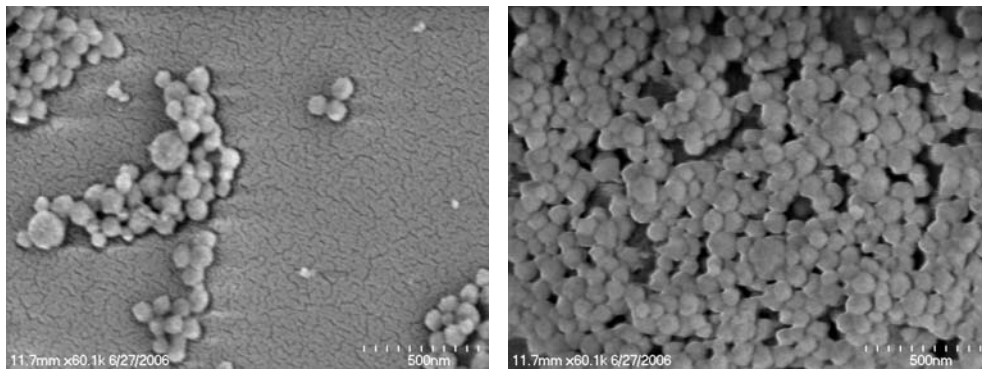
Figure 2.10. SEM images of **2-4** particles.
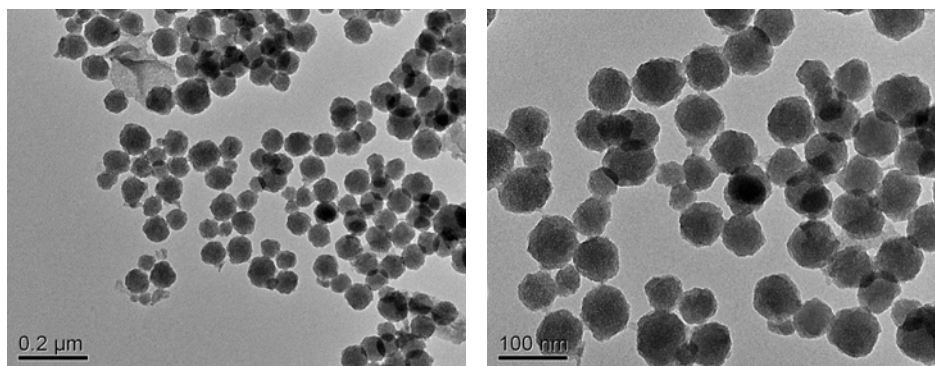
Figure 2.11. TEM images of **2-4** particles.
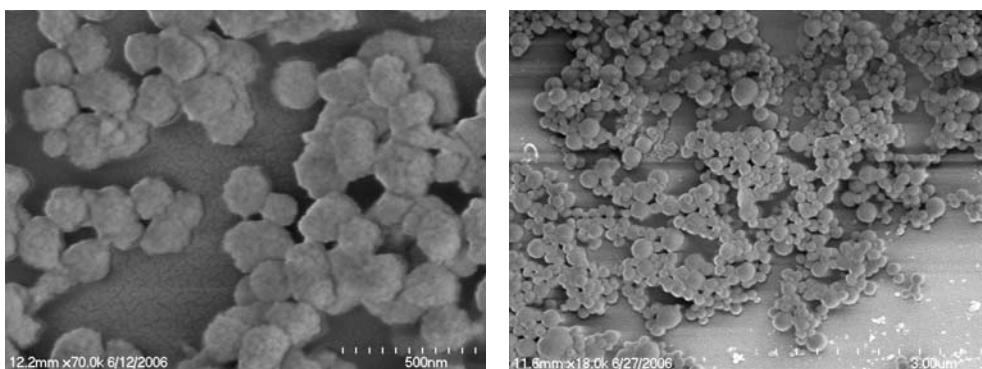
Figure 2.12. SEM images of **2-5** particles.
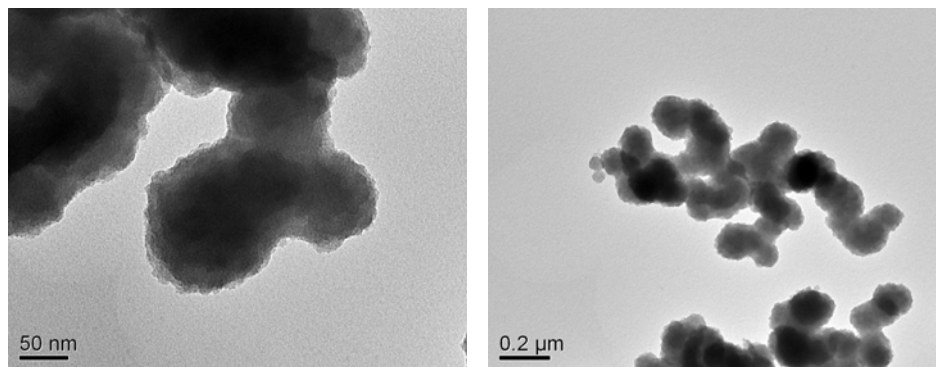
Figure 2.13. TEM images of **2-5** particles.
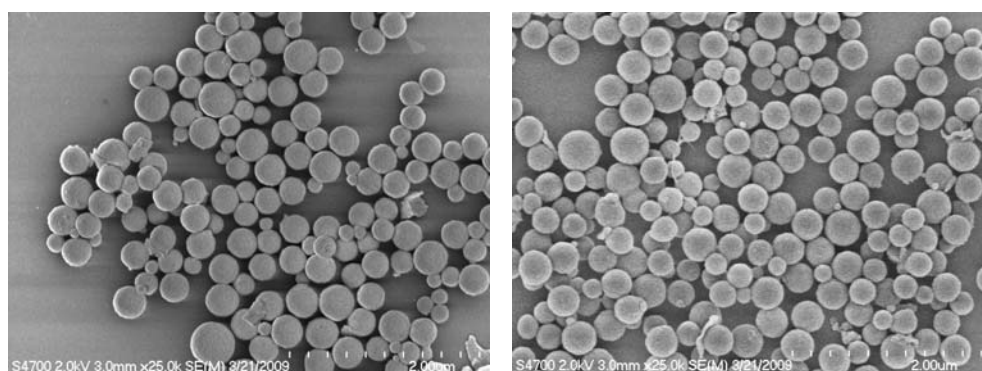
Figure 2.14. SEM images of **2-6** particles.

The pore structure of the particles was evaluated using powder X-ray diffraction (PXRD) and nitrogen gas sorption measurements. The bare MSN particles exhibit PXRD peaks at 2θ values of 2.8, 4.6, and 5.4° that are characteristic of the (100), (110), and (200) planes of the MCM-41 material, respectively (Fig. 2.15). Nitrogen gas sorption measurements indicated that the surfactant-extracted bare MSN (**2-0**) is highly porous with a surface area of 1633 m^2/g (BJH method - Barrett-Joiner-Halenda) and a pore diameter of 2.4 nm, whereas the MSN-Gd (**2-1**) material has a reduced surface area of 1470 m^2/g and a pore diameter of 0.9-1.0 nm (Fig. 2.16-2.17). A pore size can also be estimated using the d-spacing from the (100) peak at 2.8° in the PXRD. From this 2θ value, a d-spacing of 31.8 Å is calculated, which corresponds to a repeat unit of 3.67 nm. If a pore-wall thickness of 1 nm

45

is assumed, the pore diameter is calculated to be 2.67 nm, which corresponds well to the

nitrogen sorption measurements.
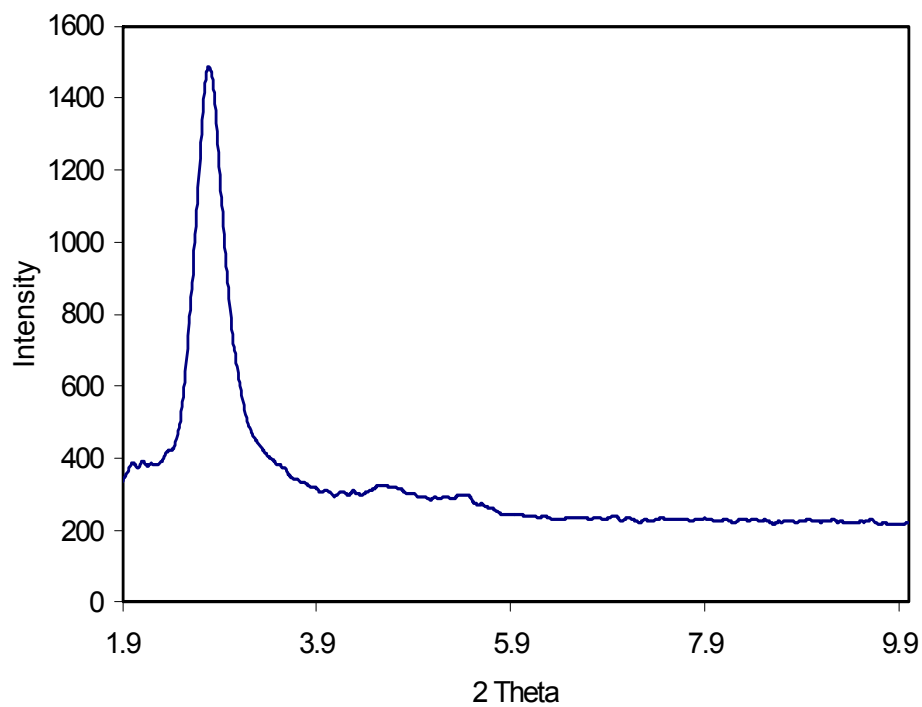
Figure 2.15. Powder X-ray diffraction pattern of bare MSN particles (**2-0**), showing peaks at 2.8°, 4.6°, and 5.4°.
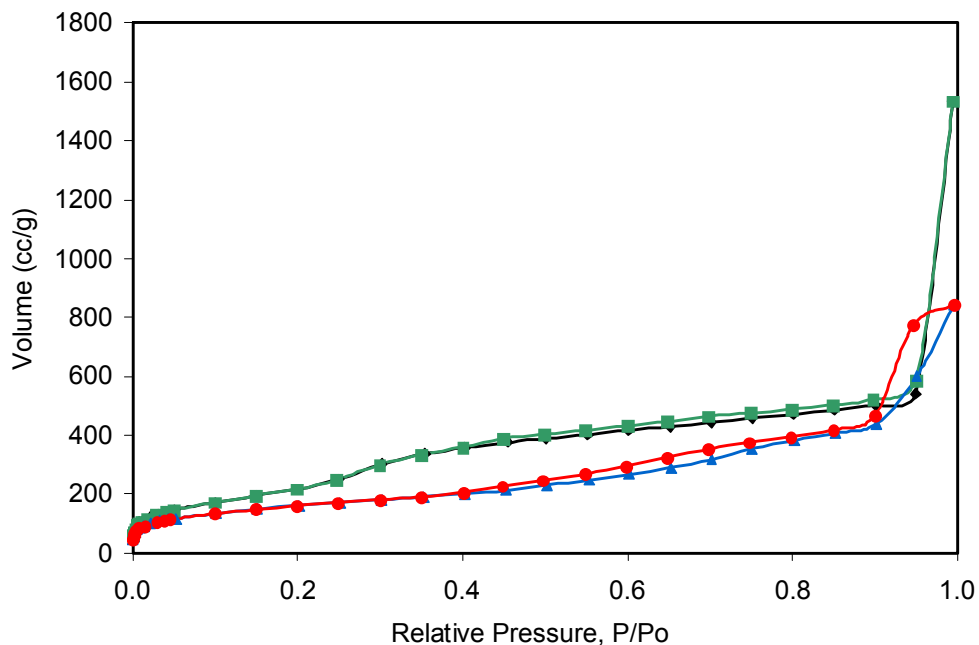
Figure 2.16. Nitrogen sorption isotherm of surfactant-extracted bare MSN (**2-0**) (black-adsorption; green-desorption) and MSN-Gd (**2-1**) (blue-adsorption; red-desorption).
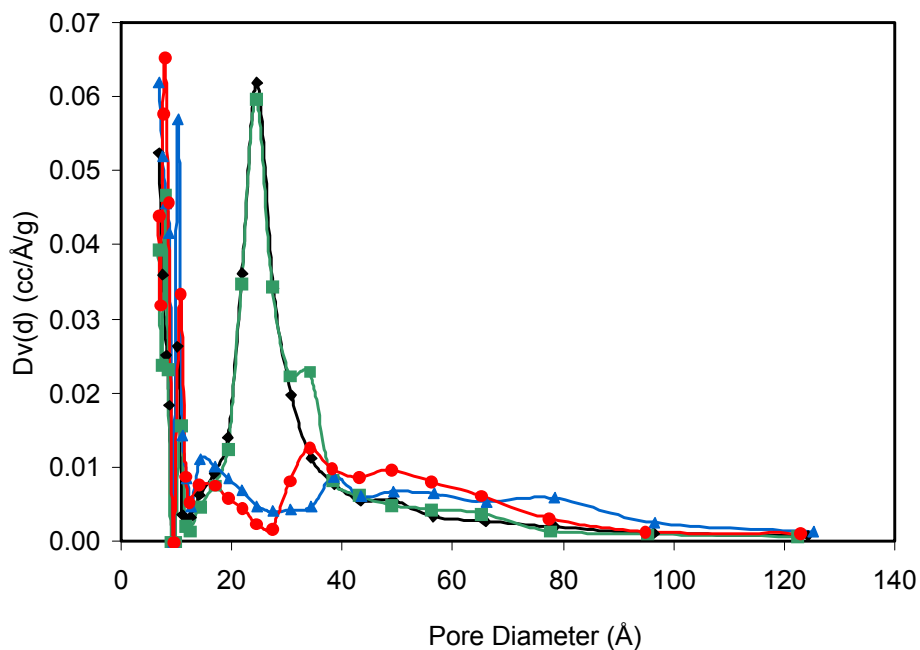
Figure 2.17. Pore size distribution of surfactant-extracted bare MSN (**2-0**) (black-adsorption; green-desorption) and MSN-Gd (**2-1**) (blue-adsorption; red-desorption).

Nitrogen sorption measurements also showed that the co-condensation particles (**2-2** through **2-6**) have large surface areas and pore diameters ranging from 1.4 to 2.9 nm in diameter (Fig. 2.18-2.27). The surface areas and pore sizes decrease with increasing incorporation of the Gd complexes (Table 2.1).

Table 2.1. Summary of surface areas and pore sizes for co-condensed MSN samples.

Particles	Amnt. Gd complex	BJH Surface Area	BJH Pore Size
2-2	10 wt% Si-DTTA-Gd	832 m^2/g	1.94 nm
2-3	10 wt% Si$_2$-DTPA-Gd	1674 m^2/g	2.91 nm
2-4	20 wt% Si$_2$-DTPA-Gd	1095 m^2/g	2.75 nm
2-5	30 wt% Si$_2$-DTPA-Gd	923 m^2/g	2.46 nm
2-6	40 wt% Si$_2$-DTPA-Gd	149 m^2/g	1.41 nm
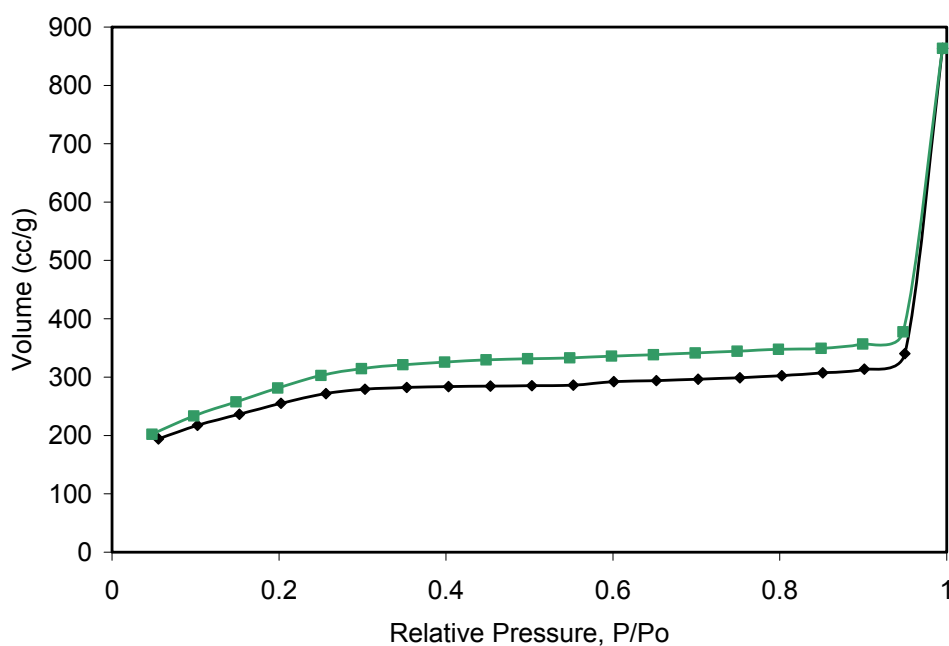
Figure 2.18. Nitrogen sorption isotherm of **2-2** (black-adsorption; green-desorption).
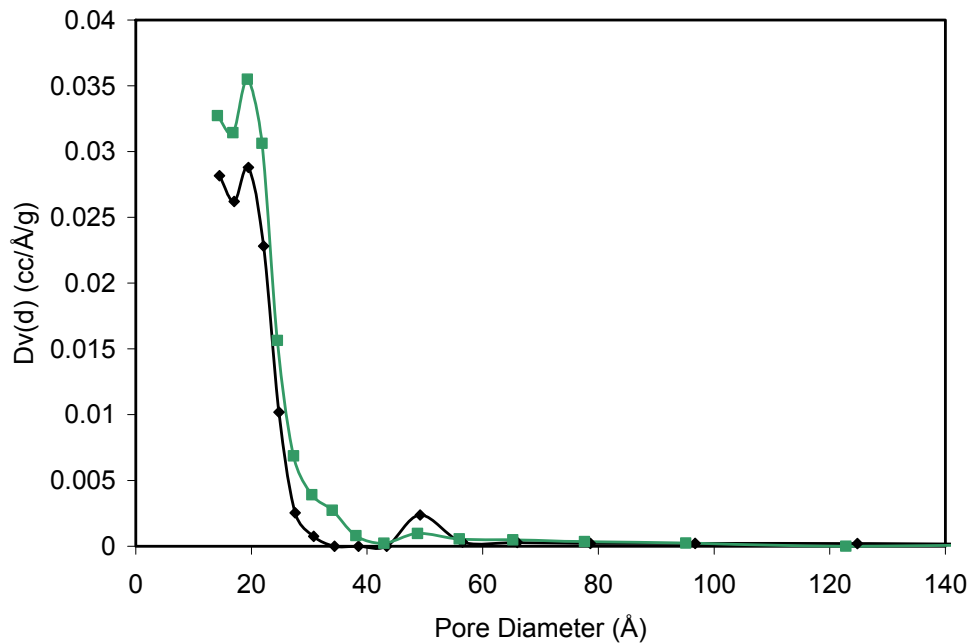
Figure 2.19. Pore size distribution of **2-2** (black-adsorption; green-desorption).
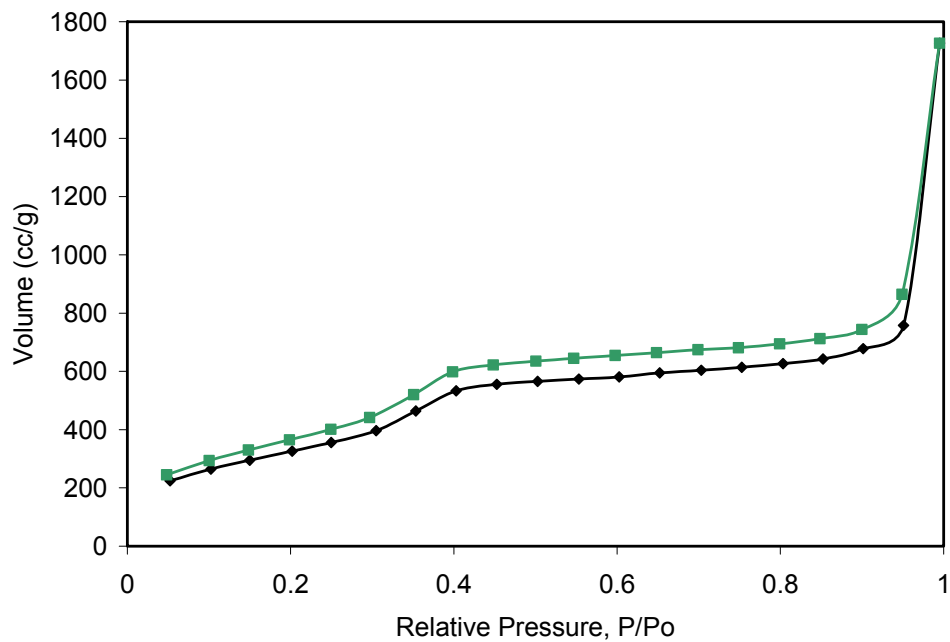
Figure 2.20. Nitrogen sorption isotherm of **2-3** (black-adsorption; green-desorption).
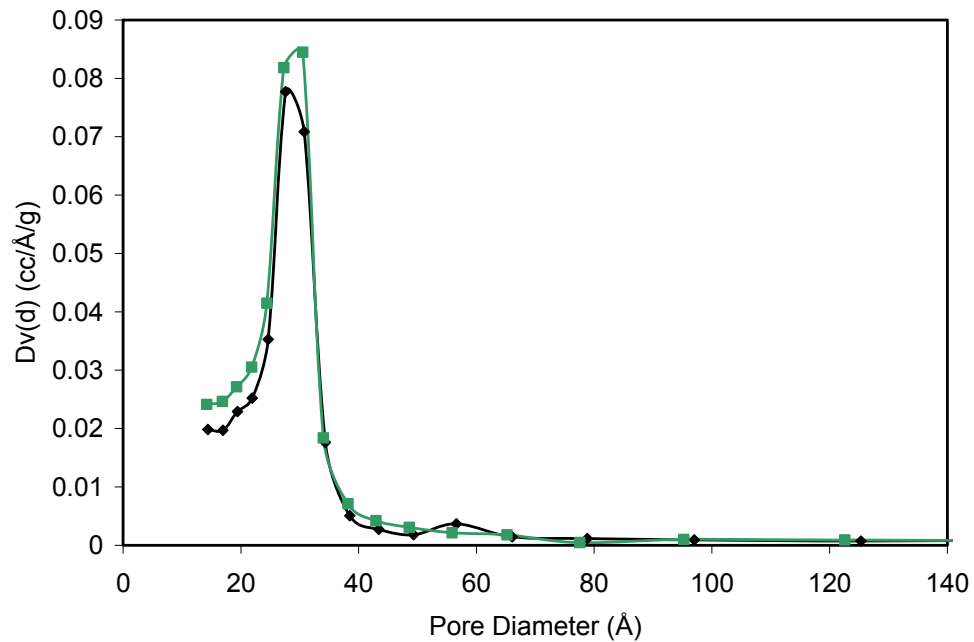
Figure 2.21. Pore size distribution of **2-3** (black-adsorption; green-desorption).
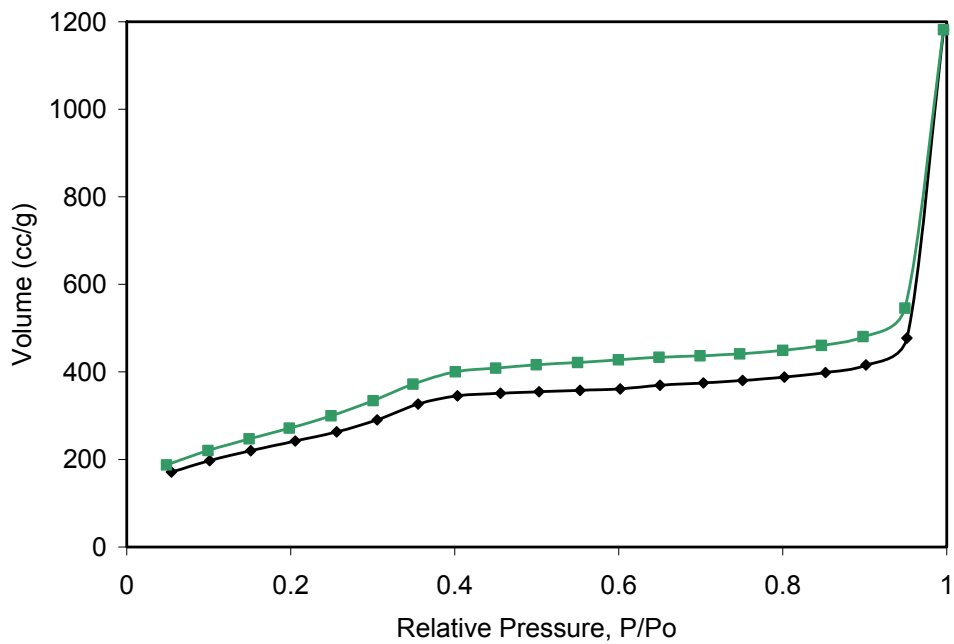
Figure 2.22. Nitrogen sorption isotherm of **2-4** (black-adsorption; green-desorption).
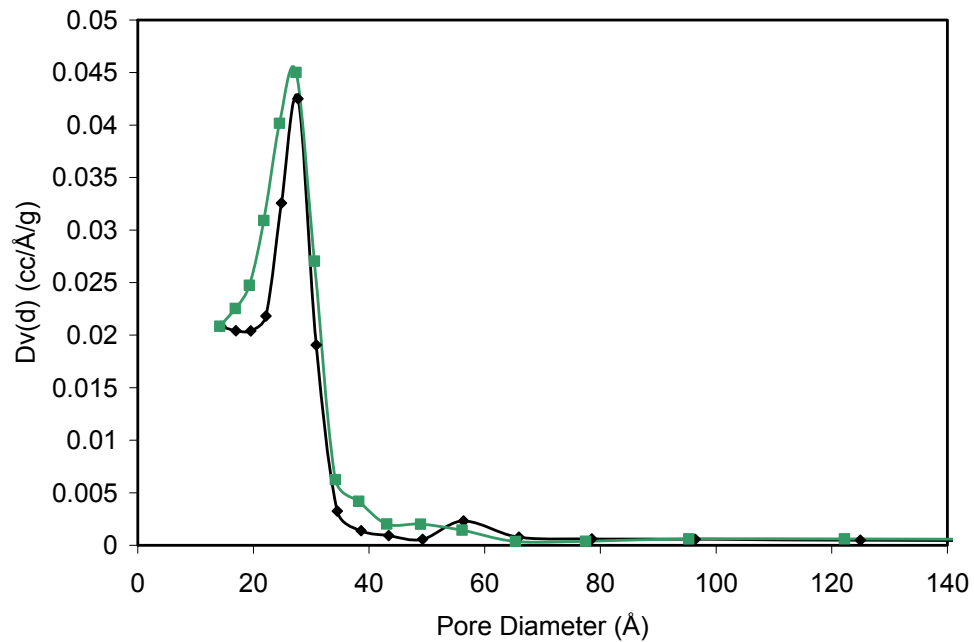
Figure 2.23. Pore size distribution of **2-4** (black-adsorption; green-desorption).
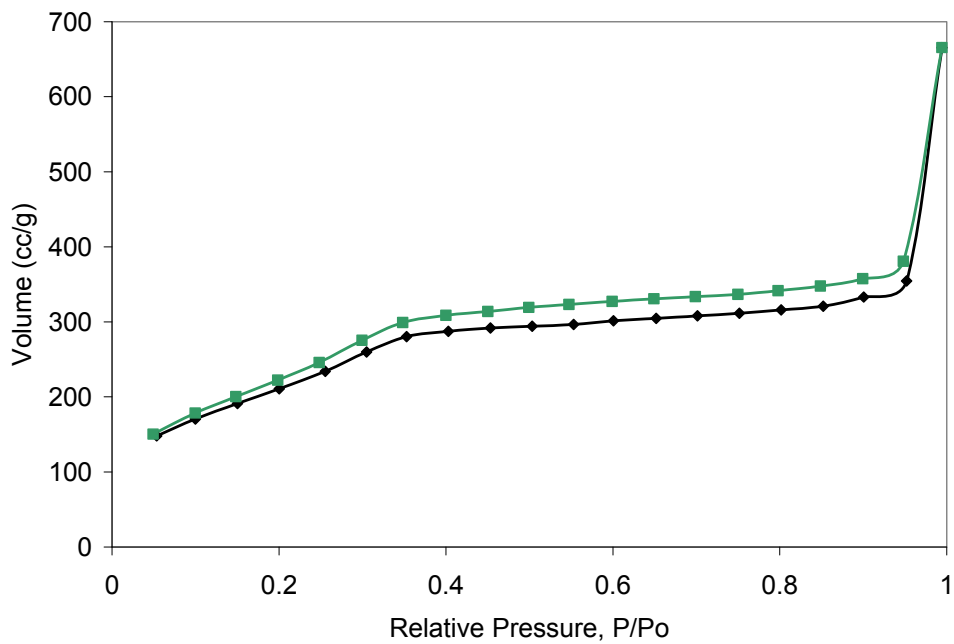
Figure 2.24. Nitrogen sorption isotherm of **2-5** (black-adsorption; green-desorption).
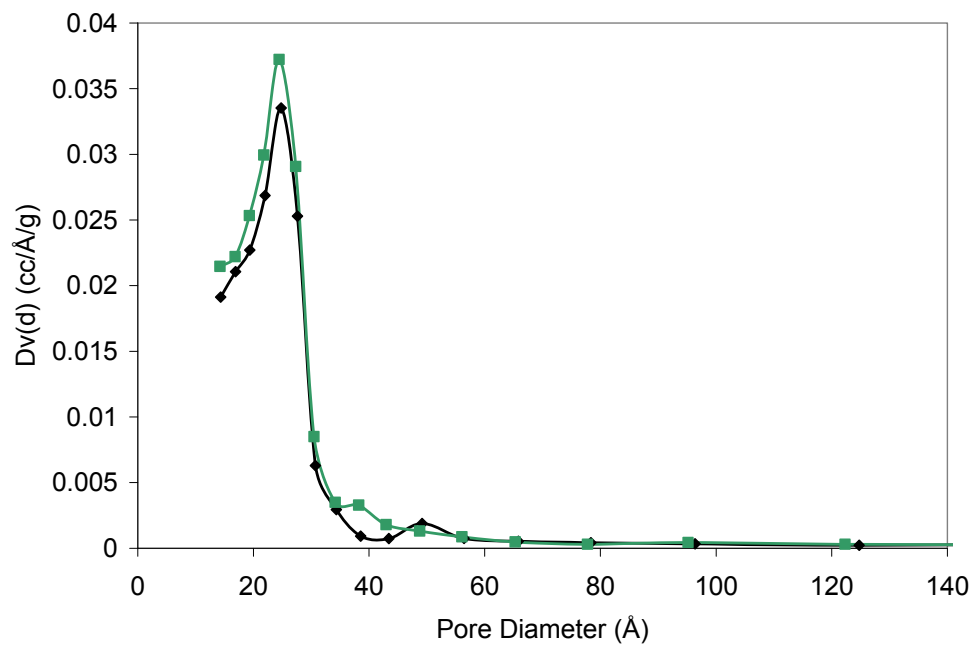
Figure 2.25. Pore size distribution of **2-5** (black-adsorption; green-desorption).
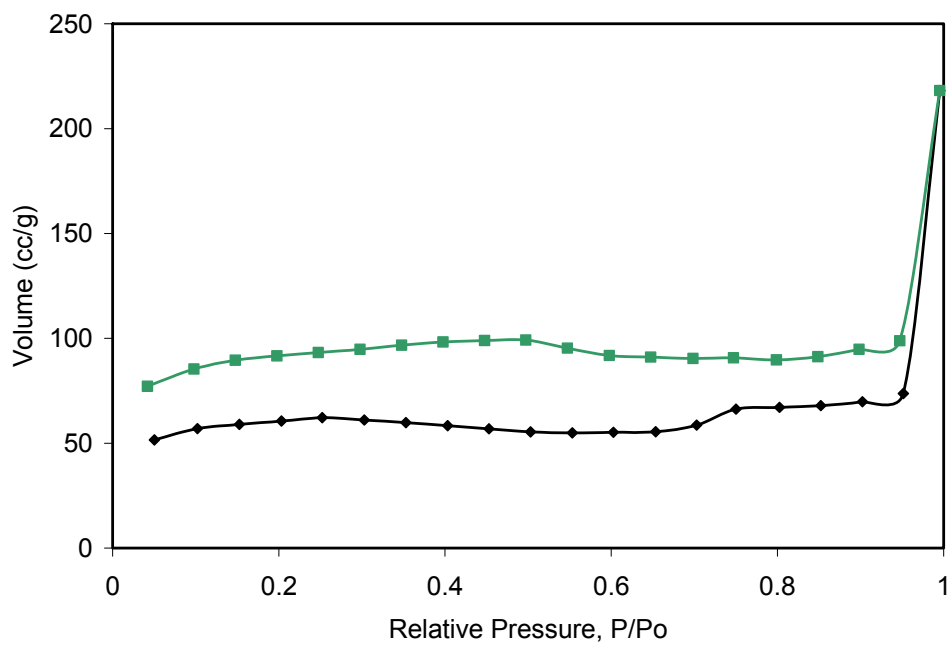
Figure 2.26. Nitrogen sorption isotherm of **2-6** (black-adsorption; green-desorption).
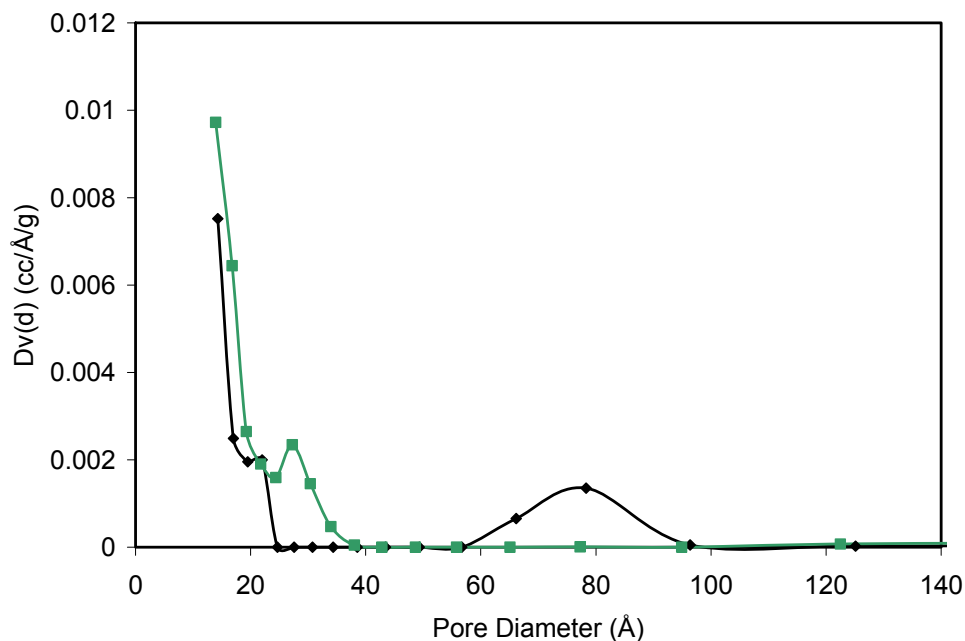
Figure 2.27. Pore size distribution of **2-6** (black-adsorption; green-desorption).

Thermogravimetric analysis (TGA) was used to verify the complete extraction of the surfactant template, and the grafting of the Si-DTTA-Gd complex for **2-1** (Fig. 2.28). The as-synthesized particles show an initial weight loss of approximately 6 wt% from room temperature to ~125 °C from adsorbed solvent, and a second weight loss of approximately 34 wt% from 150-400 °C from the loss of the surfactant template. Complete extraction of the surfactant is verified by the disappearance of the second weight loss; only a single weight loss of about 10 wt% is observed from room temperature to ~125 °C resulting from the loss of adsorbed solvent. After grafting of the Si-DTTA-Gd chelate, a weight loss of ~12 wt% is observed from about 220-500 °C, resulting from the loss of the organic portion of the Gd complex. The precise amount of Gd complex on each particle was determined by digesting a sample of the particles in concentrated nitric acid and then measuring the [Gd] using direct current plasma spectroscopy (DCP). Using DCP, the loading of Si-DTTA-Gd complex was

found to range from 15.7 to 20.1 wt%. This corresponds to an average of ~36,900 Gd chelates on each 75 nm particle.
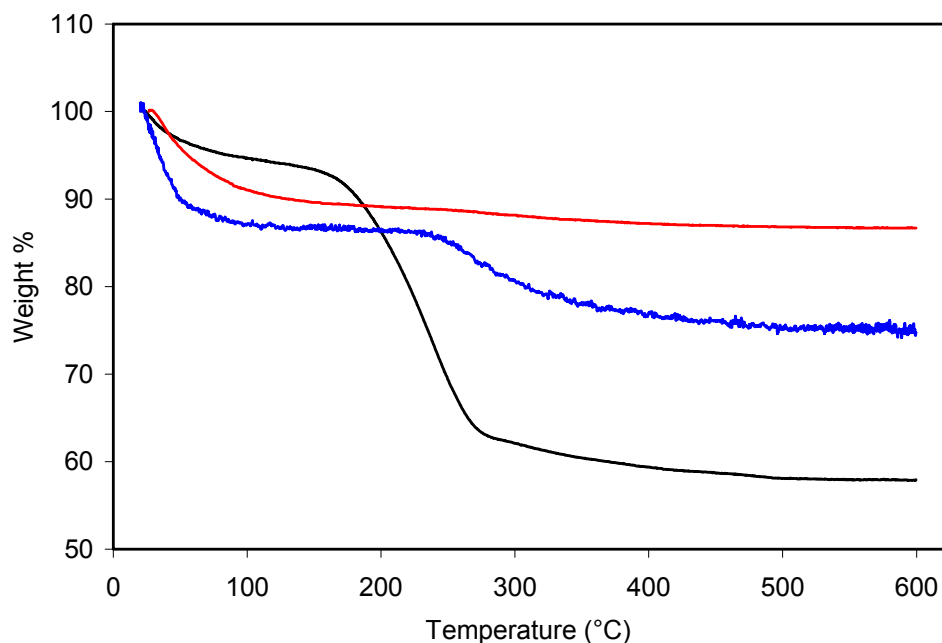
Figure 2.28. TGA curves of as-synthesized bare MSN (black), surfactant-extracted bare MSN (**2-0**) (red), and **2-1** (blue).

TGA was also used to characterize the amount of Gd chelate that had been incorporated in each of the products from the co-condensation reactions (Fig. 2.29-2.33). After extraction of the surfactant, the weight loss in the 230-450 °C temperature range corresponds to the organic portion of the incorporated Gd complexes. The precise amount of Gd complex that had been incorporated was then determined by measuring the [Gd] of a digested particle solution using DCP. The TGA and DCP gave fairly consistent results as to the amount of incorporated Gd complex (Table 2.2)
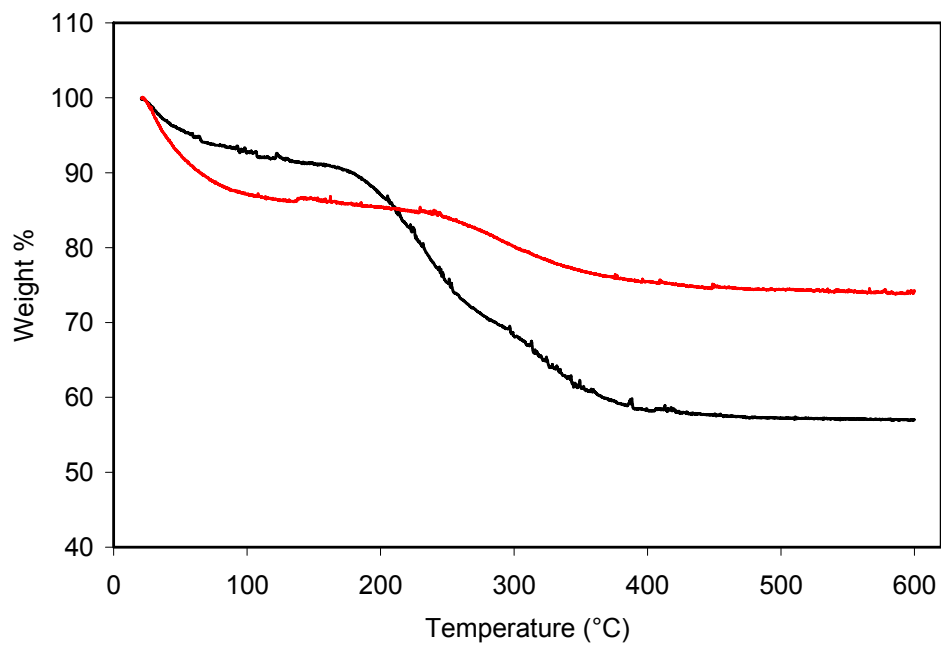
Figure 2.29. TGA of **2-2** before (black) and after (red) surfactant extraction.
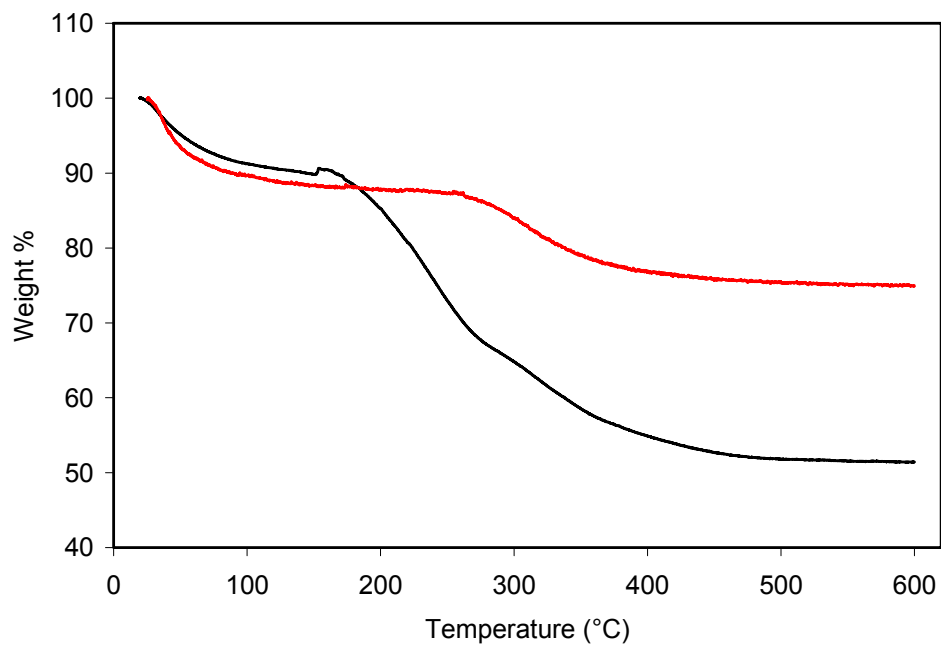
Figure 2.30. TGA of **2-3** before (black) and after (red) surfactant extraction.
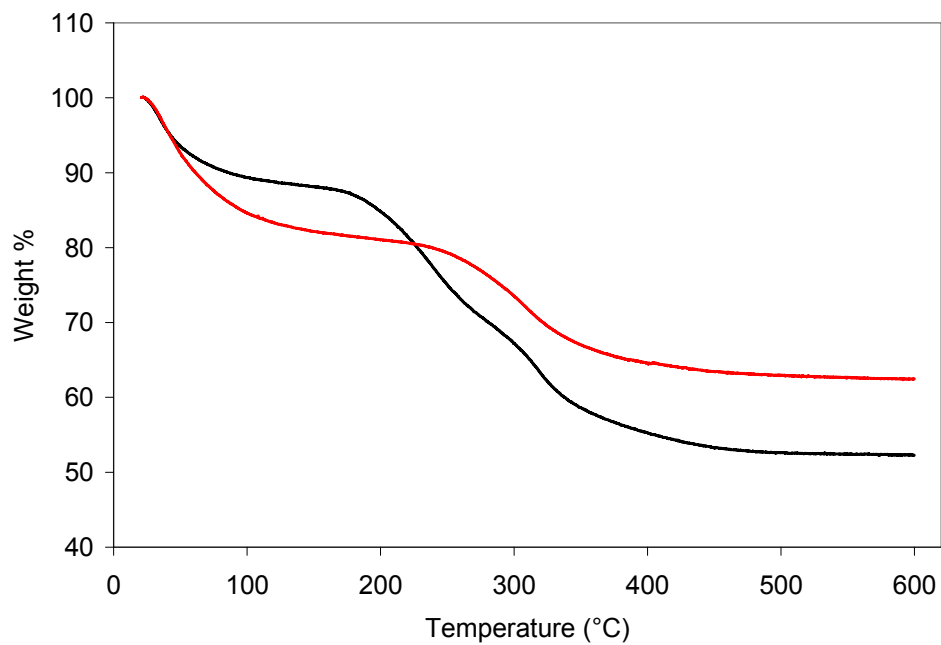
Figure 2.31. TGA of **2-4** before (black) and after (red) surfactant extraction.
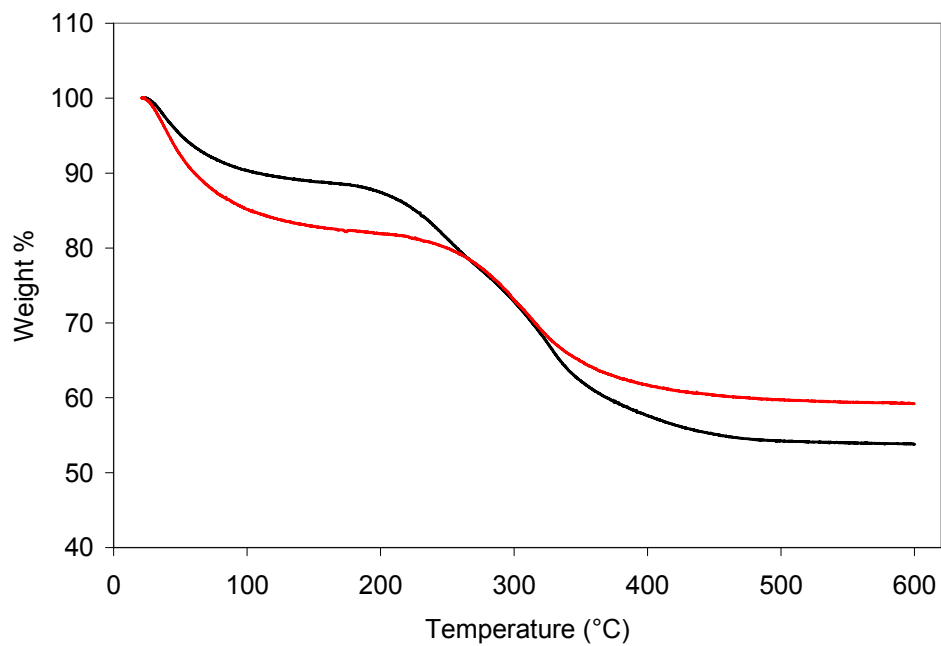
Figure 2.32. TGA of **2-5** before (black) and after (red) surfactant extraction.
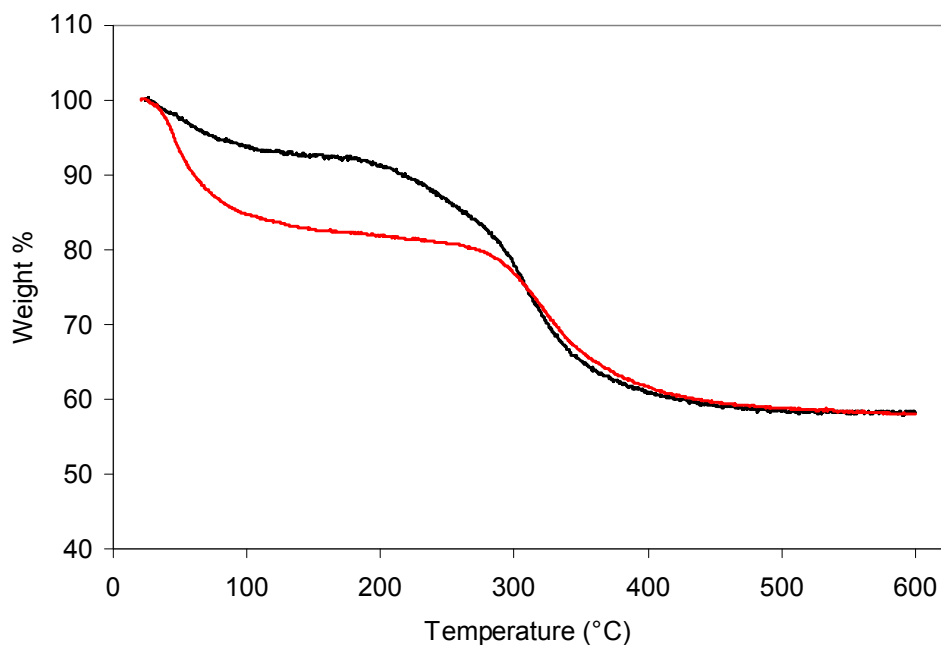
Figure 2.33. TGA of **2-6** before (black) and after (red) surfactant extraction.

Table 2.2. Summary of TGA and DCP results for co-condensed MSN samples.

Particles	TGA - Organic Wt. Loss	DCP - Wt% Gd	DCP - Calc. Wt% Ligand
2-2	15.99 wt%	5.32 wt%	15.17 wt%
2-3	14.47 wt%	3.81 wt%	15.09 wt%
2-4	23.12 wt%	4.70 wt%	18.61 wt%
2-5	27.68 wt%	6.76 wt%	26.77 wt%
2-6	28.77 wt%	8.08 wt%	32.01 wt%

In order to confirm that all free Gd chelates had been removed from **2-1** during the dialysis process and that the chelates were stable, a leaching experiment was performed. 11 mg of **2-1** was dispersed in water was dialyzed against 250 mL of distilled water (pH = 7.4) at 37 °C. Aliquots of the dialysis water were removed at different time points and dried. The residue was then redissolved in nitric acid, diluting to a final nitric acid concentration of 1 M. The [Gd] was then measured using DCP. It was found that essentially no Gd was released from the particles after 46 hours (Fig. 2.34).
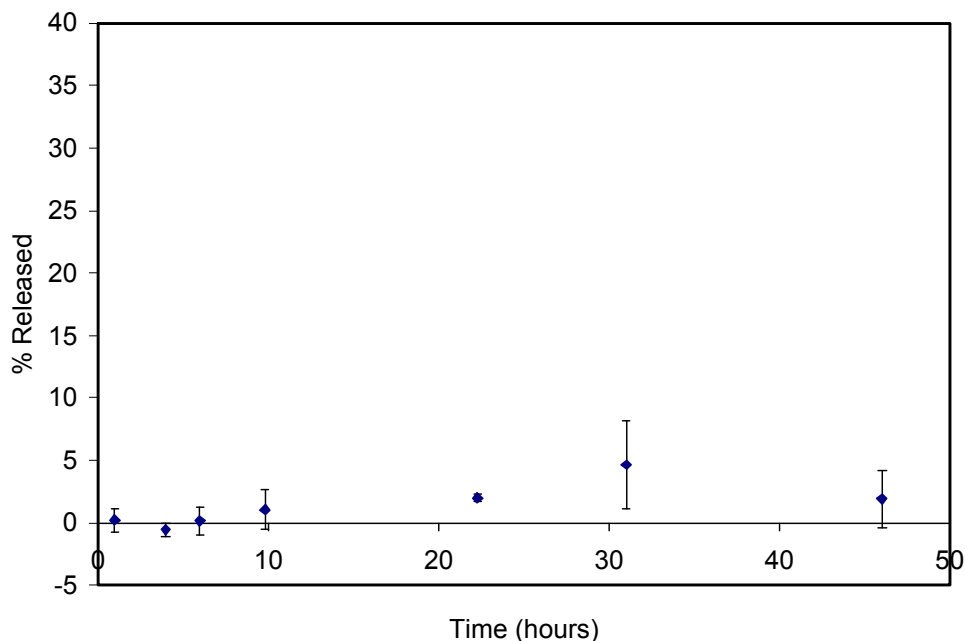
Figure 2.34. Percentage of Gd-containing species that have been released from the MSN-Gd materials in water at 37 °C as a function of time.

2.2.5 Relaxivity Measurements

The MR relaxivities of **2-1** were measured using both a 3.0 T (Fig. 2.35) and a 9.4 T (Fig. 2.36) MR scanner. The particles exhibited very large longitudinal (r_1) and transverse (r_2) relaxivities. On a per mM Gd basis, **2-1** has an r_1 of 28.8 mM^{-1}s^{-1} at 3 T and 10.2 mM^{-1}s^{-1} at 9.4 T. The r_2 relaxivities are 65.5 mM^{-1}s^{-1} at 3 T and 110.8 mM^{-1}s^{-1} at 9.4 T, respectively. Since each particle of **2-1** contains approximately 36,900 Gd ions, the r_1 and r_2 values on a per mM of particle basis are 1.06×10^6 mM^{-1}s^{-1}(3 T) / 3.76×10^5 mM^{-1}s^{-1} (9.4 T) and 2.42×10^6 mM^{-1}s^{-1} (3 T) / 4.09×10^6 (9.4 T), respectively. These relaxivity values are much larger than the solid silica nanoparticles that are coated with multilayers of Gd-DTPA derivative that was previously reported by our group.[5] We attributed the enhanced MR relaxivity to the ready access of water molecules through the nanochannels of the MSN-Gd particles.
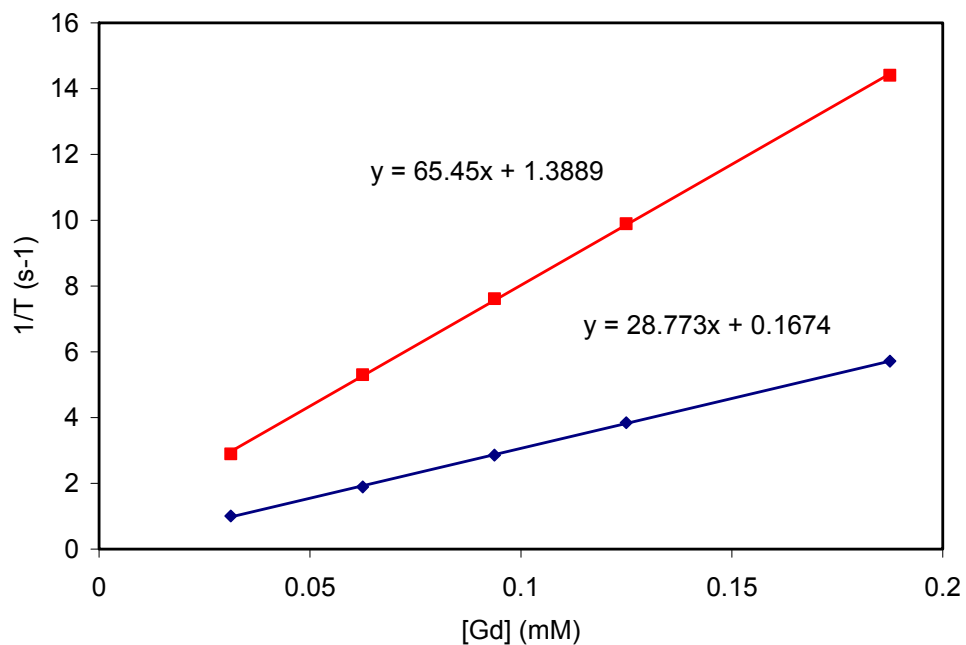
Figure 2.35. r_1 (blue) and r_2 (red) relaxivity curves of **2-1** measured at 3 T.
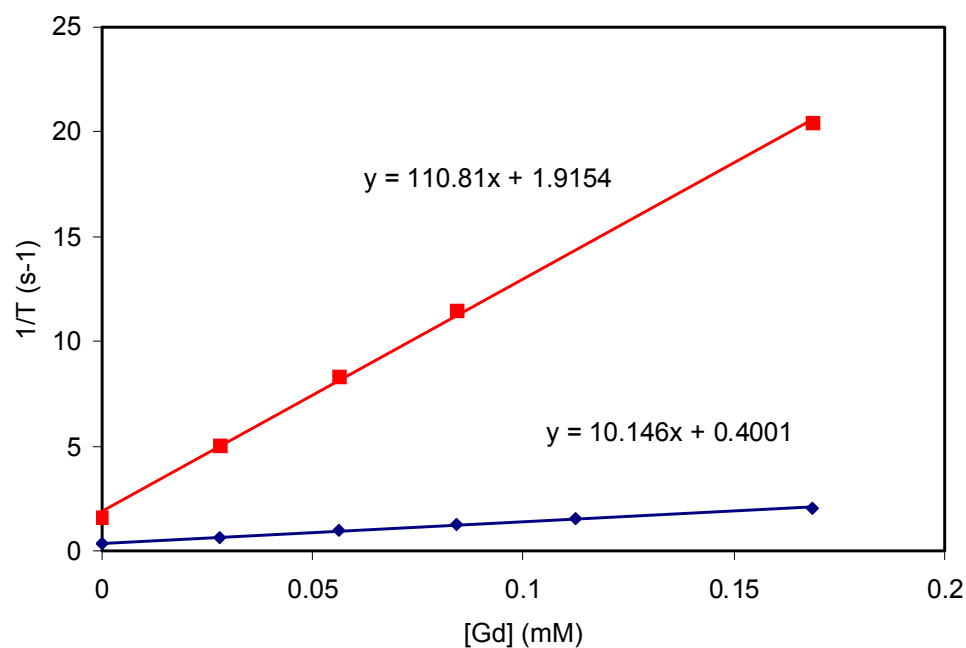
Figure 2.36. r_1 (blue) and r_2 (red) relaxivity curves of **2-1** measured at 9.4 T.

The relaxivities for the particles obtained using the co-condensation method were all measured using a 3 T MR scanner. The relaxivities for these particles were generally lower

than what was obtained for **2-1**, however there was relatively little difference in the per Gd relaxivities across samples with varying amounts of incorporated Gd complex (Table 2.3). The r_1 values ranged from 4.1 to 8.4 mM^{-1}s^{-1}, and the r_2 values ranged from 16.1 to 32.7 mM^{-1}s^{-1} (Fig. 2.37-2.41). The lower relaxivity values for the co-condensed samples may be due to the fact that some of the Gd chelates that were incorporated into the particles are not at the surface, and therefore are not available to undergo water exchange with the solvent.

Table 2.3. Summary of relaxivities for co-condensed MSN samples measured at 3 T.

Particles	r_1 (mM^{-1}s^{-1})	r_2 (mM^{-1}s^{-1})
2-2	6.2	32.7
2-3	5.1	16.1
2-4	4.1	25.3
2-5	4.8	22.9
2-6	8.4	25.6
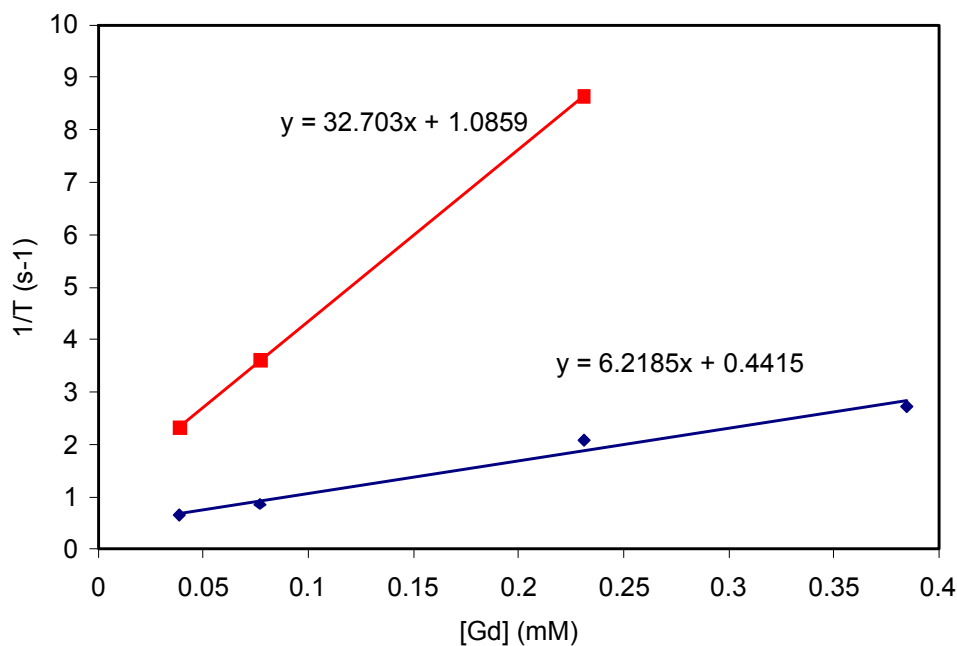
Figure 2.37. r_1 (blue) and r_2 (red) relaxivity curves of **2-2** measured at 3 T.

60
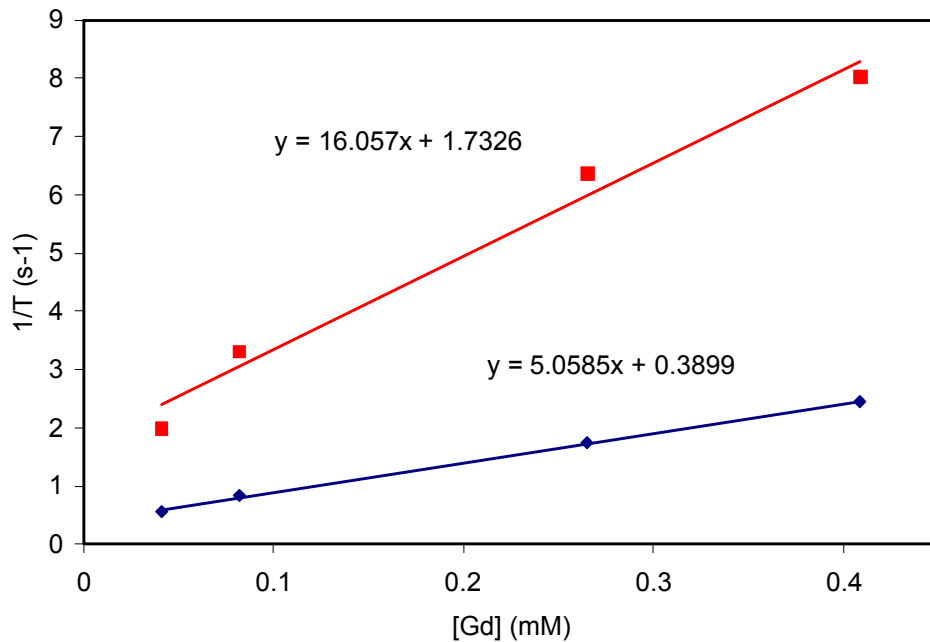
Figure 2.38. r_1 (blue) and r_2 (red) relaxivity curves of **2-3** measured at 3 T.

$y = 16.057x + 1.7326$

$y = 5.0585x + 0.3899$
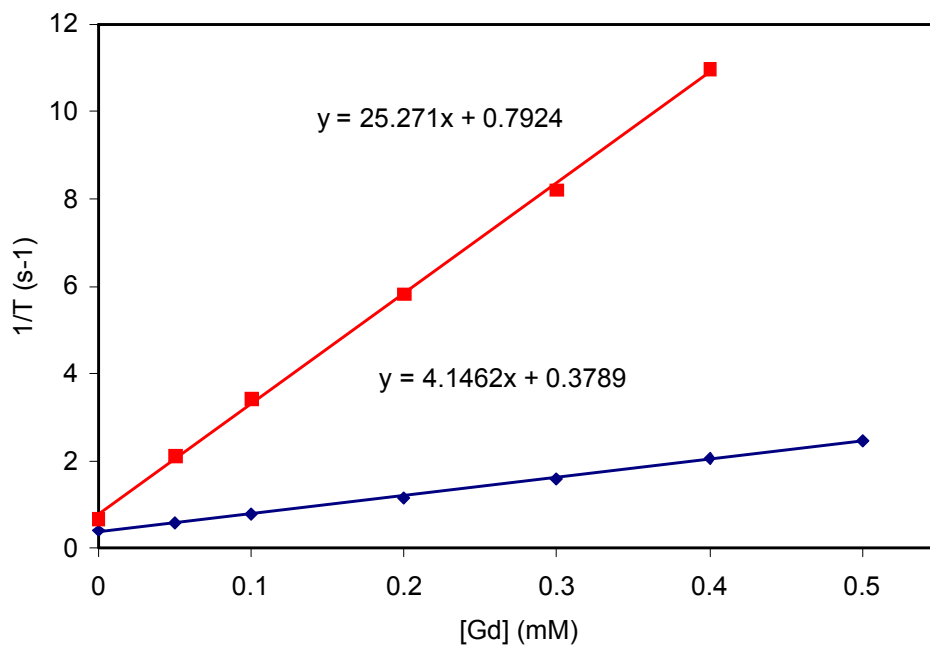
Figure 2.39. r_1 (blue) and r_2 (red) relaxivity curves of **2-4** measured at 3 T.

$y = 25.271x + 0.7924$

$y = 4.1462x + 0.3789$
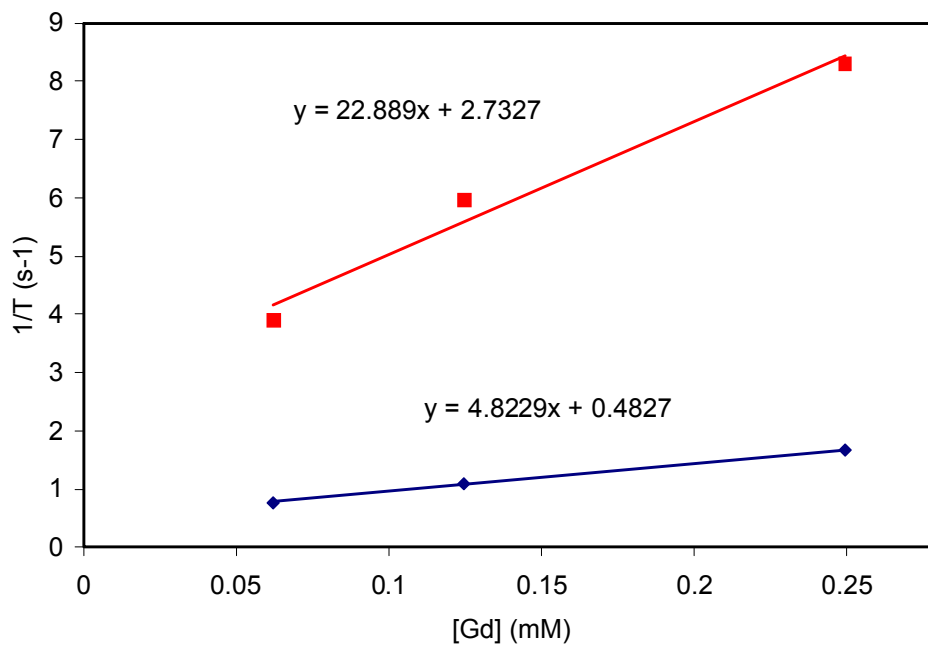
Figure 2.40. r_1 (blue) and r_2 (red) relaxivity curves of **2-5** measured at 3 T.
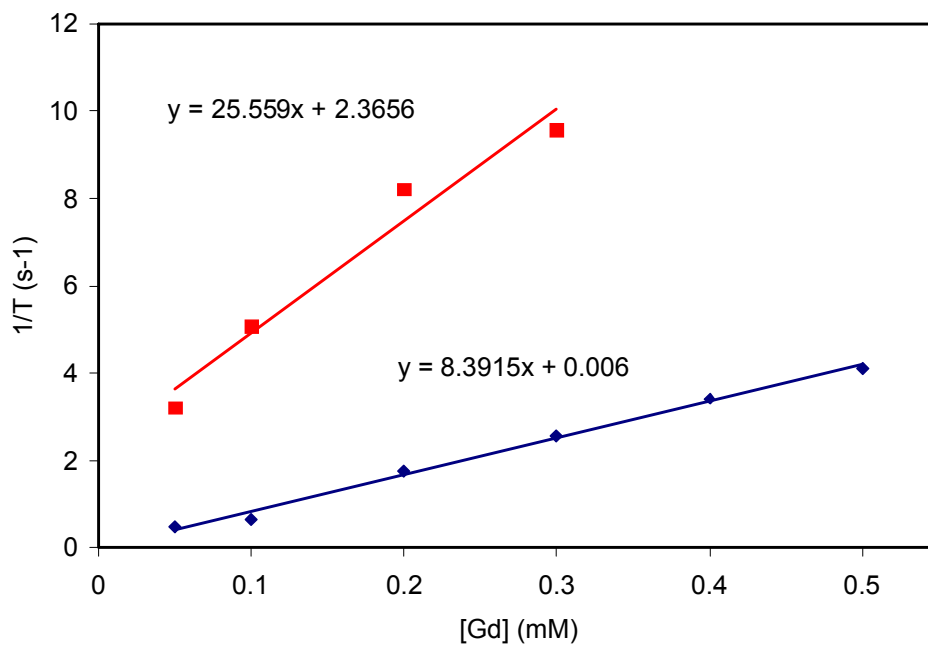
Figure 2.41. r_1 (blue) and r_2 (red) relaxivity curves of **2-6** measured at 3 T.

2.2.6 In Vitro Experiments

An immortalized murine monocyte cell line was used for the *in vitro* studies because of its phagocytic capacity.[17]   Laser scanning confocal fluorescence microscopic studies indicated the efficient uptake of **2-1a** by monocyte cells (500,000) after they were incubated with 2 mL of medium containing 4 µg of **2-1a** for 30 minutes.   The rhodamine B fluorescence is clearly visible in the confocal image of monocyte cells incubated with **2-1a**, but completely absent in the confocal image of monocyte cells alone (Fig. 2.42). We have observed significant MR image enhancement of the labeled monocytes when compared with a control of unlabeled monocytes. To prepare the cells for MR imaging, we incubated $\sim 5 \times 10^6$ cells in 3 mL of media containing 0.3 mg of **2-1** for 1 hour. The cells were isolated, washed twice with fresh media, pelleted, and finally covered with 200 µL of saline solution. As shown in Figure 2.43, significant positive signal enhancement in the T_1-weighted image and negative signal enhancement in the T_2-weighted image were observed for the labeled cells, depending on the MR pulse sequence employed when compared to the unlabeled cells. The T_1- and T_2-weighted image enhancement was corroborated with the reduction of T_1 and T_2 relaxation times observed on the relaxation time maps (Fig. 2.44). Cell viability assays showed that **2-1** particles were not toxic to monocyte cells; they were completely viable even after incubation with a nanoparticle loading of 10 µg per 5000 monocyte cells for 26 hours (Fig. 2.45). More than 85% cells were viable after incubating with 100 µg of **2-1** per 5000 cells for 26 hours.
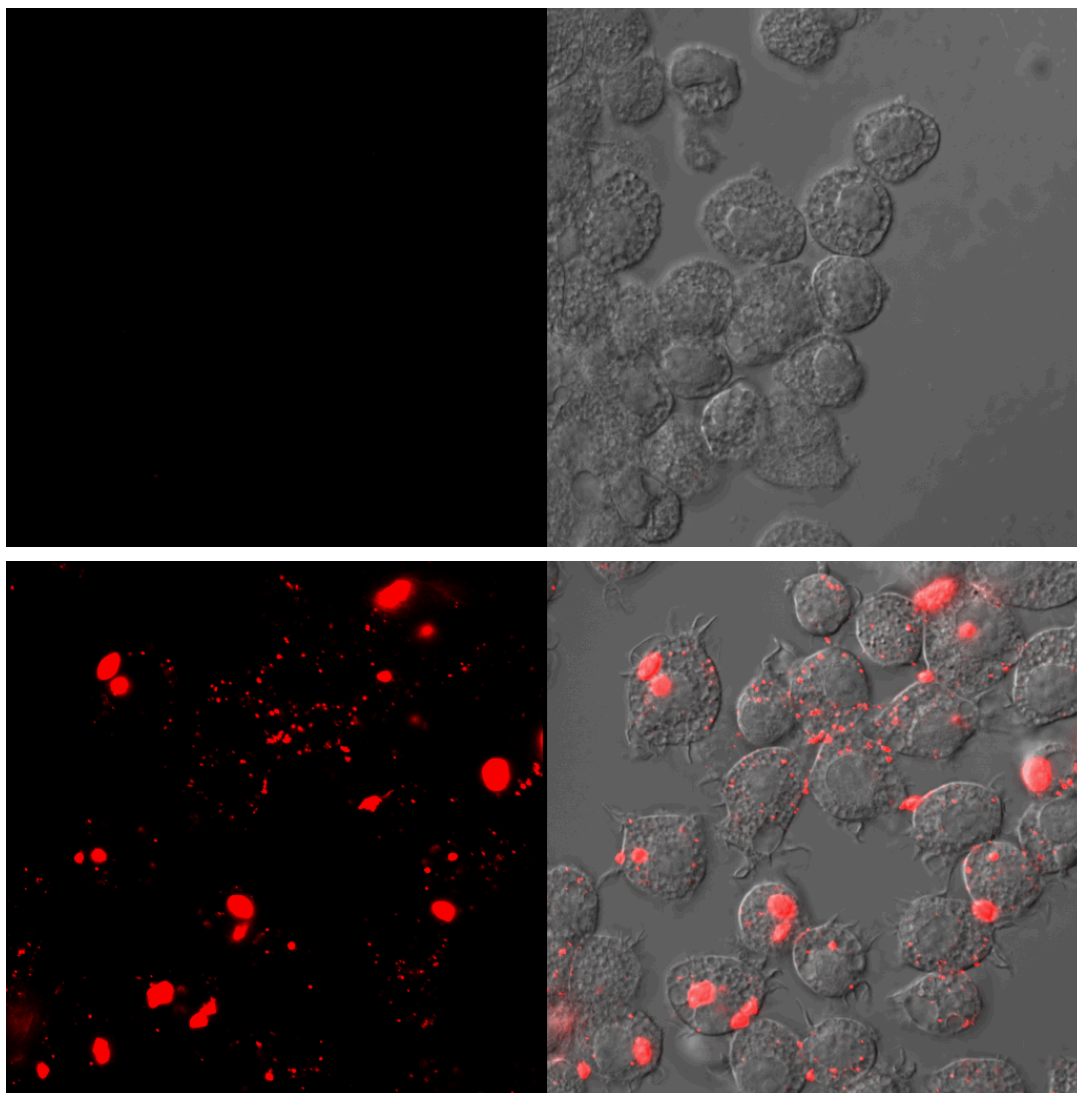
Figure 2.42. Confocal fluorescence microscopy images of rhodamine B labeled MSN-Gd (**2-1a**) in monocyte cells. Fluorescence is overlaid on DIC images of live monocytes incubated with no nanoparticles (top) and 4 μg **2-1a** per 500,000 cells (bottom).
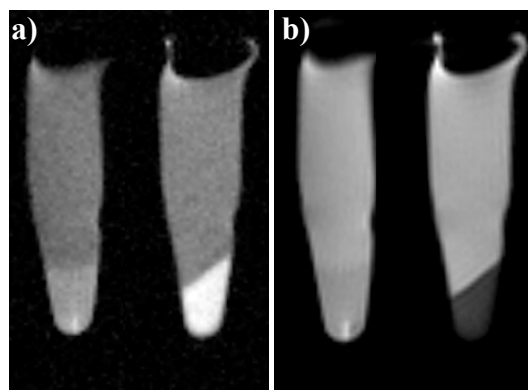
Figure 2.43. (a) T_1-weighted MR images of monocyte cell pellets incubated without **2-1** (left) and with 0.3 mg **2-1** for 5×10^6 cells in 3 mL of media (right). (b) T_2-weighted MR images of monocyte cell pellets incubated without **2-1** (left) and with 0.3 mg **2-1** for 5×10^6 cells in 3 mL of media (right).
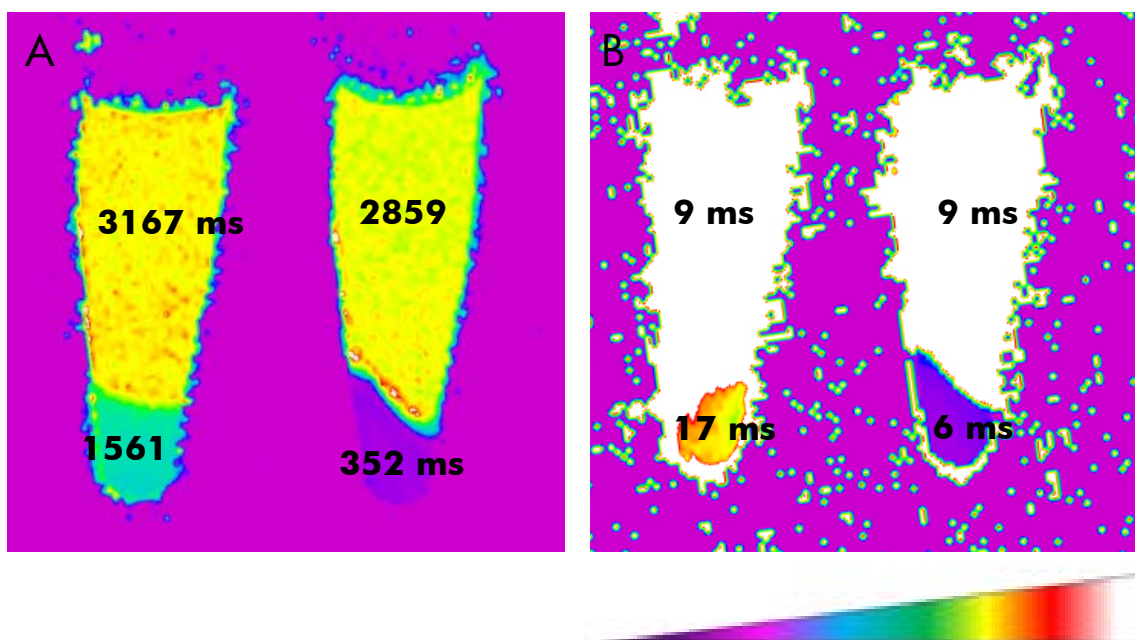
Figure 2.44. (A) T_1-Relaxation time maps for monocyte cell pellets incubated without **2-1** (left) and with 0.3 mg **2-1** for 5×10^6 cells in 3 mL of media (right). (B) T_2-Relaxation time maps for monocyte cell pellets incubated without **2-1** (left) and with 0.3 mg **2-1** for 5×10^6 cells in 3 mL of media (right).
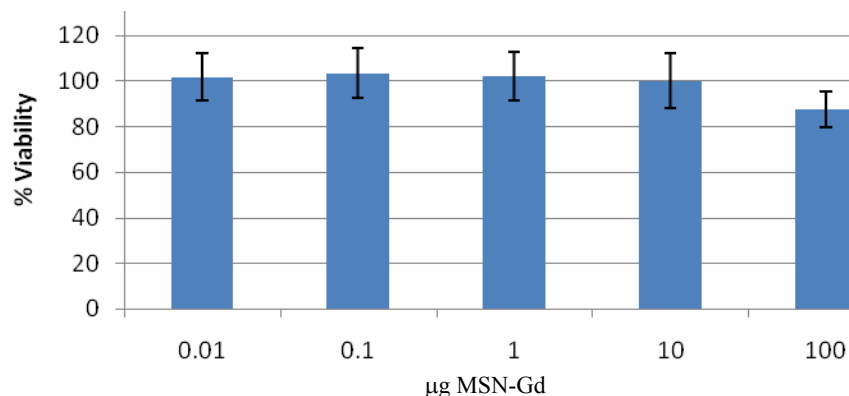
Figure 2.45. Monocyte cell viability assay after incubation with different amounts of **2-1**.

2.2.5 In Vivo Experiments

We have also evaluated the effectiveness of **2-1** as an *in vivo* MR contrast agent using a 9.4 T scanner. Upon tail vein injection of a dose of **2-1** corresponding to 2.1 µmol of Gd per kg of body weight, significant T_1-weighted enhancement is clearly visible in the aorta of a DBA/1J mouse 15 minutes post injection (Fig. 2.46), indicating the utility of **2-1** as an intravascular MR contrast agent. This dose level is much lower than what is typically required of currently used contrast agents (0.1-0.3 mmol/kg). We have also shown that **2-1** can be an efficient T_2-weighted contrast agent at a higher dosage. After tail injection of a dose of **2-1** corresponding to 31 µmol of Gd per kg of body weight, significant loss of MR signal was observed in the liver of the DBA/1J mouse 30 minutes post injection, indicating the ability of **2-1** to enhance T_2-weighted images (Fig. 2.47). The liver signal loss is probably a result of phagocytosis of the MSN-Gd particles by the liver macrophage cells, as already shown by the efficient uptake of **2-1** by the related monocyte cells. This result suggests the possibility of using **2-1** for MR imaging of liver abnormalities such as liver tumors which can be currently carried out with iron oxide nanoparticles.[18] The T_2-weighted enhancement could be observed up to 17 days after injection, indicating a slow clearance of the particles. A third study was performed using a dose corresponding to 4.15 µmol of Gd

66

per kg of body weight. At this lower dose T_1-weighted signal enhancement was observed in

the liver (Fig. 2.48-2.49).
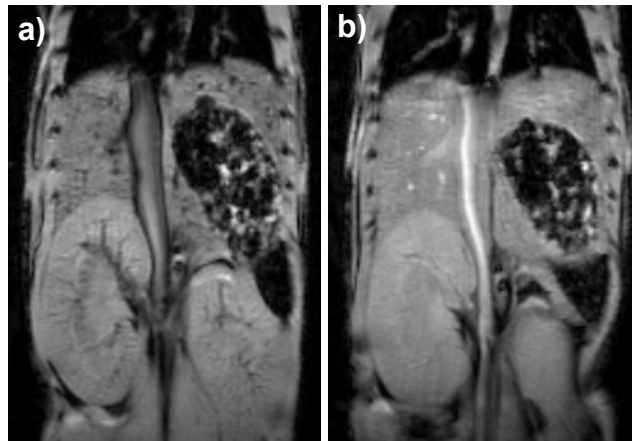
Figure 2.46. (a) Pre-contrast and (b) post-contrast (2.1 μmol/kg dose) T_1-weighted mouse MR image showing aorta signal enhancement.
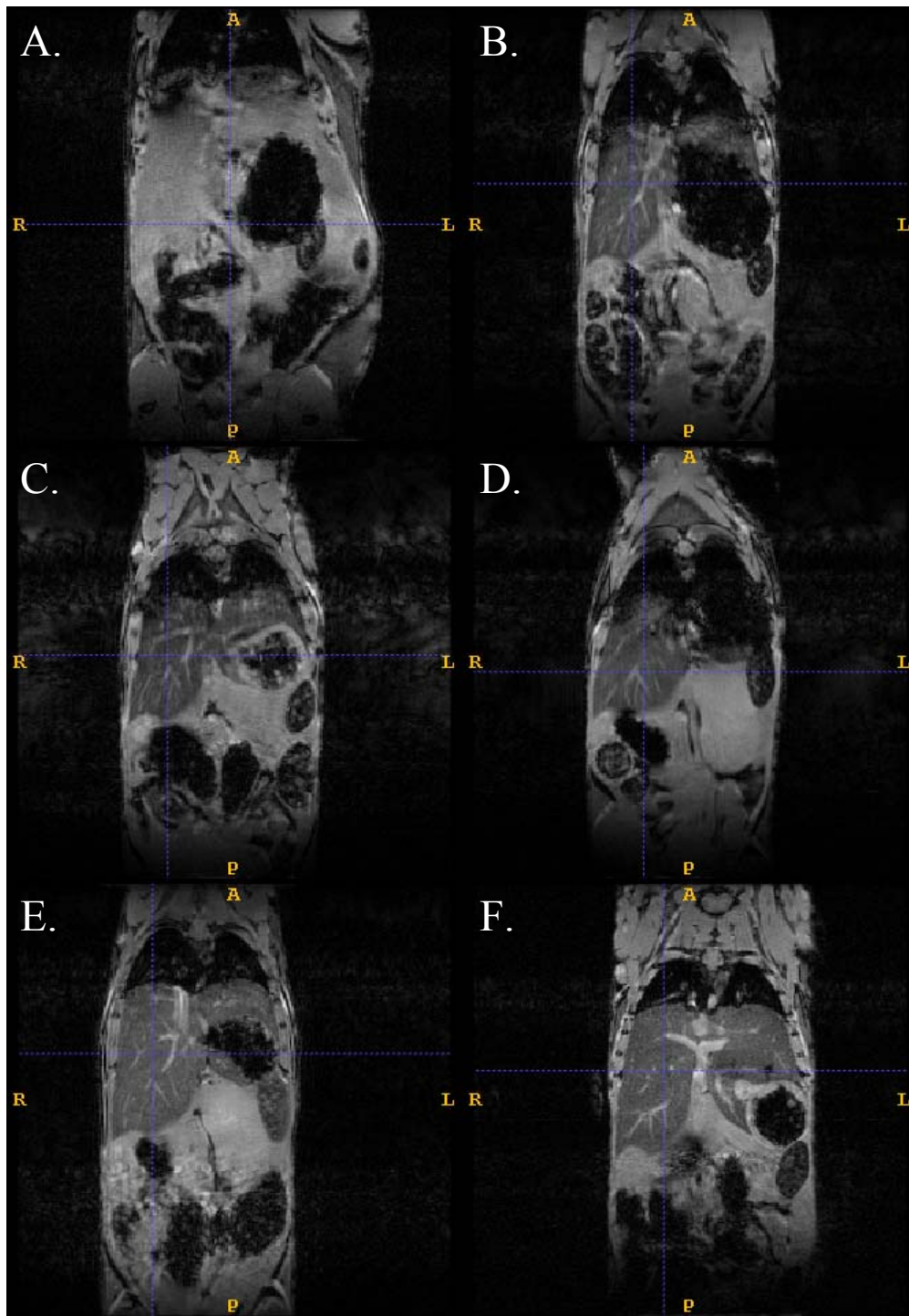
Figure 2.47. Midbody images showing T_2-weighted signal enhancement in the liver. (A) pre-contrast, (B) 30 minutes, (C) 1 day, (D) 2 days, (E) 4 days, and (F) 17 days post contrast administration via intravenous injection of a 31 µmol/kg dose of **2-1**.
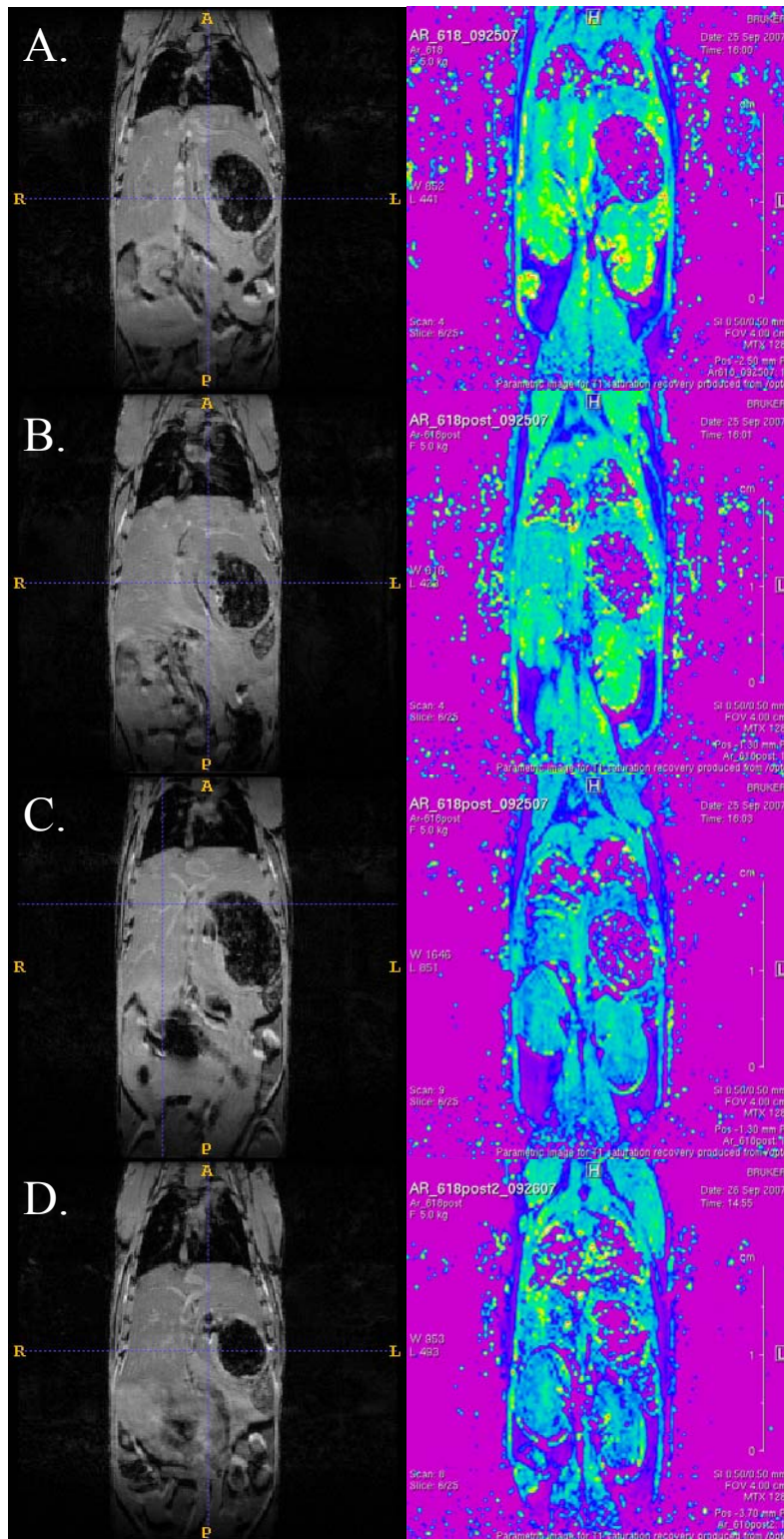
Figure 2.48. MR imaging and the associated T_1 relaxation time mapping (A) pre-contrast injection, (B) 15 minutes, (C) 1 hour, and (D) 24 hours post-contrast administration via intravenous injection of a 4.15 µmol/kg dose of **2-1**.
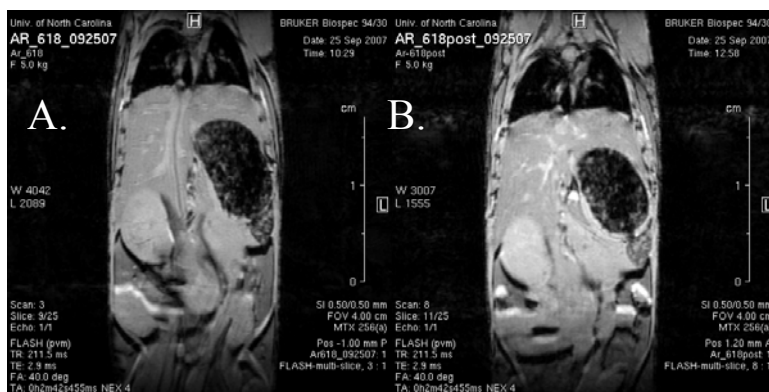
Figure 2.49. MR images (A) pre-contrast and (B) 1 hour post-contrast (4.15 µmol/kg dose) after rescaling using data from T_1 relaxation time maps.

2.3 Conclusion

We have designed and characterized several hybrid mesoporous silica nanospheres (MSN-Gd) with extraordinary ability to enhance MR images. Two different approaches were used to incorporate the Gd chelates, a post-synthetic grafting strategy and a co-condensation method. Their utility as contrast agents for optical and MR imaging has been clearly demonstrated *in vitro*. We have also shown that **2-1** is a highly efficient T_1 contrast agent for intravascular MR imaging and an excellent T_2 contrast agent for MR imaging of soft tissues when applied at a higher dosage.

2.4 Experimental Details

2.4.1 Materials and Methods

Cetyltrimethylammonium bromide (CTAB), $GdCl_3 \cdot 6H_2O$, bromoacetic acid, and tetraethyl orthosilicate (TEOS) were purchased from Aldrich and used without further purification. 3-(trimethoxysilylpropyl)diethylene triamine and 3-aminopropyltriethoxysilane were purchased from Gelest. Thermogravimetric analysis (TGA) was performed using a Shimadzu TGA-50 equipped with a platinum pan and a heating rate of 3 °C per minute,

under air. Powder X-ray diffraction (PXRD) patterns were collected on a Bruker SMART APEX II diffractometer using Cu radiation. The PXRD patterns were processed with the APEX 2 package using phase ID plug-in. A Hitachi 4700 field emission scanning electron microscope (SEM) and a JEM 100CX-II transmission electron microscope (TEM) were used to determine particle size and morphology. A Cressington 108 Auto Sputter Coater equipped with a Au/Pd (80/20) target and an MTM-10 thickness monitor was used to coat the samples with a 5 nm thick conductive layer before taking SEM images. Each SEM sample was prepared by suspending the nanoparticles in ethanol. A drop of the suspension was then placed on a glass slide and the solvent was allowed to evaporate. TEM samples were also prepared from ethanolic particle dispersions on amorphous carbon coated copper grids. An Applied Research Laboratories (ARL) SpectraSpan 7 DCP spectrometer was used to measure Gd^{3+} concentration.

MR images were acquired on a Siemens 3 T Allegra (Siemens Medical Systems, Erlangen, Germany) with a CP head coil, and a 9.4 T Bruker BioSpec (Bruker Biospin, Ettlingen, Germany) system with a 35 mm quadrature RF transmit and receive coil. For the 3 T scanner, a 3D FLASH sequence was utilized to compute T_1 maps with seven different flip angles (2, 5, 10, 20, 30, 40, and 60). Imaging parameters were: FOV=190 x 190*64 mm^3, Matrix size=128 x 128 *32, TR/TE= 40/1.64 ms, total data acquisition time was 19 minutes. A 2-D multiple echo spin echo sequence was used to estimate T_2 maps. In total, 32 echoes with an echo spacing of 6.2 ms were obtained. The first echo time was 6.2 ms. TR was 3000 ms. FOV and matrix size were set to 190 x 190 mm^2 and 128 x 128. The slice thickness was 2 mm. The total data acquisition time was about 6 minutes and 29 seconds. For the 9.4 T scanner, two 2D multiple echo spin echo sequences were used to estimate T_2 maps for a wide

range of T_2. FOV and matrix size were set to 35 x 30 mm^2 and 128 x 128. The slice thickness was 1 mm. In total, 32 echoes with an echo spacing of 3.7 ms for sequence 1 and 40 echoes with an echo spacing of 10 ms for sequence 2 were obtained. The TR/TE1 were 3.7/3000 ms and 10/4114 ms for each sequence, respectively. The total data acquisition time was about 10 minutes. T_1 maps were obtained with a variable TR rapid acquisition relaxation enhanced (RARE) sequence with a TE=5.14 ms. Twenty two variable TRs (TR=18, 25, 40, 60, 90, 120, 160, 200, 250, 300, 380, 500, 700, 1000, 1500, 2000, 2500, 3000, 4000, 5000, 6000, 7000 ms) were used with a FOV of 35 x 30 mm^2 and a matrix size of 128 x 128. RARE factor was 3 and total data acquisition was about 24 minutes.

2.4.2 Ligand and Gd Complex Synthesis

3-aminopropyl(trimethoxysilyl)diethylenetriamine tetraacetic acid (Si-DTTA). Bromoacetic acid (0.5558 g, 4.00 mmol) and 3-(trimethoxysilylpropyl)diethylene triamine (0.2654 g, 1.00 mmol) were dissolved in 1.0 mL of distilled water and 2.0 mL 2 M sodium hydroxide (4.00 mmol) with magnetic stirring. The reaction solution was subsequently heated to 50 °C, and an additional 3.0 mL of 2 M NaOH were added dropwise over approximately 30 minutes. After stirring for an additional 2 hours at 50 °C, the solvent was removed under reduced pressure to yield a viscous yellow oil. An off-white hygroscopic powder was isolated from the oil in high yield (>90%) by precipitation with ethanol, and subsequent drying under vacuum. MS (ESI negative ion): m/z 542.2 [M-H]$^-$ for the silanetriol from a basic solution. NMR: ^{1}H (D$_2$O, 300 MHz, ppm): 0.47 (2H), 1.55 (2H), 2.62-2.78 (10H), 3.14-3.21 (8H).

Synthesis of Si-DTTA-Gd Complex. The gadolinium complex was prepared by dissolving the isolated Si-DTTA product (108.6 mg, 0.2 mmol) in 4 mL of distilled water with magnetic stirring at room temperature. GdCl$_3$ (380 μL of a 0.50 M solution, 0.19 mmol) was slowly titrated into the solution while maintaining a pH of ~9 with the dropwise addition of 2 M NaOH. The reaction was then stirred at room temperature for an additional 2 hours. The resultant solution was used directly.

Bis(3-aminopropyl triethoxysilyl)diethylenetriamine pentaacetic acid (Si$_2$-DTPA). Diethylenetriamine pentaacetic acid dianhydride (5.000 g, 13.995 mmol) was dissolved in 110 mL of anhydrous pyridine under a steady flow of nitrogen. Using standard Schlenk line techniques 3-aminopropyl triethoxysilane (6.85 g, 31.00 mmol) was added and the resultant reaction mixture was magnetically stirred under nitrogen for 24 hours. The product was then precipitated with copious amounts of hexane, isolated via centrifuge, washed with additional aliquots of hexanes, and dried to yield 10.436 g (93.2 %) of the desired compound (Si$_2$-DTPA). MS (ESI negative ion): *m/z* 631.3 [M-H]$^-$ for the silanetriol from a basic solution. NMR: ^{1}H (DMSO, ppm): 0.52 (t, 4H), 1.14 (t, 18H), 1.44(p, 4H), 2.81 (t, 4H), 2.92 (t, 4H), 3.04 (q, 4H), 3.22 (s, 6H), 3.34 (s, 4H), 3.73 (q, 12H), 8.06 (t, 2H). ^{13}C{1H} (DMSO, ppm): 8.0 (2C), 18.8 (18C), 23.4 (2C), 41.8 (2C), 51.2 (2C), 52.8 (2C), 55.9 (2C), 56.7 (2C), 58.3 (1C), 58.4 (6C), 170.7 (2C), 173.4 (3C).

Synthesis of Si$_2$-DTPA-Gd Complex. To prepare the gadolinium complex, Si$_2$-DTPA (1.77 g, 2.22 mmol) was dissolved in ~3 equivalents of NaOH (6.0 mL of a 1.0 M solution) with magnetic stirring for 30 minutes. To this solution was added 0.90 equivalent of GdCl$_3$ (4.0 mL of a 0.5 M solution, 0.002 mol) and the mixture was magnetically stirred at

room temperature for several hours, the volume of the solution was adjusted to 10 mL to yield a visibly clear yellow 0.20 M solution of the modified gadodiamide complex.

2.4.3 MSN-Gd Synthesis

Bare MSN Synthesis. 0.100 g (0.274 mmol) of cetyltrimethylammonium bromide (CTAB) was dissolved in 48 mL of distilled H_2O, along with 0.35 mL of 2 M sodium hydroxide. This solution was then heated to 80 °C. Once the reaction had reached 80 °C, 0.50 mL (0.47g, 2.24 mmol) of tetraethylorthosilicate (TEOS) was rapidly injected. The reaction was then stirred for an additional 2 hours at 80 °C. At the completion of the reaction the particles were isolated by centrifuging at 10,000 rpm for 10 minutes. They were then washed with H_2O and ethanol, before being redispersed in 30 mL of ethanol. Yield: 171 mg

Extraction. The surfactant was extracted from the mesoporous materials using either a 1 wt% solution of sodium chloride in methanol or a 1 volume % solution of HCl in methanol. The particles were dispersed in the NaCl/MeOH or HCl/MeOH solution at a concentration of approximately 3.5 mg/mL. After stirring at room temperature for 3 hours, the particles were isolated by centrifuging, and then redispersed in another aliquot of the methanol solution. The extraction was performed for a total of three times. After the final extraction, the particles were washed with distilled H_2O and ethanol, before being redispersed in ethanol.

Synthesis of MSN-Gd using grafting method (2-1). Approximately 160 mg of extracted MSN particles were suspended in 10 mL of toluene. 0.78 mL (0.075 mmol) of a 0.097 M aqueous solution of Si-DTTA-Gd was then added. The mixture was then heated to reflux overnight. The particles were isolated by centrifuging, and washed with distilled

water and ethanol, before being redispersed in ethanol. Yield: 132 mg. In order to ensure there was no excess Gd remaining on the silica, the particles were washed twice with a pH 3 solution by sonicating for 10 minutes. They were then washed once with distilled water before being redispersed. The particles were also dialyzed against distilled water for 6 hours, changing the water once an hour. The dialysis was performed using dialysis tubing with a molecular weight cut off of 3500.

Synthesis of co-condensed MSN with "10 wt%" Si-DTTA-Gd (2-2). 0.0400 g (0.1098 mmol) of CTAB was dissolved in 48 mL of H_2O containing 0.14 mL of 2 M NaOH (0.28 mmol). The solution was heated to 80 °C. After reaching 80 °C, 0.2 mL of TEOS, and 2.54 mL (0.0356 mmol) of a 0.014 M aqueous solution of Si-DTTA-Gd were then added. The reaction was then stirred for an additional 2 hours at 80 °C. The product was isolated by centrifuging, and was washed with water and ethanol. The surfactant was extracted using the same procedure as used above for the bare MSN particles (1 wt% NaCl in methanol). Yield: 32.9 mg.

Synthesis of co-condensed MSN with "10 wt%" Si_2-DTPA-Gd (2-3). 0.200 g (0.549 mmol) of CTAB was dissolved in 240 mL of H_2O containing 0.70 mL of 2 M NaOH (1.40 mmol). The solution was heated to 80 °C. After reaching 80 °C, 1.0 mL of TEOS, and 0.79 mL (0.134 mmol) of a 0.17 M aqueous solution of Si_2-DTPA-Gd were then added. The reaction was then stirred for an additional 2 hours at 80 °C. The product was isolated by centrifuging, and was washed with water and ethanol. The surfactant was extracted using the same procedure as used above for the bare MSN particles (1 wt% NaCl in methanol). Yield: 150.1 mg.

Synthesis of co-condensed MSN with "20 wt%" Si$_2$-DTPA-Gd (2-4). 0.200 g (0.549 mmol) of CTAB was dissolved in 240 mL of H$_2$O containing 0.70 mL of 2 M NaOH (1.40 mmol). The solution was heated to 80 °C. After reaching 80 °C, 1.0 mL of TEOS, and 1.37 mL (0.233 mmol) of a 0.17 M aqueous solution of Si$_2$-DTPA-Gd were then added. The reaction was then stirred for an additional 2 hours at 80 °C. The product was isolated by centrifuging, and was washed with water and ethanol. The surfactant was extracted using the same procedure as used above for the bare MSN particles (1 wt% NaCl in methanol). Yield: 326.1 mg.

Synthesis of co-condensed MSN with "30 wt%" Si$_2$-DTPA-Gd (2-5). 0.200 g (0.549 mmol) of CTAB was dissolved in 240 mL of H$_2$O containing 0.70 mL of 2 M NaOH (1.40 mmol). The solution was heated to 80 °C. After reaching 80 °C, 1.0 mL of TEOS, and 2.04 mL (0.347 mmol) of a 0.17 M aqueous solution of Si$_2$-DTPA-Gd were then added. The reaction was then stirred for an additional 2 hours at 80 °C. The product was isolated by centrifuging, and was washed with water and ethanol. The surfactant was extracted using the same procedure as used above for the bare MSN particles (1 wt% NaCl in methanol). Yield: 241.0 mg.

Synthesis of co-condensed MSN with "40 wt%" Si$_2$-DTPA-Gd (2-6). 0.220 g (0.603 mmol) of CTAB was dissolved in 240 mL of H$_2$O containing 0.70 mL of 2 M NaOH (1.40 mmol). The solution was heated to 80 °C. After reaching 80 °C, 1.0 mL of TEOS, and 3.03 mL (0.455 mmol) of a 0.15 M aqueous solution of Si$_2$-DTPA-Gd were then added. The reaction was then stirred for an additional 2 hours at 80 °C. The product was isolated by centrifuging, and was washed with water and ethanol. The surfactant was extracted using the

same procedure as used above for the bare MSN particles (1 wt% NaCl in methanol). Yield: 276.3 mg.

2.4.4 Fluorescently Labeled MSN-Gd

Synthesis of Rhodamine-APS. 6.8 mg (0.0127 mmol) of rhodamine B isothiocyanate was dissolved in 1.1 mL of ethanol. 3.3 μL (3.1 mg, 0.0141 mmol) of 3-aminopropyltriethoxysilane was then added, and the reaction was stirred at room temperature, under N_2, and in the dark for 24 hours. At the completion of the reaction the solution was diluted to a total volume of 2 mL with additional ethanol to make a solution with a rhodamine-APS concentration of approximately 6 mM.

Rhodamine B functionalized MSN-Gd (2-1a). Approximately 50 mg of extracted MSN particles were suspended in 4 mL of toluene. 170 μL (0.016 mmol) of a 0.097 M solution of a Si-DTTA-Gd aqueous solution and 110 μL (0.00066 mmol) of a 6 mM solution of rhodamine-APS in ethanol were then added. The mixture was then heated to reflux overnight. The particles were isolated by centrifuging, and were washed with distilled water and ethanol, before being redispersed in ethanol. Yield: 48 mg. In order to ensure there was no excess Gd remaining on the silica, the particles were washed twice with a pH=3 solution by sonicating for 10 minutes. They were then washed once with distilled water before being redispersed. The particles were also dialyzed against distilled water for 6 hours, changing the water once an hour.

2.4.5 Calculation for Number of Gd per particle

Density of MCM-41: (0.835 g/cm^3) [19]

Volume of each 75 nm particle:

$$V = \frac{4}{3}\pi r^3 = \frac{4}{3}\pi(37.5nm)^3 = 2.2089 \times 10^5 nm^3 = 2.2089 \times 10^{-16} cm^3$$

Mass of each 75 nm particle:

$$M_{NP} = (2.2089 \times 10^{-16} cm^3) \times 0.835 \, g/cm^3 = 1.844 \times 10^{-16} g$$

Number of Gd per particle, example shown for 4.92 wt% Gd:

$$(X \times m_{Gd})/(m_{NP} + X \times m_{Gd-DTTA}) = mass\%Gd$$
$$(X \times 157.25 \, g/mol)/[(1.844 \times 10^{-16} g \times 6.022 \times 10^{23} mol^{-1}) + (X \times 566.64)] = 0.0492$$
$$X \times 157.25 \, g/mol = 5.465 \times 10^6 + X \times 27.88$$
$$X \times 129.37 = 5.465 \times 10^6$$
$$X = 42,243$$

2.4.6 In Vitro Experiments

Murine monocyte cell culture. Cells (ATCC# TIB67) were purchased from the UNC Lineberger Comprehensive Cancer Center's Tissue Culture Facility. Cells were maintained in DMEM-H containing 10% FBS and 1% penicillin/streptomycin at 37 °C and 5% CO_2.

MTS cell viability assay. Manufacturer's (Promega) protocol was used to determine cell viability of monocytes in the presence of MSN-Gd nanoparticles. Briefly, monocytes were placed in a 96-well plate at a concentration of 5000 cells (100 µL) per well and various amounts of particles (**2-1**) were added in a 20 µL volume of distilled H_2O. Each particle concentration was replicated seven times, and 100% viability was standardized to 20 µL of distilled H_2O without nanoparticles. The cells are incubated with the nanoparticles for 22 hours before addition of MTS. An additional 4 hours for MTS metabolism was allowed

before reading the plate absorbance at 492 nm. Wells with nanoparticles and without cells were used for background correction.

In vitro labeling of murine monocytes. Cells were detached from resident flasks using a cell scraper and re-plated into 6-well plates at a concentration of 300,000 cells per well. Monocyte containing plates were maintained at 37 ºC and 5% CO_2 for 24 hours, at which point 4 µg nanoparticles (**2-1**) per well (2 mL media) were added. Cells were allowed to incubate with nanoparticles at 37 ºC and 5% CO_2 for 30 minutes before extensive washing. The resulting labeled cells were imaged using an Olympus FV500 Confocal Laser Microscope at 60X using a RITC filter and DIC settings.

2.4.7 In Vivo Imaging Experiments

T_2-weighted midbody MR imaging. A 6-week old male DBA/1J mouse was imaged in a Bruker 9.4 T small animal scanner. After pre-contrast image acquisition of the animal midbody, 2.5 mg of **2-1** NPs were intravenously injected via tail vein. This corresponds to a dose of 31 µmol of Gd per kg of body weight. The animal was imaged at time points of 30 minutes, 1 day, 2 days, 4 days, and 17 days post-contrast administration.

T_1-weighted midbody MR imaging and relaxation time mapping. A 6-week old female DBA/1J mouse was imaged in a Bruker 9.4 T small animal scanner. After pre-contrast image acquisition of animal midbody, an appropriate dose of **2-1** NPs was intravenously injected via tail vein. The animal was imaged at time points of 15 minutes, 1 hour, and 24 hours post-contrast administration.

2.5 References

1. Weissleder, R.; Moore, A.; Mahmood, U.; Bhorade, R.; Benveniste, H.; Chiocca, E. A.; Basilion, J. P., *In vivo* magnetic resonance imaging of transgene expression. *Nat. Med.* **2000**, *6* (3), 351-354.

2. Morawski, A. M.; Lanza, G. A.; Wickline, S. A., Targeted contrast agents for magnetic resonance imaging and ultrasound. *Curr. Opin. Biotechnol*. **2005**, *16* (1), 89-92.

3. Frias, J.C.; Ma, Y.; Williams, K.J.; Fayad, Z.A.; Fisher, E.A., Properties of a versatile nanoparticle platform contrast agent to image and characterize atherosclerotic plaques by magnetic resonance imaging. *Nano Lett.* **2006**, *6* (10), 2220-2224.

4. Yang, H.; Santra, S.; Walter, G.A.; Holloway, P.H., Gd^{III}-Functionalized fluorescent quantum dots as multimodal imaging probes. *Adv. Mater.* **2006**, *18* (21), 2890-2894.

5. Rieter, W.J.; Kim, J.S.; Taylor, K.M.L.; An, H.; Lin, W.; Tarrant, T.; Lin, W., Hybrid silica nanoparticles for multimodal imaging. *Angew. Chem. Int. Ed*. **2007**, *46* (20), 3680-3682.

6. Kim, J.S.; Rieter, W.J.; Taylor, K.M.L.; An, H.; Lin, W.; Lin, W., Self-assembled hybrid nanoparticles for cancer-specific multimodal imaging. *J. Am. Chem. Soc*. **2007**, *129* (29), 8962-8963.

7. Kresge, C.T.; Leonowicz, M.E.; Roth, W.J.; Vartuli, J.C.; Beck, J.S., Ordered mesoporous molecular sieves synthesized by a liquid-crystal template mechanism. *Nature* **1992**, *359* (6397), 710-712.

8. Beck, J.S.; Vartuli, J.C.; Roth, W.J.; Leonowicz, M.E.; Krege, C.T.; Schmitt, K.D.; Chu, C.T-W.; Olson, D.H.; Sheppard, E.W.; McCullen, S.B.; Higgins, J.B.; Schlenker, J.L., A new family of mesoporous molecular sieves prepared with liquid crystal templates. *J. Am. Chem. Soc*. **1992**, *114* (27), 10834-10843.

9. Grün, M.; Unger, K.K.; Matsumoto, A.; Tsutsumi, K., Novel pathways for the preparation of mesoporous MCM-41 materials: control of porosity and morphology. *Microporous and Mesoporous Mater.* **1999,** *27* (2-3), 207-216.

10. Cai, Q.; Luo, Z-S.; Pang, W-Q.; Fan, Y-W.; Chen, X-H.; Cui, F-Z., Dilute solution routes to various controllable morphologies of MCM-41 silica with a basic medium. *Chem. Mater.* **2001**, *13* (2), 258-263.

11. Chen, H-T.; Huh, S.; Wiench, J.W.; Pruski, M.; Lin, V. S-Y., Dialkylaminopyridine-functionalized mesoporous silica nanosphere as an efficient and highly stable heterogeneous nucleophilic catalyst. *J. Am. Chem. Soc.* **2005**, *127* (38), 13305-13311.

12. Slowing, I.; Trewyn, B.G.; Lin, V. S-Y., Effect of surface functionalization of MCM-41-type mesoporous silica nanoparticles on the endocytosis by human cancer cells. *J. Am. Chem. Soc.* **2006,** *128* (46)*,* 14792-14793.

13. Slowing, I.; Trewyn, B.G.; Lin, V. S-Y., Mesoporous silica nanoparticles for intracellular delivery of membrane-impermeable proteins. *J. Am. Chem. Soc.* **2007,** *129* (28)*,* 8845-8849.

14. Huh, S.; Wiench, J. W.; Trewyn, B. G.; Song, S.; Pruski, M.; Lin, V. S-Y., Tuning of particle morphology and pore properties in mesoporous silicas with multiple organic functional groups. *Chem. Commun.* **2003** (18), 2364-2365.

15. Huh, S.; Wiench, J. W.; Yoo, J-C.; Pruski, M.; Lin, V. S-Y., Organic functionalization and morphology control of mesoporous silicas via a co-condensation synthesis method. *Chem. Mater.* **2003**, *15* (22), 4247-4256.

16. Lai, C-Y.; Trewyn, B.G.; Jeftinija, D.M.; Jeftinija, K.; Xu, S.; Jeftinija, S.; Lin, V. S-Y., A mesoporous silica nanosphere-based carrier system with chemically removable CdS nanoparticle caps for stimuli-responsive controlled release of neurotransmitters and drug molecules. *J. Am. Chem. Soc.* **2003**, *125* (15), 4451-4459.

17. Ma, Y.; Pope, R.M., The Role of Macrophages in Rheumatoid Arthritis. *Curr. Pharm. Des*. **2005**, *11* (5), 569-580.

18. Reimer, P.; B.Tombach, B., Ferucarbotran (Resovist): a new clinically approved RES-specific contrast agent for contrast-enhanced MRI of the liver: properties, clinical development, and applications. *Eur. Radiol*. **2003**, *13* (6), 1266-1276.

19. Edler, K. J.; Reynolds, P. A.; White, J. W.; Cookson, D. Diffuse wall structure and narrow mesopores in highly crystalline MCM-41 materials studied by X-ray diffraction. *J. Chem. Soc., Faraday Trans.* **1997**, *93*(1), 199-202.

CHAPTER 3

Degradable Mesoporous Silica Nanospheres as Contrast Agents for Magnetic Resonance Imaging

3.1 Introduction

As discussed in the previous chapter, there are many advantages to using a nanoparticle based contrast agent for magnetic resonance imaging, including large payloads, increased relaxivity on a per metal basis, and the ability to modify the surface to alter the pharmacokinetics or introduce targeting moieties. However, in order to make a nanoparticle contrast agent potentially useful for clinical applications it must be able to quickly clear from the body after the MR imaging studies. This is particularly important for Gd-containing MRI contrast agents since Gd containing MRI contrast agents have recently been shown to be the culprit for a potentially fatal condition known as nephrogenic systemic fibrosis (NSF).[1,2] This condition has been reported in patients that have some degree of renal failure, that have also received one of the commercially available Gd contrast agents. It is believed that the impaired renal function results in slower clearance of the Gd chelate, and as a result free Gd ions begin to leach from the chelates, resulting in toxicity.

This condition highlights the need to ensure the Gd chelates can be quickly cleared from the body. Based on our preliminary *in vivo* results using the MSN-Gd contrast agents (**2-1**) we learned that the particles are trafficked to the liver, and are cleared very slowly. We were able to observe significant T_2-weighted enhancement in the liver of a mouse up to 17 days after injection. We hypothesized that if we can include a degradable linkage from the

Gd chelate to the particle, the Gd chelate can be cleaved and cleared renally, just as the currently used small molecule contrast agents are.

There have been several reports on biodegradable polymeric MRI contrast agents.[3-7] These polymers contain Gd chelates either directly in the backbone of the polymer, or in pendant side chains. These polymers also contain disulfide bonds that can be cleaved *in vivo* by endogenous thiols such as cysteine and the reduced form of glutathione. Once the disulfide bonds have been cleaved, the smaller Gd chelates can then be cleared through the kidneys. Using this approach, we have been able to synthesize a degradable contrast agent based on MSN particles. A disulfide bond has been incorporated into the linkage from the chelate to the particle. Once cleaved, the Gd chelate can then be quickly cleared from the body, reducing the potential risk of toxicity that can occur if the chelates remain in the body too long resulting in the release of free Gd ions.

3.2 Results and Discussion

3.2.1 Ligand and Gd Complex Synthesis

The diethylenetriaminepenta(acetic acid)-ethyldisulfanylpropyltriethoxysilane-Gd complex (Si-S-S-DTPA-Gd) was synthesized by first reacting diethylenetriaminepenta(acetic acid) dianhydride with 0.8 equivalents of 2-pyridyldisulfanylethylamine to form the mono functionalized ligand (Scheme 3.1). The Gd complex was then formed by reacting the deprotonated form of the ligand with one equivalent of $GdCl_3$. The Gd complex was isolated from the aqueous solution by precipitating with acetone. A disulfide exchange reaction was then performed using 3-mercaptopropyltriethoxysilane to obtain the desired product.

Poly(ethylene glycol) was also modified to contain a triethoxy silane group to allow for surface functionalization of the particles. This was obtained by reacting poly(ethylene glycol) monomethyl ether (MW 2000) with 1 equivalent of (3-isocyanato-propyl)triethoxysilane in the presence of Hünig base.
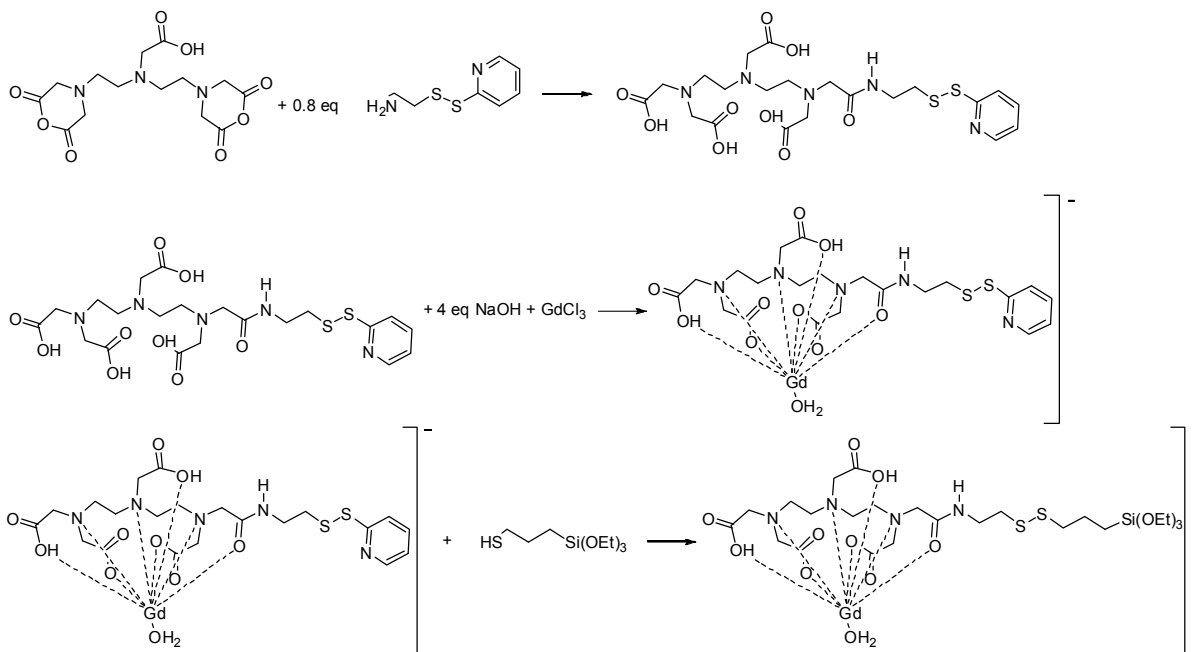
Scheme 3.1. Synthesis of diethylenetriaminepenta(acetic acid)-ethyldisulfanylpropyl-triethoxysilane-Gd complex.

3.2.2 Nanoparticle Synthesis

Initial attempts at grafting the Gd complex containing the disulfide bond into MSN particles resulted in much lower loading than what was obtained previously with the non-degradable version (**2-1**). We hypothesized that the increase in size of the chelate made transportation into the channels much less efficient. In order to resolve this problem we synthesized mesoporous silica nanoparticles with larger pore diameters. A similar surfactant-templated technique was used, with mesitylene added as a pore swelling agent.[8] Briefly, an

aqueous solution of CTAB, sodium hydroxide, and mesitylene was heated to 80 °C. Tetraethylorthosilicate (TEOS) was then added, and the reaction was stirred for an additional 2 hours at 80 °C. The particles were then isolated by centrifuging, and were washed with water and ethanol. The surfactant was then extracted from the pores using a 1% solution of HCl in methanol.

The Si-S-S-DTPA-Gd complex was grafted onto the large pore MSN particles through the siloxane linkages by adding an aqueous solution of the complex to a suspension of the extracted large pore MSN particles in toluene. The reaction was then heated to reflux for 18 hours. After cooling, the particles were isolated by centrifuging, and were washed with water and ethanol. Finally, the particles were dialyzed against distilled water to remove any free chelates adsorbed into the channels. In order to increase the loading of Gd chelates, the above procedure was repeated a second time.

To increase the circulation time of the particles *in vivo*, the surface was coated with poly(ethylene glycol) chains (PEG). The PEG grafting was performed by adding a solution of triethoxysilylpropyl carbamoyl-poly(ethylene glycol) to a suspension of the particles in basic ethanol. The reaction was then stirred at room temperature for 18 hours. The particles were then isolated by centrifuging, washed with ethanol, and then dialyzed against distilled water to remove any adsorbed PEG chains from the channels.

3.2.3 Characterization

Scanning electron and transmission electron microscopies (SEM and TEM) were used to evaluate the particle size and morphology. The as-synthesized particles were fairly

uniform, and had an average diameter of 75 nm (Fig. 3.1-3.3). No change was seen in the particle size or morphology upon grafting of the Gd complex.
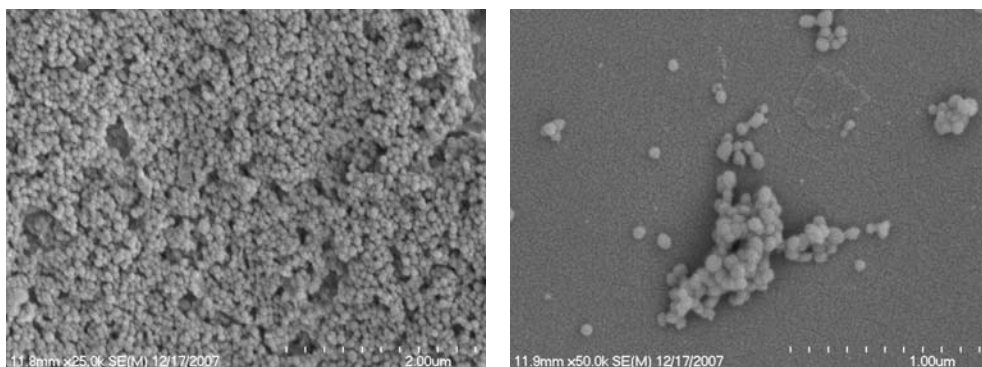
Figure 3.1. SEM images of large pore MSN particles.
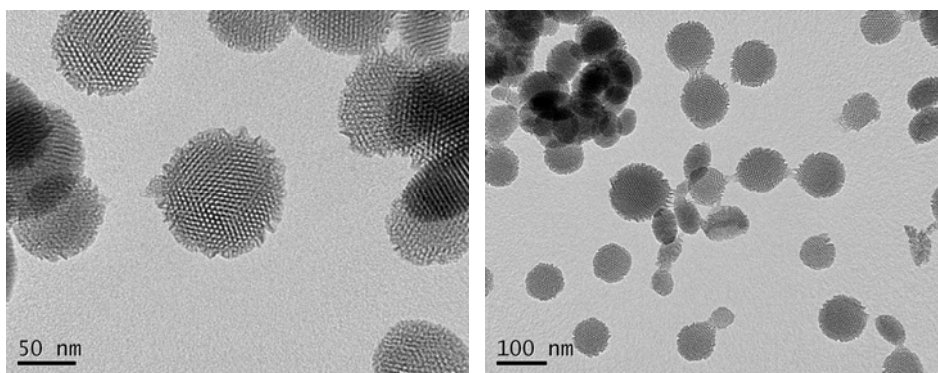
Figure 3.2. TEM images of large pore MSN particles.
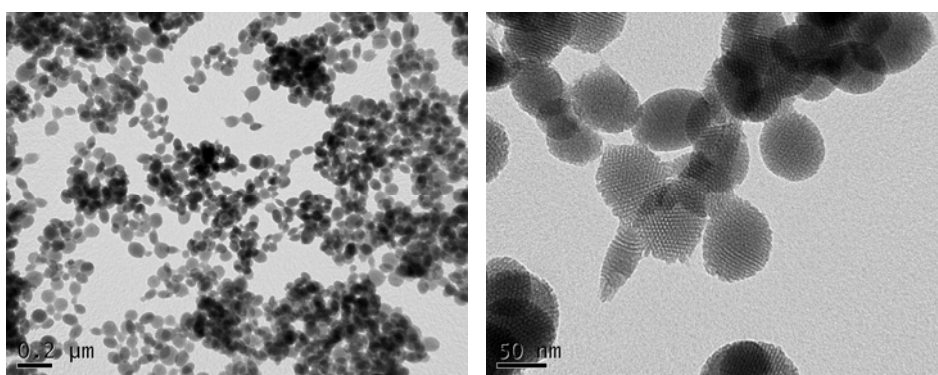
Figure 3.3. TEM images of large pore MSN-S-S-DTPA-Gd particles.

The pore size and surface area of the particles was determined using nitrogen uptake measurements (Fig. 3.4-3.9). The extracted large pore particles showed a similar surface

area to the original MSN particles. The average BJH (Barrett-Joiner-Halenda) surface area was 1535 m^2/g. The particles had an average pore diameter of 4.6 nm, compared to 2.4 nm for the original MSN particles. After coating with the Gd complexes, a slight decrease in the surface area was observed (1384 m^2/g). The average pore diameter also decreased to 3.8 nm, indicating the presence of Gd chelates in the channels. After coating with PEG, the pore diameter remained unchanged, but the surface area decreased to 872 m^2/g.
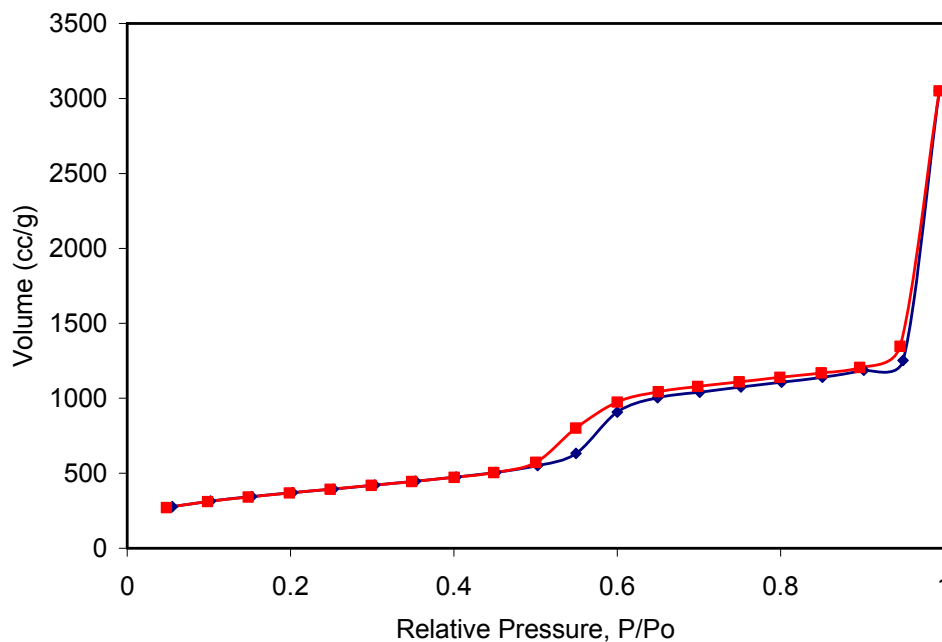
Figure 3.4. Nitrogen sorption isotherm of surfactant-extracted large pore MSN (blue-adsorption; red-desorption).
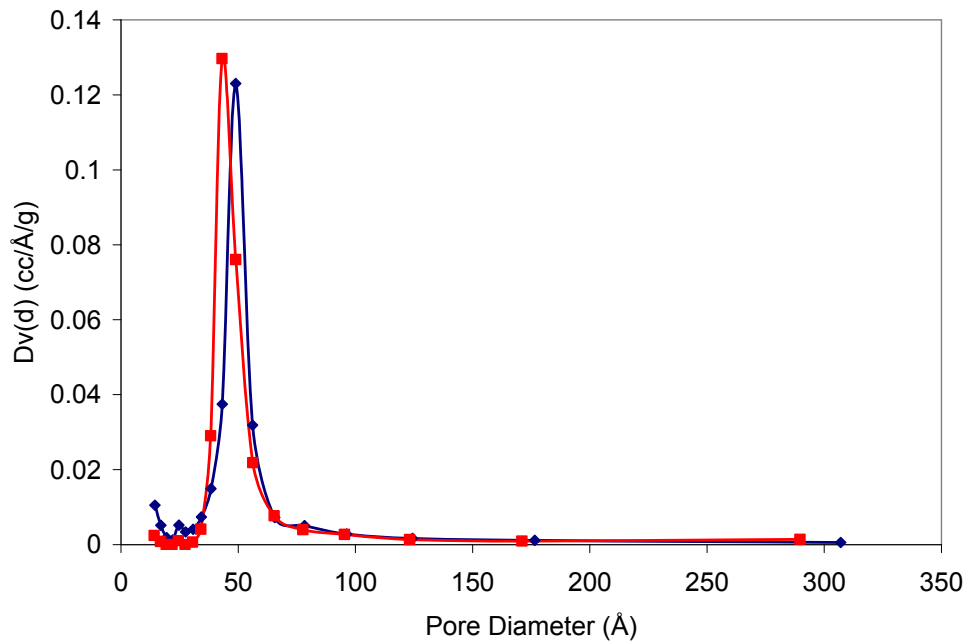
Figure 3.5. Pore size distribution of surfactant-extracted large pore MSN (blue-adsorption; red-desorption).
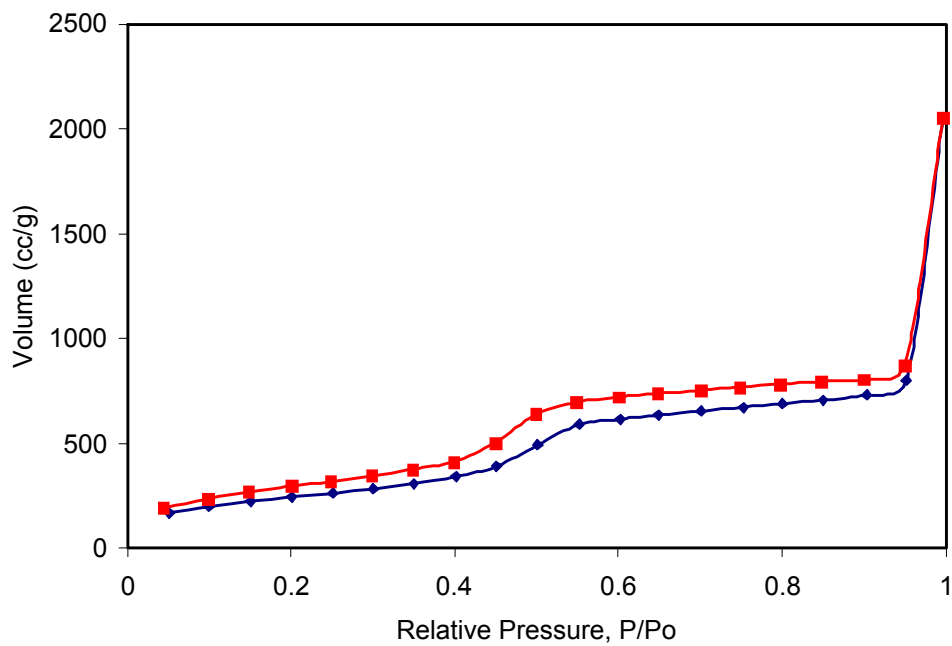
Figure 3.6. Nitrogen sorption isotherm of MSN-S-S-DTPA-Gd (blue-adsorption; red-desorption).
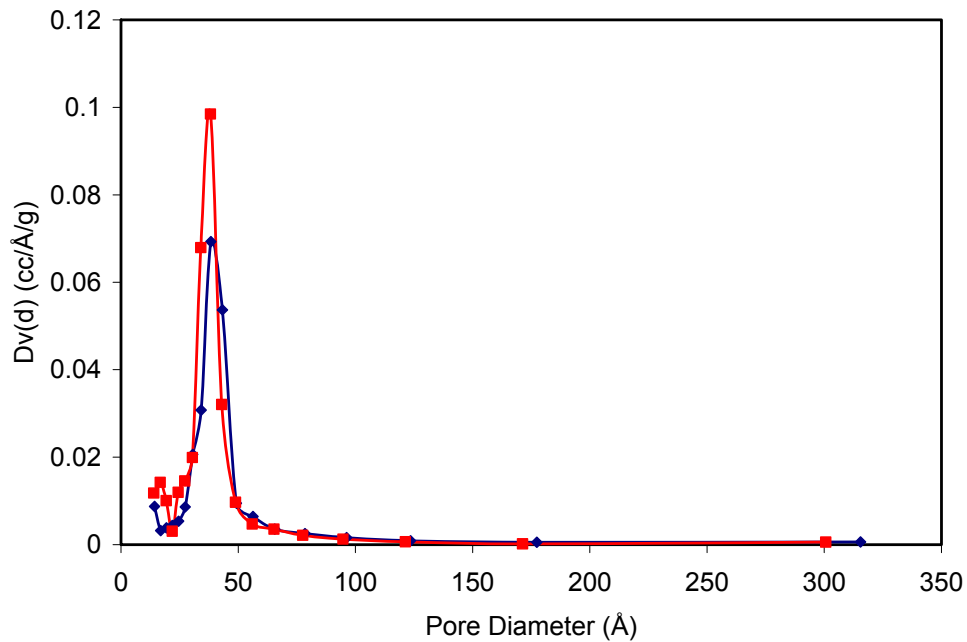
Figure 3.7. Pore size distribution of MSN-S-S-DTPA-Gd (blue-adsorption; red-desorption).
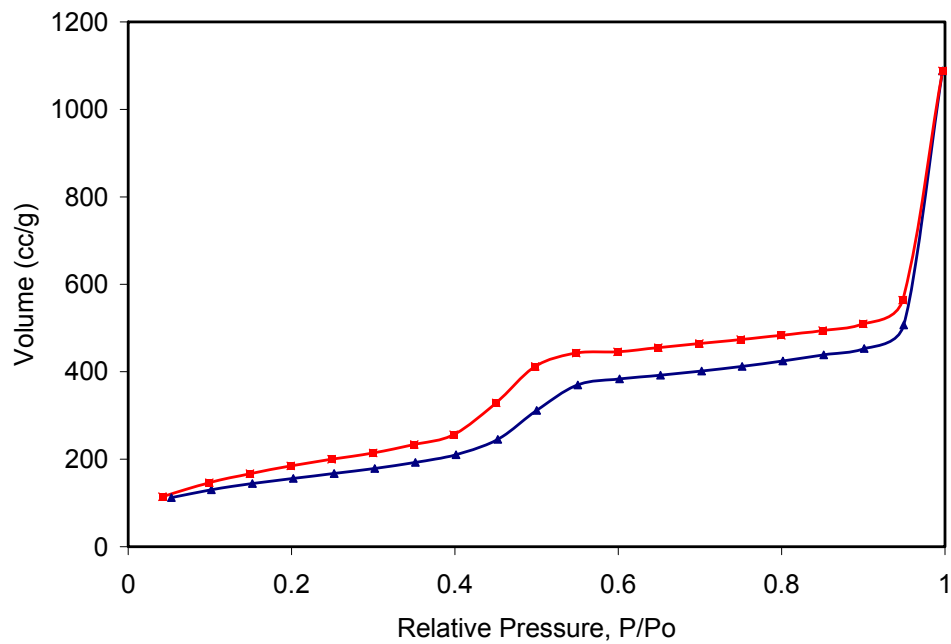
Figure 3.8. Nitrogen sorption isotherm of PEG2000 functionalized MSN-S-S-DTPA-Gd (blue-adsorption; red-desorption).
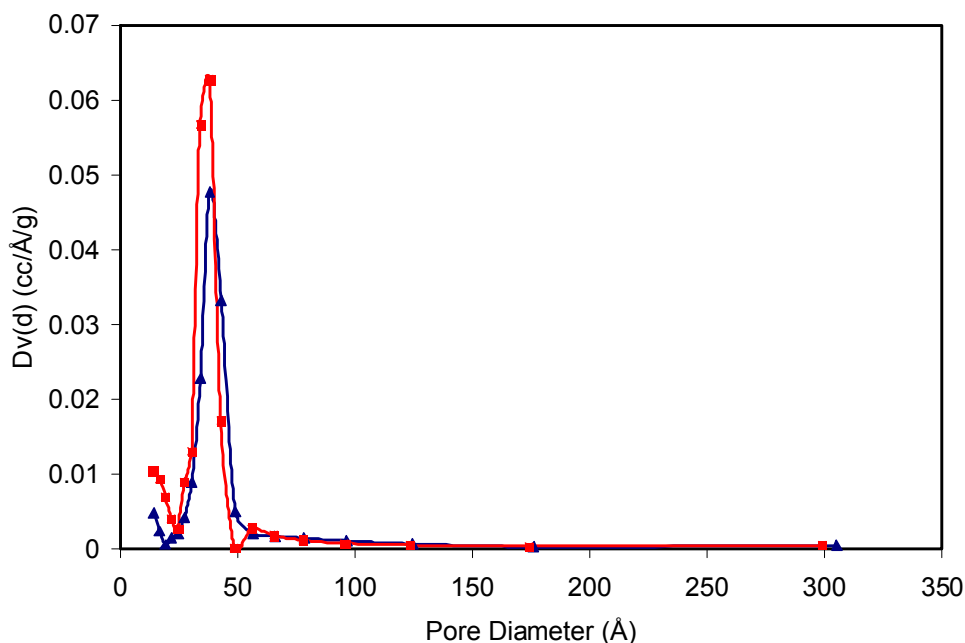
Figure 3.9. Pore size distribution of PEG2000 functionalized MSN-S-S-DTPA-Gd (blue-adsorption; red-desorption).

Thermogravimetric analysis was used to verify the complete extraction of the surfactant template, and the grafting of the Si-S-S-DTPA-Gd complex and PEG (Fig. 3.10). The extracted particles show an initial weight loss of 8.52 wt% from room temperature to 150 °C, followed by a gradual weight loss of 6.63 wt% from 150-600 °C. After coating with the Si-S-S-DTPA-Gd complex, a weight loss of 11.31 wt% is seen from room temperature to 150 °C, resulting from solvent residing in the channels, followed by a weight loss of 9.08 wt% from 250-600 °C, resulting from the organic portion of the Gd complex. After the second coating reaction (to increase the loading of the complex), the TGA shows and initial weight loss of 6.95 wt% from room temperature to 150 °C, followed by a loss of 12.35 wt% from 250-600 °C, consistent with the increased loading of the Gd complex. Finally, TGA results of the PEG2000 functionalized particles shows an initial weight loss of 8.11 wt% from room temperature to 150 °C, followed by a weight loss of 17.65% from 250-600 °C, confirming PEG functionalization. The precise amount of Gd was determined using either

direct current plasma spectroscopy (DCP) or inductively coupled plasma – mass spectroscopy. The average Gd loading was approximately 2.56 wt% after the first coating and 3.69 wt% after the second coating.
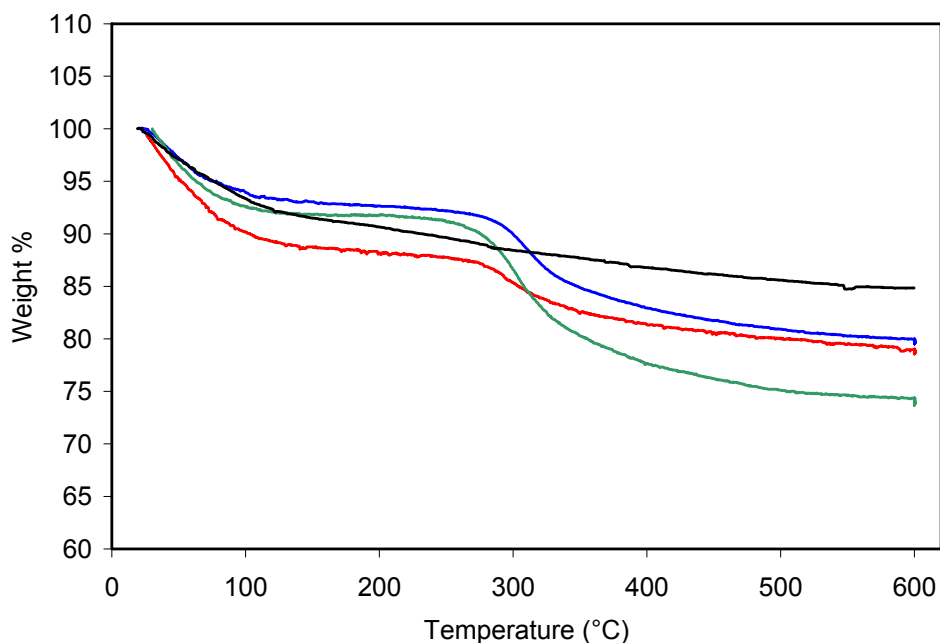
Figure 3.10. TGA curves of the surfactant extracted large pore MSN (black), MSN-S-S-DTPA-Gd (red), recoated MSN-S-S-DTPA-Gd (blue), and PEG2000 functionalized MSN-S-S-DTPA-Gd (green).

3.2.4 Relaxivity Measurements

In order to evaluate the MRI contrast enhancing ability of the particles, the relaxivity values were measured using both a 3 T and a 9.4 T scanner. The relaxivity values for the degradable MSN particles were slightly lower than what was obtained for the non-degradable version. At 3 T the MSN-S-S-DTPA-Gd particles had an r_1 relaxivity of 24.7 $mM^{-1}s^{-1}$ and an r_2 of 31.1 $mM^{-1}s^{-1}$ (Fig. 3.11). Particles that had undergone a second coating reaction had similar relaxivities of 24.9 $mM^{-1}s^{-1}$ and 35.9 $mM^{-1}s^{-1}$ for r_1 and r_2, respectively (Fig. 3.12). At 9.4 T, the r_1 dropped while the r_2 increased. For the coated particles the r_1 relaxivity was 7.1 $mM^{-1}s^{-1}$ while the r_2 increased to 53.3 $mM^{-1}s^{-1}$ (Fig. 3.13). The increased loading from

the second coating reaction resulted in a slight decrease of the relaxivities to 5.0 and 44.8 mM^{-1}s^{-1}, for r_1 and r_2, respectively (Fig. 3.14). Finally, the PEG2000 coating resulted in little change to the relaxivity values, these particles had an r_1 of 5.7 mM^{-1}s^{-1} and an r_2 of 48.7 mM^{-1}s^{-1} (Fig. 3.15).
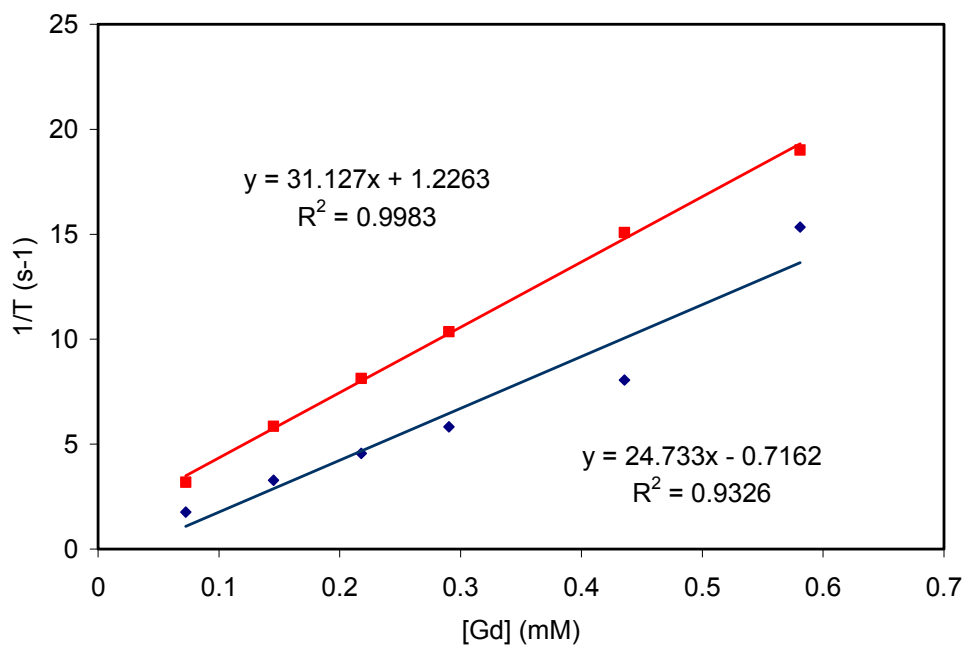
Figure 3.11. r_1 (blue) and r_2 (red) relaxivity curves of MSN-S-S-DTPA-Gd measured at 3 T.
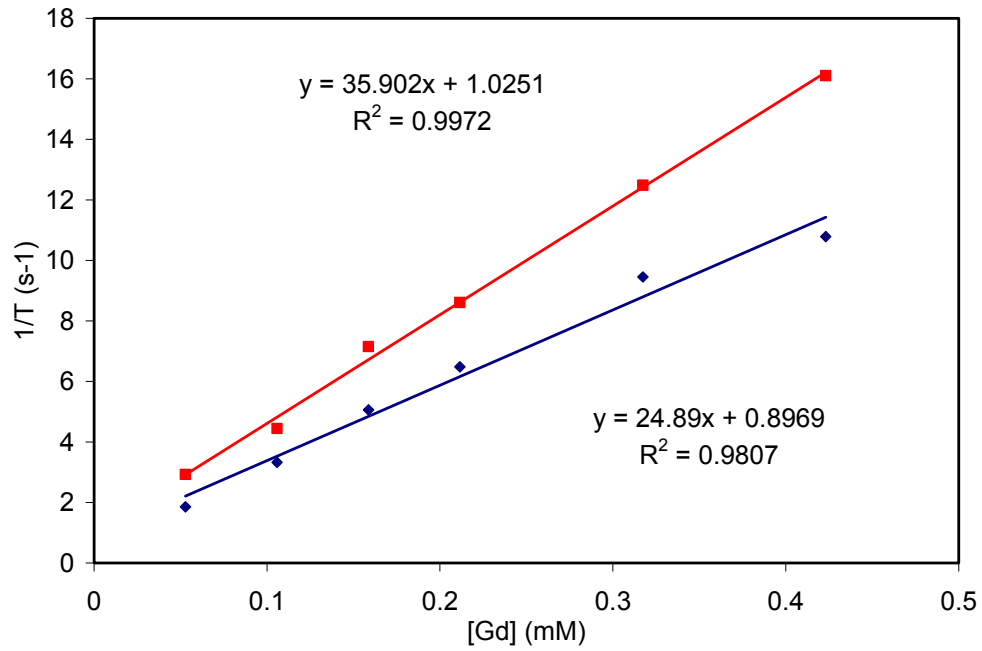
Figure 3.12. r_1 (blue) and r_2 (red) relaxivity curves of recoated MSN-S-S-DTPA-Gd measured at 3 T.
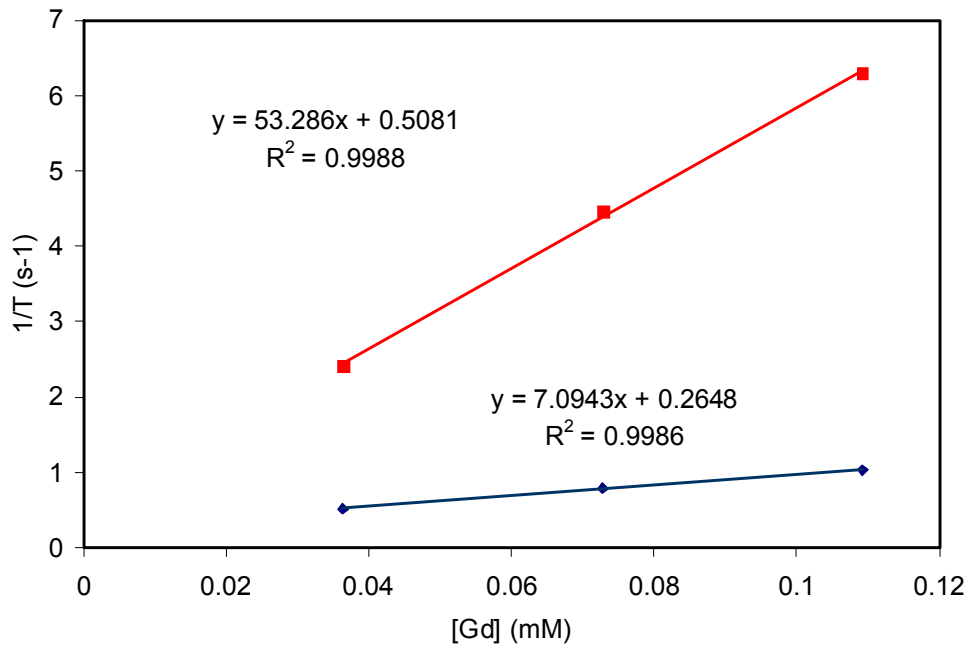
Figure 3.13. r_1 (blue) and r_2 (red) relaxivity curves of MSN-S-S-DTPA-Gd measured at 9.4 T.
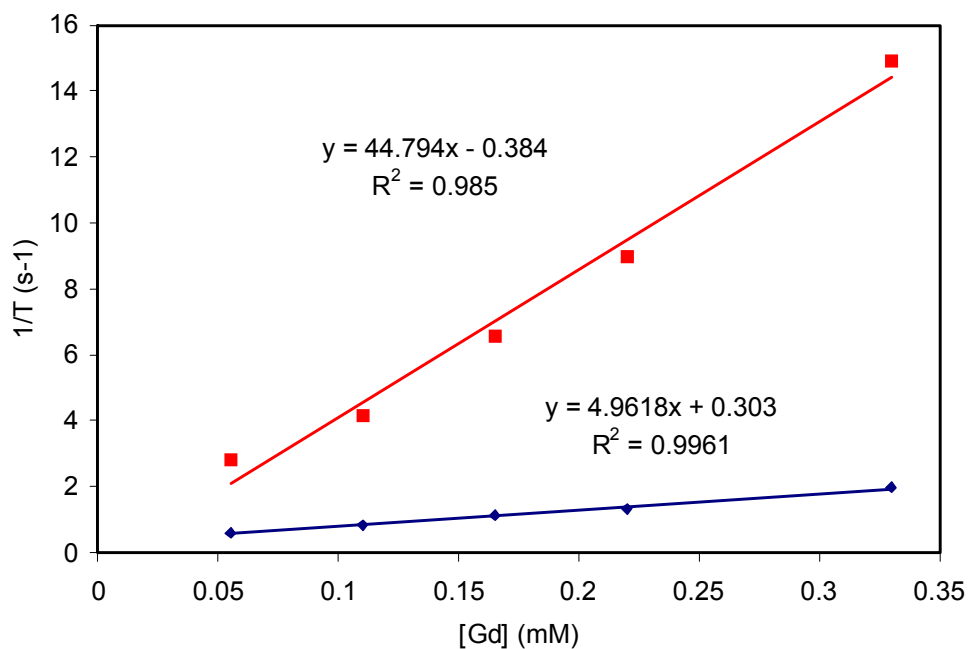
Figure 3.14. r_1 (blue) and r_2 (red) relaxivity curves of recoated MSN-S-S-DTPA-Gd measured at 9.4 T.
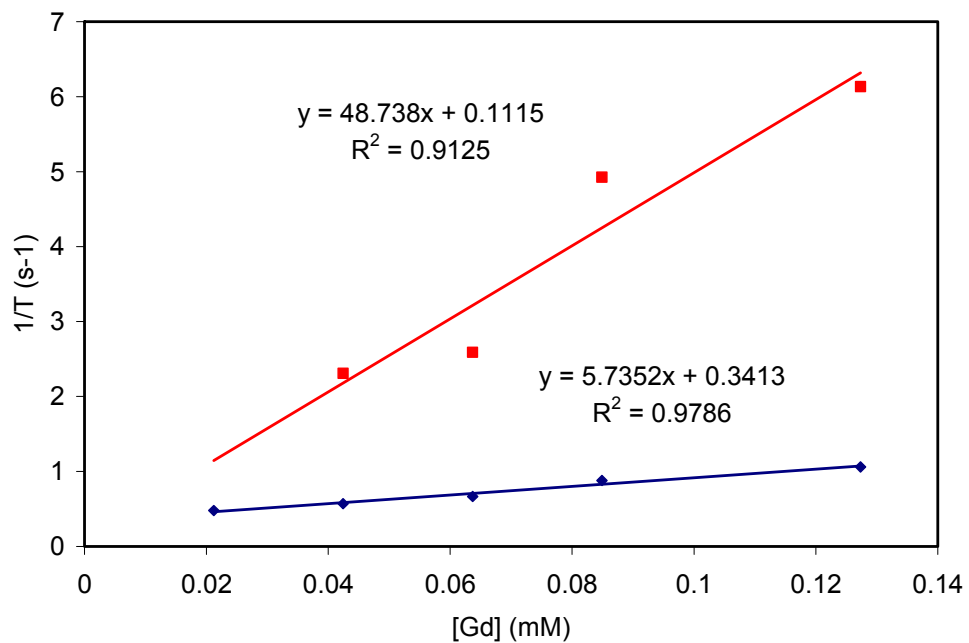
Figure 3.15. r_1 (blue) and r_2 (red) relaxivity curves of PEG2000 functionalized MSN-S-S-DTPA-Gd measured at 9.4 T.

3.2.5 Release Profile

In order to determine how quickly the disulfide bond will be cleaved to release the Gd chelate from the particle, a release profile was carried out in the presence of 10 mM cysteine, to simulate the intracellular free thiol concentration. A suspension of the particles in water was placed inside a piece of dialysis tubing with a molecular weight cut off of 3500. The dialysis bag was then submerged in 300 mL of degassed distilled water that had been heated to 37 °C. The entire vessel was kept under a nitrogen atmosphere. After the bag had been submerged for 30 minutes, a 10 mL aliquot was removed to analyze for any Gd that was released before adding the cysteine. This 10 mL aliquot was replaced with 10 mL of an aqueous solution containing 0.3636 g (0.003 mol) of L-cysteine to give a cysteine concentration of 10 mM. Aliquots of the dialysis solution were then removed a various time points, and the Gd concentration was measured using DCP. The disulfide bond release was found to have a half-life of approximately 50 hours, with approximately 82% of the chelates being released after about 5 days (Fig. 3.16).
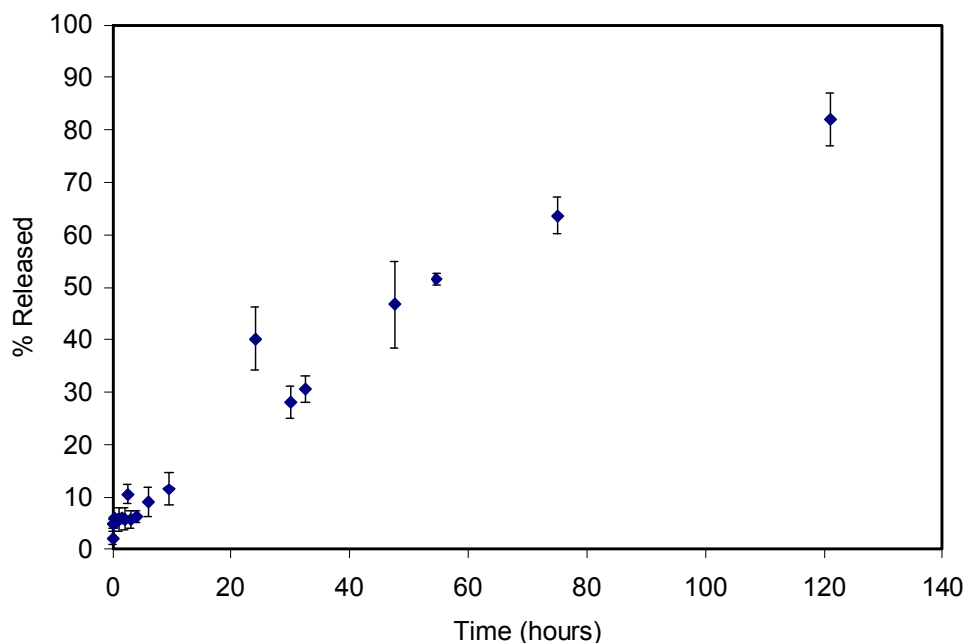
Figure 3.16. Release profile for MSN-S-S-DTPA-Gd in the presence of 10 mM cysteine at 37 °C.

3.2.6 Non-Specific Binding Assay

In order to evaluate the effectiveness of the PEG surface functionalization in reducing the non-specific binding of proteins a non-specific binding assay was performed using bovine serum albumin (BSA). Particles were incubated with Texas Red labeled BSA for 2 hours, after which time they were isolated and washed. The particles were then redispersed and the Texas Red emission intensity was used to quantify the amount of BSA that was adsorbed onto the particles. It was found that unmodified MSN-S-S-DTPA-Gd particles retained 100% of the BSA added, while those that had been surface functionalized with PEG2000 retained 87%. Increasing the PEG chain length to PEG5000 did not improve the results; these particles retained 91% of the BSA added. As a control experiment bare, large pore MSN particles were coated with PEG2000 and PEG5000, and the protein binding assay was repeated. In this case the PEG2000 and PEG5000 modified particles retained only 51 and 53% of the BSA added, respectively. Based on these results we concluded that in the case of

the MSN-S-S-DTPA-Gd particles, the majority of the exterior surface is already coated with the Gd complex, leaving little room for further surface functionalization with PEG.

3.3 Conclusion

We have developed a potentially biodegradable contrast agent based on mesoporous silica nanoparticles. The Gd chelates are attached to the nanoparticles through a disulfide bond that can be cleaved *in vivo* to release small molecule Gd chelates which can be quickly cleared form the body. We have also modified the surface of the particles with poly(ethylene glycol) to increase the circulation time of the particles. These particles show increased relaxivity compared to the small molecule Gd chelate contrast agents currently available, and the half life for cleaving the chelates was found to be approximately 50 hours in the presence of 10 mM cysteine. This will allow sufficient time for imaging before the contrast agent is cleared.

3.4 Experimental Details

3.4.1 Materials and Methods

All reagents were purchased from Aldrich and used without further purification, except 3-mercaptopropyltriethoxysilane and (3-isocyanatopropyl)-triethoxysilane which were purchased from Gelest. (3-isocyanatopropyl)triethoxysilane was purified by vacuum distillation prior to use. Thermogravimetric analysis (TGA) was performed using a Shimadzu TGA-50 equipped with a platinum pan and a heating rate of 3 °C per minute, under air. A Hitachi 4700 field emission scanning electron microscope (SEM) and a JEM 100CX-II transmission electron microscope (TEM) were used to determine particle size and

morphology. A Cressington 108 Auto Sputter Coater equipped with a Au/Pd (80/20) target and an MTM-10 thickness monitor was used to coat the samples with a 5 nm thick conductive layer before taking SEM images. Each SEM sample was prepared by suspending the nanoparticles in ethanol. A drop of the suspension was then placed on a glass slide and the solvent was allowed to evaporate. TEM samples were also prepared from ethanolic particle dispersions on amorphous carbon coated copper grids. An Applied Research Laboratories (ARL) SpectraSpan 7 DCP spectrometer and a Varian 820-MS Inductively Couple Plasma mass spectrometer were used to measure Gd^{3+} concentrations.

MR images were acquired on a Siemens 3 T Allegra (Siemens Medical Systems, Erlangen, Germany) with a CP head coil, and a 9.4 T Bruker BioSpec (Bruker Biospin, Ettlingen, Germany) system with a 35 mm quadrature RF transmit and receive coil. For the 3 T scanner, a 3D FLASH sequence was utilized to compute T_1 maps with seven different flip angles (2, 5, 10, 20, 30, 40, and 60). Imaging parameters were: FOV=190x 190*64 mm^3, Matrix size=128 x 128 *32, TR/TE= 40/1.64 ms, total data acquisition time was 19 minutes. A 2-D multiple echo spin echo sequence was used to estimate T_2 maps. In total, 32 echoes with an echo spacing of 6.2 ms were obtained. The first echo time was 6.2 ms. TR was 3000 ms. FOV and matrix size were set to 190x 190 mm^2 and 128 x 128. The slice thickness was 2 mm. The total data acquisition time was about 6 minutes and 29 seconds. All images were acquired on a 9.4 T Bruker BioSpec (Bruker Biospin, Ettlingen, Germany) system with a 35 mm quadrature RF transmit and receive coil. For the 9.4 T scanner, two 2D multiple echo spin echo sequences were used to estimate T_2 maps for a wide range of T_2. FOV and matrix size were set to 35 x 30 mm^2 and 128 x 128. The slice thickness was 1 mm. In total, 32 echoes with an echo spacing of 3.7 ms for sequence 1 and 40 echoes with an echo spacing of

10 ms for sequence 2 were obtained. The TR/TE1 were 3.7/3000 ms and 10/4114 ms for each sequence, respectively. The total data acquisition time was about 10 minutes. T_1 maps were obtained with a variable TR rapid acquisition relaxation enhanced (RARE) sequence with a TE=5.14 ms. Twenty two variable TRs (TR=18, 25, 40, 60, 90, 120, 160, 200, 250, 300, 380, 500, 700, 1000, 1500, 2000, 2500, 3000, 4000, 5000, 6000, 7000 ms) were used with a FOV of 35x30 mm^2 and a matrix size of 128 x 128. RARE factor was 3 and total data acquisition was about 24 minutes.

3.4.2 Ligand and Gd Complex Synthesis

Diethylenetriaminepenta(acetic acid)-ethyldisulfanylpropyltriethoxysilane-Gd complex (Si-S-S-DTPA-Gd). 0.200 g (0.5589 mmol) of DTPA-bisanhydride was dissolved in 4 mL of anhydrous DMSO in a 2-neck round bottom flask. 0.0834 g (0.4478 mmol) of 2-pyridyldisulfanylethylamine was dissolved in 1 mL of anhydrous DMSO. This solution was then added dropwise to the DTPA-bisanhydride solution. After the addition was complete the reaction was stirred at room temperature, under N_2, overnight. The product was then precipitated upon the addition of acetone and diethyl ether. The product (DTPA-PDS) was isolated by centrifuging, and was washed with additional acetone and diethyl ether. Yield: 0.2671 g, (0.4756 mmol, 106.2 %) 0.200 g (0.3561 mmol) of the DTPA-PDS ligand was dissolved in 0.71 mL of 2 M NaOH (1.4244 mmol, 4 eq). 0.1324 g (0.356 mmol) of GdCl$_3$·6H$_2$O was dissolved in ~0.5 mL of water. This solution was then slowly added to the ligand solution. After all the GdCl$_3$ had been added, the solution was stirred at room temperature for an additional 30 minutes. The product was then precipitated upon the addition of acetone, and was collected by centrifuging. Yield: 0.20481 g (0.2787 mmol, 78.3

%) A disulfide exchange reaction was then performed to obtain the desired product. 2.6728 g (3.637 mmol) of the monoPDS-DTPA-Gd complex was dissolved in 50 mL of methanol. The solution was then filtered to remove any insoluble impurities. 0.973 mL (0.960 g, 4.028 mmol) of 3-mercaptopropyltriethoxysilane was then added, and the reaction was stirred at room temperature, under N_2, overnight. The reaction solution was then concentrated, and the product was precipitated upon the addition of diethyl ether. Yield: 2.1583 g (2.503 mmol, 74.6 %)

Synthesis of triethoxysilylpropyl carbamoyl-poly(ethylene glycol)2000. 1.000 g (0.50 mmol) of poly(ethylene glycol)-2000-monomethylether was dried under vacuum at 100 °C for 1 hour. After cooling to room temperature, under N_2, the PEG was dissolved in 3 mL of anhydrous DMSO. 0.124 mL (0.124 g, 0.50 mmol) of distilled (3-isocyanatopropyl)triethoxysilane was then added, followed by 1 μL of Hünig base (0.742 mg, 0.0057 mmol, 1.15 mol %). The reaction was then stirred at room temperature, under N_2, for 24 hours. The DMSO was then removed under vacuum at 50°C. ^{1}H NMR (DMSO-d_6, 300 MHz,): δ 0.51 (t, 2H), δ 1.14 (t, 9H), δ 1.43 (t, 2H), δ 2.92 (q, 2H), δ 3.35 (s, 3H), δ 3.50 (s, 128H), δ 3.73 (q, 6H), δ 4.03 (t, 2H), δ 7.22 (t, 1H).

3.4.3 MSN Synthesis

Large Pore MSN Particles. 0.400 g (1.096 mmol) of cetyltrimethylammonium bromide (CTAB) was dissolved in 192 mL of distilled H_2O, along with 1.4 mL of 2 M sodium hydroxide and 2.8 mL (19.52 mmol) of mesitylene. This solution was then heated to 80 °C. Once the reaction had reached 80 °C, 2.0 mL (1.868 g, 8.96 mmol) of tetraethylorthosilicate (TEOS) was rapidly injected. The reaction was then stirred for an

additional 2 hours at 80 °C. At the completion of the reaction the particles were isolated by centrifuging at 10,000 rpm for 10 minutes. They were then washed with H_2O and ethanol, before being redispersed in 80 mL of ethanol. The surfactant was extracted from the mesoporous materials using a 1 volume % solution of HCl in methanol. The particles were dispersed in the HCl/MeOH solution at a concentration of approximately 3.5 mg/mL. After stirring at 60 °C for 3 hours, the particles were isolated by centrifuging, and then redispersed in another aliquot of the HCl/MeOH solution. The extraction was performed a total of three times. After the final extraction, the particles were washed with distilled H_2O and ethanol, before being redispersed in ethanol.

Coating of MSN with Si-S-S-DTPA-Gd complex. Approximately 400 mg of extracted MSN particles were suspended in 13 mL of toluene. 0.150 g (0.174 mmol) of the Si-S-S-DTPA-Gd complex was then dissolved in 1 mL of distilled water, and this solution was added to the reaction mixture. The mixture was then heated to reflux overnight. The particles were isolated by centrifuging, and were washed with distilled water and ethanol, before being redispersed in ethanol. In order to remove any adsorbed Gd complexes the particles were the dialyzed against 250 mL of distilled water for 4.5 hours, changing the water once an hour.

Recoated MSN-LP-Gd. In order to increase the Gd loading of the particles, the above coating procedure was repeated. Approximately 190 mg of particles were dispersed in 11 mL of toluene, and 0.075 g (0.087 mmol) of the Si-S-S-DTPA-Gd complex was dissolved in 0.75 mL of distilled water and added to the reaction. The mixture was then heated to reflux overnight. The particles were isolated by centrifuging, and washed with distilled

water and ethanol, before being redispersed in ethanol. After coating, the particles were also dialyzed against 250 mL of distilled water for 4.5 hours

PEG2000 Functionalization. Approximately 100 mg of MSN-S-S-DPTA-Gd particles were dispersed in 8 mL of ethanol. The pH was adjusted to approximately 9 using ammonium hydroxide. 20.8 mg of Si-PEG-2000 was then dissolved in 2 mL of ethanol, and this solution was added to the particle suspension. The reaction was then stirred at room temperature 18 hours. The particles were isolated by centrifuging at 13,000 rpm for 15 minutes, and were washed twice with ethanol before being redispersed in 12 mL of ethanol. The particles were then dialyzed against 250 mL of distilled water for 5 hours, changing the water once an hour.

3.4.4 Release Profile

1.5 mL of an 18.08 mg/mL suspension of MSN-S-S-DTPA-Gd particles (27.12 mg) was centrifuged to isolate the particles, which were then redispersed in 2 mL of water. This suspension was then placed inside a piece of dialysis tubing (MWCO 3500). 300 mL of distilled water was placed in a vessel and was heated to 37 °C in an oil bath. The water was then degassed by bubbling with N_2 for 20 minutes. The dialysis bag containing the particles was then submerged. After 30 minutes, a 10 mL aliquot of the dialysis water was removed, and was replaced with a 10 mL solution containing 0.3636 g (0.003 mol) of L-cysteine, giving a final cysteine concentration of 10 mM. Aliquots were then removed at various time points. Each aliquot that was removed was dried, and the residue was redissolved in 1.5 mL of 1 M nitric acid. The Gd concentration of each sample was then measured using DCP.

3.5 References

1. Idée, J-M.; Port, M.; Medina, C.; Lancelot, E.; Fayoux, E.; Ballet, S.; Corot, C., Possible involvement of gadolinium chelates in the pathophysiology of nephrogenic systemic fibrosis: A critical review. *Toxicology.* **2008**, *248* (2-3), 77-88.

2. Stratta, P.; Canavese, C.; Aime, S., Gadolinium-enhanced magnetic resonance imaging, renal failure and nephrogenic systemic fibrosis /nephrogenic fibrosing dermopathy. *Current Medicinal Chemistry*. **2008**, *15* (12), 1229-1235.

3. Mohs, A. M.; Wang, X.; Goodrich, K. C.; Zong, Y.; Parker, D. L.; Lu, Z-R., PEG-*g*-poly(GdDTPA-*co*-L-cystine): A biodegradable macromolecular blood pool contrast agent for MR imaging. *Bioconjugate Chem.* **2004**, *15* (6), 1424-1430.

4. Wang, X.; Feng, Y.; Ke, T.; Schabel, M.; Lu, Z-R., Pharmacokinetics and tissue retention of (Gd-DTPA)-cystamine copolymers, a biodegradable macromolecular magnetic resonance imaging contrast agent. *Pharmaceutical Research.* **2005**, *22* (4), 596-602.

5. Ke, T.; Feng, Y.; Guo, J.; Parker, D. L.; Lu, Z-R., Biodegradable cystamine spacer facilitates the clearance of Gd(III) chelates in poly(glutamic acid) Gd-DO3A conjugates for contrast-enhanced MR imaging. *Magnetic Resonance Imaging.* **2006**, *24* (7), 931-940.

6. Feng, Y.; Zong, Y.; Ke, T.; Jeong, E-K.; Parker, D. L.; Lu, Z-R., Pharmacokinetics, biodistribution and contrast enhanced MR blood pool imaging of Gd-DTPA cystine copolymers and Gd-DTPA cystine diethyl ester copolymers in a rat model. *Pharmaceutical Research*. **2006**, *24* (8), 1736-1742.

7. Mohs, A. M.; Nguyen, T.; Jeong, E-K.; Feng, Y.; Emerson, L.; Zong, Y.; Parker, D. L.; Lu, Z-R., Modification of Gd-DTPA cystine copolymers with PEG-1000 optimizes pharmacokinetics and tissue retention for magnetic resonance angiography. *Magnetic Resonance in Medicine.* **2007**, *58* (1), 110-118.

8. Slowing, I.; Trewyn, B.G.; Lin, V. S-Y., Mesoporous silica nanoparticles for intracellular delivery of membrane-impermeable proteins. *J. Am. Chem. Soc.* **2007,** *129* (28)*,* 8845-8849.

CHAPTER 4

Gadolinium-Based Nanoscale Metal-Organic Frameworks for Multimodal Imaging

4.1 Introduction

Metal-organic frameworks (MOFs) are an interesting class of hybrid materials that are built from metal ion connectors and polydentate bridging ligands and have shown potential in a number of applications such as nonlinear optics,[1,2] gas adsorption,[3-6] catalysis,[7-9] and even controlled drug release.[10,11] MOFs on the nanometer scale can offer an interesting approach to designing functional nanomaterials for biological and biomedical applications because of the ability to systematically tune their compositions via judicious choice of building blocks. This tunability, provided by the ability to choose from a wide selection of metal ion connectors and an infinite number of organic bridging ligands, makes this class of nanomaterials much different than other well studied nanomaterials that are either purely inorganic or organic in composition. To date, there have been very few publications on these nanoscale coordination polymer materials.

Our group has previously utilized a reverse-phase microemulsion technique to synthesize nanoscale metal-organic frameworks (NMOFs) built from Gd^{3+} ions and two benzene carboxylate bridging ligand, 1,4-benzenedicarboxylate and 1,2,4-benzenetricarboxylate.[12] This synthetic technique can be applied to other metal and ligand combinations, however in some cases it led to gel-like amorphous materials presumably as a result of the rapid and irreversible metal-ligand coordination bond formation at room temperature. As a result, alternative synthetic methods had to be developed in order to take full advantage of the intrinsic tunability of NMOFs in designing functional NMOFs for ultimate applications in imaging, biosensing, and drug delivery. Hydrothermal reactions have proven to be an excellent method for the synthesis of a variety of nanomaterials.[13-16] Presumably, the elevated temperatures alter the relative kinetics for nucleation and

nanocrystal growth in favor of the formation of uniform nanomaterials under hydrothermal conditions.[17,18]

Using these two techniques we were able to synthesize four new Gd^{3+} containing metal organic frameworks using three different bridging ligands. Gd(III) NMOFs were developed as potential contrast agents for magnetic resonance imaging (MRI). Contrast agents containing paramagnetic metal ions, such as Gd(III) and Mn(II), are often administered during an MRI scan in order to enhance contrast. Incorporation of the paramagnetic ion in a nanoparticle platform further serves to increase the contrast enhancing ability by reducing the rotational diffusion rate, which results in increased relaxivity. Using a nanoparticle platform also provides an increased payload; hundreds of thousands of metal centers can be incorporated into each NMOF particle. This increased payload allows for the potential of site specific imaging because a single targeting moiety can deliver a very large payload of contrast agent. The Gd-containing NMOFs can also be doped with a small percentage of other luminescent lanthanide ions, such as Tb(III) and Eu(III), forming multimodal contrast agents, i.e. optical and MR.

4.2 Results and Discussion

4.2.1 Synthesis of Gd NMOFs

Two different Gd containing NMOFs were synthesized using aliphatic dicarboxylate ligands, succinic acid and adipic acid. Both of these NMOFs can be synthesized using a high temperature surfactant assisted procedure, and the adipic acid NMOFs can also be obtained from a room temperature reaction. Two different Gd NMOFs were also synthesized using benzene hexacarboxylate (BHC) as the bridging ligand. By varying the pH of the reaction,

two different phases can be obtained from the same starting materials. The Gd-BHC NMOFs were also synthesized using the high temperature surfactant assisted procedure.

Gd-succinic acid NMOFs (**4-1**) were synthesized by first forming two separate cetyltrimethylammonium bromide (CTAB)/1-hexanol/n-heptane/water microemulsions with W-values of 5 (W = water/surfactant ratio), one containing a 0.10 M solution of $GdCl_3$ and the other containing a 0.075 M solution of succinic acid methyl ammonium salt. Once the two microemulsions had formed, they were combined and transferred to a Teflon-lined Parr reactor. The reaction was then heated in a 120 °C oven for 16 hours. After cooling to room temperature, the product was isolated by centrifuging, and was washed with ethanol to remove the surfactant.

The Gd-adipic acid NMOFs (**4-2**) can be synthesized using either the room temperature microemulsion or the high temperature surfactant assisted method. For the room temperature synthesis, two separate CTAB/1-hexanol/n-heptane/water microemulsions with W-values of 10 were formed using a 0.075 M solution of adipic acid sodium salt and a 0.10 M solution of $GdCl_3$. Once the two microemulsions had formed, they were combined and stirred at room temperature for an additional 2 hours. The product was then collected by centrifuging, and was washed with ethanol. For the high-temperature surfactant assisted synthesis a similar procedure as that used for **4-1** was used. Two W=5 CTAB/1-hexanol/n-heptane/water microemulsions were formed using a 0.075 M adipic acid sodium salt solution and a 0.05 M $GdCl_3$ solution. After forming, the two microemulsions were combined and transferred to a Teflon-lined Parr reactor. The reaction was then heated in a 120 °C oven for 2.5 hours. After cooling to room temperature, the particles were isolated by centrifuging and were washed with ethanol.

[Gd$_2$(BHC)(H$_2$O)$_6$] nanoparticles (**4-3**) were synthesized using the high temperature surfactant assisted method. Briefly, two CTAB/1-hexanol/n-heptane/water microemulsions with $W = 10$ were formed using a 0.1 M solution of BHC methylammonium salt and a 0.1 M solution of GdCl$_3$. After forming, the two microemulsions were combined and transferred to a Teflon-lined Parr reactor. The reaction mixture was then heated at 120 °C for 18 hours to afford nanoparticles of [Gd$_2$(BHC)(H$_2$O)$_6$]. The nanoparticles of **4-3** were isolated in 84.4% yield by centrifugation and washing with ethanol. Eu^{3+} and Tb^{3+} doped nanoparticles of **4-3** (**4-3a** and **4-3b**, respectively) were also synthesized using a similar procedure, replacing 5 mol% of GdCl$_3$ with either TbCl$_3$ or Eu(NO$_3$)$_3$. In order to reduce aggregation the **4-3** NMOFs were also coated with poly(vinylpyrrolidone) (PVP). To a suspension of 1 mg of **4-3** in 2 mL of ethanol was added 20 μL of a 5 mM solution of PVP in ethanol. The reaction was then stirred at room temperature, overnight. The particles were then isolated by centrifuging and were washed with additional ethanol.

Nanorods of [Gd$_2$(BHC)(H$_2$O)$_8$](H$_2$O)$_2$ (**4-4**) were also synthesized using a surfactant assisted method with microwave heating. Two CTAB/1-hexanol/iso-octane/water microemulsions with $W=10$ were formed using a 0.1 M mellitic acid (BHC-H$_6$) aqueous solution and a 0.2 M GdCl$_3$ aqueous solution. The two microemulsions were then combined and transferred to a microwave vessel. The reaction was then heated to 60 °C in a 400 W microwave, and held at this temperature for 15 minutes. The particles were then isolated by centrifuging and were washed with ethanol. Using a similar procedure micron sized particles of **4-4** can be synthesized by increasing the reaction temperature to 120 °C. Single crystals of **4-4** were synthesized by heating an aqueous solution of mellitic acid and GdCl$_3$ in a 60 °C oven, overnight.

4.2.2 Characterization of NMOFs

The NMOFs were characterized using a variety of methods. First, the size and morphology of the particles were determined using scanning electron and transmission electron microscopies (SEM and TEM). As seen in the SEM and TEM images the succinic acid NMOFs (**4-1**) were rods approximately 100-300 nm in diameter and had lengths ranging from 2 to 10 microns (Fig. 4.1-4.2). Both the room temperature and high temperature syntheses of **4-2** yielded high aspect ratio nanorods. The nanorods formed at room temperature are approximately 25-50 nm in diameter and range in length from approximately 400-1500 nm (Fig. 4.3). The nanorods formed at 120 °C are approximately 50-75 nm in diameter and 1 to 1.5 microns in length (Fig. 4.4).
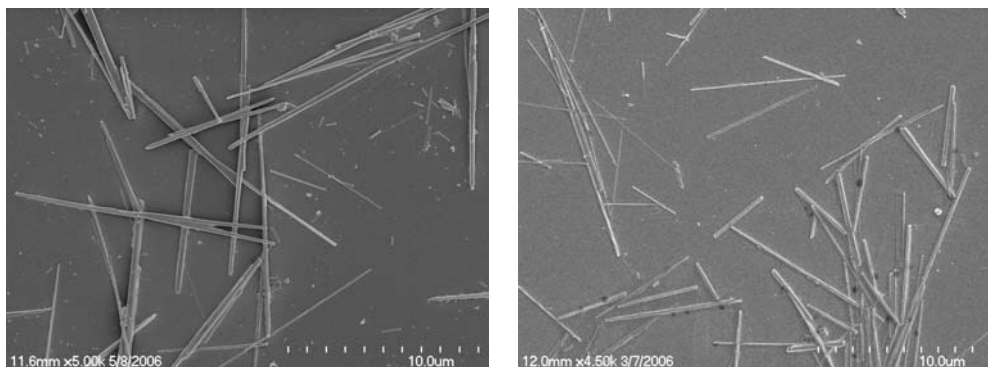
Figure 4.1. SEM images of succinic acid-Gd nanorods (**4-1**).
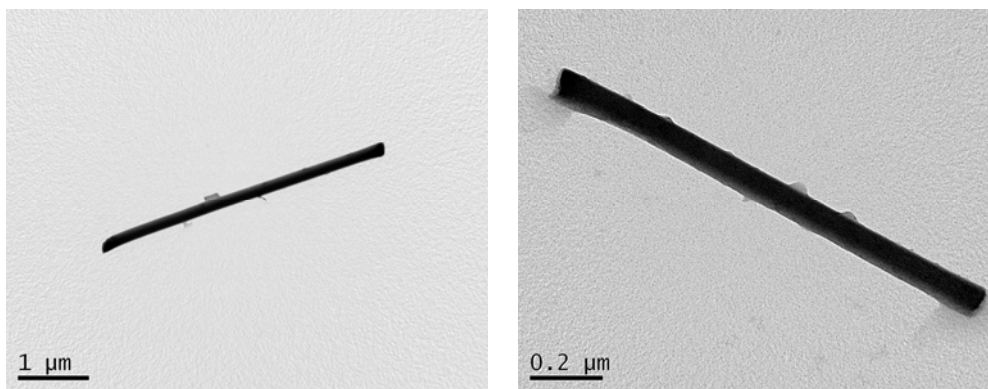
Figure 4.2. TEM images of succinic acid-Gd nanorods (**4-1**).
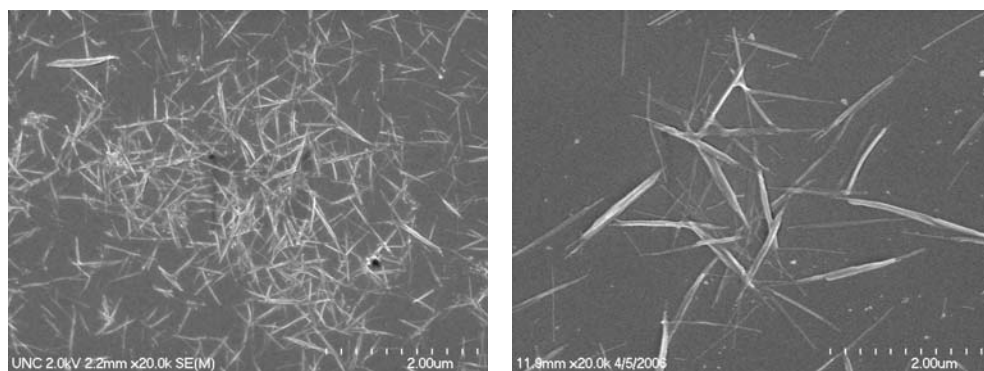
Figure 4.3. SEM images of adipic acid-Gd nanorods (**4-2**) synthesized at room temperature.
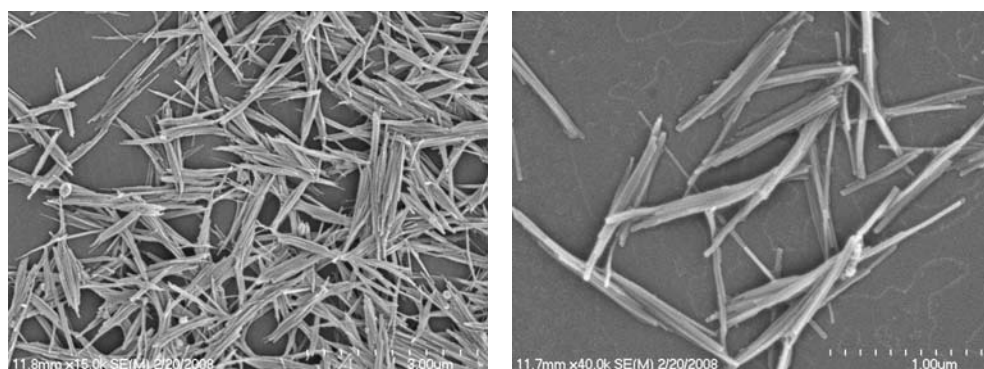
Figure 4.4. SEM images of adipic acid-Gd nanorods (**4-2**) synthesized at 120 °C.

The SEM and TEM images revealed that NMOFs of **4-3** formed fairly uniform block like nanoparticles that are approximately 25 nm by 50 nm by 100 nm (Fig. 4.5-4.7). NMOFs **4-3a** and **4-3b** (Eu^{3+} and Tb^{3+} doped) had similar size and morphology to **4-3** (Fig. 4.8-4.11). When NMOF **4-4** was synthesized at 60 °C nanorods of approximately 100-300 nm in diameter and several microns in length were obtained (Fig. 4.12-4.13). When the reaction temperature was increased to 120 °C, micrometer-sized particles with predominantly octahedra and truncated octahedra shapes along with a small fraction of nanorods were obtained (Fig. 4.14).
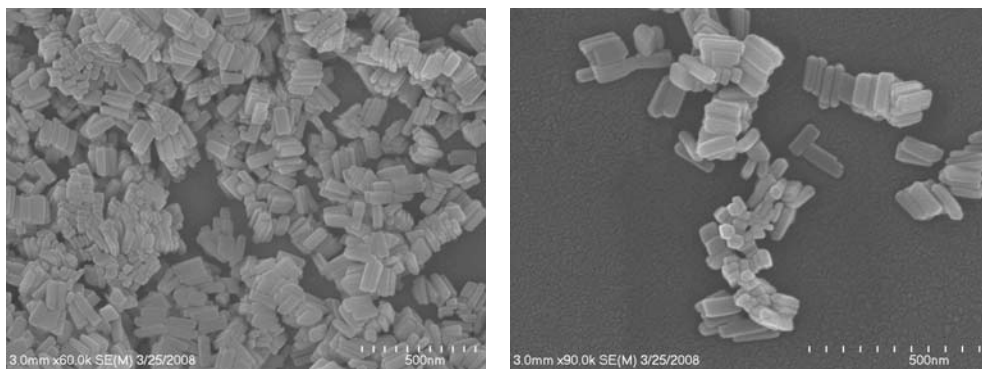
Figure 4.5. SEM images of [Gd$_2$(BHC)(H$_2$O)$_6$] nanoparticles (**4-3**).
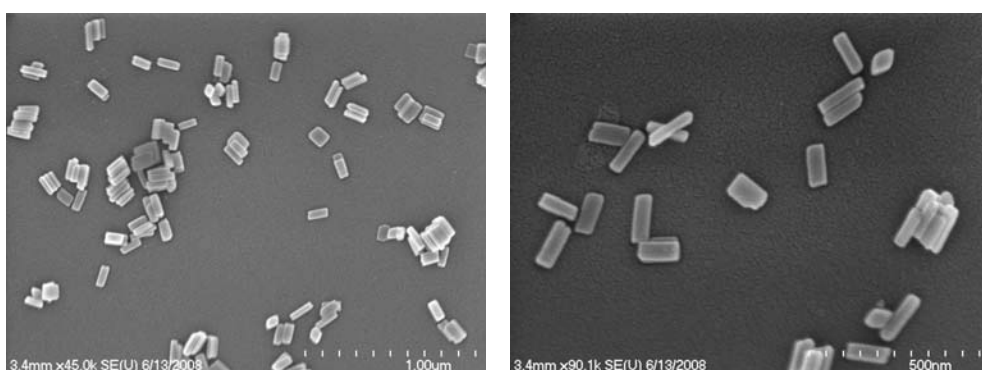
Figure 4.6. SEM images of PVP coated [Gd$_2$(BHC)(H$_2$O)$_6$] nanoparticles (**4-3**).
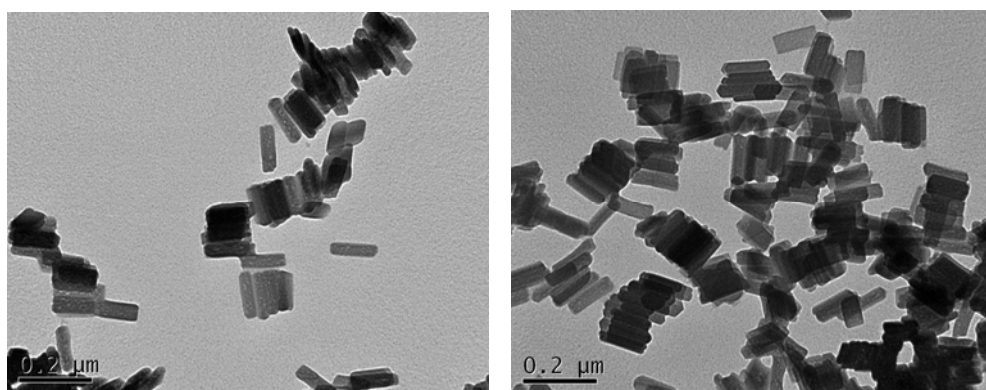
Figure 4.7. TEM images of [Gd$_2$(BHC)(H$_2$O)$_6$] nanoparticles (**4-3**).
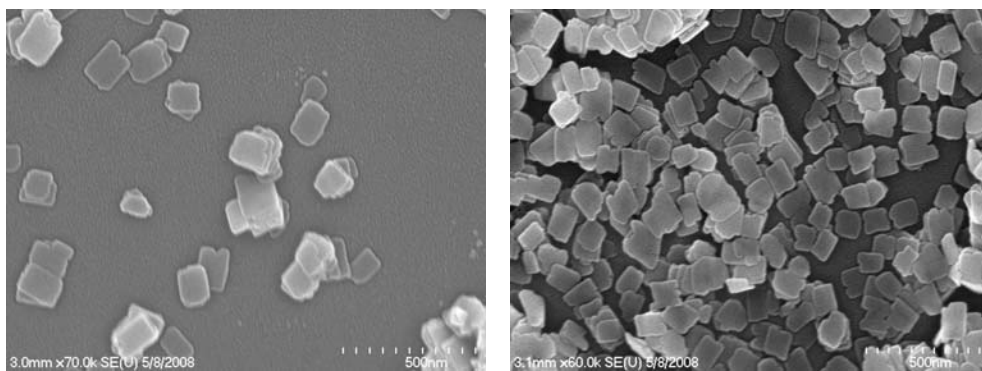
Figure 4.8. SEM images of $[Gd_{1.9}Eu_{0.1}(BHC)(H_2O)_6]$ (**4-3a**) nanoparticles.
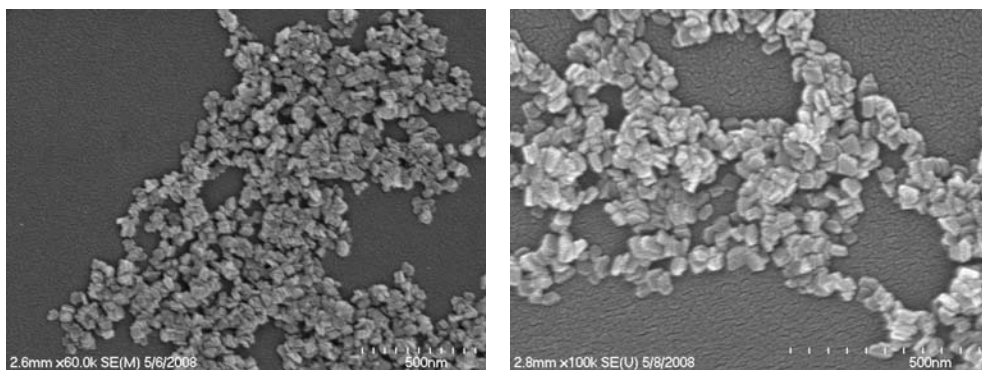
Figure 4.9. SEM images of $[Gd_{1.9}Tb_{0.1}(BHC)(H_2O)_6]$ (**4-3b**) nanoparticles.
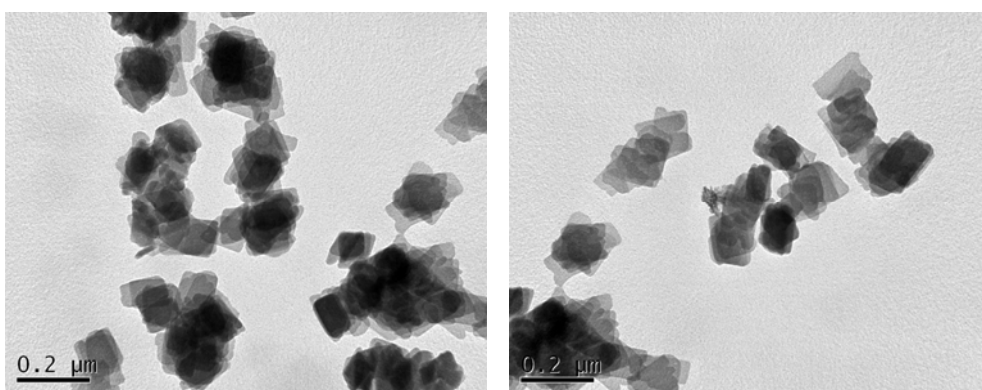
Figure 4.10. TEM images of $[Gd_{1.9}Eu_{0.1}(BHC)(H_2O)_6]$ (**4-3a**) nanoparticles.
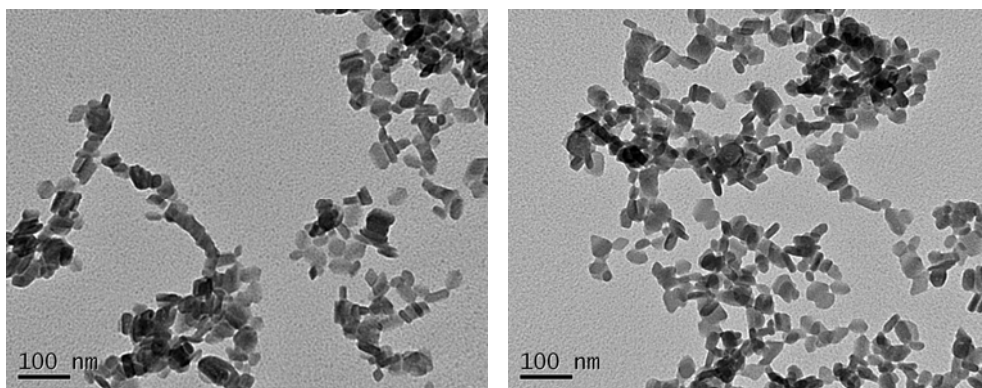
Figure 4.11. TEM images of $[Gd_{1.9}Tb_{0.1}(BHC)(H_2O)_6]$ (**4-3b**) nanoparticles.
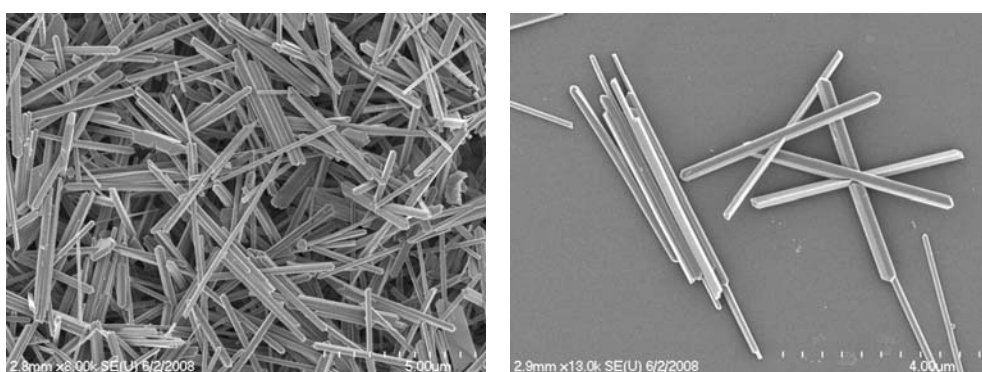
Figure 4.12. SEM images of $[Gd_2(BHC)(H_2O)_8](H_2O)_2$ nanorods (**4-4**) synthesized at 60 °C.
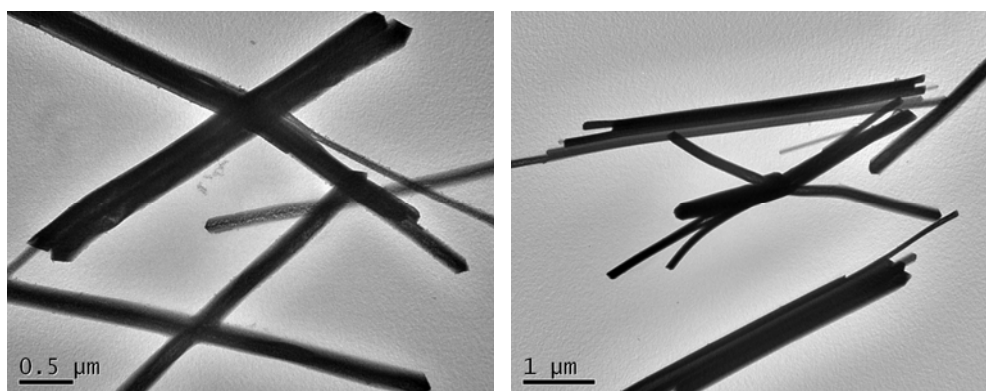
Figure 4.13. TEM images of $[Gd_2(BHC)(H_2O)_8](H_2O)_2$ nanorods (**4-4**) synthesized at 60 °C.

113
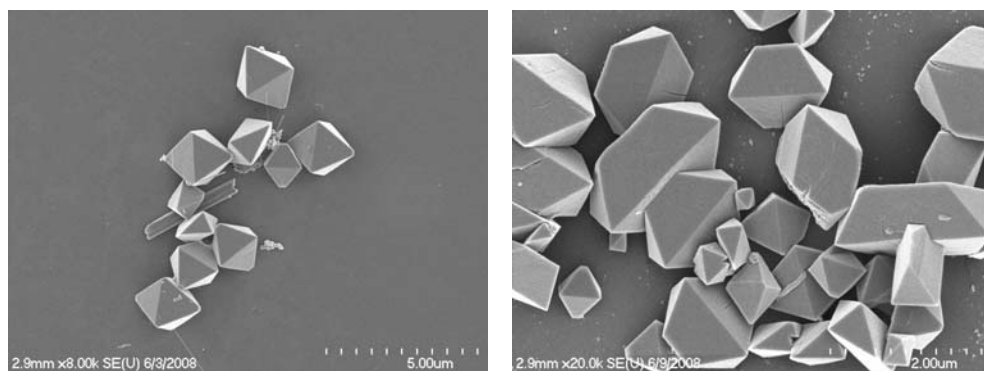
Figure 4.14. SEM images of $[Gd_2(BHC)(H_2O)_8](H_2O)_2$ nanorods (**4-4**) synthesized at 120 °C.

Powder X-ray diffraction was used to determine the crystallinity and in some cases the phase of the NMOFs obtained. Both the succinic acid and adipic acid-Gd NMOFs (**4-1** and **4-2**) were crystalline as seen in the PXRD patterns (Fig. 4.15-4.16). The powder pattern obtained for **4-1** did not match any known phases, and the powder pattern for **4-2** was similar to a known phase, but not an exact match.[19] Both the room temperature and high temperature syntheses gave NMOFs of the same phase.
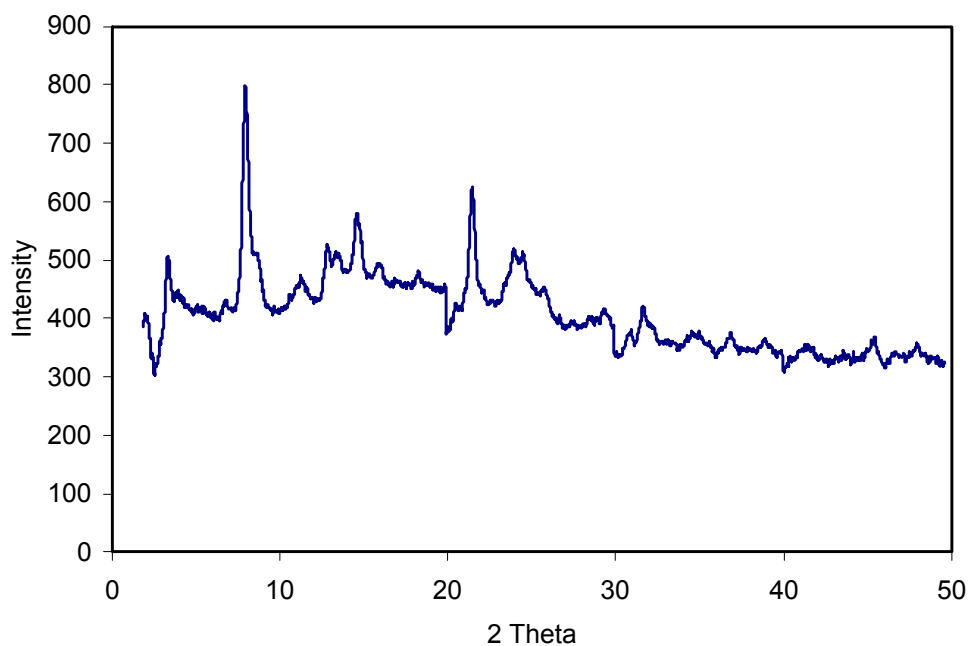
Figure 4.15. PXRD pattern of succinic acid-Gd nanorods (**4-1**).
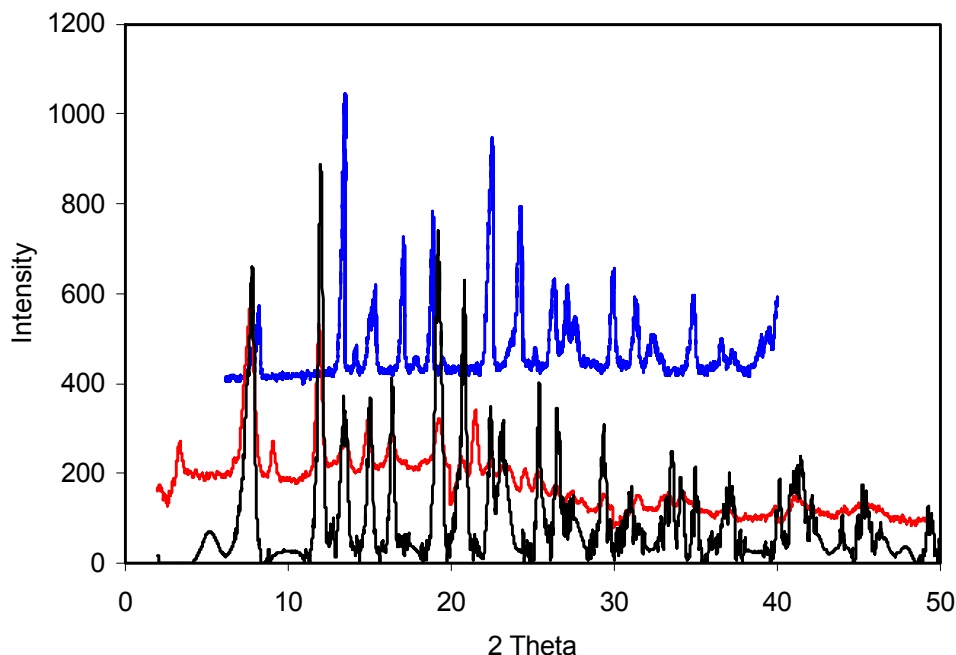
Figure 4.16. PXRD patterns for adipic acid-Gd nanorods (**4-2**) synthesized at room temperature (black) and 120 °C (red) compared to the known [Gd$_2$(ad)$_3$(H$_2$O)$_4$]xH$_2$O phase[19] (blue).

Powder X-ray diffraction studies showed that the nanoparticles of **4-3** are crystalline, and correspond to a known La bulk phase [La$_2$(BHC)(H$_2$O)$_6$] (Fig. 4.17).[20] The slight shift in the 2θ values is consistent with the smaller radius of Gd^{3+} *vs*. La^{3+} as a result of lanthanide contraction. The crystal structure of **4-3** can thus be described as a 3D MOF with the (4,8) connecting nodes. The Gd centers are 9-coordinate, binding to two chelating carboxylate and two bridging carboxylate groups from four different BHC ligands. The water molecules occupy the three remaining coordination sites (Fig. 4.18a). The BHC ligand binds to a total of eight Gd centers, with four carboxylate groups chelating to four Gd centers and the other two carboxylate groups bridging four Gd centers (Fig. 4.18b). The four-connected Gd centers and eight-connected BHC ligands link to each other to form a 3D MOF with the fluorite topology (Fig. 4.18c). Thermogravimetric analysis (TGA) results supported the formulation of **4-3** (Fig. 4.19). TGA showed a weight loss of 4.68% in the 90-125 °C

temperature range and a loss of 9.67% from 160-225 °C, corresponding to the three coordinating water molecules (14.35% observed; 14.25% expected). After loss of the BHC ligand in the 350-560 °C range, 46.58% of the mass remained, corresponding to Gd_2O_3 (47.78% expected). PXRD also confirmed that the Eu and Tb doped NMOFs (**4-3a** and **4-3b**) are of the same phase as **4-3** (Fig. 4.20).
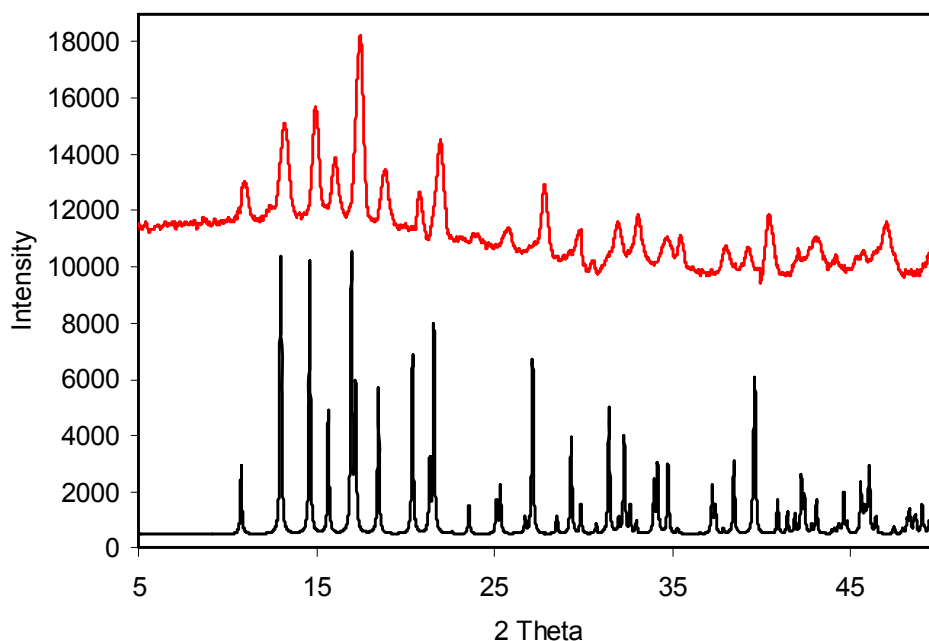
Figure 4.17. PXRD pattern of $[Gd_2(BHC)(H_2O)_6]$ nanoparticles (**4-3**) (red) compared to the simulated pattern from the known $[La_2(BHC)(H_2O)_6]$ phase (black).
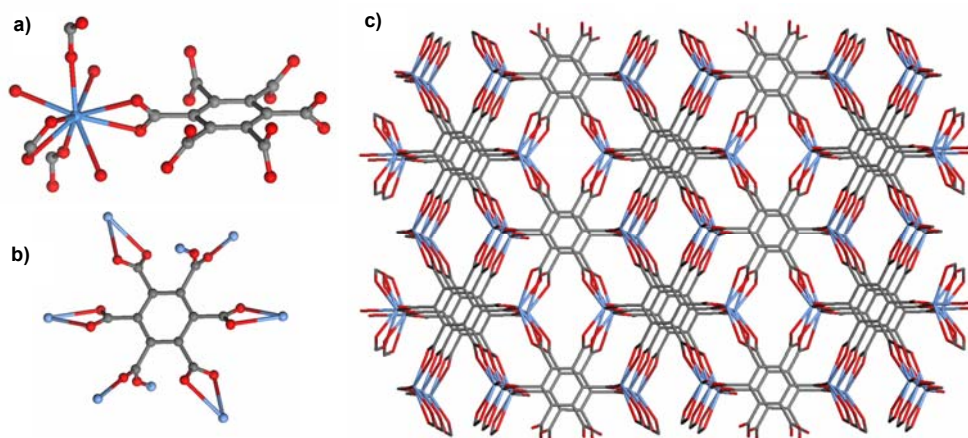
Figure 4.18. (a) Gd coordination environment in **4-3**. (b) Linking of BHC ligand to eight different Gd centers in **4-3**. (c) Packing of **4-3** as viewed slightly off the *b* axis. All the

116

figures were drawn using the cif file of isostructural $[La_2(BHC)(H_2O)_6]$ (the coordinated water molecules were omitted for clarity).
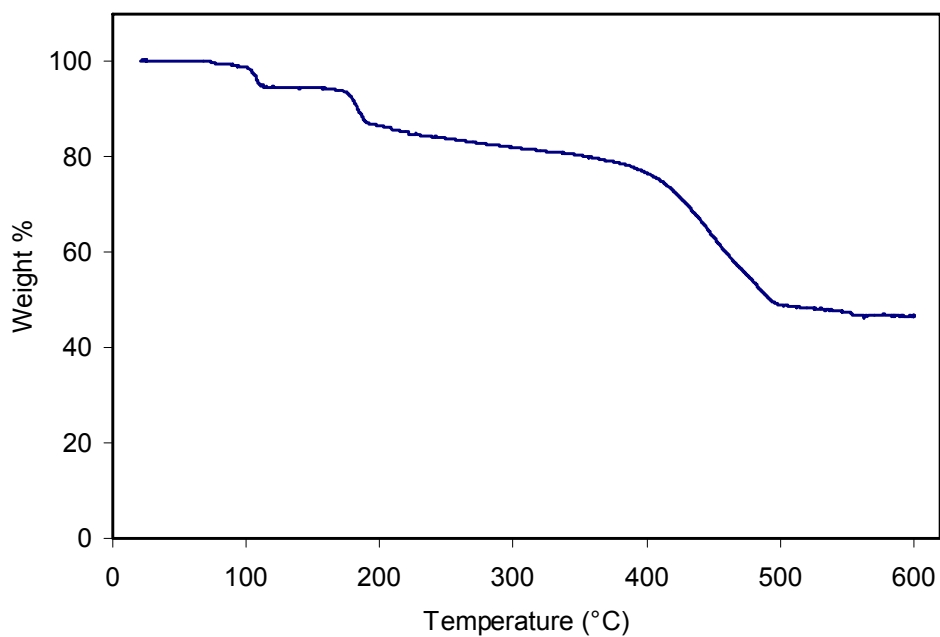
Figure 4.19. TGA of $[Gd_2(BHC)(H_2O)_6]$ nanoparticles (**4-3**).
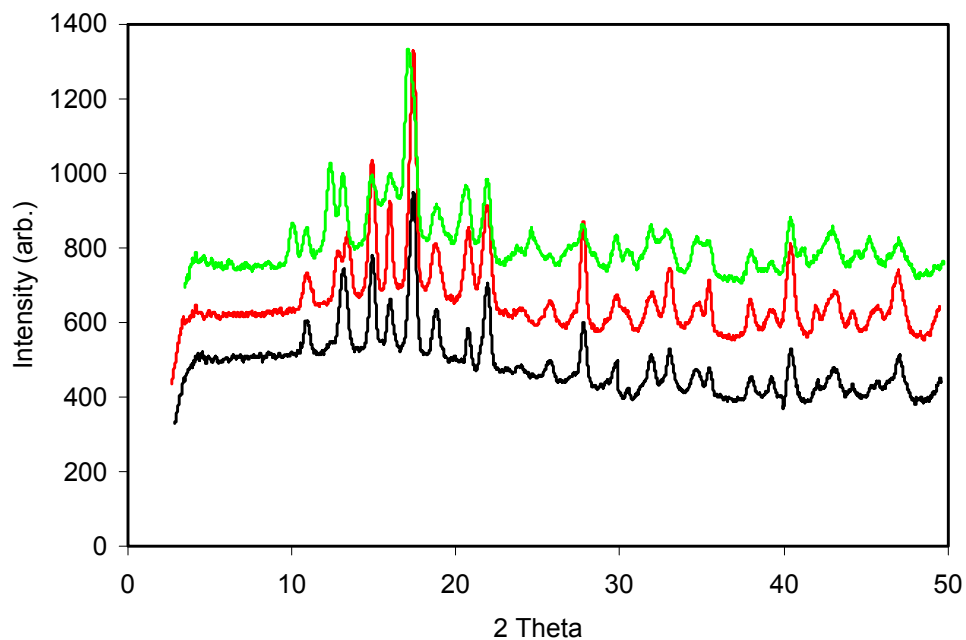
Figure 4.20. PXRD patterns for $[Gd_2(BHC)(H_2O)_6]$ NMOFs (**4-3**) (black), Eu-doped (**4-3a**) (red) and Tb-doped (**4-3b**) (green).

PXRD studies indicated that the NMOFs **4-4** obtained from the reactions between mellitic acid and $GdCl_3$ at 60 and 120 °C are of the same phase despite their very different morphologies (Fig. 4.21). Single crystal X-ray diffraction studies were carried out using single crystals of **4-4**. These studies showed that **4-4** crystallizes in the centrosymmetric space group $P2_1/n$ with one Gd(III) center, one half of the BHC ligand, four coordinating water molecules, and one included water solvate molecule in the asymmetric unit. The BHC ligand sits on the inversion center and coordinates to four Gd centers in a chelating fashion and to two Gd centers in a monodentate fashion. Each Gd center coordinates to two chelating carboxylates and one monodentate carboxylate from three different BHC ligands and four water molecules. The BHC ligand thus acts as a six-connected node whereas the Gd center acts as a three-connected node to lead to a 3D framework with the inverse rutile topology (Fig. 4.22-26). Thermogravimetric analysis (TGA) results supported the formulation of **4-4** (Fig. 4.27). TGA showed a total weight loss of 19.72% in the 85-200 °C temperature range corresponding to the loss of 10 water molecules (21.7% expected). After loss of the BHC ligand in the 390-540 °C range, 46% of the mass remained, corresponding to Gd_2O_3 (40.1% expected).
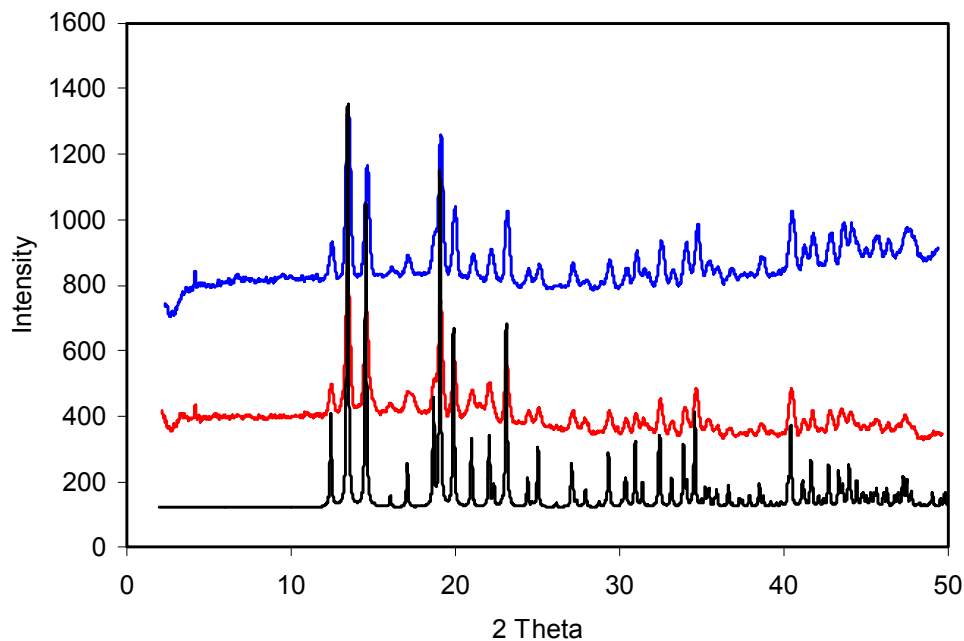
Figure 4.21. PXRD pattern of **4-4** synthesized at 60 °C (blue) and 120 °C (red) compared to the simulated PXRD using X-ray structure of $[Gd_2(BHC)(H_2O)_8](H_2O)_2$ single crystal (black).
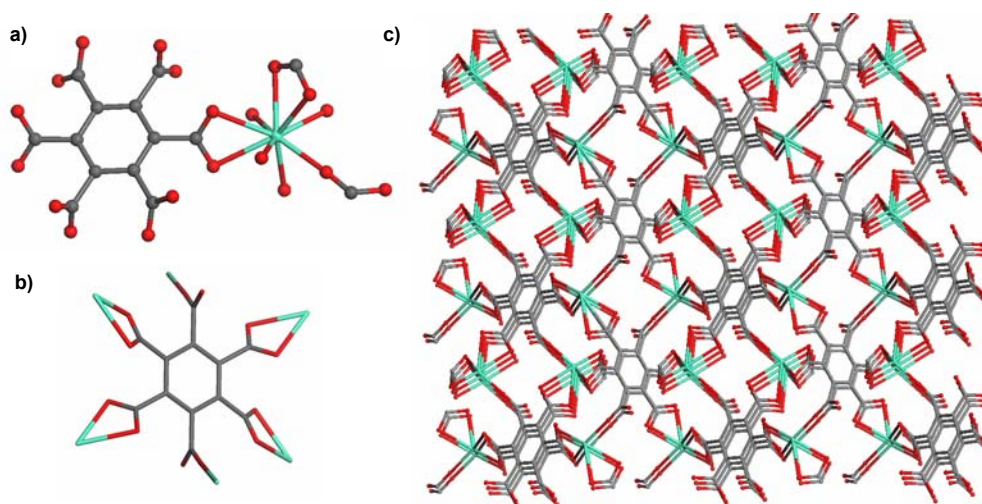
Figure 4.22. (a) Gd coordination environment in **4-4**. (b) Linking of BHC ligand to six different Gd centers in **4-4**. (c) Packing of **4-4** as viewed slightly off the *a* axis (the coordinated water molecules were omitted for clarity).
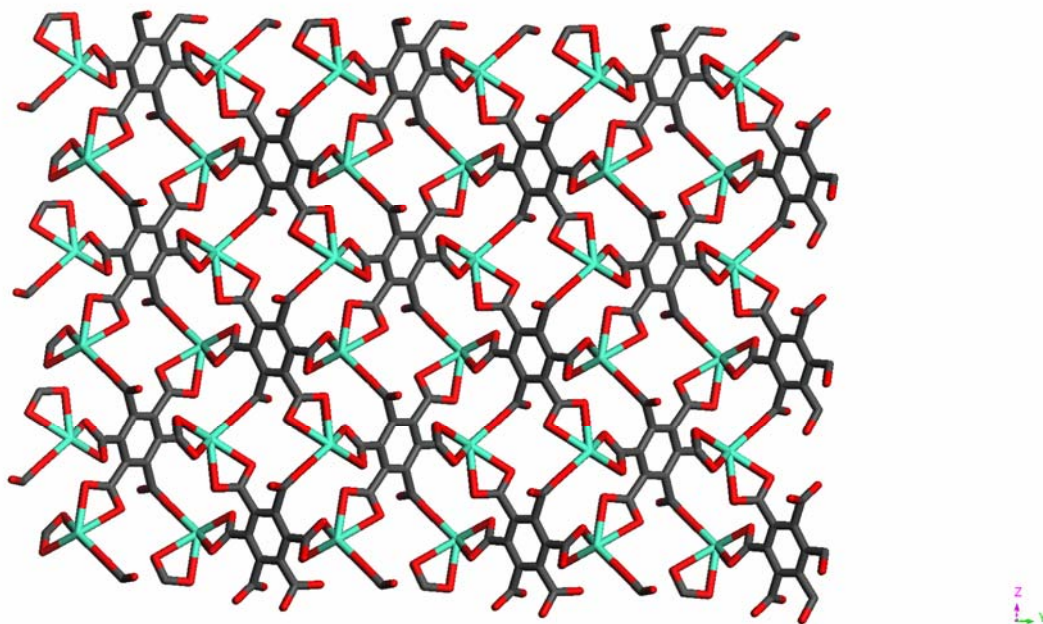
Figure 4.23. [Gd$_2$(BHC)(H$_2$O)$_8$](H$_2$O)$_2$ (**4-4**) as viewed down the *a* axis. The water molecules are omitted for clarity.
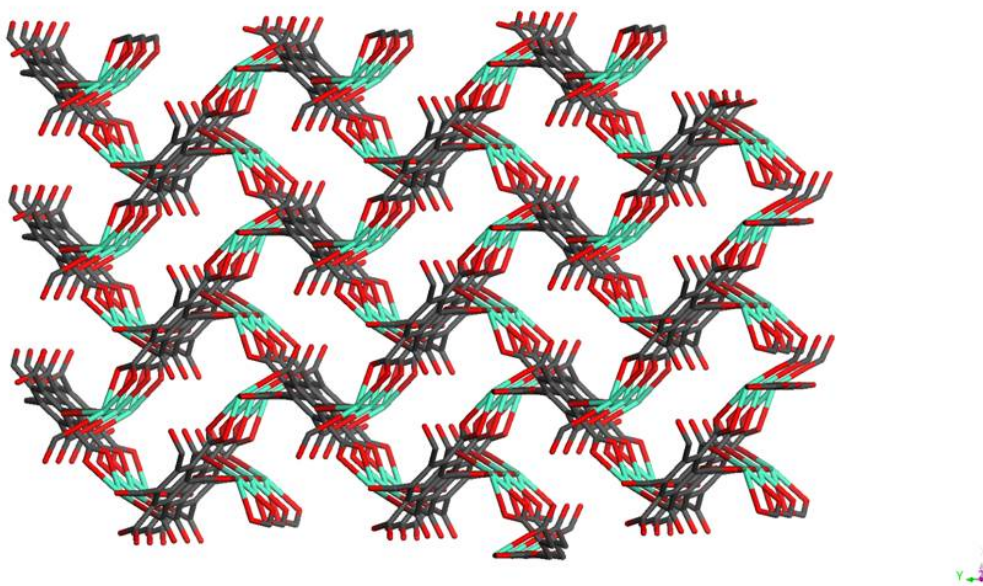
Figure 4.24. [Gd$_2$(BHC)(H$_2$O)$_8$](H$_2$O)$_2$ (**4-4**) as viewed slightly off the *c* axis. The water molecules are omitted for clarity.
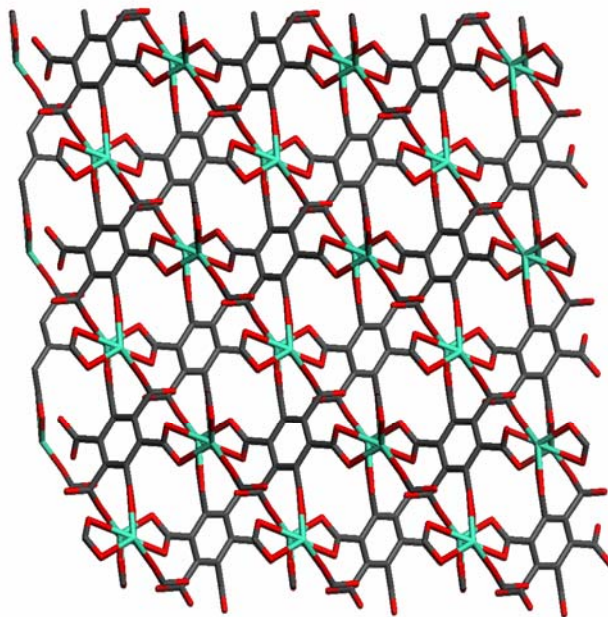
Figure 4.25. [Gd$_2$(BHC)(H$_2$O)$_8$](H$_2$O)$_2$ (**4-4**) as viewed down the b axis. The water molecules are omitted for clarity.
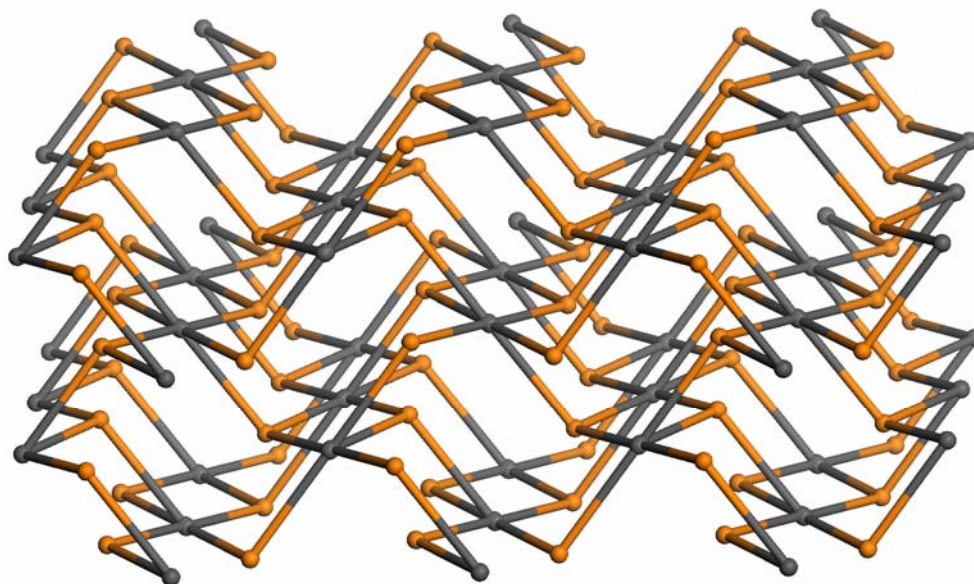
Figure 4.26. Network connectivity of **4-4** showing the rutile topology.
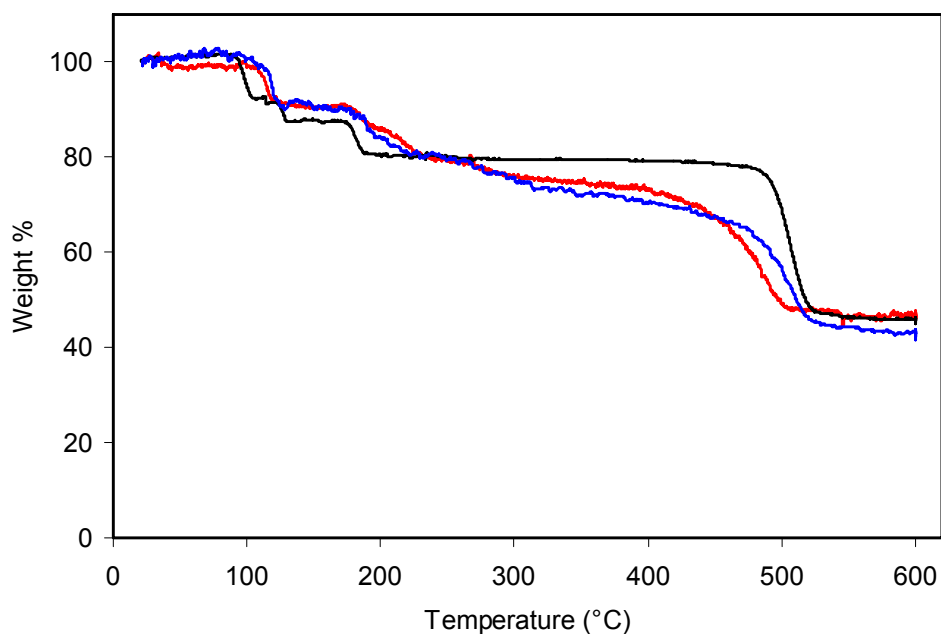
Figure. 4.27. TGA of $[Gd_2(BHC)(H_2O)_8](H_2O)_2$ nanoparticles (**4-4**) synthesized at 60 °C (blue) and 120 °C (red), and $[Gd_2(BHC)(H_2O)_8](H_2O)_2$ single crystals (black).

The synthesis of two different NMOFs based on the Gd/BHC building blocks is a result of the different metal-ligand coordination modes in **4-3** and **4-4**. PXRD studies further showed that the synthesis of **4-3** *vs*. **4-4** is pH dependent but not temperature dependent. This work illustrates the ability to synthesize different NMOFs from the same metal/ligand combination by exploiting the versatile metal-ligand coordination modes.

4.2.3 Relaxivity Measurements

In order to evaluate the potential use of these NMOFs as contrast agents for magnetic resonance imaging, the relaxivity values of **4-2** and **4-3** were measured using a 3 T and a 9.4 T MR scanner, respectively. Nanoparticles of **4-2** were found to have fairly high longitudinal and transverse relaxivities. The r_1 for **4-2** measured at 3 T on a per Gd^{3+} basis was 8.5 mM^{-1}s^{-1} and the r_2 was 14.5 mM^{-1}s^{-1} (Fig. 4.28). For comparison the r_1 of commercially available Gd^{3+} containing contrast agents is on the order of 4-5 mM^{-1}s^{-1}. These results indicate the

potential of these NMOFs for T_1-weighted imaging. The **4-3** particles were found to have a modest longitudinal relaxivity (r_1) of 1.5 mM^{-1}s^{-1} and an impressive transverse relaxivity (r_2) of 122.6 mM^{-1}s^{-1} on a per Gd basis at 9.4 T (Fig. 4.29-4.30). Based on the particle size and the calculated crystal density, we determined the r_1 and r_2 values to be ~8.36 x 10^5 and ~6.83 x 10^7 mM^{-1}s^{-1} on a per particle basis, respectively. This magnitude of r_2 relaxivity is very large compared to other Gd containing nanoparticle contrast agents, and clearly indicates the potential of these nanoparticles in T_2-weighted MR imaging.[21-23] For comparison, Gd$_2$O$_3$ nanoparticles synthesized by Tillement *et. al.* had r_2 relaxivities of 28.9 mM^{-1}s^{-1} when measured at 7 T.[22]
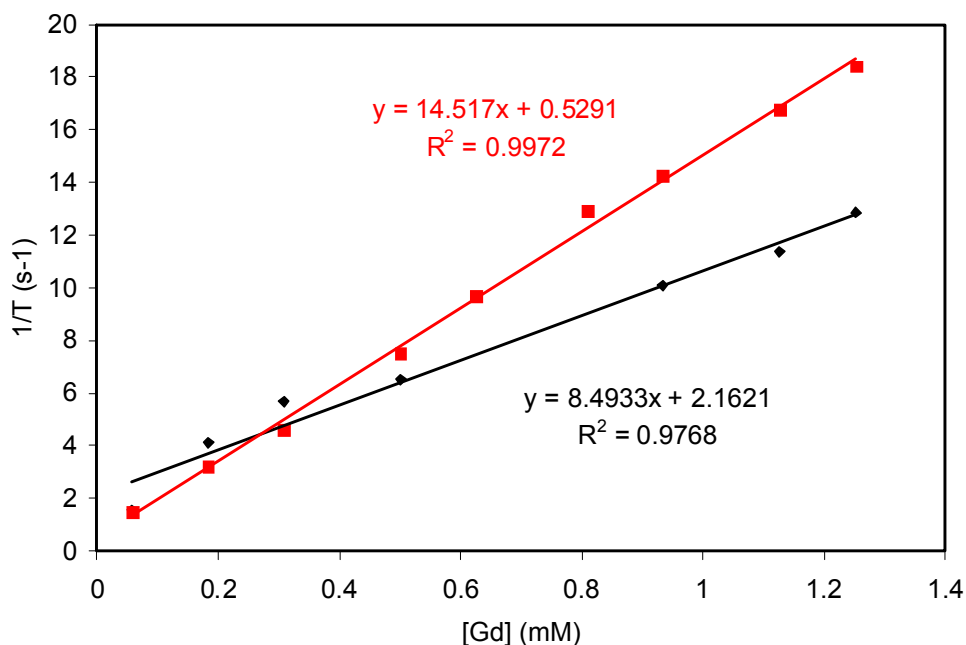
Figure. 4.28. Relaxivity of adipic acid-Gd nanorods (**4-2**) measured at 3 T. r_1 = 8.5 mM^{-1}s^{-1}, r_2 = 14.5 mM^{-1}s^{-1}.
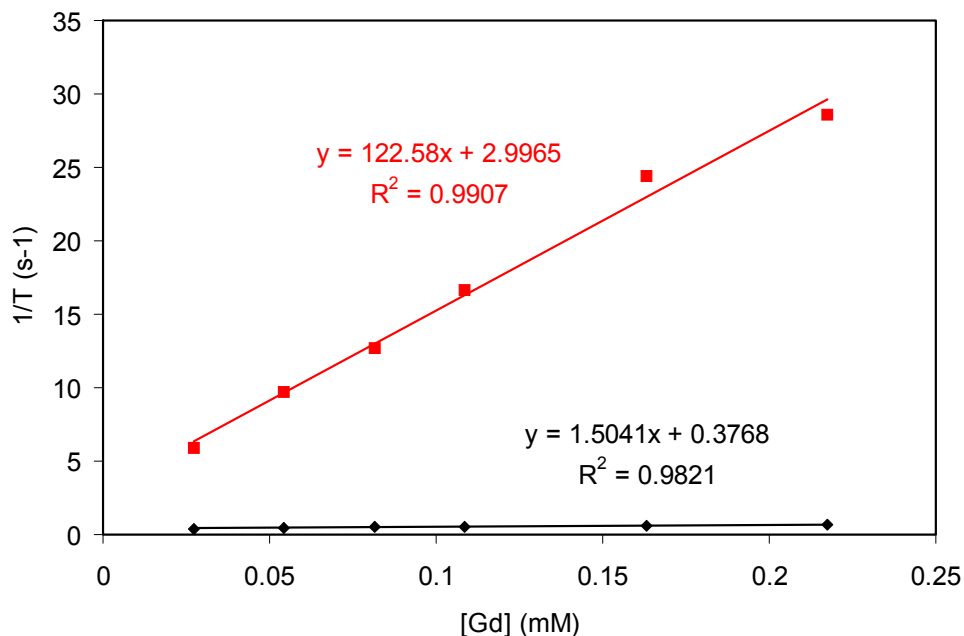
Figure 4.29. Relaxivity of $[Gd_2(BHC)(H_2O)_6]$ nanoparticles (**4-3**) measured at 9.4 T. $r_1 = 1.5$ $mM^{-1}s^{-1}$, $r_2 = 122.6$ $mM^{-1}s^{-1}$.
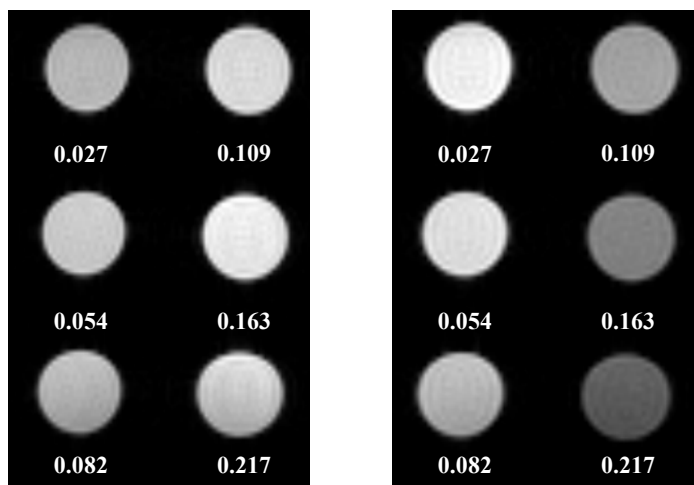
Figure 4.30. T_1 (left) and T_2-weighted (right) phantom images of $[Gd_2(BHC)(H_2O)_6]$ NMOFs (**4-3**) at 9.4 T (Gd^{3+} concentrations listed in mM).

4.2.4 Luminescent Measurements

NMOFs **4-3a** and **4-3b** exhibit characteristic Eu and Tb luminescence under ultraviolet excitation (Fig. 4.31-4.32).[24] Emission and excitation spectra were obtained using

diluted ethanolic dispersions of the doped nanoparticles with excitation and emission wavelengths of 250 nm and 614 nm for **4-3a** (Eu^{3+} doped) and 309 nm and 544 nm for **4-3b** (Tb^{3+} doped). The combination of luminescent and paramagnetic properties allows for possible multimodal imaging, i.e. optical and MR.
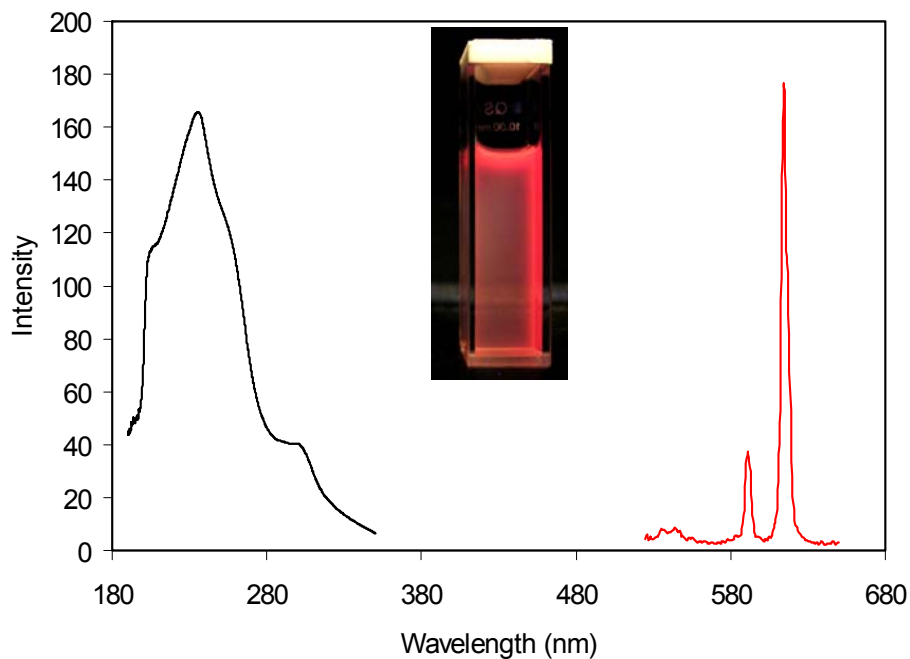
Figure 4.31. Excitation (black) and emission (red) spectra of Eu-doped $[Gd_2(BHC)(H_2O)_6]$ NMOFs (**4-3a**). The emission spectrum was taken with an excitation wavelength of 250 nm. The inset shows a photo taken of a suspension of **4-3a** in ethanol under uv light (254 nm).
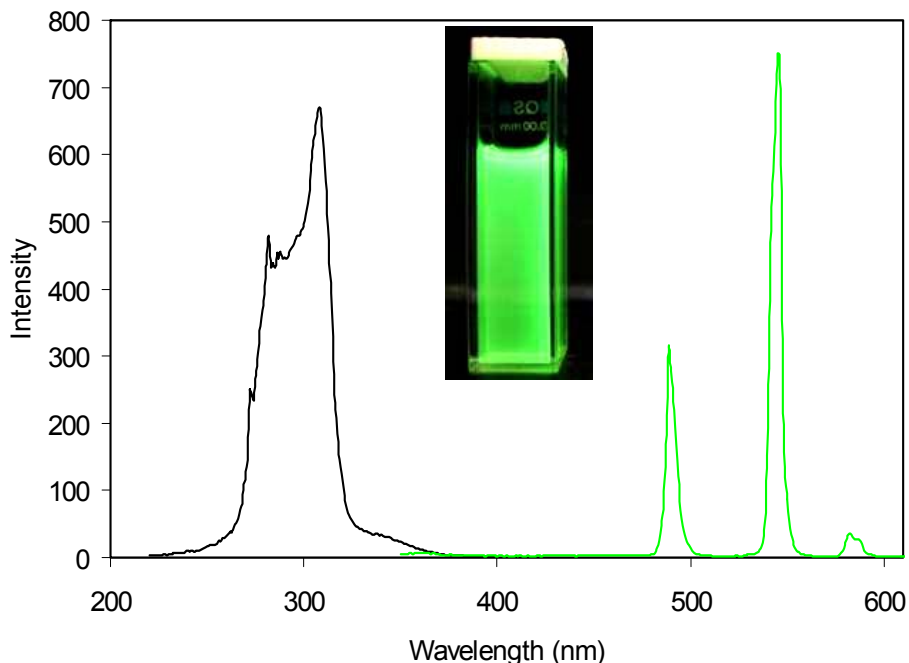
Figure 4.32. Excitation (black) and emission (green) spectra of Tb-doped [Gd$_2$(BHC)(H$_2$O)$_6$] NMOFs (**4-3b**). The emission spectrum was taken with an excitation wavelength of 309 nm. The inset shows a photo taken of a suspension of **4-3b** in ethanol under uv light (254 nm).

4.3. Conclusion

In summary, we have synthesized four different Gd containing NMOFs with three different bridging ligands using both a room temperature microemulsion synthesis and a surfactant-assisted method at elevated temperatures. In one case, two NMOFs of different particle sizes and morphologies were obtained using identical building blocks as a result of different metal-ligand coordination modes that are dependent on the pH of the reaction. We have also shown the potential use of these NMOFs as contrast agents for magnetic resonance and optical imaging.

4.4 Experimental Details

4.4.1 Materials and Methods

All starting materials and surfactants were purchased from Aldrich and used without further purification. All solvents were purchased from Fisher. Thermogravimetric analysis (TGA) was performed using a Shimadzu TGA-50 equipped with a platinum pan and heated at a rate of 3 °C per minute, under air. Powder X-ray diffraction (PXRD) analyses were carried out using a Rigaku Multiflex powder diffractometer using Cu radiation or on a Bruker SMART APEX II diffractometer using Cu radiation. In the latter, the PXRD patterns were processed with the APEX 2 package using phase ID plug-in. A Hitachi 4700 field emission scanning electron microscope (SEM) and a JEM 100CX-II transmission electron microscope (TEM) were used to determine particle size and morphology. A Cressington 108 Auto Sputter Coater equipped with a Au/Pd (80/20) target and an MTM-10 thickness monitor was used to coat the samples with a 5 nm thick conductive layer before taking SEM images. Each SEM sample was prepared by suspending the nanoparticles in ethanol. A drop of the suspension was then placed on a glass slide and the solvent was allowed to evaporate. TEM samples were also prepared from ethanolic particle dispersions on amorphous carbon coated copper grids. An Applied Research Laboratories (ARL) SpectraSpan 7 DCP spectrometer and a Varian 820-MS Inductively Couple Plasma mass spectrometer were used to measure Gd^{3+} concentrations. Excitation and emission spectra were taken on a Shimadzu RF-5301PC fluorimeter.

The methyl ammonium salts of the ligands were made by dissolving the ligand in a 40 wt % solution of methyl amine in water. The excess methyl amine and water were then evaporated under reduced pressure, and the isolated salt was then redissolved in distilled

water to give an aqueous solution of desired concentration. The sodium salts of the ligands were made by dissolving the ligand and the appropriate amount of NaOH in water, and then diluting to give the desired concentration.

T_1 and T_2 values were acquired on a Siemens 3 T Allegra (Siemens Medical Systems, Erlangen, Germany) with a CP head coil, and a 9.4 T Bruker BioSpec (Bruker Biospin, Ettlingen, Germany) system with a 35 mm quadrature RF transmit and receive coil. For the 3 T scanner, a 3D FLASH sequence was utilized to compute T_1 maps with seven different flip angles (2, 5, 10, 20, 30, 40, and 60). Imaging parameters were: FOV=190 x 190*64 mm^3, Matrix size=128 x 128 * 32, TR/TE= 40/1.64 ms, total data acquisition time was 19 minutes. A 2-D multiple echo spin echo sequence was used to estimate T_2 maps. In total, 32 echoes with an echo spacing of 6.2 ms were obtained. The first echo time was 6.2 ms. TR was 3000 ms. FOV and matrix size were set to 190 x 190 mm^2 and 128 x 128. The slice thickness was 2 mm. The total data acquisition time was about 6 minutes and 29 seconds. For the 9.4 T scanner, two 2D multiple echo spin echo sequences were used to estimate T_2 maps for a wide range of T_2. FOV and matrix size were set to 35 x 30 mm^2 and 128 x 128. The slice thickness was 1 mm. In total, 32 echoes with an echo spacing of 3.7 ms for sequence 1 and 40 echoes with an echo spacing of 10 ms for sequence 2 were obtained. The TR/TE1 were 3.7/3000 ms and 10/4114 ms for each sequence, respectively. The total data acquisition time was about 10 minutes. T_1 maps were obtained with a variable TR rapid acquisition relaxation enhanced (RARE) sequence with a TE=5.14 ms. Twenty two variable TRs (TR=18, 25, 40, 60, 90, 120, 160, 200, 250, 300, 380, 500, 700, 1000, 1500, 2000, 2500, 3000, 4000, 5000, 6000, 7000 ms) were used with a FOV of 35x30 mm^2 and a matrix size of 128 x 128. RARE factor was 3 and total data acquisition was about 24 minutes.

4.4.2 Synthesis of NMOFs

Succinic Acid-Gd nanoparticles (**4-1**) were prepared via the high temperature surfactant assisted method. 0.0911 g (0.25 mmol) of cetyltrimethylammonium bromide (CTAB) was added to 2 round bottom flasks. 5 mL of a 0.5 M solution of 1-hexanol in n-heptane was then added, and the mixture was stirred for 10 minutes at room temperature. A $W = 5$ microemulsion was then formed by the addition of 24 μL of a 0.075 M succinic acid methylammonium salt aqueous solution and 24 μL of a 0.10 M $GdCl_3$ aqueous solution to the two separate 5 mL 0.05 M CTAB/0.5 M 1-hexanol/n-heptane mixtures while vigorously stirring at room temperature. The separate microemulsions were stirred vigorously for 10 minutes at room temperature, after which the they were combined, and the resultant 10 mL microemulsion with $W = 5$ was transferred to a Teflon-lined Parr reactor and heated to 120 °C for 16 hours. After cooling to room temperature, the nanoparticles were isolated via centrifugation at 13,000 rpm for 15 minutes. After the removal of the supernatant, the particles were washed by redispersement via sonication in 5 mL of ethanol. The ethanol suspension was then centrifuged again for 15 minutes at 13,000 rpm, to recover the nanoparticles.

Adipic Acid-Gd (**4-2**) nanoparticles were prepared either via the CTAB/1-hexanol/n-heptane/water microemulsion system or the high temperature surfactant-assisted method. For the microemulsion synthesis, a $W = 10$ microemulsion was prepared by the addition of 48 μL of a 0.075 M adipic acid sodium salt aqueous solution and 48 μL of a 0.10 M $GdCl_3$ aqueous solution to separate 5 mL aliquots of a 0.05 M CTAB/1-hexanol/n-heptane solution while vigorously stirring at room temperature. The separate microemulsions were stirred vigorously for 10 minutes at room temperature, after which the two microemulsions were

combined, and the resultant 10 mL microemulsion with $W = 5$ was stirred for an additional 2 hours at room temperature. The nanoparticles were isolated via centrifugation at 10,000 rpm for 10 minutes. After the removal of the supernatant, the particles were washed by redispersement via sonication in 5 mL of ethanol. The ethanol suspension was then centrifuged again for 10 minutes at 10,000 rpm, to recover the nanoparticles. For the high temperature surfactant assisted method, 0.0911 g (0.25 mmol) of CTAB was added to 2 round bottom flasks. 5 mL of a 0.5 M solution of 1-hexanol in n-heptane was then added, and the mixture was stirred for 10 minutes at room temperature. A $W = 5$ microemulsion was then formed by the addition of 24 µL of a 0.075 M adipic acid sodium salt aqueous solution and 24 µL of a 0.05 M GdCl$_3$ aqueous solution to the two separate 5 mL 0.05 M CTAB/0.5 M 1-hexanol/n-heptane mixtures while vigorously stirring at room temperature. The separate microemulsions were stirred vigorously for 10 minutes at room temperature, after which the they were combined, and the resultant 10 mL microemulsion with $W = 5$ was transferred to a Teflon-lined Parr reactor and heated to 120 °C for 2.5 hours. After cooling to room temperature, the nanoparticles were isolated via centrifugation at 13,000 rpm for 15 minutes. After the removal of the supernatant, the particles were washed by redispersement via sonication in 5 mL of ethanol. The ethanol suspension was then centrifuged again for 15 minutes at 13,000 rpm, to recover the nanoparticles.

[Gd$_2$(BHC)(H$_2$O)$_6$] nanoparticles (**4-3**) were prepared via the high temperature surfactant-assisted method. 0.0911 g (0.25 mmol) of CTAB was added to 2 round bottom flasks. 5 mL of a 0.5 M solution of 1-hexanol in n-heptane was then added to each flask, and the mixture was stirred for 10 minutes at room temperature. Two $W = 10$ microemulsions were then formed by the addition of 48 µL of a 0.1 M mellitic acid methylammonium salt

aqueous solution and 48 μL of a 0.1 M GdCl$_3$ aqueous solution to the two separate 5 mL 0.05 M CTAB/0.5 M 1-hexanol/n-heptane mixtures while vigorously stirring at room temperature. The separate microemulsions were stirred vigorously for 10 minutes at room temperature, after which they were combined, and the resultant 10 mL microemulsion with $W = 10$ was transferred to a Teflon-lined Parr reactor and heated to 120 °C for 18 hours. After cooling to room temperature, the nanoparticles were isolated via centrifugation at 13,000 rpm for 15 minutes. After the removal of the supernatant, the particles were washed by redispersement via sonication in 5 mL of ethanol. The ethanol suspension was then centrifuged again for 15 minutes at 13,000 rpm, to recover the nanoparticles. Yield: 2.02 mg (84.4 %). Nanoparticles of [Gd$_2$(BHC)(H$_2$O)$_6$] were successfully doped with the photoluminescent lanthanide ions Eu^{3+} or Tb^{3+} by preparing nanoparticles of **4-3** using 5 mol % of the corresponding Eu^{3+} or Tb^{3+} salt.

[Gd$_2$(BHC)(H$_2$O)$_8$](H$_2$O)$_2$ nanorods (**4-4**) were prepared via a surfactant-assisted method at 60 °C. 0.4555 g (1.25 mmol) of CTAB was added to 2 round bottom flasks. 25 mL of a 0.5 M solution of 1-hexanol in iso-octane was then added to each flask, and the mixtures were stirred for 10 minutes at room temperature. Two $W = 10$ microemulsions were then formed by the addition of 225 μL of a 0.1 M mellitic acid aqueous solution and 225 μL of a 0.2 M GdCl$_3$ aqueous solution to the two separate 25 mL 0.05 M CTAB/0.5 M 1-hexanol/iso-octane mixtures while vigorously stirring at room temperature. The separate microemulsions were stirred vigorously for 10 minutes at room temperature, after which the they were combined, and the resultant 50 mL microemulsion with $W = 10$ was transferred to a microwave vessel. The reaction was then rapidly heated to 60 °C in a 400 W microwave. Once reaching 60 °C, the reaction was held at this temperature for 15 minutes. After cooling

to room temperature, the nanoparticles were isolated via centrifugation at 13,000 rpm for 15 minutes. After the removal of the supernatant, the particles were washed by redispersement via sonication in 5 mL of ethanol. The ethanol suspension was then centrifuged again for 15 minutes at 13,000 rpm, to recover the nanoparticles. Yield: 1.63 mg (11.1 %). Micron sized particles of **4-4** can also be synthesized in 9.1 % yield using this procedure, increasing the reaction temperature to 120 °C.

4.4.3 Single Crystal Data

Single crystals of $[Gd_2(BHC)(H_2O)_8](H_2O)_2$ (**4-4**) were formed by first dissolving 0.855 mg (2.50 μmol) of mellitic acid in 0.5 mL of distilled water. 50 μL of a 0.1 M $GdCl_3$ (5.0 μmol) was then added. The vial was capped and placed in a 60 °C oven, overnight.

Single-crystal X-ray diffraction data were measured at 293 K on a Bruker SMART Apex II CCD-based X-ray diffractometer system equipped with a Mo-target X-ray tube (λ = 0.71073 Å). Crystal data for **4-4**: Monoclinic, space group: $P2_1/n$, a = 8.4856(12) Å, b = 13.1281(17) Å, c = 9.5225(13) Å, α = 90º, β = 94.620(3)º, γ = 90º, V = 1057.4(2) Å^3, Z = 2, ρ_{calcd} = 2.546 g/cm^3, μ(Mo Kα) = 6.328 mm^{-1}, $2\theta_{max}$=55.0°, Data/restrains/parameters: 2188/0/163 , R1(I > 2σ(I)) = 0.0301, wR2 = 0.1076, R1(all data) = 0.0317, wR2(all data) = 0.1099, GOF = 0.992.

4.4.4 Calculations

Calculation to explain peak shift in PXRD of 4-3 as compared to the $[La_2(BHC)(H_2O)_6]$ single crystal phase.

$n\lambda = 2d \sin \theta$

Calculated La phase (2 0 0) reflection: $2\theta = 12.96°$

Experimental Gd phase (2 0 0) reflection: $2\theta = 13.18°$

$\lambda = 1.5418$ Å, $n = 1$

La phase – d-spacing:

$$d = \frac{n\lambda}{2\sin\theta}$$

$$d = \frac{1.5418}{2\sin(6.48)}$$

$$d = 6.831$$

$$a = 2d$$

$$a = 13.662 \text{ Å}$$

Gd phase – d-spacing:

$$d = \frac{n\lambda}{2\sin\theta}$$

$$d = \frac{1.5418}{2\sin(6.59)}$$

$$d = 6.717$$

$$a = 2d$$

$$a = 13.434$$

Difference in length a = 0.228 Å (i.e., experimentally, the a axis length is 0.228 shorter for the Gd phase than the La phase).

Difference in ionic radii × 2 = 0.188 Å (i.e., based on lanthanide contraction, the a axis length is expected to be 0.188 shorter for the Gd phase than the La phase)

Calculation of number of Gd per particle

$$\text{density of } \mathbf{1} = 2.809 \text{ g/cm}^3$$

$$\text{cell volume} = 897.185 \text{ Å}^3$$

$$\text{Approximate size of NMOF} = 25 \text{ nm x } 50 \text{ nm x } 100 \text{ nm}$$

NMOF volume = 1.25 x 10^{-16} cm^3

Mass of NMOF = 3.511 x 10^{-16} g

NMOFs are 41.45 wt% Gd, so one NMOF contains 1.4554 x 10^{-16} g of Gd

1.4554 x 10^{-16} g of Gd ~ **5.574 x 10^5 atoms/particle**

4.5 References

1. Evans, O. R.; Lin, W., Crystal engineering of NLO materials based on metal−organic coordination networks. *Acc. Chem. Res.* **2002**, *35* (7), 511-522.

2. Liu, Y.; Li, G.; Li, X.; Cui, Y., Cation-dependent nonlinear optical behavior in an octupolar 3D anionic metal-organic open framework. *Angew. Chem. Int. Ed.* **2007,** *46* (33), 6301-6304.

3. Wu, H.; Zhou, W.; Yildirim, T., Hydrogen storage in a prototypical zeolitic imidazolate framework-8. *J. Am. Chem. Soc.* **2007**, *129* (17), 5314-5315.

4. Kesanli, B.; Cui, Y.; Smith, M.; Bittner, E.; Bockrath, B.; Lin, W., Highly interpenetrated metal-organic frameworks for hydrogen storage. *Angew. Chem., Int. Ed.* **2005**, *44* (1), 72-75.

5. Rowsell, J. L. C.; Yaghi, O. M., Strategies for hydrogen storage in metal-organic frameworks. *Angew. Chem. Int. Ed.* **2005**, *44* (30), 4670-4679.

6. Chen, B.; Zhao, X.; Putkham, A.; Hong, K.; Lobkovsky, E. B.; Hurtado, E. J.; Fletcher, A. J.; Thomas, K. M., Surface interactions and quantum kinetic molecular sieving for H_2 and D_2 adsorption on a mixed metal−organic framework material. *J. Am. Chem. Soc.* **2008**, *130* (20), 6411-6423.

7. Wu, C-D.; Hu, A.; Zhang, L.; Lin, W., A homochiral porous metal−organic framework for highly enantioselective heterogeneous asymmetric catalysis. *J. Am. Chem. Soc.* **2005**, *127* (25)*,* 8940-8941.

8. Cho, S-H.; Ma, B.; Nguyen, S. T.; Hupp, J. T.; Albrecht-Schmitt, T. E., A metal–organic framework material that functions as an enantioselective catalyst for olefin epoxidation. *Chem. Commun.* **2006** (24), 2563-2565.

9. Wu, C-D.; Lin, W., Heterogeneous asymmetric catalysis with homochiral metal-organic frameworks: network-structure-dependent catalytic activity. *Angew. Chem. Int. Ed.* **2007**, *46* (7), 1075-1078.

10. Horcajada, P.; Serre, C.; Vallet-Regí, M.; Sebban, M.; Taulelle, F.; Férey, G., Metal-organic frameworks as efficient materials for drug delivery. *Angew. Chem. Int. Ed.* **2006**, *45* (36), 5974-5978.

11. Horcajada, P.; Serre, C.; Maurin, G.; Ramsahye, N. A.; Balas, F.; Vallet-Regí, M.; Sebban, M.; Taulelle, T.; Férey, G., Flexible porous metal-organic frameworks for a controlled drug delivery. *J. Am. Chem. Soc.* **2008**, *130* (21), 6774-6780.

12. Rieter, W. J.; Taylor, K. M. L.; An, H.; Lin, W.; and Lin, W., Nanoscale metal−organic frameworks as potential multimodal contrast enhancing agents. *J. Am. Chem. Soc.* **2006**, *128* (28), 9024-9025.

13. Lu, A-H.; Salabas, E. L.; Schüth, F., Magnetic nanoparticles: synthesis, protection, functionalization, and application. *Angew. Chem. Int. Ed.* **2007**, *46* (8), 1222-1244.

14. Wang, X.; Zhang, J.; Peng, Q.; Li, Y., A general strategy for nanocrystal synthesis. *Nature* **2005**, *437* (7055), 121-124.

15. Yan, R.; Sun, X.; Wang, X.; Peng, Q.; Li, Y., Crystal structures, anisotropic growth, and optical properties: controlled synthesis of lanthanide orthophosphate one-dimensional nanomaterials. *Chem. Eur. J.*, **2005**, *11* (7), 2183-2195.

16. Song, S-Y.; Ma, J-F.; Yang, J.; Cao, M-H.; Zhang, H-J.; Wang, H-S.; Yang, K-Y., Systematic synthesis and characterization of single-crystal lanthanide phenylphosphonate nanorods. *Inorg. Chem*. **2006**, *45* (3), 1201-1207.

17. Wiley, B.; Sun, Y.; Xia, Y., Synthesis of silver nanostructures with controlled shapes and properties. *Acc. Chem. Res*. **2007**, *40* (10), 1067-1076.

18. Yu, W. W.; Peng, X., Formation of high-quality CdS and other II-VI semiconductor nanocrystals in noncoordinating solvents: tunable reactivity of monomers. *Angew. Chem. Int. Ed.* **2002,** *41* (13), 2368-2371.

19. Dimos, A.; Tsaousis, D.; Michaelides, A.; Skoulika, S.; Golhen, S.; Ouahab, L.; Didierjean, C.; Aubry, A., Microporous rare earth coordination polymers: effect of lanthanide contraction on crystal architecture and porosity. *Chem. Mater*. **2002**, *14* (*6*), 2616-2622.

20. Chui, S. S-Y.; Siu, A.; Feng, X.; Zhang, Z. E.; Mak, T. C. W.; Williams, I. D., Hydrothermal synthesis of three new 3-D framework rare-earth mellitates. *Inorg. Chem. Commun.* **2001**, *4* (9), 467-470.

21. Engström, M.; Klasson, A.; Pedersen, H.; Vahlberg, C.; Käll, P-O.; Uvdal, K., High proton relaxivity for gadolinium oxide nanoparticles. *Magn. Reson. Mater. Phy.*, **2006**, *19* (4), 180-186.

22. Bridot, J-L.; Faure, A-C.; Laurent, S.; Rivière, C.; Billotey, C.; Hiba, B.; Janier, M.; Josserand, V.; Coll, J-L.; Elst, L. V.; Muller, R.; Roux, S.; Perriat, P.; Tillement, O., Hybrid gadolinium oxide nanoparticles: multimodal contrast agents for in vivo imaging. *J. Am. Chem. Soc.* **2007**, *129* (16), 5076-5084.

23. Fortin, M-A.; Petoral Jr., R. M.; Söderlind, F.; Klasson, A.; Engström, M.; Veres, T.; Käll, P-O.; Uvdal, K., Polyethylene glycol-covered ultra-small Gd_2O_3 nanoparticles for positive contrast at 1.5 T magnetic resonance clinical scanning. *Nanotechnology*, **2007**, *18* (39), 395501 (1-9).

24. Choppin, G. R.; Peterman, D. R., Applications of lanthanide luminescence spectroscopy to solution studies of coordination chemistry. *Coord. Chem. Rev.* **1998**, *174* (1), 283-299.

CHAPTER 5

Manganese-Based Nanoscale Metal-Organic Frameworks for Magnetic Resonance Imaging

5.1 Introduction

Magnetic resonance imaging (MRI) is a powerful non-invasive diagnostic tool that provides high spatial resolution images and does not involve radioactivity.[1] Intrinsically low sensitivity of MRI however necessitates the use of contrast agents that are often administered in high doses.[2-3] Paramagnetic and superparamagnetic nanomaterials have recently emerged as promising MR contrast agents owing to their ability to carry large payloads of magnetic centers.[4-9] They can work at very low concentrations and be made target-specific by conjugation with affinity molecules.[10]

The majority of the commercially available MRI contrast agents are Gd(III) complexes formed with chelating ligands such as DTPA or DOTA. The stability of these complexes is a major concern due to the high toxicity of free Gd^{3+} ions (LD_{50} for the Gd(III) aqua ion is 0.1 mmol/kg body weight for mice[11]). There are currently only two Mn(II) containing contrast agents approved for use: $MnCl_2$ and Mn(DPDP). These manganese contrast agents differ from the gadolinium contrast agents in that they work by releasing free Mn^{2+} ions in order to increase the longitudinal relaxation rate. Mn^{2+} ions are much less toxic than Gd^{3+} ions and have been shown to exhibit very high *in vivo* longitudinal (r_1) MR relaxivities by binding to intracellular proteins.[12] The ideal situation for a manganese-containing contrast agent would be to have a compound that has a good short-term stability in water, so that it can be delivered to the desired cells, and then once inside the cells it would break down to release free Mn^{2+} ions.

We have synthesized two Mn containing nanoscale metal-organic frameworks (NMOFs) and evaluated their potential as MRI contrast enhancing agents. The as-synthesized NMOFs have a relatively low stability in aqueous media, and therefore have

been stabilized with a silica shell, which also allows for the conjugation of targeting moieties and organic fluorophores. The silica shell stabilization allows for delivery of the particles to sites of interest, where they will then release free Mn^{2+} ions which will increase the longitudinal relaxivity.

5.2 Results and Discussion

5.2.1 NMOF Synthesis

Two different Mn NMOFs were synthesized with the bridging ligands terephthalic acid (BDC) and trimesic acid (BTC) using reverse-phase microemulsions. Nanorods with the formula $Mn(BDC)(H_2O)_2$ (**5-1**) were synthesized by first forming two separate CTAB/1-hexanol/n-heptane/water microemulsions with W-values of 5, one containing $MnCl_2$ and the other containing the methyl ammonium salt of terephthalic acid, $[NMeH_3]_2(BDC)$ (1:1 BDC:Mn molar ratio). After forming, the two microemulsions were combined and stirred for an additional 18 hours at room temperature. The NMOFs were then isolated by centrifuging, and were washed with ethanol to remove the surfactant. Nanoparticles of $Mn_3(BTC)_2(H_2O)_6$, (**5-2**), were similarly prepared using a CTAB/1-hexanol/iso-octane/water microemulsion with a W-value of 10. In this case the trisodium salt of trimesic acid, $Na_3(BTC)$, was used along with $MnCl_2$ in a molar ratio of 2:3. After combining the two separate microemulsions the reaction was stirred at room temperature for 1 hour, after which time the particles were isolated by centrifuging, and were washed with ethanol.

We also carried out surfactant-assisted synthesis of **5-1** and **5-2** under microwave heating in an attempt to alter their morphologies. For the surfactant-assisted synthesis of **5-1** two separate CTAB/1-hexanol/n-heptane/water microemulsions containing $MnCl_2$ and

[NMeH$_3$]$_2$(BDC) in 1:1 molar ratio with a *W*-value of 10 were formed. The microemulsions were then combined and heated at 120 °C for 10 minutes in an 800 W microwave. Similarly, **5-2** was synthesized by first forming two CTAB/1-hexanol/iso-octane/water microemulsions containing Na$_3$(BTC) and MnCl$_2$ (in 2:3 molar ratio) with a *W*-value of 10.   The two microemulsions were then combined and heated at 120 °C for 10 minutes in an 800 W microwave.

5.2.2 Silica Coating

In order to stabilize **5-2** against dissolution and facilitate further functionalization with a fluorophore and cell-targeting peptide, the particles were coated with a shell of amorphous silica. The particles were first coated with poly(vinylpyrrolidone) (PVP). After the particles had formed in the microemulsion, an aliquot of a 5 mM aqueous solution of PVP (MW=40,000) corresponding to 10 mol% was added to the microemulsion. In the case of the microwave heated reactions, the reactions were allowed to cool to room temperature, after which time an aliquot of PVP was added and the reactions were stirred at room temperature for an additional 18 hours. The particles were then isolated by centrifuging and were washed with ethanol to remove the surfactant and excess PVP.

Silica-coated Mn$_3$(BTC)$_2$(H$_2$O)$_6$ nanoparticles (**5-2'**) were prepared by treating the PVP-coated particles with tetraethylorthosilicate (TEOS) under sol-gel conditions.   An aliquot of an ethanol suspension of PVP coated NMOFs was diluted with additional ethanol to give a particle concentration of about 0.5 mg/mL. An aliquot of aqueous ammonia corresponding to 3 vol% (based on total volume of ethanol used) was diluted in ethanol then added to the particle suspension. Finally, an aliquot of tetraethylorthosilicate (TEOS)

corresponding to ~3.8 µL/mg of particle was added and the reaction was stirred for two hours at room temperature. The particles were then isolated by centrifuging and were washed with ethanol. In order to obtain a thicker silica shell, the above reaction was repeated starting from the particles with a thin silica shell.

5.2.3 Surface Functionalization

In order to make the NMOFs target specific the surface was further functionalized with a cyclic arginine-glycine-aspartate (RGD) peptide. An organic fluorophore (rhodamine B) was also added to the surface to make the particles visible using confocal microscopy. Both the c(RGDfK) peptide and rhodamine B isothiocyanate were first reacted with a propyltriethoxysilane derivative. This allowed for covalent attachment of the peptide and fluorophore to the silica shell through the triethoxysilane functional group (Scheme 5.1)

The peptide and fluorophore were immobilized onto the silica shell using the following procedure. An aliquot of a suspension of **5-2'** was diluted to a final concentration of 2 mg/mL in ethanol. An aliquot of aqueous ammonia corresponding to 4 vol% was then added. Finally, aliquots of a 4 mg/mL solution of the modified c(RGDfK) in DMSO and a 6 mM solution of RITC-APS in ethanol, corresponding to 10 wt% and 1.5 wt% respectively, were added to the particle suspension. The reaction was then stirred at room temperature for 24 hours. The particles were then isolated by centrifuging and were washed with ethanol.
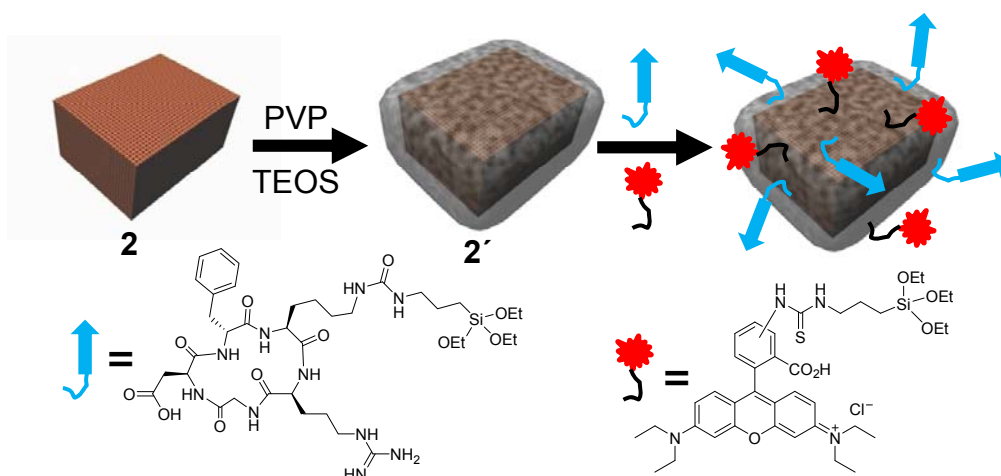
Scheme 5.1. Schematic showing the coating and surface functionalization of NMOFs **5-2**.

5.2.4 Characterization of NMOFs

The NMOFs were characterized using a variety of methods. First, the size, morphology, and polydispersity of the particles were determined using scanning electron and transmission electron microscopies (SEM and TEM). SEM and TEM micrographs show that particles of **5-1** synthesized at room temperature adopt a rod-like morphology with diameters of 50-100 nm and lengths of 750 nm-several μm (Fig. 5.1-5.3). NMOFs of **5-1** synthesized at 120 °C show similar size and morphology to the particles synthesized at room temperature (Fig. 5.4). SEM and TEM micrographs show that particles of **5-2** synthesized at room temperature are fairly uniform and adopt an unusual spiral rod morphology with diameters of 50-100 nm and lengths of 1-2 μm (Fig. 5.5-5.7). Unlike **5-1**, **5-2** synthesized at 120 °C under microwave heating shows much different size and morphology when compared to the sample synthesized at room temperature. SEM images showed that the particles obtained under microwave heating have a block-like morphology, with lengths ranging from ~50 to 300 nm in the three dimensions (Fig. 5.8-5.9).
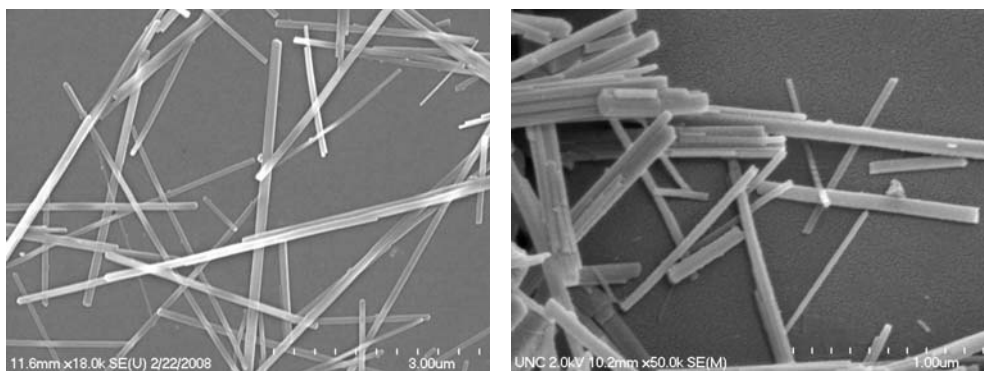
Figure 5.1. SEM images of Mn(BDC)(H$_2$O)$_2$ nanorods (**5-1**) synthesized at room temperature.
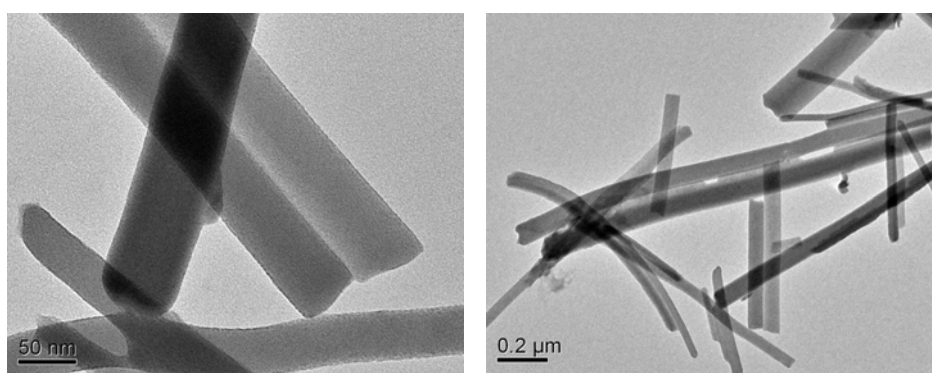
Figure 5.2. TEM images of Mn(BDC)(H$_2$O)$_2$ nanorods (**5-1**) synthesized at room temperature.
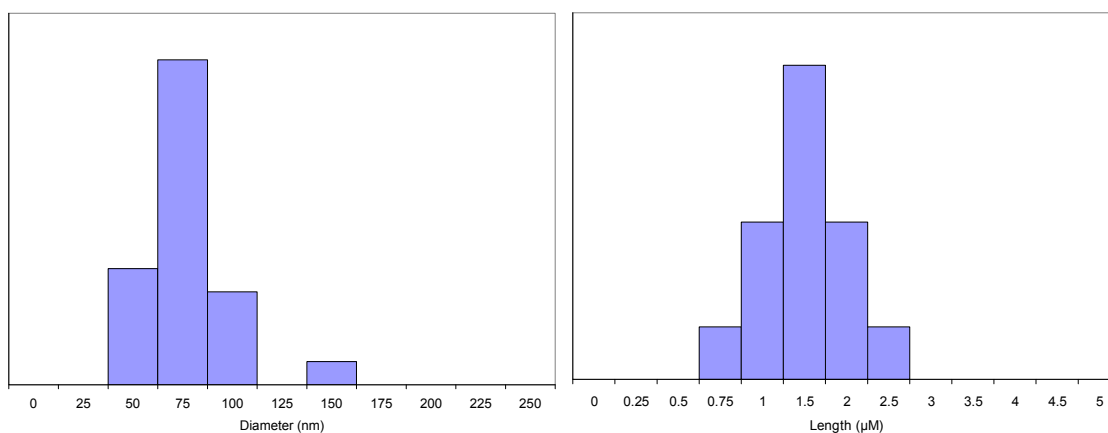
Figure 5.3. Size distributions of Mn(BDC)(H$_2$O)$_2$ nanorods (**5-1**) synthesized at room temperature. Left, diameter; Right, length.
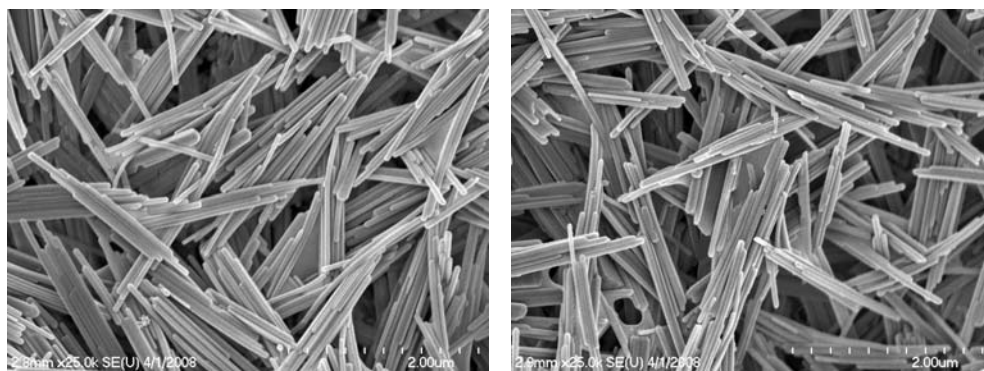
Figure 5.4. SEM images of Mn(BDC)(H$_2$O)$_2$ nanorods (**5-1**) synthesized at 120 °C under microwave heating.
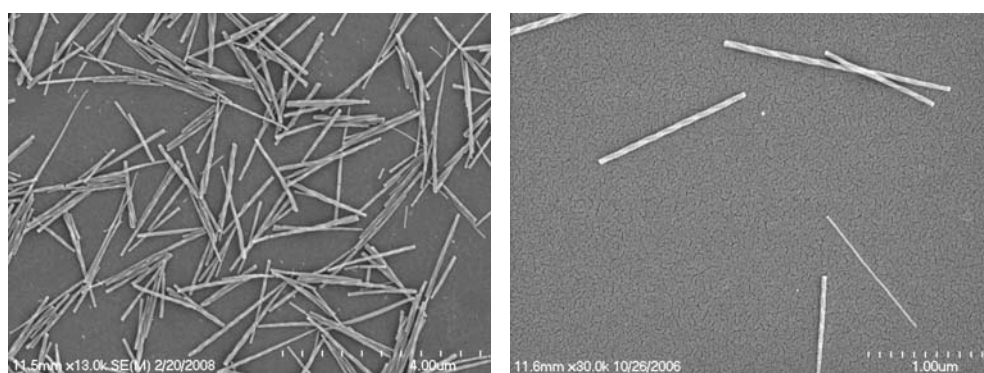
Figure 5.5. SEM images of Mn$_3$(BTC)$_2$(H$_2$O)$_6$ nanoparticles (**5-2**) synthesized at room temperature.
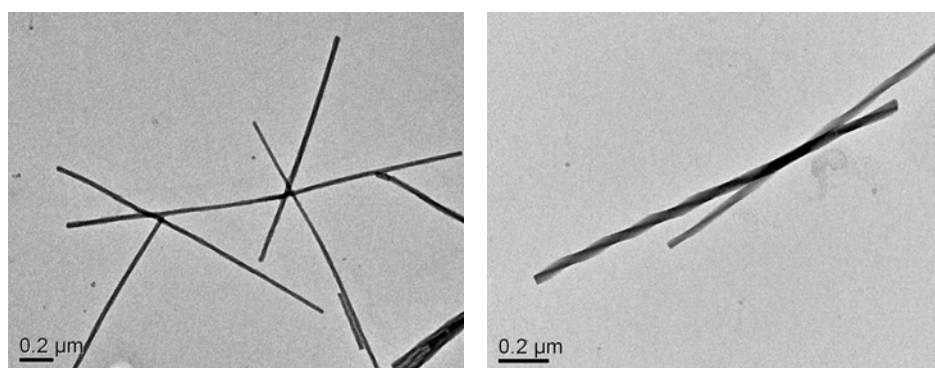
Figure 5.6. TEM images of Mn$_3$(BTC)$_2$(H$_2$O)$_6$ nanoparticles (**5-2**) synthesized at room temperature.
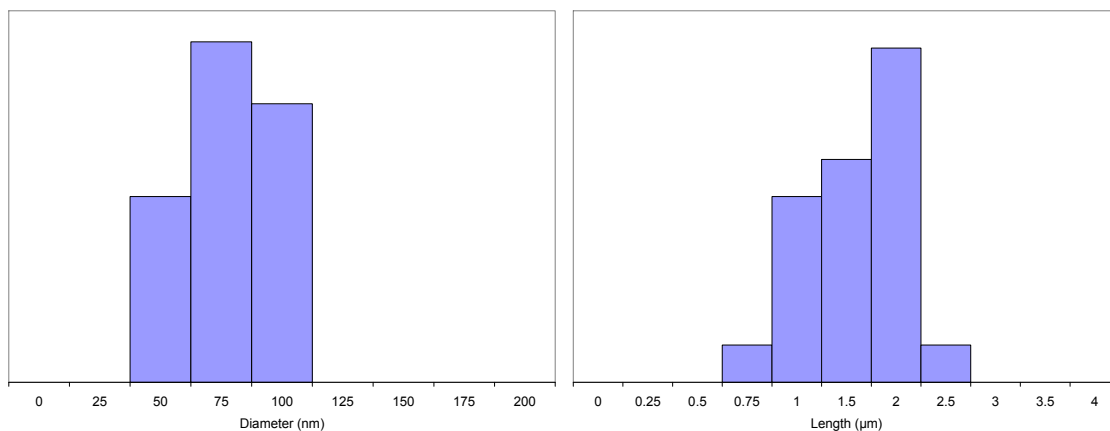
Figure 5.7. Size distributions of $Mn_3(BTC)_2(H_2O)_6$ spiral nanorods (**5-2**) synthesized at room temperature. Left, diameter; Right, length.
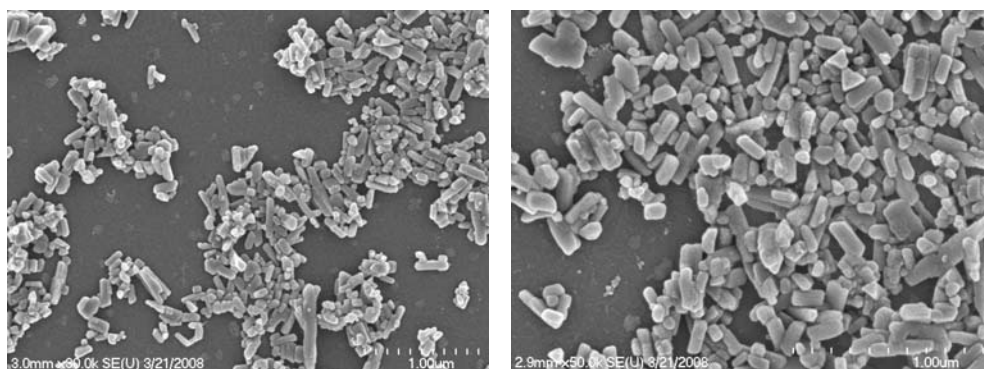
Figure 5.8. SEM images of $Mn_3(BTC)_2(H_2O)_6$ nanoparticles (**5-2**) synthesized at 120 °C under microwave heating.
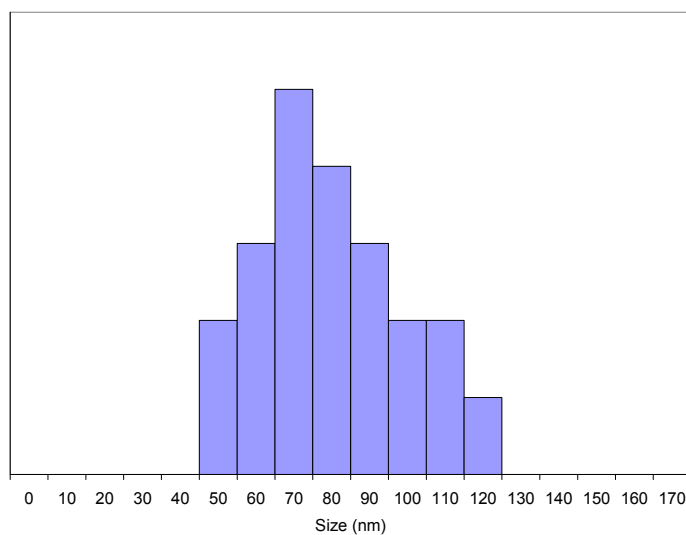
Figure 5.9. Size distributions of $Mn_3(BTC)_2(H_2O)_6$ nanoparticles (**5-2**)synthesized at 120 °C under microwave heating.

146

Powder X-ray diffraction (PXRD) was used to determine the crystallinity and phase of the NMOFs obtained. For **5-1** the PXRD pattern corresponded to a known bulk phase of $Mn(BDC)(H_2O)_2$ (Fig. 5.10-5.11).[13] This formula was also confirmed using thermogravimetric analysis (TGA) and inductively coupled plasma – mass spectrometry (ICP-MS). The TGA shows an initial weight loss of 11.5 wt% corresponding to the loss of two water molecules (expected:14.13 wt%, % difference: 20.5%) and a second weight loss of approximately 54.5 wt%, leaving 34 wt% remaining (Fig. 5.12). Assuming the final product is MnO_2, 34 wt% remaining corresponds to 21.49 wt% Mn (expected: 21.54 wt%, % difference: 0.23%). ICP-MS analysis showed that the NMOFs are 22.6 wt% Mn (calculated: 21.5 %, % difference: 4.99%). The PXRD and TGA results also show that the NMOFs synthesized at room temperature and at 120 °C are of the same phase.
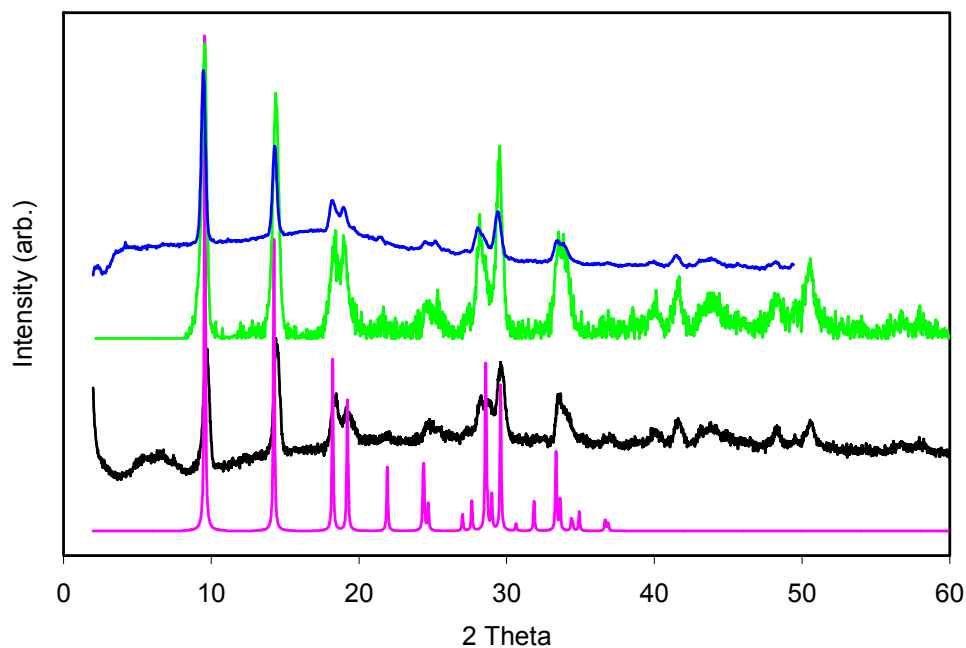
Figure 5.10. Simulated PXRD pattern of the known $Mn(BDC)(H_2O)_2$ phase[13] (pink), and experimental PXRD patterns for the bulk $Mn(BDC)(H_2O)_2$ particles (black), the $Mn(BDC)(H_2O)_2$ nanorods synthesized at room temperature (green), and the $Mn(BDC)(H_2O)_2$ nanorods synthesized at 120 °C (blue).
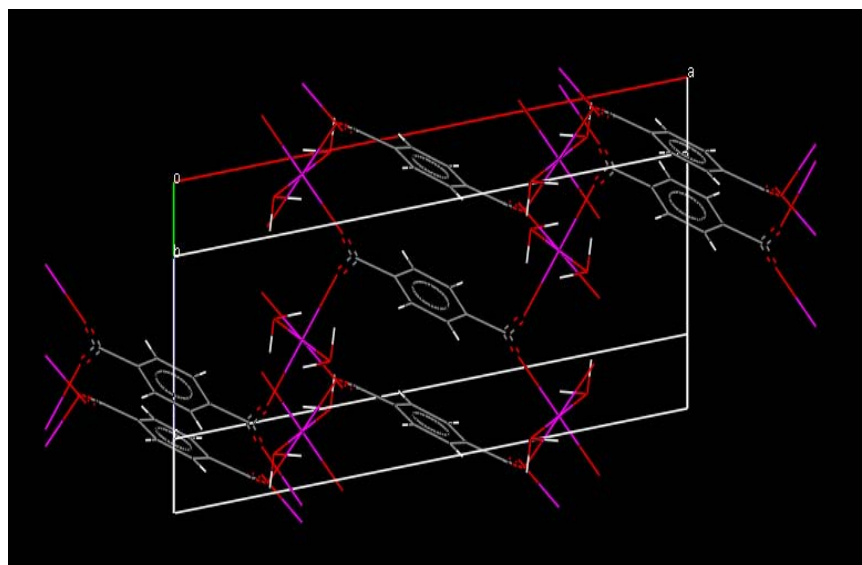
Figure 5.11. Crystal Structure of known $Mn(BDC)(H_2O)_2$ phase.[13]
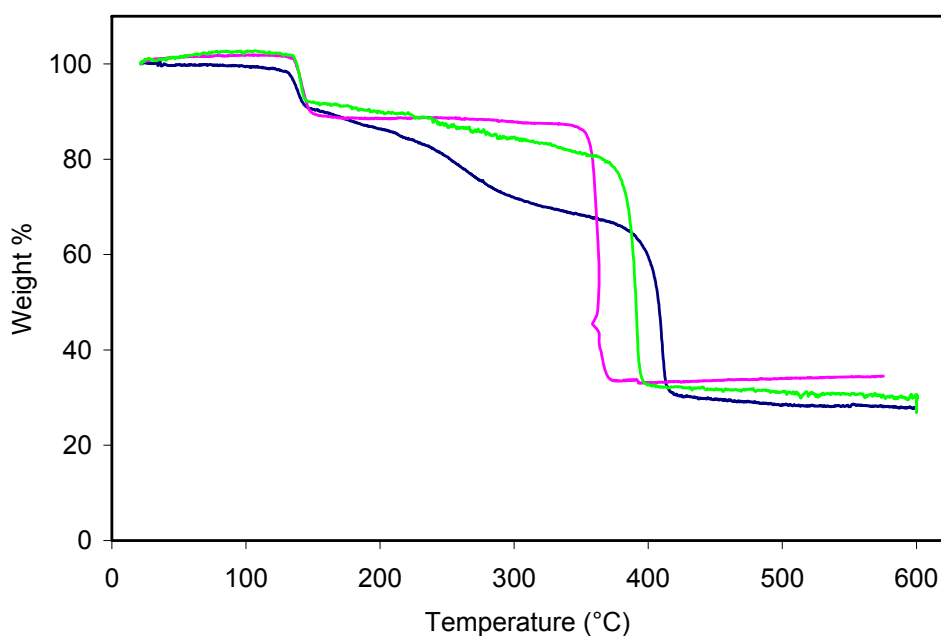
Figure 5.12. TGA of $Mn(BDC)(H_2O)_2$ nanoparticles (**5-1**) synthesized at room temperature (blue), at 120 °C (green), and the bulk sample (pink).

The NMOFs of **5-2** are crystalline based on PXRD, but do not correspond to any known phase of Mn-BTC MOFs (Fig. 5.13).[14-15] Numerous attempts to grow single crystals of the corresponding phase were unsuccessful. The composition of **5-2** $[Mn_3(BTC)_2(H_2O)_6]$

was established based on TGA and ICP-MS results. The TGA showed an initial weight loss of 12.1 wt% corresponding to the loss of six water molecules (Calculated: 13.2 wt%, % difference = 8.3%), followed by a loss of about 50.9 wt% leaving 36.9 wt% remaining (Fig. 5.14). Assuming the final product is MnO_2, 36.9 wt% remaining corresponds to 23.3 wt% Mn (expected: 24.0 wt%, % difference: 2.70%). ICP-MS analysis showed that the NMOFs are 24.2 wt% Mn (calculated: 24.0 wt%, % difference: 0.83%).
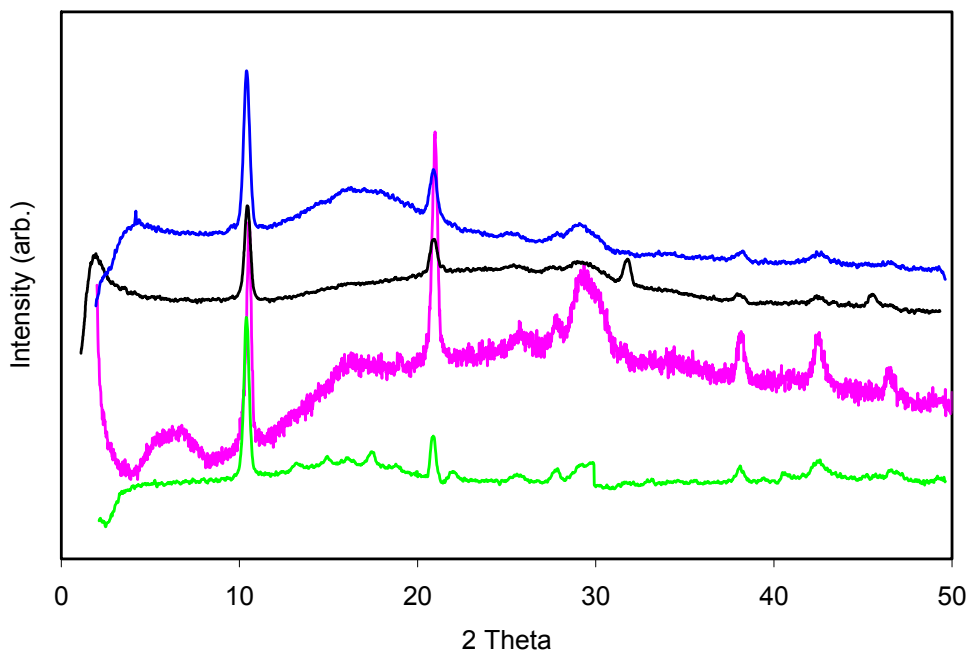
Figure 5.13. PXRD pattern of $Mn_3(BTC)_2(H_2O)_6$ bulk particles (pink), the $Mn_3(BTC)_2(H_2O)_6$ nanoparticles synthesized at room temperature (black), the $Mn_3(BTC)_2(H_2O)_6$ nanoparticles synthesized at 120 °C (green), and the silica coated $Mn_3(BTC)_2(H_2O)_6$ nanoparticles (blue).
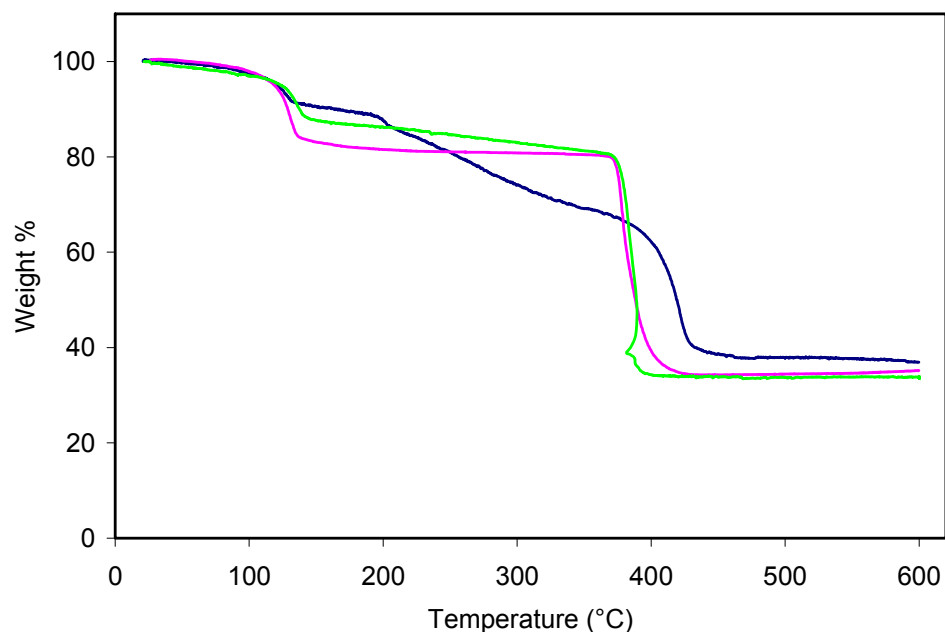
Figure 5.14. TGA of $Mn_3(BTC)_2(H_2O)_6$ nanoparticles (**5-2**) synthesized at room temperature (blue), at 120 °C (green), and the bulk sample (pink).

5.2.5 Characterization of Silica Coating

The PVP and silica coating of NMOFs **5-2** was characterized using SEM, TEM, and TGA. Upon coating with PVP less aggregation is seen in the SEM images (Fig. 5.15), and additional weight loss is seen in the TGA resulting from the increase in organic component (Fig. 5.16). Upon coating with a silica shell, no difference is seen in the particle size and morphology in the SEM images (Fig. 5.17) or in the PXRD pattern (Fig. 5.13), however the presence of the silica shell can be seen in TEM images (Fig. 5.18-5.19). The presence of the silica shell also results in an increase in the weight percent remaining after TGA (Fig. 5.16).

150
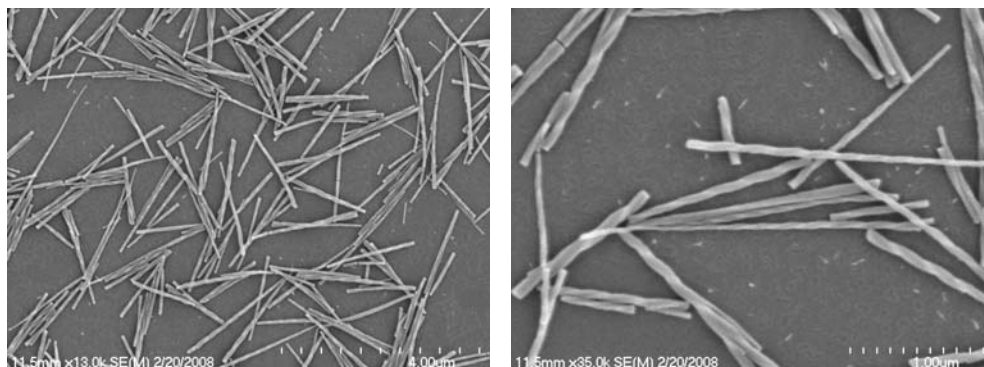
Figure 5.15. SEM images of poly(vinylpyrrolidone)-modified $Mn_3(BTC)_2(H_2O)_6$ nanoparticles (**5-2**) synthesized at room temperature.
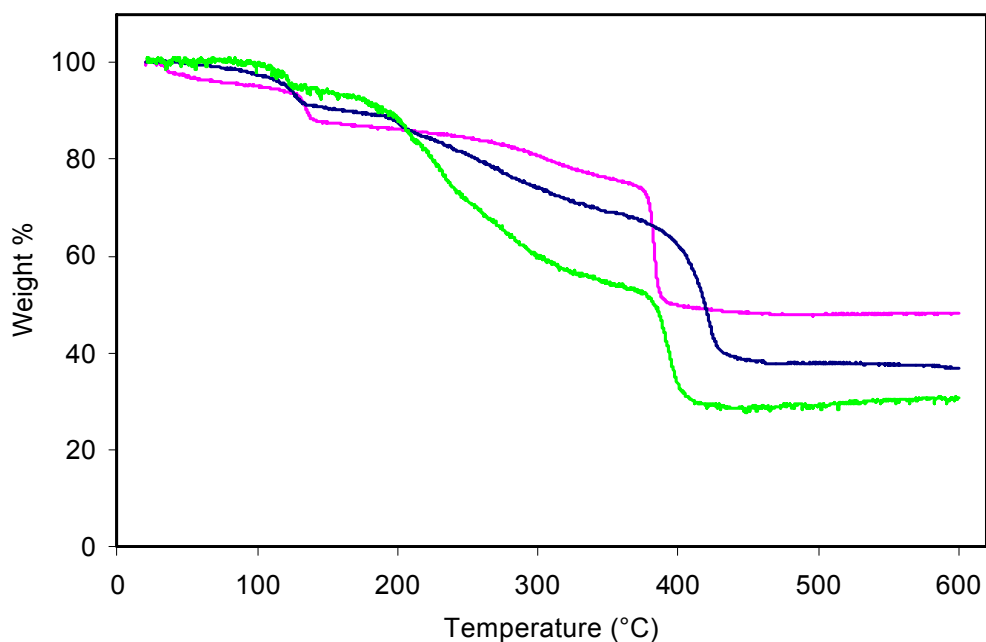
Figure 5.16. TGA of as synthesized $Mn_3(BTC)_2(H_2O)_6$ nanoparticles (**5-2**) (blue), PVP-coated (green), and silica coated (**5-2'**) (pink).

151
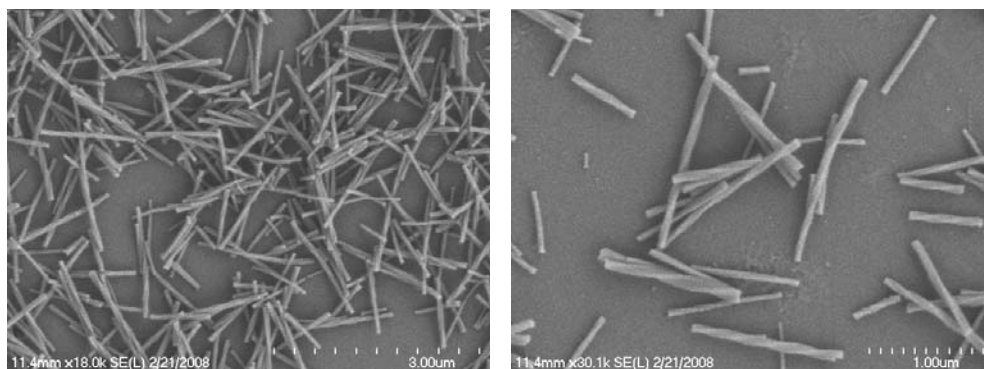
Figure 5.17. SEM images of silica-coated $Mn_3(BTC)_2(H_2O)_6$ nanoparticles (**5-2'**) synthesized at room temperature.
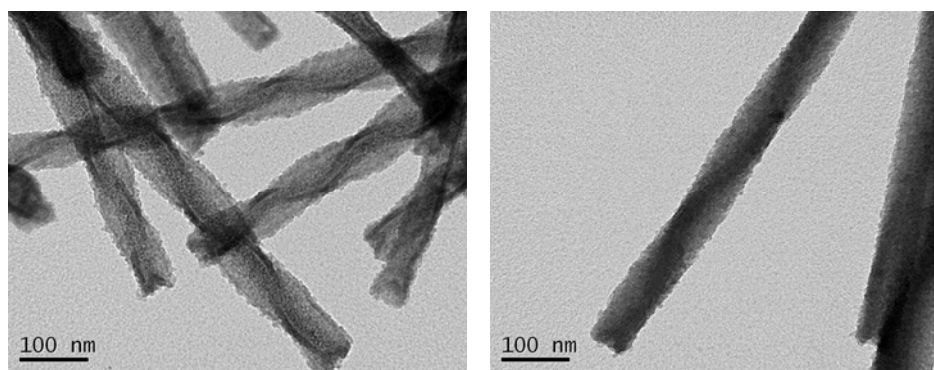
Figure 5.18. TEM images of silica-coated $Mn_3(BTC)_2(H_2O)_6$ nanoparticles (**5-2'**) synthesized at room temperature.
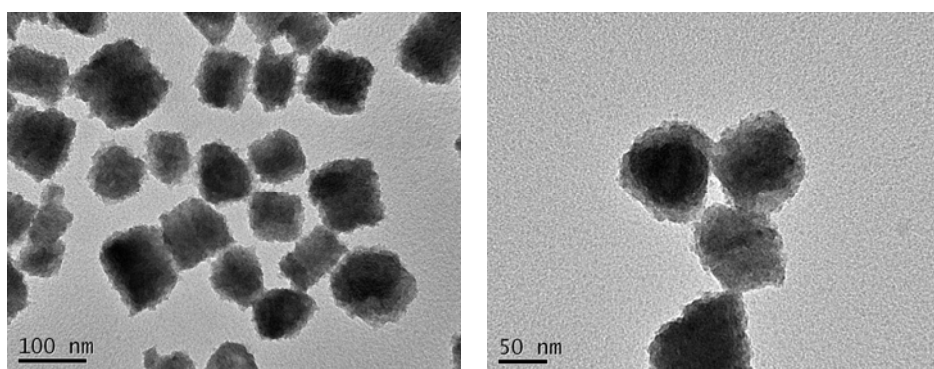
Figure 5.19. TEM images of silica-coated $Mn_3(BTC)_2(H_2O)_6$ nanoparticles (**5-2'**) synthesized at 120 °C.

5.2.6 Stability of NMOFs

In order to evaluate the stability of the NMOFs, release profiles were performed in both water and phosphate buffered saline (PBS) at 37 °C. In both water and PBS the silica

coating greatly slowed the dissolution and release of free Mn (Fig. 5.20-5.23). For the uncoated NMOFs, **5-2**, the half-life in water was found to be approximately 3.5 hours, while the silica coated NMOFs had a half-life of approximately 7.5 hours. The half-life is defined as the point where 50% of the Mn^{2+} ions have been released from the particles. In PBS the half-life was reduced to 18 minutes for the uncoated particles and 1.44 hours for the silica coated particles. In PBS complete release of Mn^{2+} ions is never observed, likely due to the formation of insoluble manganese phosphate species. For the calculation of half-life in PBS, it was assumed that the final data point represented 100% dissolution. These results indicate the stabilization of the NMOFs by the silica coating, and suggest that silica-coated particles should have adequate time to reach the site of interest where they will then release free Mn^{2+} to give T_1-weighted contrast enhancement.
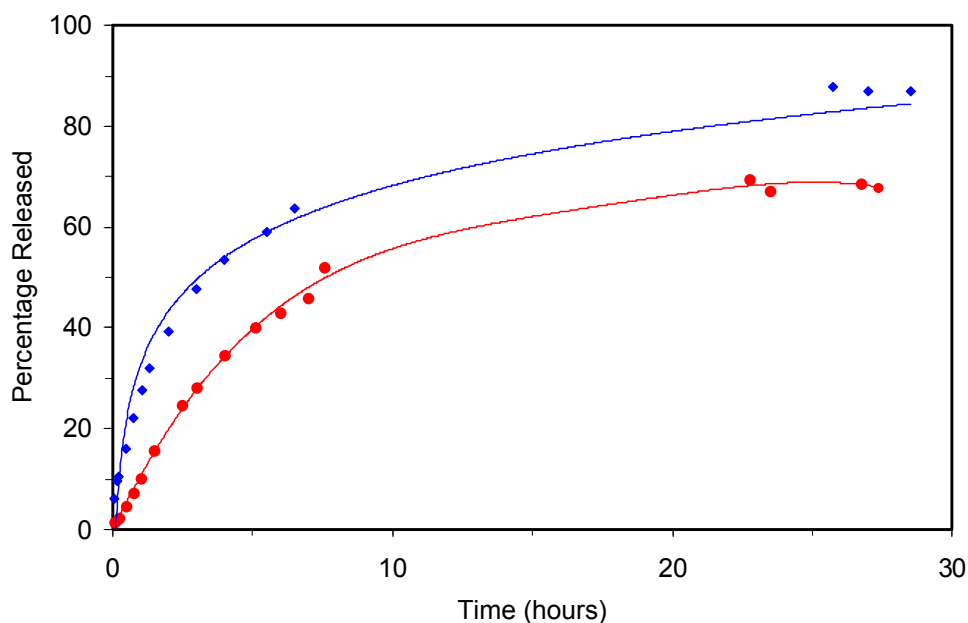
Figure 5.20. Dissolution curves of uncoated (blue) and silica coated (red) $Mn_3(BTC)_2(H_2O)_6$ nanoparticles (**5-2** and **5-2'**) in water at 37 °C. Percentage released versus time.
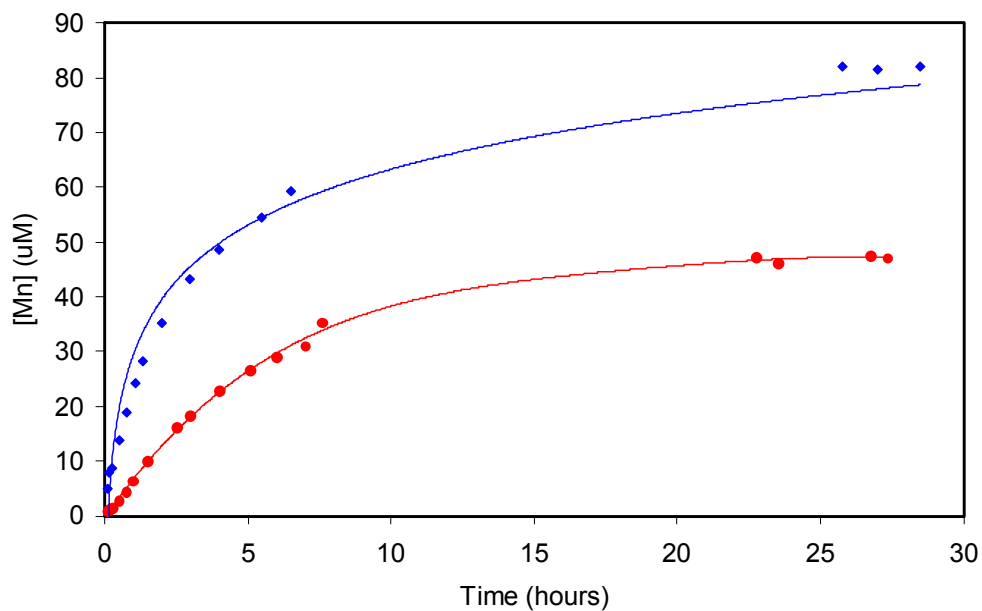
Figure 5.21. Dissolution curves of uncoated (blue) and silica coated (red) $Mn_3(BTC)_2(H_2O)_6$ nanoparticles (**5-2** and **5-2'**) in water at 37 °C. [Mn] versus time.
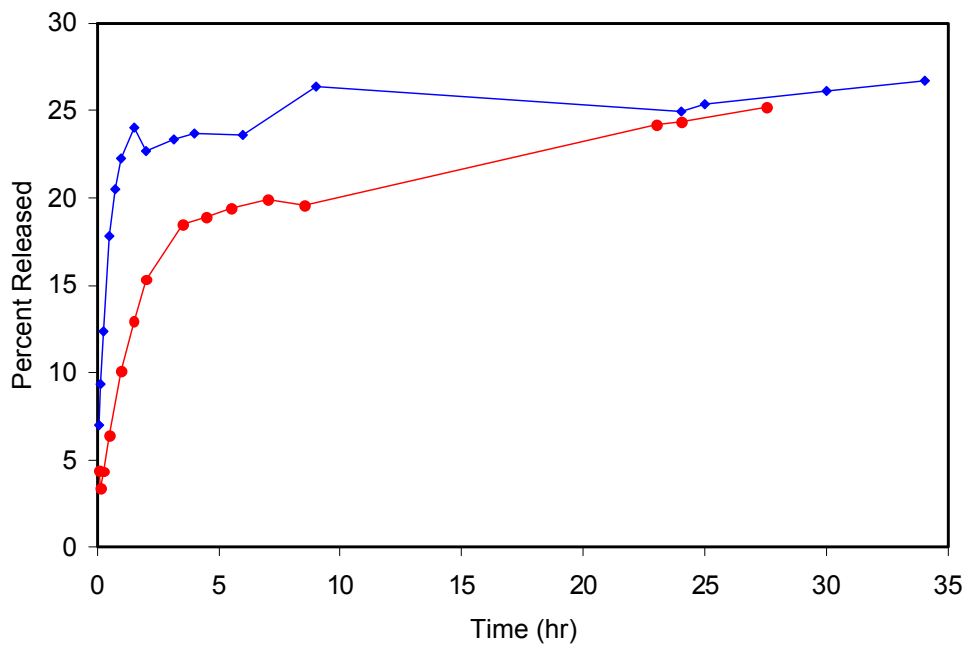
Figure 5.22. Dissolution curves of uncoated (blue) and silica coated (red) $Mn_3(BTC)_2(H_2O)_6$ nanoparticles (**5-2** and **5-2'**) in PBS at 37 °C. Percentage released versus time.
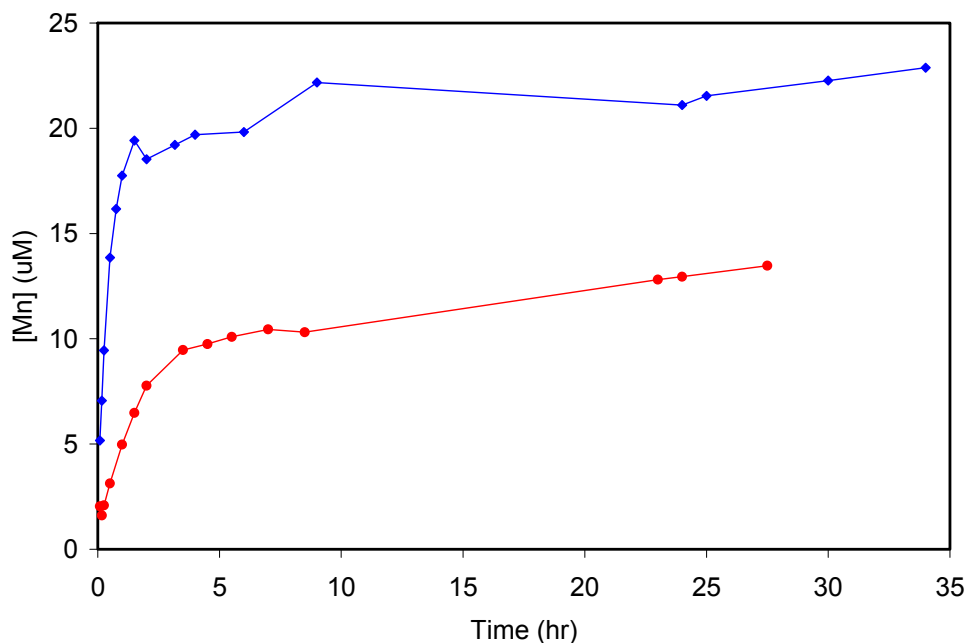
Figure 5.23. Dissolution curves of uncoated (blue) and silica coated (red) $Mn_3(BTC)_2(H_2O)_6$ nanoparticles (**5-2** and **5-2'**) in PBS at 37 °C. [Mn] versus time.

5.2.7 Relaxivity Measurements

The MR relaxivities of **5-1** and **5-2** were determined using a 3 T scanner. The relaxivities are determined by measuring the T_1 and T_2 values for a series of nanoparticle suspensions with [Mn] ranging from approximately 0.05 mM to 0.5 mM. The exact [Mn] concentration of the suspensions is then determined afterwards using ICP-MS. The slope of a plot of $1/T$ vs. [Mn] is the relaxivity value. Nanorods of **5-1** were found to have a longitudinal relaxivity (r_1) of 5.5 $mM^{-1}s^{-1}$ and a transverse relaxivity (r_2) of 80.0 $mM^{-1}s^{-1}$ on a per Mn basis (Fig. 5.24), whereas nanorods of **5-2** exhibited an r_1 of 7.8 $mM^{-1}s^{-1}$ and an r_2 of 70.8 $mM^{-1}s^{-1}$ on a per Mn basis (Fig. 5.25). These results are similar to what is obtained for free Mn^{2+} ions in solution; $MnCl_2$ has an r_1 of 7.2 $mM^{-1}s^{-1}$ and an r_2 of 72.3 $mM^{-1}s^{-1}$ (Fig. 5.26). Consistent with this, nanorods of **5-2** had an r_1 of 4.6 $mM^{-1}s^{-1}$ and an r_2 of 141.2 $mM^{-1}s^{-1}$ on a per Mn basis at 9.4 T (Fig. 5.27). **5-2'** has slightly lower r_1 of 4.0 $mM^{-1}s^{-1}$ and r_2 of

155

$112.8 \text{ mM}^{-1}\text{s}^{-1}$ at 9.4 T (Fig. 5.28). The slight decrease of MR relaxivities is expected due to the reduced influence of the Mn centers on the surrounding water molecules.
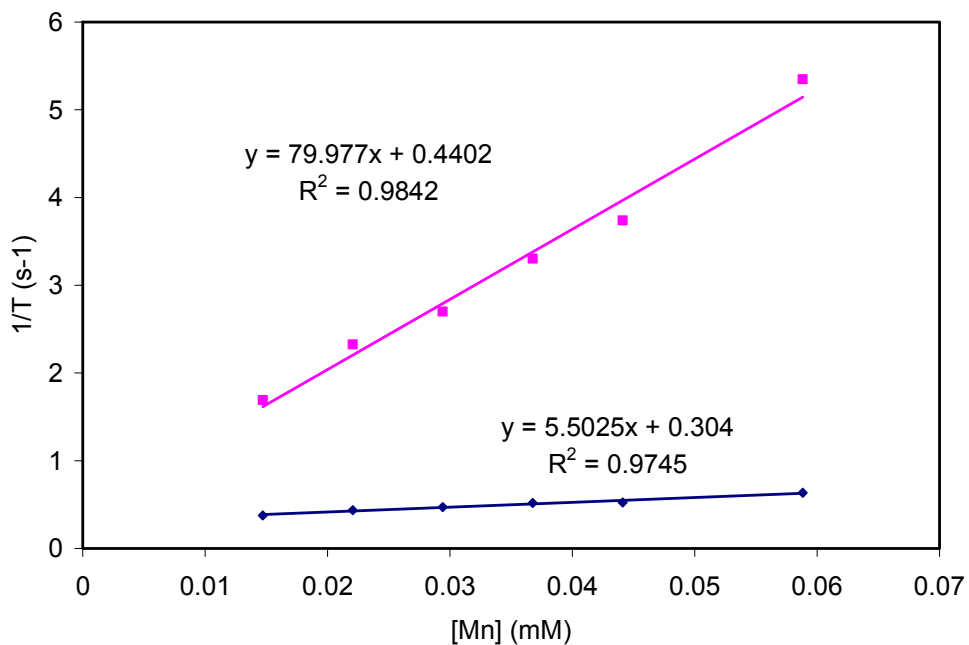
Figure 5.24. Relaxivity of $Mn(BDC)(H_2O)_2$ nanorods (**5-1**) measured at 3 T. $r_1 = 5.5 \text{ mM}^{-1}\text{s}^{-1}$, $r_2 = 80.0 \text{ mM}^{-1}\text{s}^{-1}$.
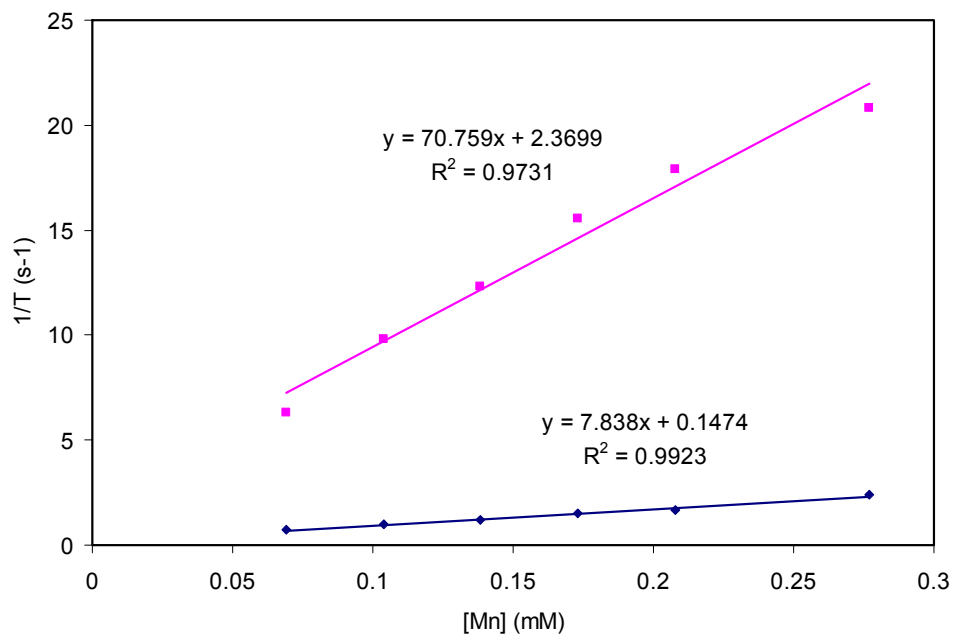
Figure 5.25. Relaxivity of $Mn_3(BTC)_2(H_2O)_6$ nanoparticles (**5-2**) measured at 3.0 T. $r_1 = 7.8$ mM^{-1}s^{-1}, $r_2 = 70.8$ mM^{-1}s^{-1}.
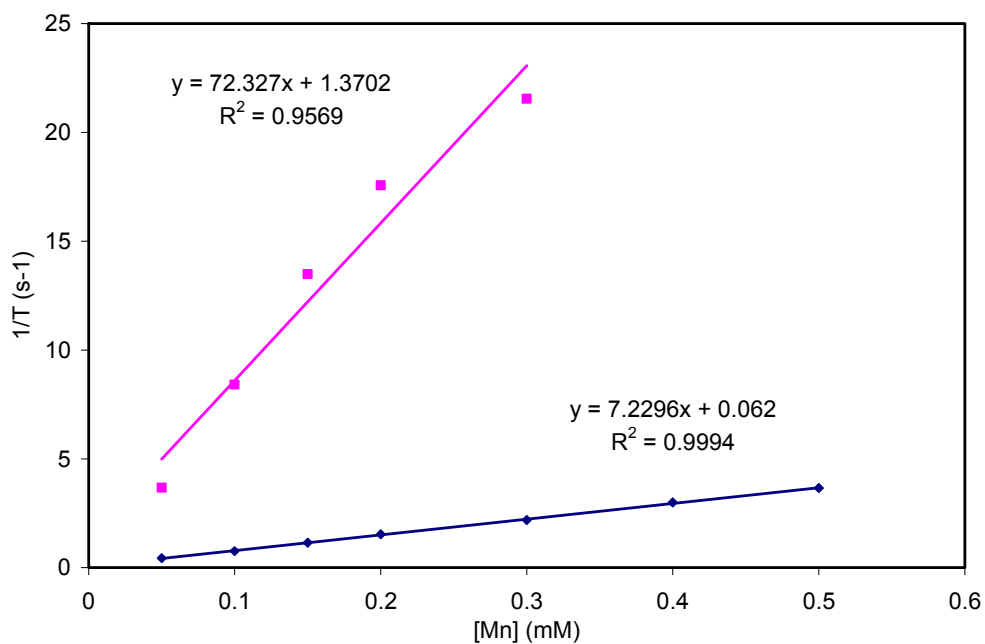
Figure 5.26. Relaxivity of $MnCl_2$ at 3 T. $r_1 = 7.2$ mM^{-1}s^{-1}, $r_2 = 72.3$ mM^{-1}s^{-1}.
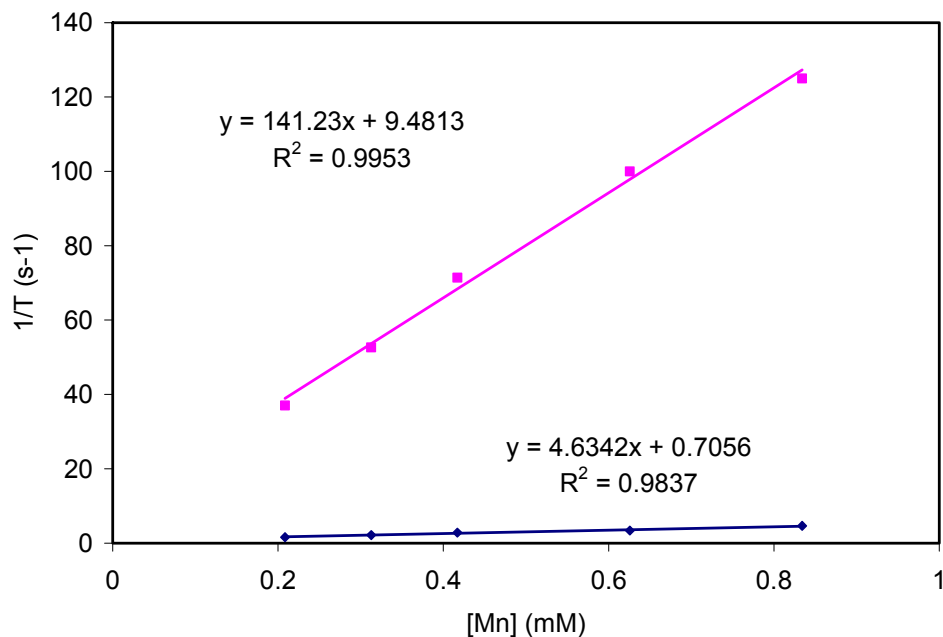
Figure 5.27. Relaxivity of $Mn_3(BTC)_2(H_2O)_6$ nanoparticles (**5-2**) measured at 9.4 T. $r_1 = 4.6$ mM^{-1}s^{-1}, $r_2 = 141.2$ mM^{-1}s^{-1}.
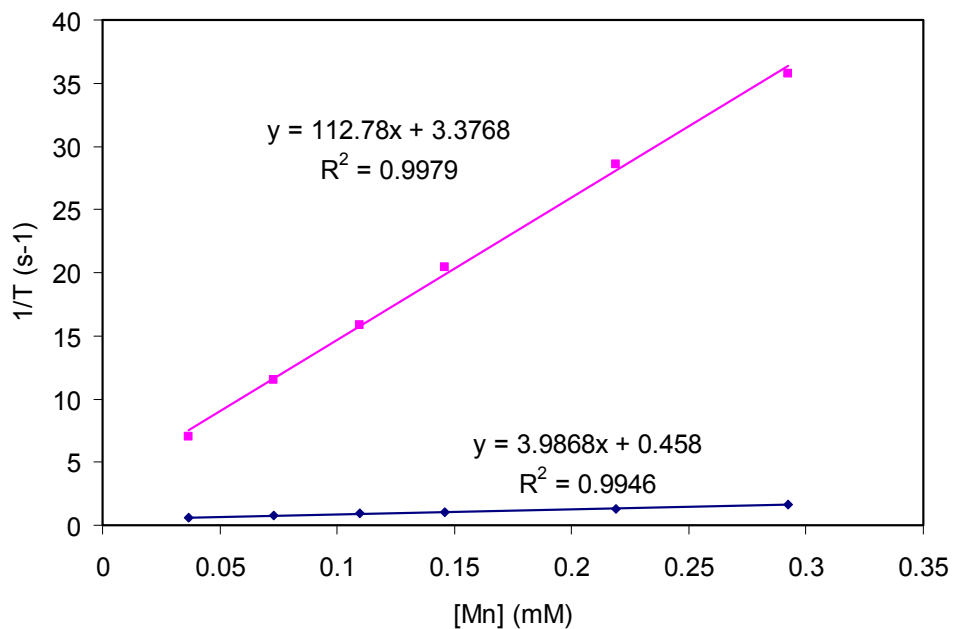
Figure 5.28. Relaxivity of $Mn_3(BTC)_2(H_2O)_6$ nanoparticles with a silica shell (**5-2'**) measured at 9.4 T. $r_1 = 4.0$ mM^{-1}s^{-1}, $r_2 = 112.8$ mM^{-1}s^{-1}.

5.2.8 In Vitro and In Vivo Experiments

We evaluated the efficacy of **5-2'** particles that have been surface-functionalized with rhodamine B and c(RGDfK) as MR and optical contrast agents *in vitro*. Human colon cancer (HT-29) cells were incubated with rhodamine B-functionalized nanoparticles of **5-2'** with and without the c(RGDfK) targeting peptide. *In vitro* MR imaging of HT-29 cells showed the selective uptake of **5-2'** and thus the intracellular delivery of Mn^{2+} ions. As shown in Figure 5.29, the HT-29 cells incubated with the targeted particles gave much higher signals in T_1-weighted MR images than those that were not incubated with nanoparticles as well as those that were incubated with the non-targeted particles. Little difference was seen in the T_2 weighted images (Fig. 5.30). ICP-MS analysis supported the enhanced uptake of **5-2'** by HT-29 cells: the cell pellets (~3.2 million cells) contained 0.05, 0.33, and 2.29 μg of Mn after incubating with no particles, non-targeted **5-2'**, and targeted **5-2'**, respectively. Confocal microscopic imaging studies further confirmed the enhanced uptake of the particles with the targeting peptide, compared to those without the targeting peptide (Fig. 5.31-5.32). These results demonstrate the target specific uptake of the c(RGDfK)-modified Mn NMOFs by angiogenic cancer cells, presumably via receptor-mediated endocytosis. Finally, we also demonstrated the *in vivo* utility of Mn NMOFs for Mn^{2+} ion delivery. T_1-weighted contrast enhancement was observed in a mouse liver, kidneys, and aorta ~1 hour after tail vein injection of **5-2'** at a 10 μmol/kg Mn dose, apparently caused by the Mn^{2+} ions released from the nanoparticles (Fig. 5.33).
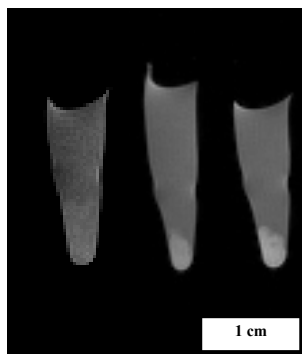
Figure 5.29. *In vitro* T_1-weighted MR images of HT-29 cells incubated with no **5-2'** (left), non-targeted **5-2'** (middle), and c(RGDfK)-targeted **5-2'** (right).
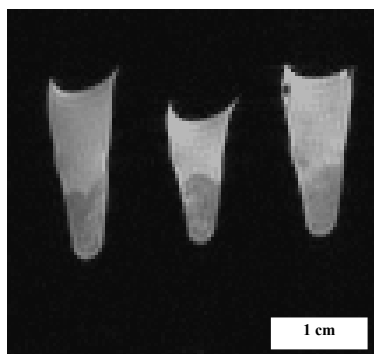
Figure 5.30. *In vitro* T_2-weighted MR images of HT-29 cells incubated with no **5-2'** (left), non-targeted **5-2'** (middle), and c(RGDfK)-targeted **5-2'** (right).
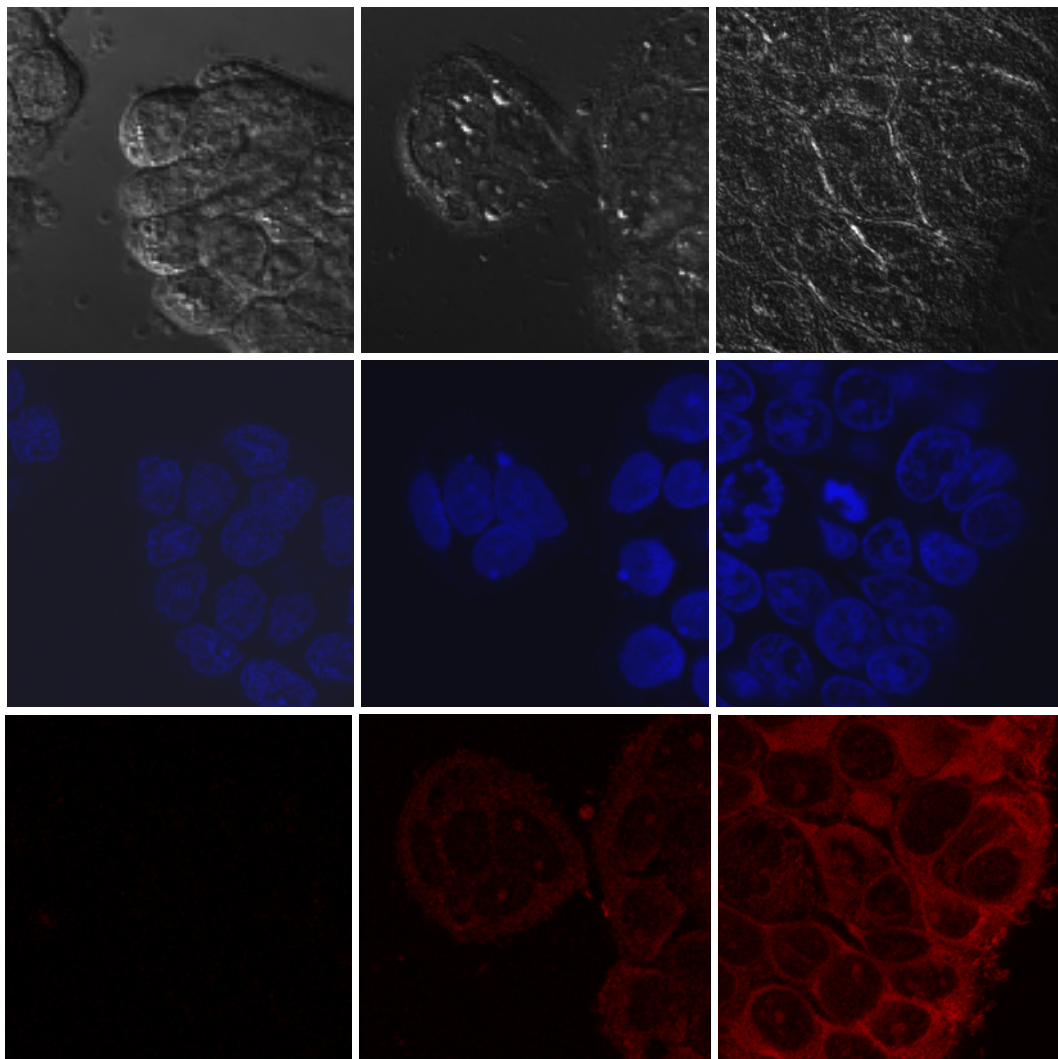
Figure 5.31. Confocal images of HT-29 cells that were incubated with no **5-2'** (left), non-targeted **5-2'** (middle), and c(RGDfK)-targeted **5-2'** (right). The top, middle, and bottom images show the bright-field image, signal from the DRAQ5 nuclear stain (blue), and the signal from rhodamine B (red), respectively.
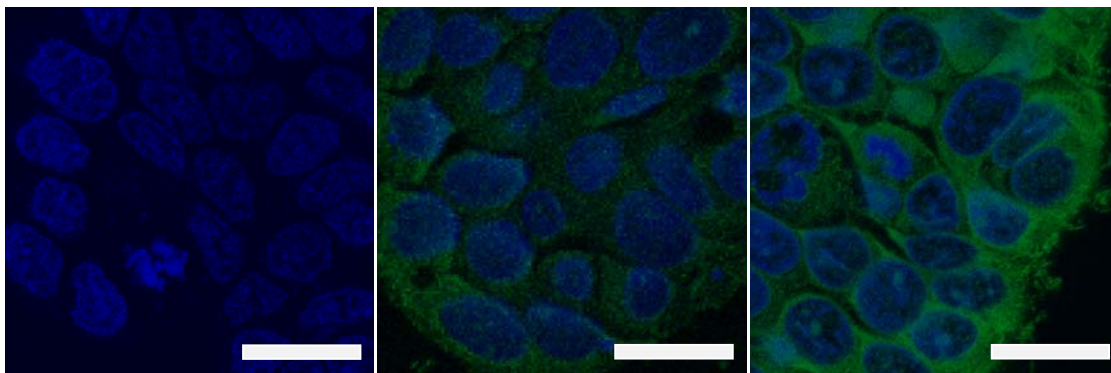
Figure 5.32. Merged confocal images of HT-29 cells that were incubated with no **5-2'** (left), non-targeted **5-2'** (center), c(RGDfK)-targeted **5-2'** (right). The blue color was from DRAQ5 used to stain the cell nuclei while the green color was from rhodamine B. The bars represent 20 μm.
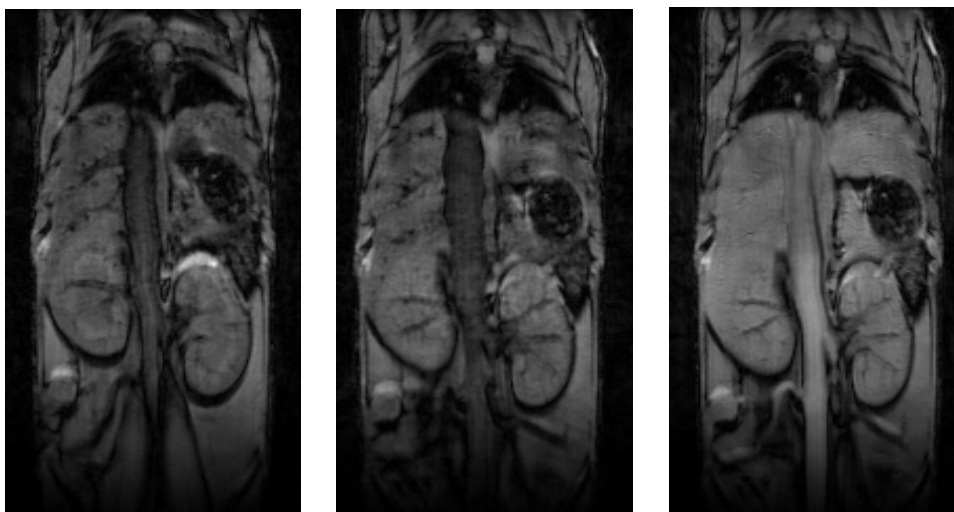
Figure 5.33. T_1-weighted images of the midbody of a mouse model before contrast (left), 13 minutes (middle) and 65 minutes (right) after the injection of **5-2'** (at a 10 μmol/kg Mn dose).

5.3 Conclusion

In summary, we have synthesized Mn NMOFs with controllable morphologies and demonstrated their potential for MR contrast enhancement. Surface functionalization of the Mn NMOFs with a cell-targeting molecule enhances their delivery to cancer cells to allow for target-specific MR imaging. Such a core-shell nanostructure platform can be used for targeted delivery of other imaging and therapeutic agents.

5.4 Experimental Details

5.4.1 Materials and Methods

All starting materials and surfactants were purchased from Aldrich and used without further purification. All solvents were purchased from Fisher. Microwave reactions were carried out in a CEM MARS 5 microwave. Thermogravimetric analysis (TGA) was performed using a Shimadzu TGA-50 equipped with a platinum pan and heated at a rate of 3 °C per minute under air. Powder X-ray diffraction (PXRD) analyses were carried out using a Rigaku Multiflex powder diffractometer using Cu radiation or on a Bruker SMART APEX II diffractometer using Cu radiation. In the latter, the PXRD patterns were processed with the APEX 2 package using phase ID plug-in. Scanning electron microscopy (SEM) was used to image the particles obtained from each reaction. A Hitachi 4700 field emission scanning electron microscope was used. A Cressington 108 Auto Sputter Coater equipped with a Au/Pd (80/20) target and an MTM-10 thickness monitor was used to coat the samples with a conductive layer before taking SEM images. Each SEM sample was prepared by first suspending the nanomaterial in ethanol, then a drop of the suspension was placed on a glass slide and the solvent was allowed to evaporate. An Applied Research Laboratories (ARL) SpectraSpan 7 DCP spectrometer and a Varian 820-MS Inductively Coupled Plasma-Mass Spectrometer were used to measure Mn^{2+} concentrations, for both stability tests and to accurately determine concentrations in samples from relaxivity measurements.

The methyl ammonium salts of the ligands were made by dissolving the ligand in a 40 wt % solution of methyl amine in water. The excess methyl amine and water were then evaporated under reduced pressure, and the isolated salt was then redissolved in distilled water to give an aqueous solution of desired concentration. The sodium salts of the ligands

were made by dissolving the ligand and the appropriate amount of NaOH in water, and then diluting to give the desired concentration.

MR images were acquired on a Siemens 3 T Allegra (Siemens Medical Systems, Erlangen, Germany) with a CP head coil, and a 9.4 T Bruker BioSpec (Bruker Biospin, Ettlingen, Germany) system with a 35 mm quadrature RF transmit and receive coil. For the 3 T scanner, a 3D FLASH sequence was utilized to compute T_1 maps with seven different flip angles (2, 5, 10, 20, 30, 40, and 60). Imaging parameters were: FOV=190 x 190*64 mm^3, Matrix size=128 x 128 * 32, TR/TE= 40/1.64 ms, total data acquisition time was 19 minutes. A 2-D multiple echo spin echo sequence was used to estimate T_2 maps. In total, 32 echoes with an echo spacing of 6.2 ms were obtained. The first echo time was 6.2 ms. TR was 3000 ms. FOV and matrix size were set to 190 x 190 mm^2 and 128 x 128. The slice thickness was 2 mm. The total data acquisition time was about 6 minutes and 29 seconds. For the 9.4 T scanner, two 2D multiple echo spin echo sequences were used to estimate T_2 maps for a wide range of T_2. FOV and matrix size were set to 35 x 30 mm^2 and 128 x 128. The slice thickness was 1 mm. In total, 32 echoes with an echo spacing of 3.7 ms for sequence 1 and 40 echoes with an echo spacing of 10 ms for sequence 2 were obtained. The TR/TE1 were 3.7/3000 ms and 10/4114 ms for each sequence, respectively. The total data acquisition time was about 10 minutes. T_1 maps were obtained with a variable TR rapid acquisition relaxation enhanced (RARE) sequence with a TE=5.14 ms. Twenty two variable TRs (TR=18, 25, 40, 60, 90, 120, 160, 200, 250, 300, 380, 500, 700, 1000, 1500, 2000, 2500, 3000, 4000, 5000, 6000, 7000 ms) were used with a FOV of 35x30 mm^2 and a matrix size of 128 x 128. RARE factor was 3 and total data acquisition was about 24 minutes.

5.4.2 Synthesis and Surface Functionalization of Nanoscale Metal-Organic Frameworks.

Room temperature synthesis of Mn(BDC)(H$_2$O)$_2$ nanorods (5-1). Mn(BDC)(H$_2$O)$_2$ nanoparticles were prepared via the CTAB/1-hexanol/iso-octane/water microemulsion system. Two $W = 5$ microemulsions were prepared by the addition of 0.675 mL of a 0.05 M benzene dicarboxylic acid methyl ammonium salt aqueous solution and 0.675 mL of a 0.05 M MnCl$_2$ aqueous solution to two separate 150 mL aliquots of a 0.05 M CTAB/0.5 M 1-hexanol/iso-octane mixture while vigorously stirring at room temperature. The separate microemulsions were stirred vigorously for 10 minutes at room temperature, after which the two microemulsions were combined, and the resultant 300 mL microemulsion with $W = 5$ was stirred for an additional 18 hours at room temperature. The nanoparticles were isolated via centrifugation at 13,000 rpm for 10 minutes. After the removal of the supernatant, the particles were washed by redispersement via sonication in 30 mL of ethanol. The ethanol suspension was then centrifuged again for 10 minutes at 13,000 rpm to recover the nanoparticles. Yield: 4.9 mg (66.3 %).

High Temperature Synthesis of Mn(BDC)(H$_2$O)$_2$ nanorods (5-1). Two microemulsions with $W = 10$ were prepared by the addition of 180 μL of a 0.1 M benzene dicarboxylic acid methylammonium salt aqueous solution and 180 μL of a 0.1 M MnCl$_2$ aqueous solution to separate 10 mL aliquots of a 0.1 M CTAB/0.5 M 1-hexanol/iso-octane mixture while vigorously stirring at room temperature. The separate microemulsions were stirred vigorously for 10 minutes at room temperature, after which the two microemulsions were combined, and the resultant 20 mL microemulsion with $W = 10$ was transferred to a microwave vessel. The reaction was then rapidly heated to 120 °C in the microwave. Once

reaching 120 °C, the reaction was held at this temperature for 10 minutes. After cooling, the nanoparticles were isolated via centrifugation at 13,000 rpm for 10 minutes. After the removal of the supernatant, the particles were washed by redispersement via sonication in 5 mL of ethanol. The ethanol suspension was then centrifuged again for 10 minutes at 13,000 rpm to recover the nanoparticles. Yield: 3.6 mg (91.3 %)

Room temperature synthesis of Mn$_3$(BTC)$_2$(H$_2$O)$_6$ nanorods (5-2). Mn$_3$(BTC)$_2$(H$_2$O)$_6$ nanorods were prepared via the CTAB/1-hexanol/iso-octane/water microemulsion system. Two $W = 10$ microemulsions were prepared by the addition of 240 μL of a 0.1 M 1,3,5-benzenetricarboxylic acid sodium salt aqueous solution and 240 μL of a 0.15 M MnCl$_2$ aqueous solution to two separate 25 mL aliquots of a 0.05 M CTAB/0.5 M 1-hexanol/iso-octane mixture while vigorously stirring at room temperature. The separate microemulsions were stirred vigorously for 10 minutes at room temperature, after which the two microemulsions were combined, and the resultant 50 mL microemulsion with $W = 10$ was stirred for an additional 1 hour at room temperature. The nanoparticles were isolated via centrifugation at 13,000 rpm for 10 minutes. After the removal of the supernatant, the particles were washed by redispersement via sonication in 5 mL of ethanol. The ethanol suspension was then centrifuged again for 10 minutes at 13,000 rpm to recover the nanoparticles. Yield: 5.1 mg (74.2 %).

High temperature synthesis of Mn$_3$(BTC)$_2$(H$_2$O)$_6$ nanoparticles (5-2). Two microemulsions with $W = 10$ were prepared by the addition of 90 μL of a 0.2 M 1,3,5-benzenetricarboxylic acid sodium salt aqueous solution and 90 μL of a 0.3 M MnCl$_2$ aqueous solution to separate 10 mL aliquots of a 0.05 M CTAB/0.5 M 1-hexanol/iso-octane mixture while vigorously stirring at room temperature. The separate microemulsions were stirred

vigorously for 10 minutes at room temperature, after which the two microemulsions were combined, and the resultant 20 mL microemulsion with $W = 10$ was transferred to a microwave vessel. The reaction was then rapidly heated to 120 °C in the microwave. Once reaching 120 °C, the reaction was held at this temperature for 10 minutes. After cooling, the nanoparticles were isolated via centrifugation at 13,000 rpm for 10 minutes. After the removal of the supernatant, the particles were washed by redispersement via sonication in 5 mL of ethanol. The ethanol suspension was then centrifuged again for 10 minutes at 13,000 rpm to recover the nanoparticles. Yield: 4.85 mg (93.1 %)

Synthesis of Poly(vinylpyrrolidone)-modified $Mn_3(BTC)_2(H_2O)_6$ nanoparticles. PVP-coated $Mn_3(BTC)_2(H_2O)_6$ nanoparticles were prepared via the CTAB/1-hexanol/iso-octane/water microemulsion system. A $W = 10$ microemulsion was prepared by the addition of 48 µL of a 0.1 M 1,3,5-benzenetricarboxylic acid sodium salt aqueous solution and 48 µL of a 0.15 M $MnCl_2$ aqueous solution to separate 5 mL aliquots of a 0.05 M CTAB/0.5 M 1-hexanol/iso-octane mixture while vigorously stirring at room temperature. The separate microemulsions were stirred vigorously for 10 minutes at room temperature, after which the two microemulsions were combined, and the resultant 10 mL microemulsion with $W = 10$ was stirred for an additional 1 hour at room temperature. After the particles had formed, 96 µL of a 5 mM aqueous solution of PVP (10 mol%) was added to the microemulsion. The reaction was then stirred at room temperature for an additional 2 hours. The coated nanoparticles were isolated via centrifugation at 13,000 rpm for 10 minutes. After the removal of the supernatant, the particles were washed by redispersement via sonication in 5 mL of ethanol. The ethanol suspension was then centrifuged again for 10 minutes at 13,000 rpm to recover the nanoparticles. Similarly, $Mn_3(BTC)_2(H_2O)_6$ nanoparticles synthesized at

120 °C were cooled to room temperature, and an aliquot of an aqueous solution of PVP was added. The resulting mixture was stirred at room temperature for 18 hours to afford PVP-coated $Mn_3(BTC)_2(H_2O)_6$ nanoparticles.

Synthesis of silica-coated $Mn_3(BTC)_2(H_2O)_6$ nanoparticles (5-2'). Silica-coated $Mn_3(BTC)_2(H_2O)_6$ nanoparticles were prepared by treating the PVP-coated particles with tetraethylorthosilicate (TEOS) under sol-gel conditions. 9.0 mg of PVP coated $Mn_3(BTC)_2(H_2O)_6$ particles suspended in 9 mL of ethanol were placed in a round bottom flask. 0.54 mL of aqueous ammonia was diluted in an additional 9 mL of ethanol and added to the particle suspension (3 vol.% NH_4OH). 34 µL of TEOS was then added to the stirring suspension, and the mixture was then stirred for an additional two hours at room temperature. The coated nanoparticles were isolated via centrifugation at 10,000 rpm for 10 minutes. After the removal of the supernatant, the particles were washed by redispersement via sonication in 5 mL of ethanol. The ethanol suspension was then centrifuged again for 10 minutes at 10,000 rpm to recover the nanoparticles. To obtain at thicker silica shell, the above procedure was repeated. For example, 7 mg of nanoparticles with a thin silica shell dispersed in 7 mL of ethanol were placed in a round bottom flask. 0.42 mL of aqueous ammonia was diluted in an additional 7 mL of ethanol and added to the particle suspension (3 vol.% NH_4OH). 27 µL of TEOS was then added to the stirring suspension, and the mixture was then stirred for an additional two hours at room temperature. The coated nanoparticles were isolated via centrifugation at 10,000 rpm for 10 minutes. After the removal of the supernatant, the particles were washed by redispersement via sonication in 5 mL of ethanol. The ethanol suspension was then centrifuged again for 10 minutes at 10,000 rpm to recover the nanoparticles.

Synthesis of tri(ethoxy)silylpropyl carbamoyl c(RGDfK). Cyclic(RGDfK) (2.0 mg, 3.313 μmol) was placed in a small round bottom flask and dried under high vacuum for 1 hour. The c(RGDfK) was then dissolved in 0.5 mL of anhydrous DMSO and 0.2 μL of Hünig base. 0.86 μL (3.44 μmol) of (3-isocyanatopropyl)triethoxysilane was then added, and the reaction was stirred under argon for 18 hours. The solution (4 mg c(RGDfK)/mL DMSO) was placed in a freezer for later use.

Synthesis of Rhodamine-APS. 6.8 mg (0.0127 mmol) of rhodamine B isothiocyanate was dissolved in 1.1 mL of ethanol. 3.3 μL (3.1 mg, 0.0141 mmol) of 3-aminopropyltriethoxy silane was then added, and the reaction was stirred at room temperature, under N_2, and in the dark for 24 hours. At the completion of the reaction the solution was diluted to a total volume of 2 mL with additional ethanol to make a solution with a rhodamine-APS concentration of approximately 6 mM.

Synthesis of Rhodamine and c(RGDfK)-functionalized $Mn_3(BTC)_2(H_2O)_6$. An aliquot of a 4 mg/mL c(RGDfK) DMSO solution corresponding to 10 wt% and an aliquot of the 6 mM solution of rhodamine-APS corresponding to 1.5 wt% were added to a dispersion of **5-2'** in 4 % NH_4OH in ethanol (~2 mg/mL). The mixture was stirred at room temperature for 24 hours. The c(RGDfK)-functionalized nanoparticles were then isolated via centrifugation and washed with ethanol.

5.4.3 Dissolution Studies

Dissolution studies of $Mn(BDC)(H_2O)_2$ nanorods. 1.5 mL of a suspension of $Mn(BDC)(H_2O)_2$ nanorods in ethanol (2.55 mg) was placed inside a piece of dialysis tubing (MWCO 3500). The dialysis tubing was submerged in either distilled water or 8 mM

phosphate buffer at 37 °C, with gentle stirring. Aliquots of the solution were then removed at different time points. The water was evaporated and the residue was redissolved in either 1.2 mL of 1 M nitric acid for DCP measurements, or the aliquot was diluted and made into 4 mL of a 2% nitric acid solution for ICP-MS measurements.

Dissolution studies of Mn$_3$(BTC)$_2$(H$_2$O)$_6$ nanoparticles. 7.8 mg of Mn$_3$(BTC)$_2$-(H$_2$O)$_6$ nanoparticles were dispersed in 2 mL of ethanol. The suspension was placed inside a piece of dialysis tubing (MWCO 3500).   The dialysis tubing was submerged in either distilled water or 8 mM phosphate buffer at 37 °C, with gentle stirring. Aliquots of the solution were then removed a different time points. The water was evaporated and the residue was redissolved in either 1.2 mL of 1 M nitric acid for DCP measurements, or the aliquot was diluted and made into 4 mL of a 2% nitric acid solution for ICP-MS measurements.

5.4.4 ICP-MS Characterization

Elemental Analysis of 5-1.   0.61 mg of Mn(BDC)(H$_2$O)$_2$ NMOFs (**5-1**) were digested in 2.865 mL of 15.8 M nitric acid, overnight. The sample was then diluted to a total volume of 50 mL, and 1 mL of this solution was further diluted to a total volume of 10 mL to give a 2% nitric acid solution of ICP-MS analysis.

Elemental Analysis of 5-2.   1.24 mg of Mn$_3$(BTC)$_2$(H$_2$O)$_6$ NMOFs (**5-2**) were digested in 2.865 mL of 15.8 M nitric acid, overnight. The sample was then diluted to a total volume of 50 mL, and 1 mL of this solution was further diluted to a total volume of 10 mL to give a 2% nitric acid solution of ICP-MS analysis.

5.4.5 Imaging Studies

***In vitro* labeling and fluorescence imaging of live cancer cells.** HT-29 cells were grown in 6-well plates on sterile glass cover slips at 37 °C in a 5% CO_2 incubator containing 10% FBS and 1% penicillin/streptomycin. Cells were incubated in 1 mL fresh media with 0.6 mg **5-2'** either with or without RGD targeting ligand for 1 hour at 37 °C in 5% CO_2. Cells were washed three times with 2 mL of PBS (pH 7.4) per well, before the addition of 2 mL of fresh media. Subsequently, 2 µL of DRAQ5 (5 mM) was added and allowed to incubate for 30 minutes before imaging by laser scanning confocal fluorescence microscopy at the UNC Michael Hooker Microscopy Facility. Images were merged and processed using Adobe Photoshop CS2.

Elemental analysis of cancer cells incubated with 5-2'. HT-29 cells were grown in 6-well plates at 37 °C in a 5% CO2 incubator containing 10% FBS and 1% penicillin/ streptomycin. Cells were incubated in 1 mL fresh media and with 0.6 mg **5-2'** either with or without RGD targeting ligand for 1 hour at 37 °C in 5% CO2. Cells were washed three times with 2 mL of PBS (pH 7.4) per well, before the addition of 2 mL of fresh media. Finally, the cells were digested in 2 % nitric acid for ICP-MS elemental analysis.

***In Vitro* MR Image Acquisition.** HT-29 cells were cultured in 25 cm^3 T-flasks with McCoy's 5A media (Cellgro) containing 10% FBS and 1% penicillin/streptomycin (12 mL) at 37°C and 5% CO_2 until approximately 70% confluency (~3.2×10^6 cells per flask) was observed. Cells were then washed with PBS (Aldrich), and incubated in 10 mL media with 1.145 mg RGD-functionalized nanoparticles of **5-2'**, 1.145 mg unfunctionalized nanoparticles of **5-2'**, or negative control (media only). After 30 minutes, the media was removed and cells were washed 3 times with PBS (10 mL) prior to trypsinizing and

centrifugation at 1500 rpm for 5 minutes. Cell pellets were placed into small PCR tubes with 200 µL PBS, then re-centrifuged (1500 rpm, 1 min) before MR imaging.

In vivo T_1**-weighted midbody MR imaging.** An 8-week old female DBA/1J mouse was imaged in a Bruker 9.4 T Small Animal scanner. After pre-contrast image acquisition of the animal midbody, a dose of **5-2'** corresponding to 10 µmol of Mn per kg of body weight was intravenously injected via the tail vein. The animal was imaged at time points of 13 and 65 minutes post-contrast administration.

5.5 References

1. Stark, D. D.; Bradley Jr., W.G. *Magnetic Resonance Imaging*. Mosby: St. Louis, 1999.

2. Merbach, A. E.; Tóth, É.; *The Chemistry of Contrast Agents in Medical Magnetic Resonance Imaging*. John Wiley & Sons: Chichester, 2001.

3. Caravan, P.; Ellison, J. J.; McMurry, T. J.; Lauffer, R. B., Gadolinium(III) chelates as MRI contrast agents: structure, dynamics, and applications. *Chem. Rev.* **1999**, *99* (9), 2293-2352.

4. Morawski, A. M.; Lanza, G. A.; Wickline, S. A., Targeted contrast agents for magnetic resonance imaging and ultrasound. *Curr. Opin. Biotechnol*. **2005**, *16* (1), 89-92.

5. Weissleder, R.; Moore, A.; Mahmood, U.; Bhorade, R.; Benveniste, H.; Chiocca, E. A.; Basilion, J. P., *In vivo* magnetic resonance imaging of transgene expression. *Nat. Med.* **2000**, *6* (3), 351-354.

6. Na, H.B.; Lee, J.H.; An, K.; Park, Y.I; Park, M.; Lee, I.S.; Nam, D.-H.; Kim, S.T.; Kim, S.-H.; Kim, S.-W.; Lim, K.-H.; Kim, K.-S.; Kim, S.-O.; Hyeon, T., Development of a T_1 contrast agent for magnetic resonance imaging using MnO nanoparticles. *Angew. Chem., Int. Ed*. **2007**, *46* (28), 5397-5401.

7. Seo, W.S.; Lee, J.H.; Sun, X.; Suzuki, Y.; Mann, D.; Liu, Z.; Terashima, M.; Yang, P.C.; McConnell, M.V.; Nishimura, D.G.; Dai, H., FeCo/graphitic-shell nanocrystals as advanced magnetic-resonance-imaging and near-infrared agents**.** *Nature Mater*. **2006**, *5* (12), 971-976.

8. Rieter, W.J.; Kim, J.S.; Taylor, K.M.L.; An, H.; Lin, W.; Tarrant, T.; Lin, W., Hybrid silica nanoparticles for multimodal imaging. *Angew. Chem. Int. Ed*. **2007**, *46* (20), 3680-3682.

9. Taylor, K.M.L.; Kim, J.S.; Rieter, W.J.; An, H.; Lin, W.; Lin, W., Mesoporous silica nanospheres as highly efficient MRI contrast agents. *J. Am. Chem. Soc*. **2008**, *130* (7), 2154-2155.

10. Kim, J.S.; Rieter, W.J.; Taylor, K.M.L.; An, H.; Lin, W.; Lin, W., Self-assembled hybrid nanoparticles for cancer-specific multimodal imaging. *J. Am. Chem. Soc*. **2007**, *129* (29), 8962-8963.

11. Raymond, K.N., Pierre, V.C., Next generation, high relaxivity gadolinium MRI agents. *Bioconjugate Chem.*, **2005**, *16* (1), 3-8.

12. Elizondo, G.; Fretz, C.J.; Stark, D.D.; Rocklage, S.M.; Quay, S.C.; Worah, D.; Tsang, Y-M.; Chen, M.C-M.; Ferrucci, J.T., Preclinical evaluation of MnDPDP: new paramagnetic hepatobiliary contrast agent for MR imaging. *Radiology*, **1991**, *178* (1), 73-78.

13. Kaduk, J. A., Terephthalate salts of dipositive cations. *Acta Crystallogr. B*, **2002**, *58* (5), 815-822.

14. Gutschke, S.O.H.; Molinier, M.; Powell, A.K.; Winpenney, R.E.P.; Wood, P.T., Engineering coordination architecture by hydrothermal synthesis; preparation, X-ray crystal structure and magnetic behaviour of the coordination solid [$Mn_3\{C_6H_3(CO_2)_3$-1,3,5$\}_2$]. *Chem. Commun.*, **1996** (7), 823-824.

15. Chen, J.; Ohba, M.; Kitagawa, S., Two new coordination polymers based on hexanuclear metal cluster cores. *Chem. Lett*. **2006**, *35* (5), 526-527.

CHAPTER 6

Iron-Based Nanoscale Metal Organic Frameworks for Drug Delivery and Imaging

6.1 Introduction

As discussed in the previous two chapters, metal-organic frameworks (MOFs) are a class of hybrid materials that have infinite tunability resulting from the large number of metals and the limitless number of organic bridging ligands that can be used. MOFs can also be designed to exhibit unprecedentedly high porosity. There have been several reports on M(III) containing MOFs that have extremely high surface areas and large pores.[1-7] Three of these MOFs, known as MIL-53, MIL-88B, and MIL-101, are built using the same organic bridging ligand, terephthalic acid (BDC), connected by M(III) ions, where M = Cr(III), Fe(III), or Al(III).

MIL-53 has the formula $M^{III}(OH) \cdot [O_2C-C_6H_4-CO_2] \cdot H_2O$ (M^{III} = Cr, Fe).[5] The pore size of this MOF changes depending on the treatment of the material. As synthesized the pores contain free BDC molecules. These guest molecules can be removed upon calcination to give the high temperature structure. At room temperature, the MOF adsorbs atmospheric water to give the so-called low temperature structure which contains water molecules as guests. The surface area and pore sizes of these materials change depending on the guest present in the framework. The as-synthesized material shows no capacity for N_2 adsorption, while both the high temperature and low temperature materials do. The high temperature materials have Langmuir surface areas of greater than 1500 m^2/g, and the hydrated low

temperature materials have Langmuir surface areas of 1150 m²/g.[5] Figure 6.1 shows the so-called breathing effect of the material.[4]
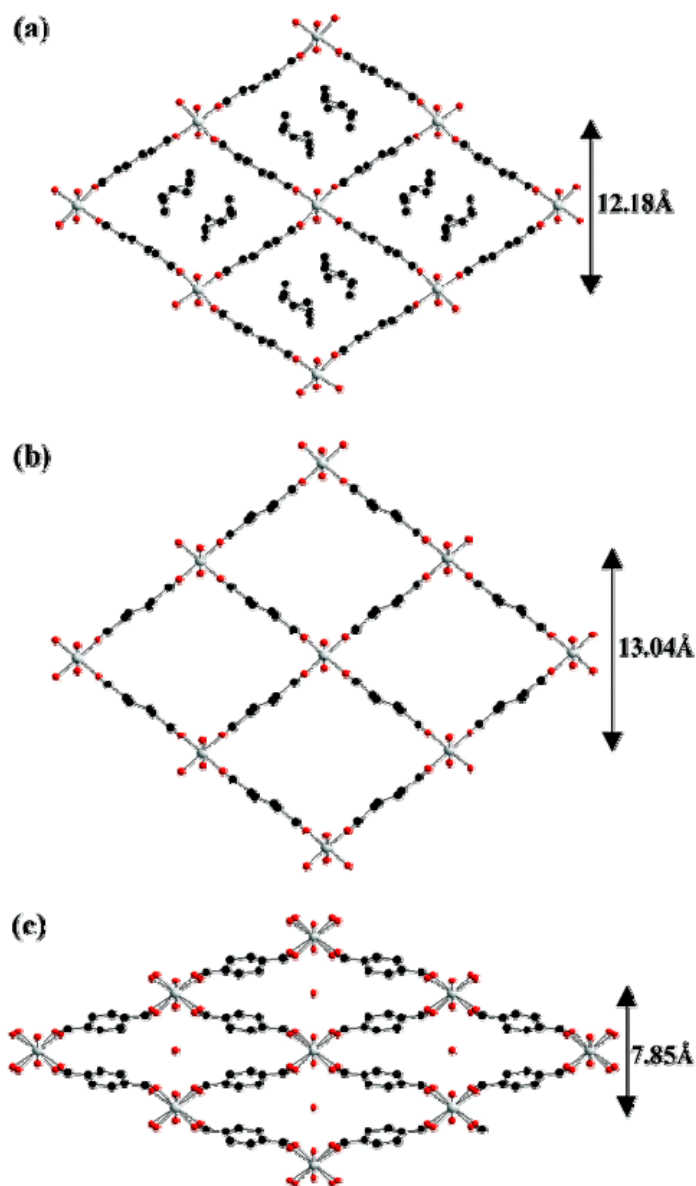
Figure 6.1. View of the pore systems of (a) MIL-53as, (b) MIL-53ht, and (c) MIL-53lt.

MIL-88B and MIL-101 are also built from M(III) and BDC, but have different structures from MIL-53. MIL-88B has the formula $[M_3^{III}O(H_2O)_2X(BDC)_3]$·guest (M = Fe, Cr; X = F, Cl, acetate)[7], and MIL-101 has the formula $Cr_3F(H_2O)_2O(BDC)_3 \cdot nH_2O$ (where n

is ~25).[1] To date, the MIL-101 structure has only been reported using Cr^{III}. The MIL-101 material has one of the highest surface areas reported for a MOF, with a Langmuir surface area that ranges for 4500 to 5500 m^2/g for the as-synthesized material or 5900 m^2/g for the activated material.[1] MIL-101 contains two types of mesoporous cages within the framework, which have internal free diameters of ~29 Å and 34 Å. These values correspond to accessible pore volumes of ~12,700 $Å^3$ and ~20,600 $Å^3$, respectively.[1]

Férey and co-workers have shown that they can use the large pores in these MOFs for loading of organic drug molecules. They have shown that MIL-101 can adsorb 138 wt% ibuprofen, and MIL-53 can adsorb 20 wt%.[8-9] The release of ibuprofen from the MOFs was evaluated using simulated body fluid at 37 °C. It was found that the MIL-101 MOFs release ibuprofen slowly in several stages, reaching completion only after 6 days.[8] The MIL-53 material showed an even slower release, reaching completion only after 3 weeks.[9]

In order for these materials to be useful as *in vivo* drug delivery vehicles, the particle size must be carefully controlled. As previously discussed, we have been able to synthesize nanoscale metal-organic frameworks (NMOFs) using several different methods, including reverse phase microemulsions, and high temperature surfactant assisted syntheses. In order to synthesize these Fe(III) NMOFs we utilized a surfactant free, solvothermal method, with microwave heating.

A recent report showed that the BDC could be replaced with 2-aminoterephthalic acid in forming the three MOFs discussed above (MIL-53, MIL-88B, and MIL-101).[10] The incorporation of an amine group in the framework of the materials allows for the possibility of post-synthetic modifications; other molecules can be covalently attached to the framework by reacting with these amine groups.

Several groups have recently demonstrated post-synthetic modification using MOFs. The first report came from Stephen Lee and coworkers in 1999. In this report they showed that they could react an alcohol functional group present in the channel of a MOF with trifluoroacetic anhydride to form the ester.[11] In 2000, Kim and coworkers demonstrated the *N*-alkylation of pyridyl groups present in a homo-chiral MOF without changing the framework structure.[12] In 2005, our group demonstrated the post-synthetic modification of a MOF resulting in an active heterogeneous catalyst. In this case, $Ti(O^iPr)_4$ was reacted with the dihydroxy groups of a BINOL ligand present in the MOF to form the active catalyst.[13] In 2007, a report by Wang and Cohen, showed the post-synthetic modification of IRMOF-3, which is a MOF synthesized from $Zn(NO_3)_2$ and 2-aminoterephalic acid.[14] They showed that they were able to react acetic anhydride with the amine groups present in the framework. Using ^1H NMR integration, the percent conversion (acetylation) of IRMOF-3 was estimated to be greater than 80% after 5 days.[14]

We have synthesized a series of Fe(III) NMOFs with either the MIL-101 or MIL-88B structure using terephthalic acid and 2-aminoterephthalic acid in varying ratios. We have also been able to further functionalize these materials with imaging agents and anti-cancer drugs, using post-synthetic modification.

6.2 Results and Discussion

6.2.1 Fe(III) NMOF Synthesis

Fe(III) NMOF particles were synthesized using a high temperature, surfactant free method, with microwave heating. Terephthalic acid (BDC) was used as the bridging ligand, and dimethylformamide (DMF) was used as the solvent. The particles were formed by

simply heating a solution of FeCl$_3$ and terephthalic acid (1:1 ratio) in DMF to 150 °C using an 800 Watt microwave, and holding at this temperature for 10 minutes. The particles were then isolated by centrifuging and were washed with DMF and ethanol to remove any unreacted starting materials. Similar Fe(III) NMOFs could also be synthesized by replacing all or a percentage of the terephthalic acid with 2-aminoterephthalic acid (Table 6.1). Incorporation of the amino group allows for post-synthetic modification of the NMOFs.

Table 6.1. Composition and phase of Fe(III) NMOFs.

Compound	Mol% NH$_2$BDC	Mol% NH$_2$BDC by NMR	Phase
6-1	0	-	MIL-101
6-2	5	6.6	MIL-101
6-3	10	16	MIL-101
6-4	12.5	-	MIL-101
6-5	15	-	MIL-101
6-6	17.5	17.4	MIL-101
6-7	20	25	MIL-88B
6-8	50	-	MIL-88B
6-9	100	-	MIL-88B

6.2.2 Characterization

The particles were characterized using a variety of methods. The particle size and morphology was first determined using scanning electron microscopy (SEM). The particles were found to have similar size and morphology regardless of the percentage of incorporation of 2-aminoterephthalic acid. The particles had an unusual octahedron morphology and an average diameter of about 200 nm (Fig. 6.2-6.10). Some reactions also resulted in the formation of micron sized particles, which could be easily separated from the desired particles by centrifuging at low speeds (3000 rpm).
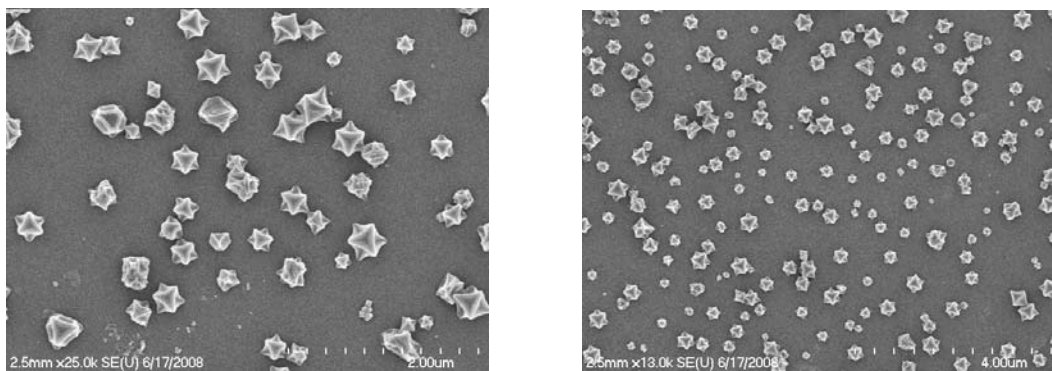
Figure 6.2. SEM images of Fe$_3$O(DMF)$_3$Cl(BDC)$_3$ nanoparticles (**6-1**).
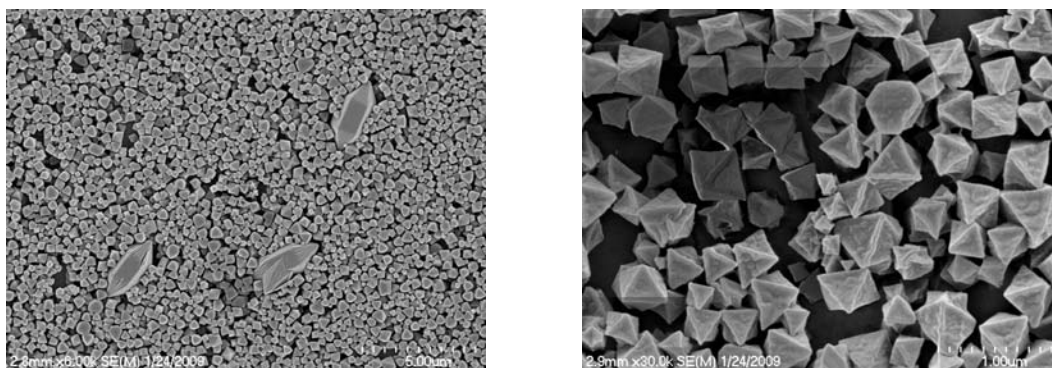
Figure 6.3. SEM images of Fe$_3$O(DMF)$_3$Cl(BDC)$_3$ nanoparticles synthesized with 5 mol% NH$_2$-BDC (**6-2**).
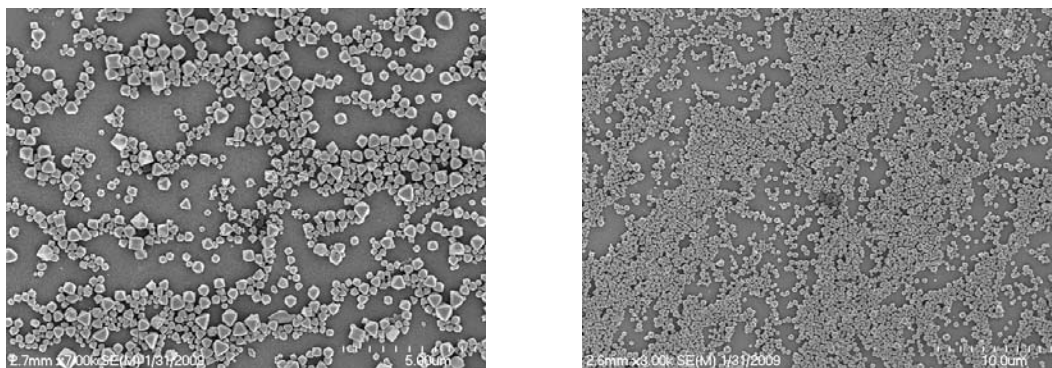
Figure 6.4. SEM images of Fe$_3$O(DMF)$_3$Cl(BDC)$_3$ nanoparticles synthesized with 10 mol% NH$_2$-BDC (**6-3**).
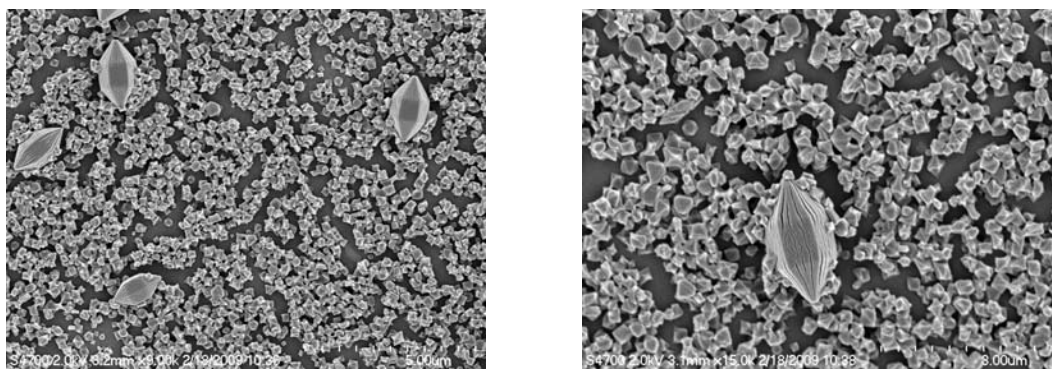
Figure 6.5. SEM images of $Fe_3O(DMF)_3Cl(BDC)_3$ nanoparticles synthesized with 12.5 mol% NH_2-BDC (**6-4**).
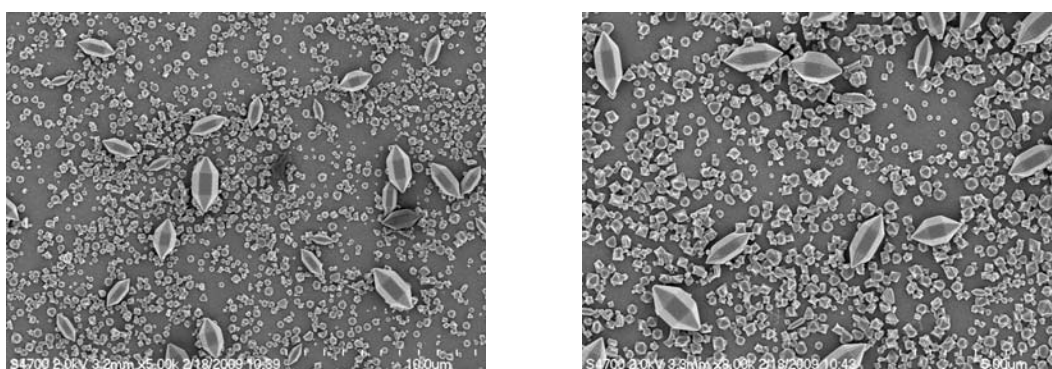
Figure 6.6. SEM images of $Fe_3O(DMF)_3Cl(BDC)_3$ nanoparticles synthesized with 15 mol% NH_2-BDC (**6-5**).
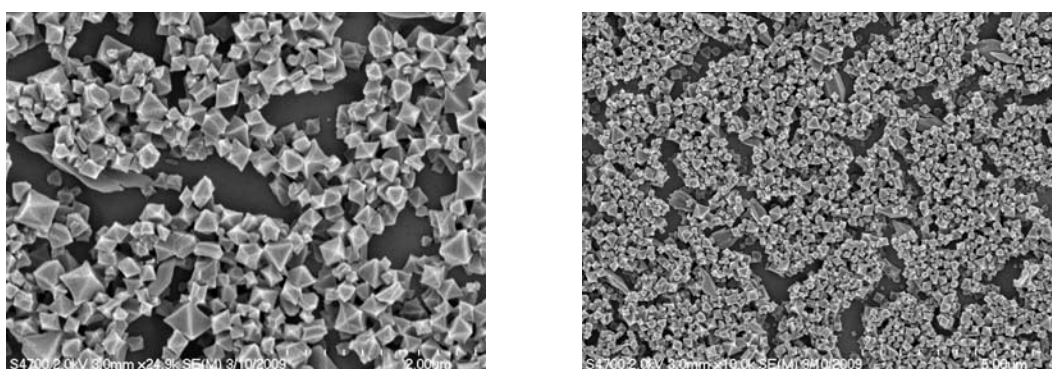
Figure 6.7. SEM images of $Fe_3O(DMF)_3Cl(BDC)_3$ nanoparticles synthesized with 17.5 mol% NH_2-BDC (**6-6**).
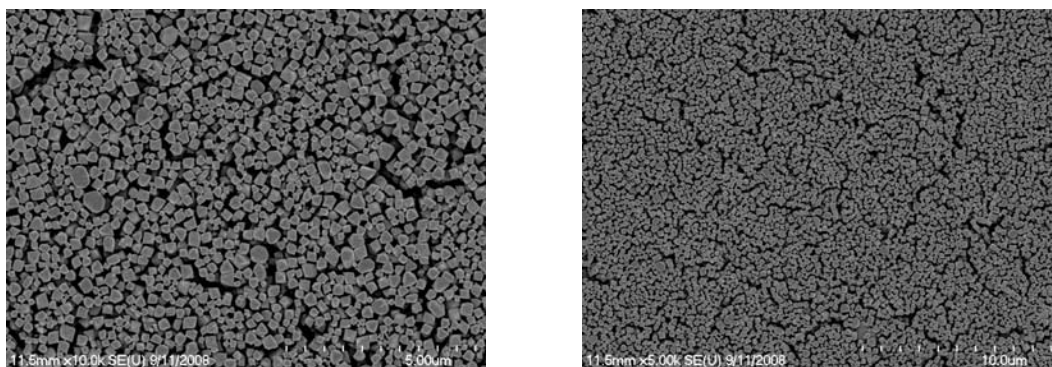
Figure 6.8. SEM images of $Fe_3O(DMF)_3Cl(BDC)_3$ nanoparticles synthesized with 20 mol% NH_2-BDC (**6-7**).
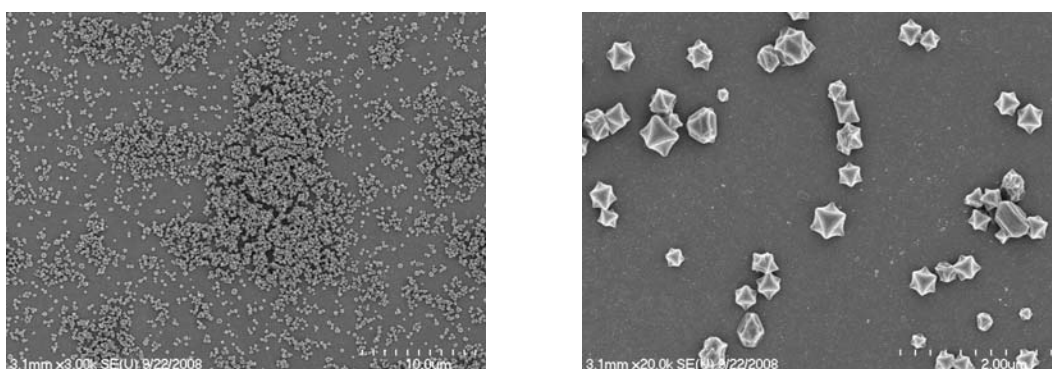
Figure 6.9. SEM images of $Fe_3O(DMF)_3Cl(BDC)_3$ nanoparticles synthesized with 50 mol% NH_2-BDC (**6-8**).
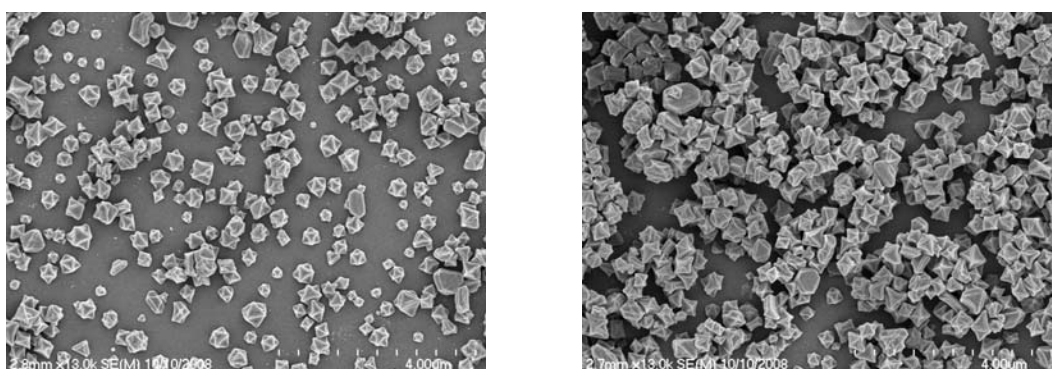
Figure 6.10. SEM images of $Fe_3O(DMF)_3Cl(BDC)_3$ nanoparticles synthesized with 100 mol% NH_2-BDC (**6-9**).

Powder X-ray diffraction (PXRD) was used to determine the crystallinity and phase of the NMOFs obtained. Comparisons to the simulated powder pattern for the known $Cr_3F(H_2O)_2O[(O_2C)-C_6H_4-(CO_2)]_3 \cdot nH_2O$ MOF (MIL-101), showed that the NMOFs

182

synthesized with 100% terephthalic acid (**6-1**) are the same phase (Fig. 6.11).[1] The Fe(III)

analog of the Cr(III) MIL-101 MOF has not been previously reported. When the terephthalic

acid was replaced with 2-aminoterephthalic acid, PXRD experiments showed that these

particles were not the same phase. It was found that the powder pattern for these particles

matched the simulated powder pattern for the $[Fe_3O(H_2O)_2X(1,4-BDC)_3]\cdot$guest (X=F, Cl,

acetate) MOF known as MIL-88B (Fig. 6.12).[7] For NMOFs **6-2** through **6-8** PXRD

diffraction studies revealed that the phase obtained was dependent on the amount of 2-

aminoterephthalic acid incorporated. NMOFs **6-2** through **6-6** (5 through 17.5% aminoBDC)

were the MIL-101 phase, and particles with higher incorporation of 2-aminoterephthalic acid

(**6-7** and **6-8**, 20 and 50%) were the MIL-88B phase (Fig. 6.13-6.14).
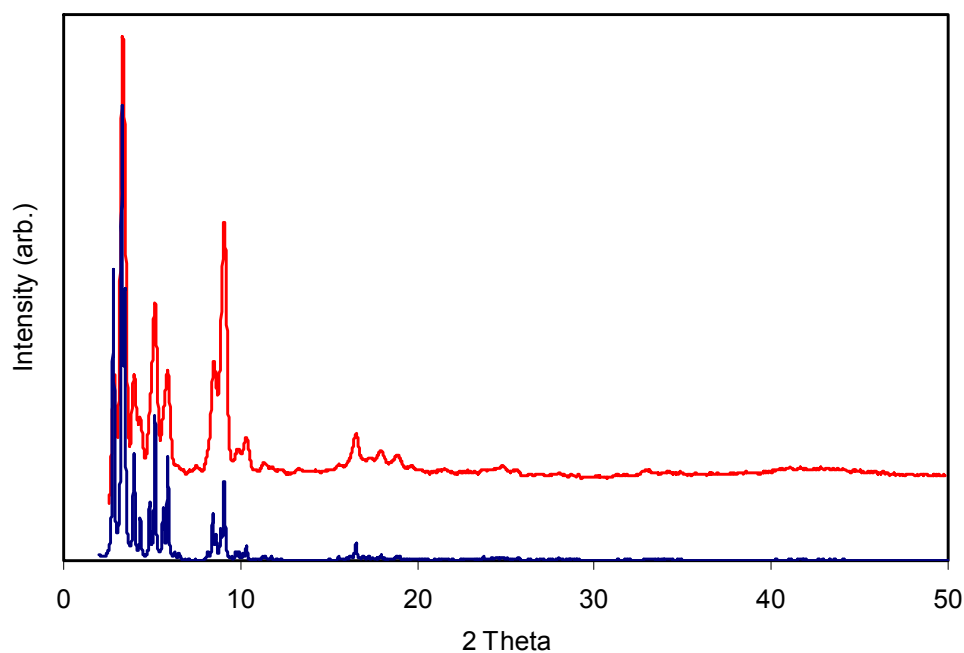
Figure 6.11. PXRD pattern of NMOFs **6-1** (red) compared to the simulated pattern for MIL-101 (blue).
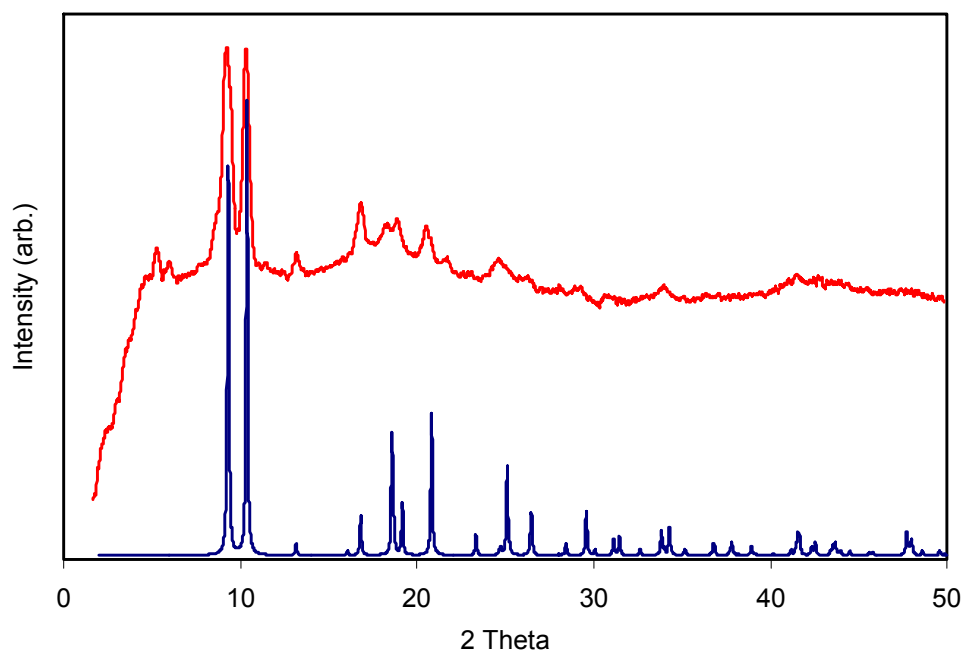
Figure 6.12. PXRD pattern of NMOFs **6-9** (red) compared to the simulated pattern for MIL-88B (blue).
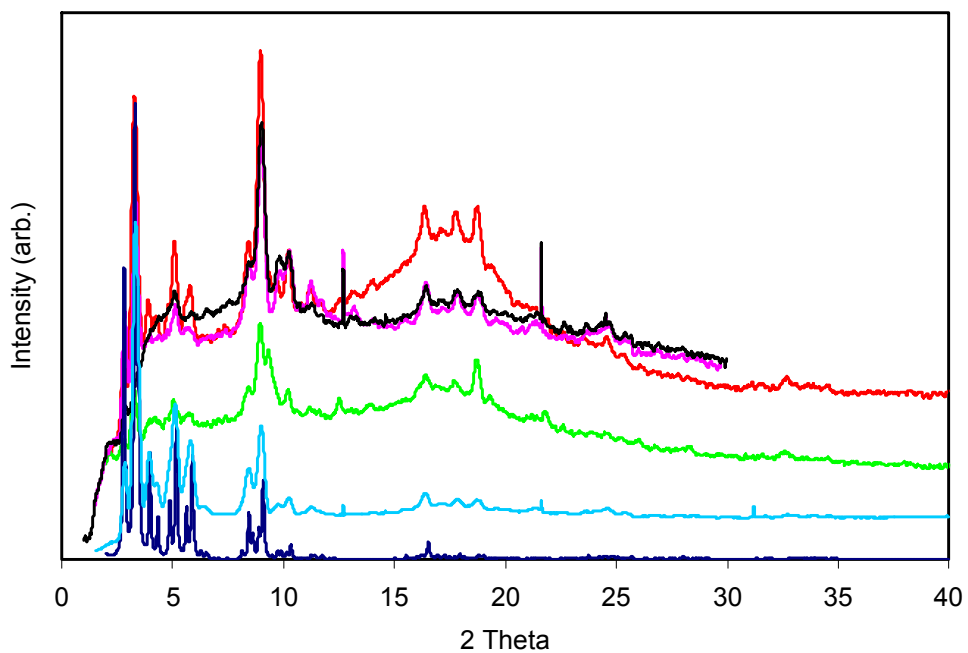
Figure 6.13. PXRD pattern of NMOFs **6-2** (red), **6-3** (green), **6-4** (pink), **6-5** (black), and **6-6** (light blue) compared to the simulated pattern for MIL-101 (dark blue).
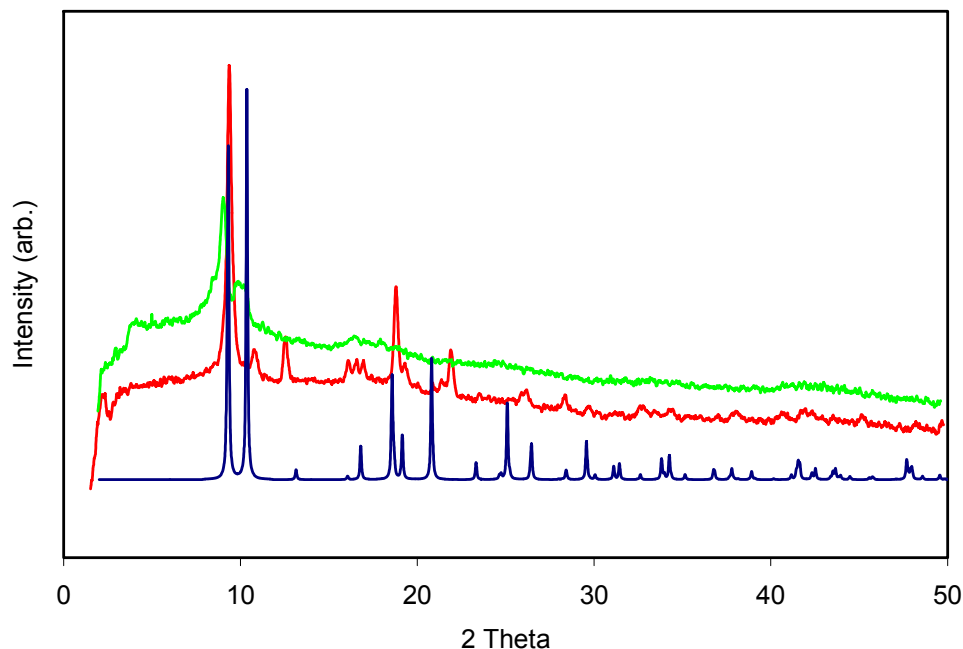
Figure 6.14. PXRD pattern of NMOFs **6-7** (red) and **6-8** (green) compared to the simulated pattern for MIL-88B (blue).

Since these particle synthesis reactions always gave low yields (~20%), the actual amount of incorporated 2-aminoterephthalic acid was determined by NMR. The particles were first digested using silica-supported triaminetetraacetate sodium salt. After the digestion was complete, the silica was removed by centrifuging and the supernatant was dried. A methylation reaction was then performed by redissolving the residue obtained from drying the supernatant in methanol and adding a catalytic amount of concentrated sulfuric acid. The reaction was then heated to reflux overnight. The product was then extracted with ethyl acetate. NMR was then used to determine the ratio between the methyl esters of terephthalic acid and 2-aminoterephthalic acid. In most cases the incorporation of 2-aminoterephthalic acid was slightly higher than the ratio added (Table 6.1).

The surface area of the NMOFs was evaluated using nitrogen sorption measurements. Uptake measurements on **6-1** indicated that the particles have Langmuir surface areas of ranging from approximately 3700 m^2/g to 4535 m^2/g and an average pore diameter ranging

185

from approximately 4.3 to 6.2 Å using the HK (Horvath-Kawazoe) method (Fig. 6.15-6.16). This surface area is lower than what was reported for the Cr(III) MIL-101 MOFs (4500-5900 m^2/g).[1] The NMOFs synthesized with 100% 2-aminoterephthalic acid were also characterized using nitrogen uptake measurements. These NMOFs were found to have an average Langmuir surface area of 2550 m^2/g and an average HK pore diameter of 5.9 Å (Fig. 6.17-6.18).
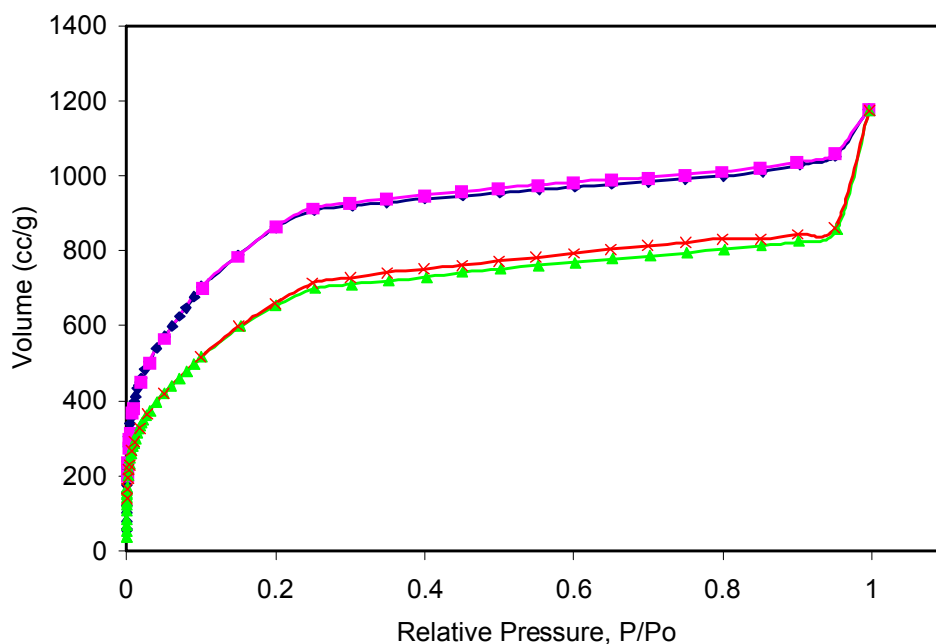
Figure 6.15. Nitrogen sorption isotherm of NMOFs **6-1** synthesized using oven (blue-adsorption, pink-desorption) and microwave heating (green-adsorption, red-desorption).
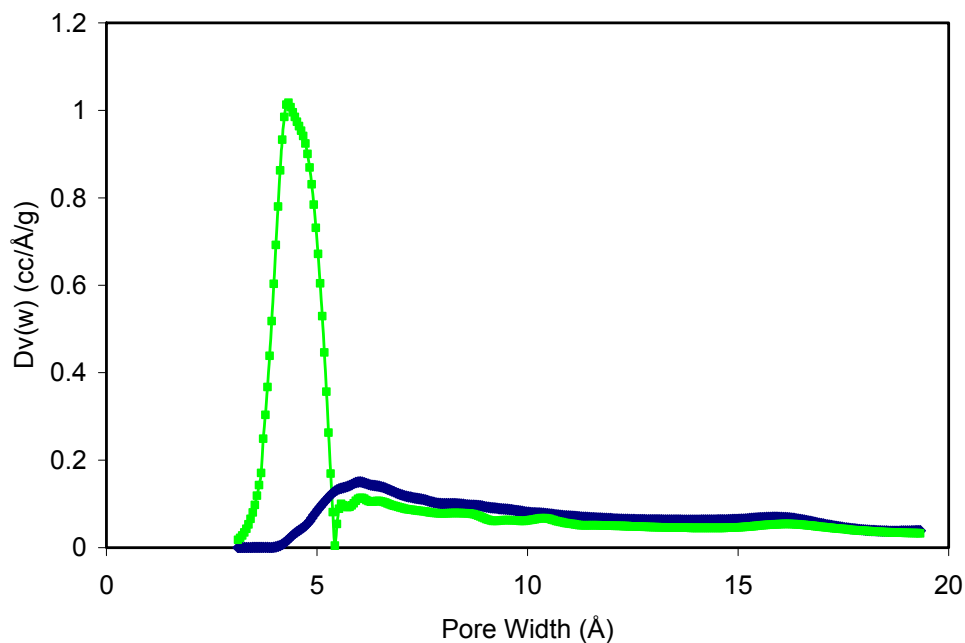
Figure 6.16. Pore size distribution (HK method) for NMOFs **6-1** synthesized using oven heating (blue) or microwave heating (green).
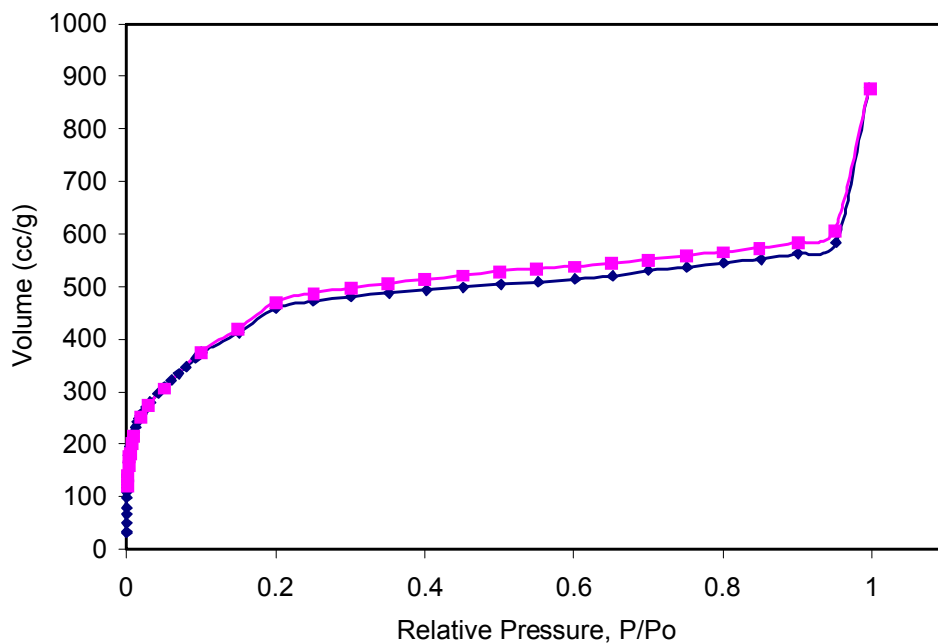
Figure 6.17. Nitrogen sorption isotherm of NMOFs **6-9** (blue-adsorption, pink-desorption).
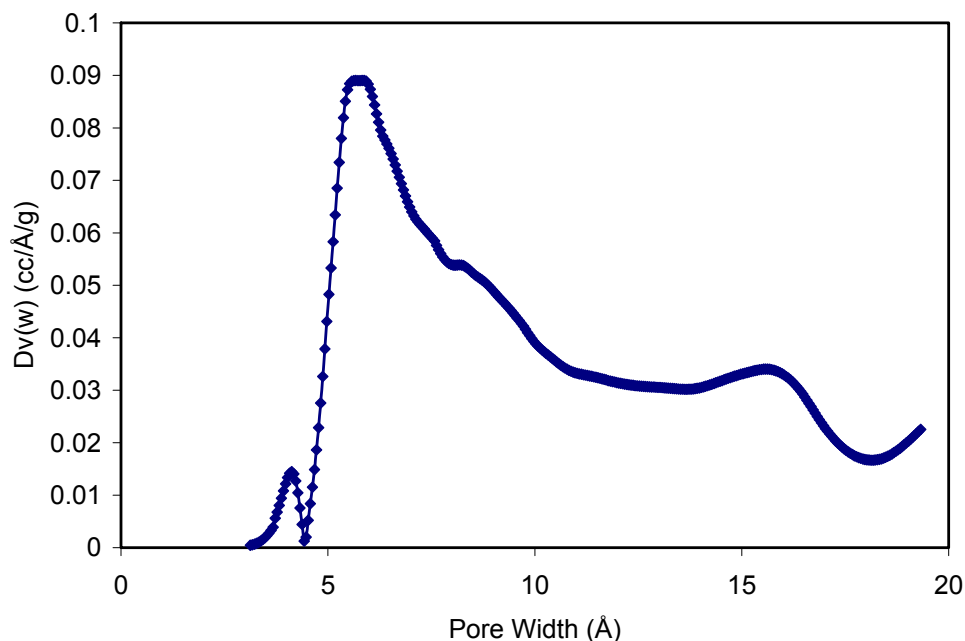
Figure 6.18. Pore size distribution (HK Method) for NMOFs **6-9**.

6.2.3 Post-Synthetic Modification

Using the primary amine groups in the structure of the framework different molecules can be covalently attached through post-synthetic modification. This allows for the use of the NMOFs as delivery vehicles for various cargoes, by attaching the cargo to the framework. We have demonstrated this idea for the use of delivering imaging agents and anti-cancer drugs using the amine functionalized NMOFs. We have been able to attach several optical contrast agents, as well as a Gd^{3+} complex for potential MR imaging. We have also been able to attach a Pt(IV) complex, which can be reduced *in vivo* to form the anti-cancer drug cisplatin.

Initial attempts at post synthetic modification were performed using **6-9**. The organic fluorophore, fluorescein, was covalently attached by reacting fluorescein isothiocyanate (FITC) with **6-9**, in ethanol. Once the reaction was complete the particles were isolated by

centrifuging, and were extensively washed with ethanol to remove any unbound fluorescein. The fluorescence from the bound fluorescein is quenched by the framework, so in order to determine the loading the particles were digested using ethylenediaminetetraacetate (EDTA). 2-aminoterephthalic acid was also reacted with FITC to form the molecular complex. This compound was then used to construct a calibration curve. The emission intensity of the particle digestion solution was then used to calculate the amount of fluorescein that had been grafted. The fluorescein loading was found to range from approximately 3 to 5.3 wt%.

Rhodamine B was also grafted onto **6-9**. Two different approaches were used to couple the carboxylate group from rhodamine B to the primary amine in the framework. The first approach involved reaction rhodamine B with thionyl chloride to form the acyl chloride. This was then reacted with dried **6-9** in DMF. The particles were isolated by centrifuging and extensively washed to remove any free dye. The particles were then digested using EDTA and the emission intensity was measured. Again the molecular complex was made by reacting rhodamine B with 2-aminoterephthalic acid, and this compound was used to construct a calibration curve. Using this method a loading of only 0.2 wt% was obtained. In order to increase the loading an alternate coupling method was employed. In this case rhodamine B was first reacted with 1,1-carbonyldiimidazole (CDI) to activate the carboxylate group. The rhodamine B imidazole was then reacted with **6-9** in DMF. The particles were then isolated by centrifuging, and were extensively washed to remove any free rhodamine B. Again the particles were digested and the concentration of rhodamine B was determined by measuring the emission intensity. Using this coupling method, a slightly higher loading of 1.85 wt% was obtained.

The third and final dye that was loaded into the NMOFs by post-synthetic modification was a derivative of boron-dipyrromethene (BODIPY) or 4,4-difluoro-4-bora-3a,4a-diaza-s-indacene. The 8-position was modified to contain a CH_2-Br group, which could then react with the primary amine in the framework. This dye has several advantages over the other two, including higher photostability and hydrophobicity. It is much easier to remove any unreacted BODIPY dye from the NMOFs by washing with organic solvents. This dye was grafted onto **6-3** and **6-6** by simply combining the particles with a solution of the Br-BODIPY in tetrahydrofuran (THF) and stirring at room temperature for 2 days. The particles were then isolated by centrifuging, and any unreacted dye was removed by washing with THF. Again the loading was determined by digesting the particles with EDTA. In this case the absorbance was used to quantify the amount of BDC-NH-BODIPY in the digested sample, and a calibration curve was constructed using the molecular BDC-NH-BODIPY compound that was synthesized independently. The loadings for this dye ranged from approximately 5.6 wt% to 11.6 wt%.

In an attempt to formulate a new nanoparticle based contrast agent for MRI, a Gd chelate was also grafted onto the amine containing NMOFs. This was done by first reacting DPTA dianhydride with particles **6-9**. The anhydride can then react with the primary amines in the framework to form an amide bond. Once the DTPA had been grafted, Gd^{3+} ions were loaded into the DTPA chelating ligand by adding a solution of $GdCl_3$ to a suspension of the DTPA functionalized NMOFs in water, and adjusting the pH to approximately 7. After loading of the Gd, the particles were extensively washed, and were dialyzed against distilled water to remove any free Gd^{3+} ions.

The Gd loaded particles were characterized using several methods including SEM, thermogravimetric analysis (TGA), PXRD, and inductively coupled–mass spectroscopy (ICP-MS). SEM images showed no change in the particles after DTPA functionalization or Gd loading (Fig. 6.19). TGA showed an increase in organic weight loss of approximately 2.6 wt% for the DPTA functionalized NMOFs, and in increase in weight remaining of approximately 6.6 wt% for the Gd loaded particles, consistent with the increase in inorganic component (Fig. 6.20). Powder X-ray diffraction confirmed that there was no change in the phase after the grafting of the Gd complex (Fig. 6.21). ICP-MS was used to determine the Gd loading by comparing the ratio of Fe to Gd in a digested sample of functionalized particles. The Fe/Gd ratio was found to range from approximately 4.1 to 6.0.
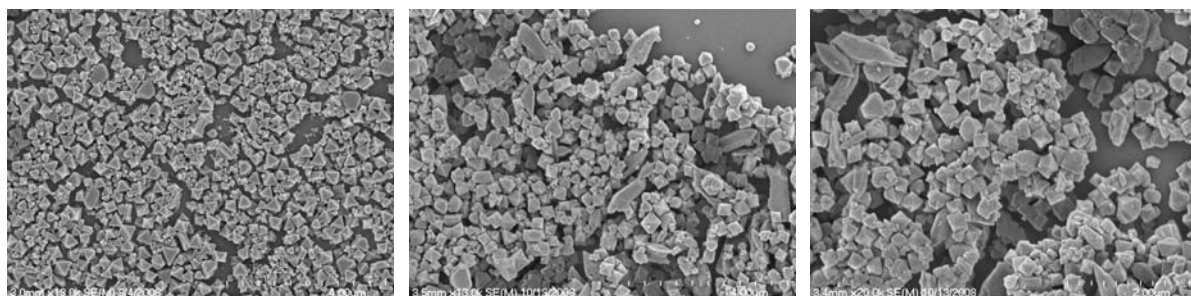
Figure 6.19. SEM images of NMOFs **6-9** as synthesized (left), after functionalization with DTPA (center), and after Gd loading (right).
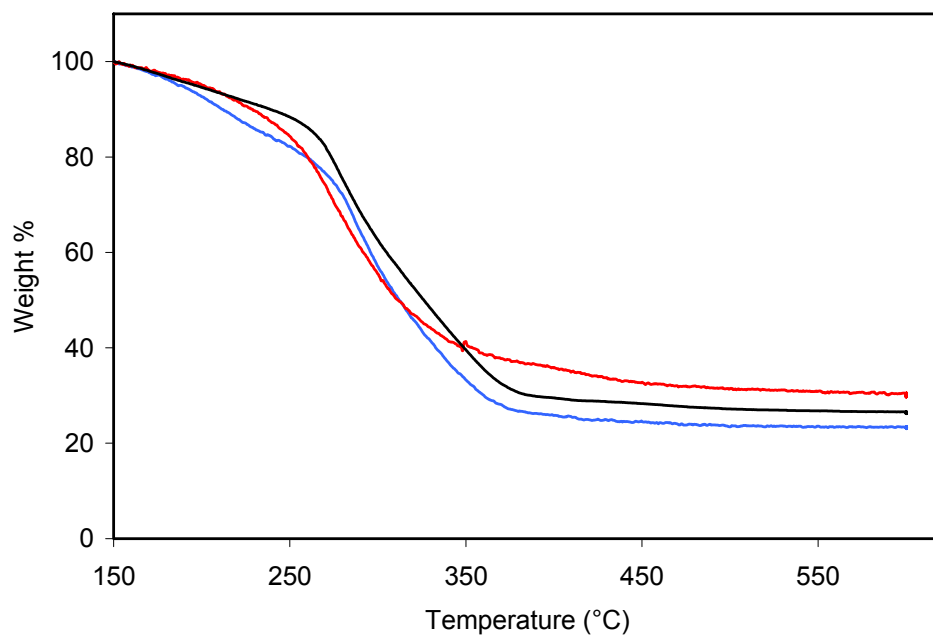
Figure 6.20. TGA of NMOFs **6-9** as synthesized (black), after functionalization with DTPA (blue), and after Gd loading (red).
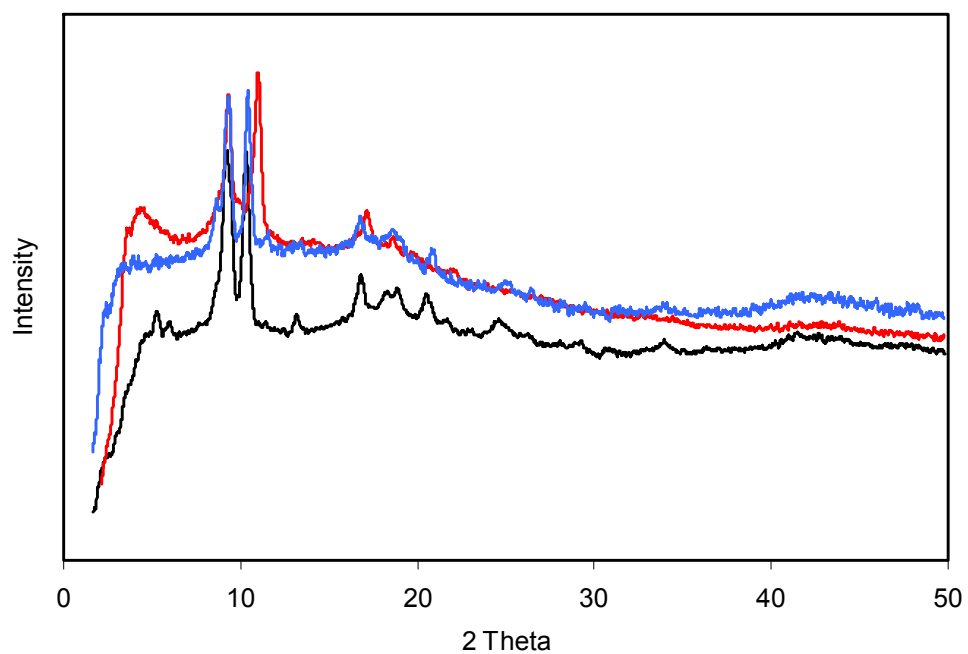
Figure 6.21. PXRD of **6-9** as synthesized (black), after functionalization with DTPA (blue), and after loading with Gd (red).

The final post-synthetic modification attempted involved the grafting of a Pt(IV) complex. This complex can be reduced to the Pt(II) anti-cancer drug cisplatin *in vivo*. Two different approaches were tested to determine the most efficient grafting method. The initial method consisted of reacting succinic anhydride with the primary amine groups of the frameworks **6-7** to **6-9**. The acyl chloride was then formed by adding thionyl chloride to a suspension of the carboxylic acid functionalized NMOFs in dry dichloromethane. After the reaction was complete the solvent and excess thionyl chloride were removed under vacuum. The resulting acyl chloride was then reacted with *c,c,t*-[Pt(IV)Cl$_2$(NH$_3$)$_2$(OH)(OEt)] in anhydrous DMF. The particles were again isolated by centrifuging, extensively washed, and then dialyzed against distilled water to remove any free Pt complexes.

The Pt loaded particles were characterized using SEM, TGA, PXRD, and ICP-MS. The SEM images indicated some degradation of the particles after functionalizing with succinic acid (Fig. 6.22). This could be a result of the succinic acid competing for coordination of the iron. TGA analysis shows an increase of 6.94 wt% remaining after grafting of the Pt complex onto the succinic acid functionalized NMOFs, consistent with the increase in inorganic component (Fig. 6.23). PXRD showed interesting results. For **6-7** (20% aminoBDC) there was no change in the phase after grafting of the Pt complex, the material remained the MIL-88B phase (Fig. 6.24). For NMOFs **6-8** and **6-9**, the material appeared to transform from the MIL-88B phase to the MIL-101 phase after grafting of the Pt complex (Fig. 6.25-6.26). The Pt loading by ICP-MS varied greatly from batch to batch. Initial loadings gave Fe/Pt ratios as high as 2.5, however these results proved to be irreproducible and much lower loadings were consistently obtained for subsequent batches.
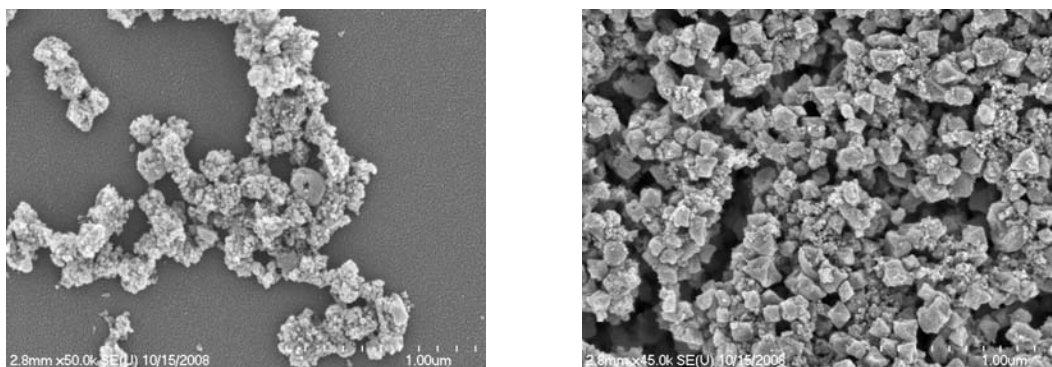
Figure 6.22. SEM images of NMOFs **6-9** after functionalization with succinic acid (left) and after Pt loading (right).
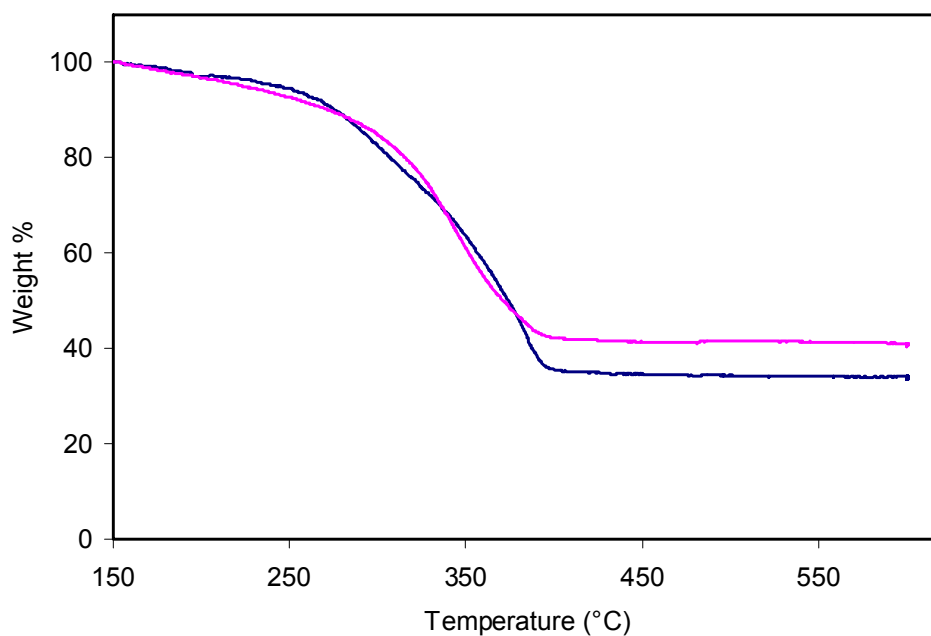
Figure 6.23. TGA of NMOFs **6-7** after functionalization with succinic acid (blue) and after loading with Pt (pink).
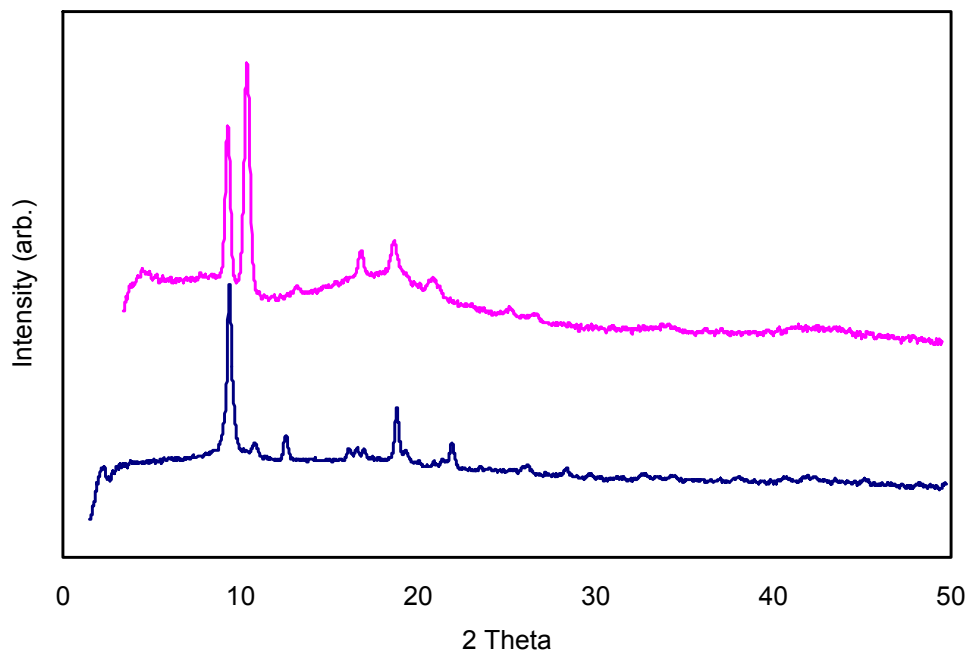
Figure 6.24. PXRD pattern of NMOFs **6-7** as synthesized (blue) and after Pt loading (pink) compared to the simulated pattern for MIL-88B (black).
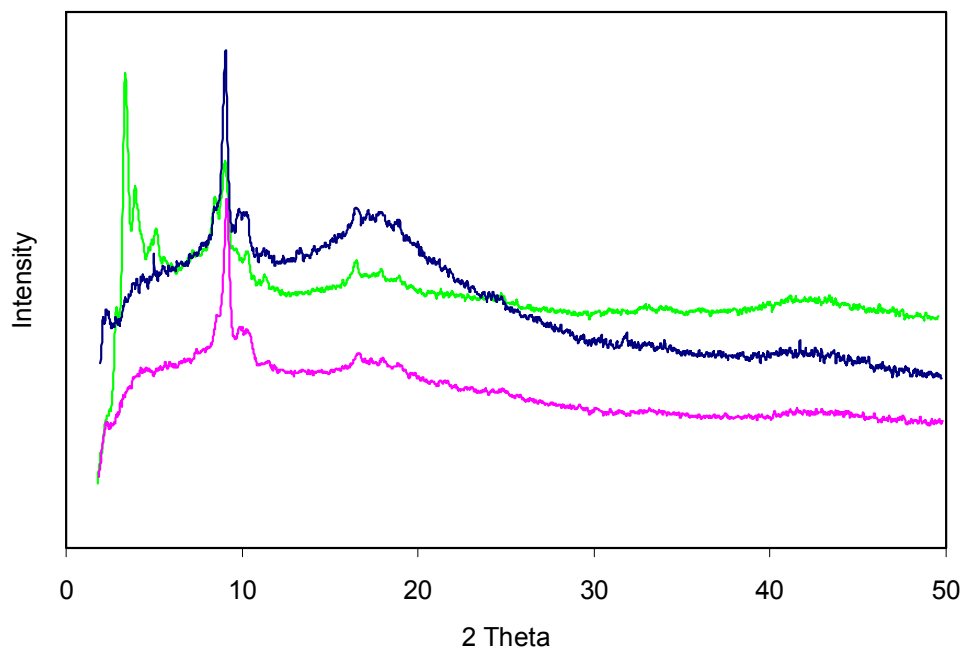
Figure 6.25. PXRD of NMOFs **6-8** as synthesized (blue), succinic acid functionalized (pink), and Pt loaded (green).
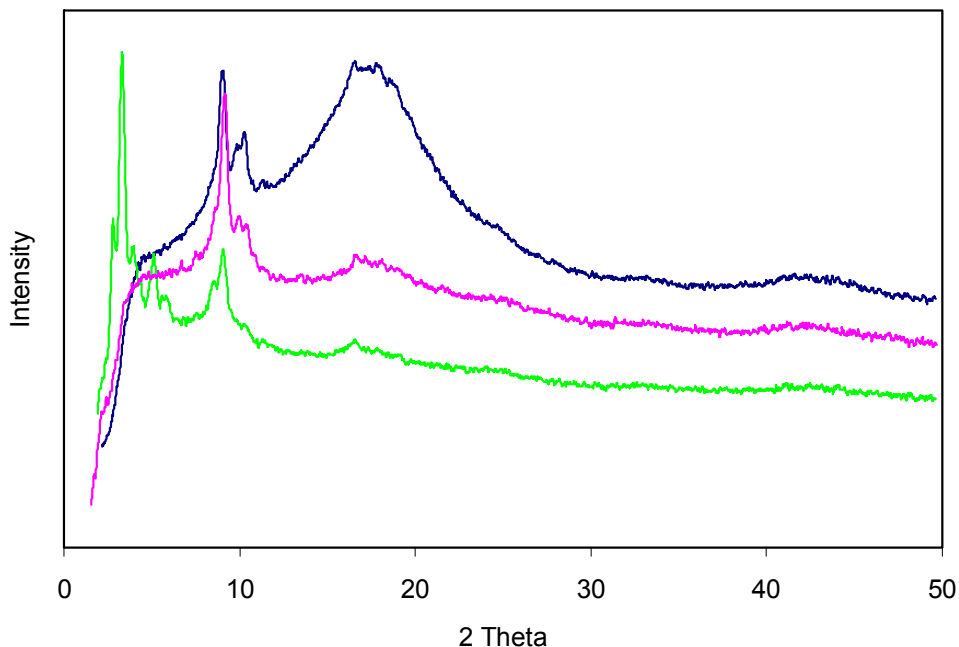
Figure 6.26. PXRD of NMOFs **6-9** as synthesized (blue), succinic acid functionalized (pink), and Pt loaded (green).

Based on the fact that the SEM showed degradation of the particles, and sufficient loadings were irreproducible an alternate method for Pt complex grafting was developed. In addition, based on the fact that the MIL-101 phase has larger pores compared to the MIL-88B phase, NMOFs **6-3** and **6-6** were used to maximize the Pt loading. This method of Pt complex grafting consisted of first forming the c,c,t-[Pt(IV)Cl$_2$(NH$_3$)$_2$(OEt)-(O$_2$CCH$_2$CH$_2$CO$_2$H)] complex. CDI coupling was then performed using by reacting 1,1-carbonydiimidazole with c,c,t-[Pt(IV)Cl$_2$(NH$_3$)$_2$(OEt)(O$_2$CCH$_2$CH$_2$CO$_2$H)]. The dried NMOFs **6-3** or **6-6** were then added to the DMF solution of the complex, and the reaction was stirred at room temperature. The particles were then isolated by centrifuging, and were washed several times with DMF.

The particles were again characterized using SEM, PXRD, and ICP-MS. SEM imaging showed no change in the particle size or morphology after Pt loading using this

method (Fig. 6.27-6.28). PXRD showed that the Pt loaded particles retained the MIL-101 structure (Fig. 6.29-6.30). The ICP-MS results showed that the Fe/Pt ratio for **6-3** was 4.8. The theoretical maximum for the Pt loading if all of the amine groups react would give a Fe/Pt ratio of 1.79, so a Fe/Pt ratio of 4.8 represents a 37.3% conversion. For **6-6**, ICP-MS results revealed an Fe/Pt ratio of 4.1, which represents a 40.2% conversion.
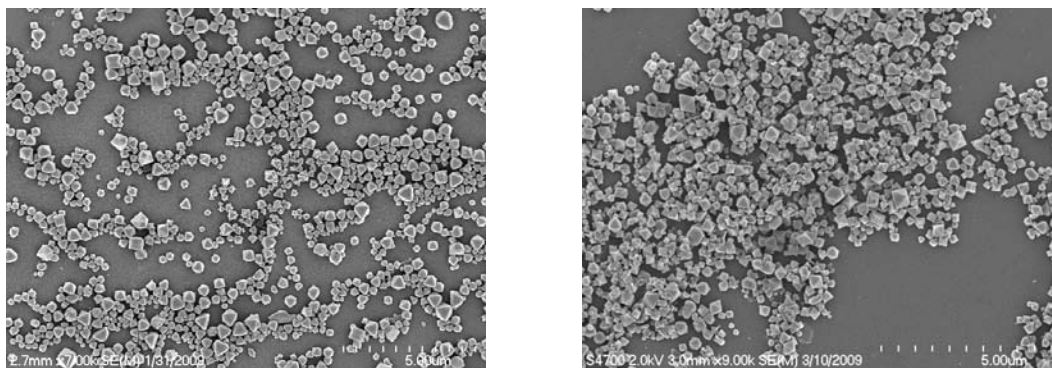
Figure 6.27. SEM images of NMOFs **6-3** as synthesized (left) and after Pt loading using CDI coupling method (right).
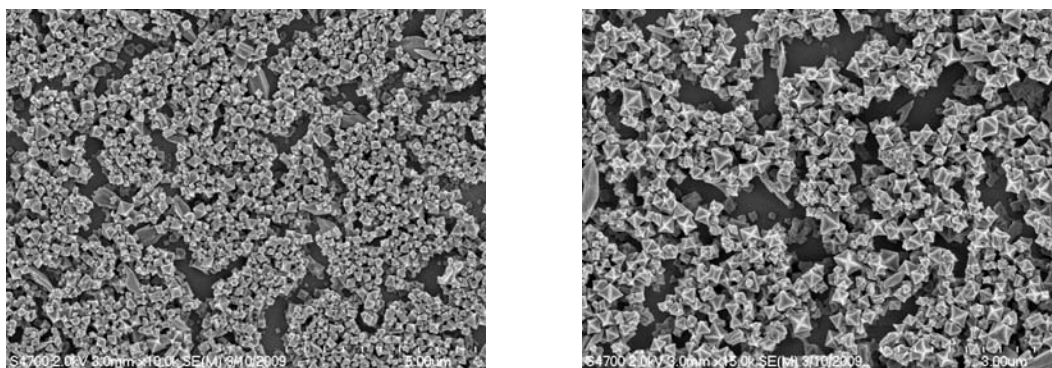
Figure 6.28. SEM images of NMOFs **6-6** as synthesized (left) and after Pt loading using CDI coupling method (right).
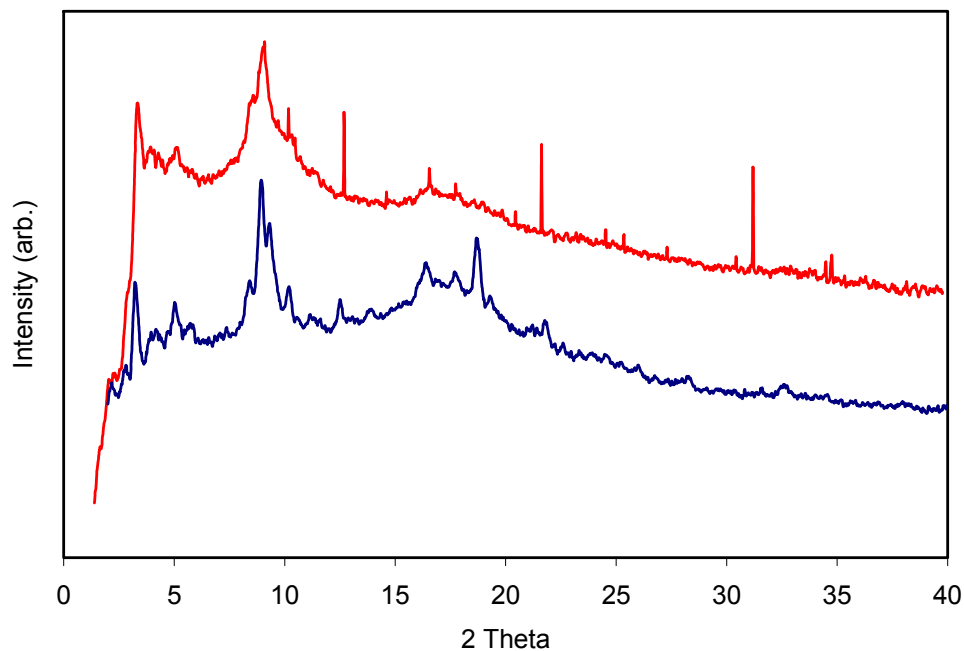
Figure 6.29. PXRD of NMOFs **6-3** as synthesized (blue) and after Pt loading using CDI coupling method (red).
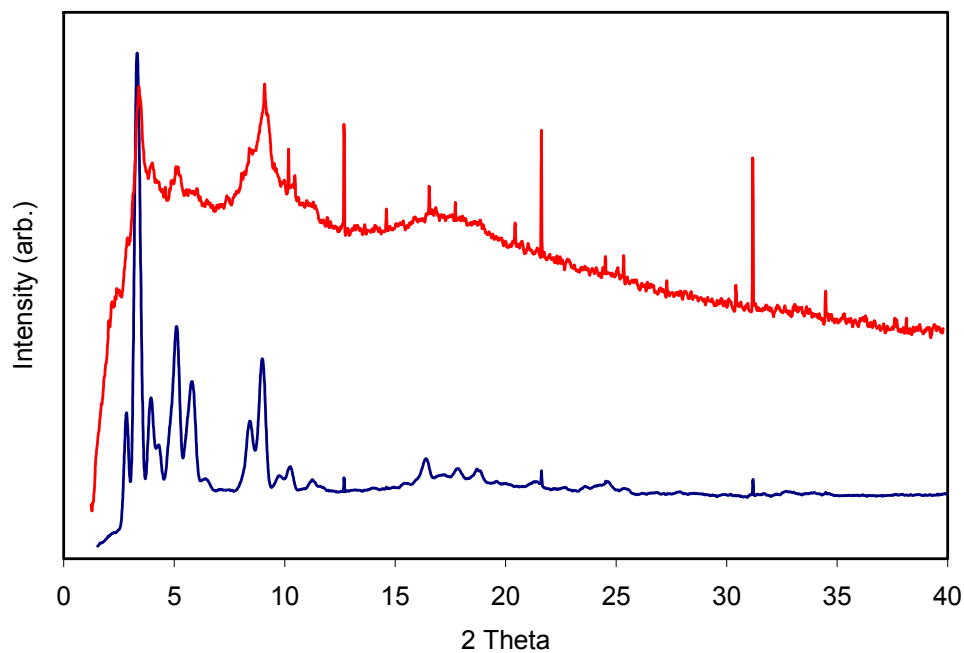
Figure 6.30. PXRD of NMOFs **6-6** as synthesized (blue) and after Pt loading using CDI coupling method (red).

6.2.4 Stability

In order to determine if these Fe containing NMOFs were stable enough for *in vitro* and *in vivo* experiments, their stability was evaluated in phosphate buffer at 37 °C. The Pt loaded NMOFs were used to evaluate the stability. Approximately 2.5 mg of Pt loaded **6-6** was placed inside a piece of dialysis tubing (MWCO = 3500) along with a few mL of the phosphate buffer. The bag was then submerged in 8 mM phosphate buffer that had been heated to 37 °C. Aliquots of the dialysis solution were then removed at various time points, and the Pt concentration was determined using ICP-MS. The Pt loaded NMOFs were used to determine the stability because upon dissolution in phosphate buffer the Fe forms some insoluble complex, likely some form of iron phosphate, which is not released from the bag, therefore ICP-MS analysis for Fe does not give true stability results. The ICP-MS results showed that the particles had a half life of just over 1 hour, i.e. about half of the Pt had been released (Fig. 6.31).
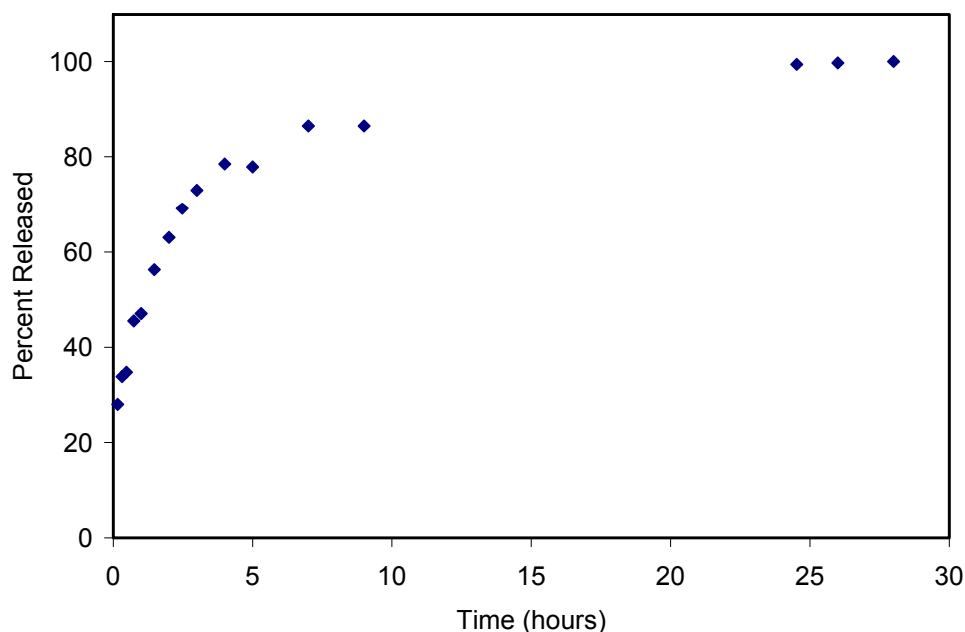
Figure 6.31. Release profile for Pt loaded NMOFs **6-6**. Chart shows percentage released versus time.

6.3 Conclusion

In conclusion, we have been able to synthesize several iron(III) containing nanoscale metal organic frameworks that have the either the MIL-88B or MIL-101 structure. By incorporating an amine containing ligand, we have shown that the frameworks can be modified to incorporate different functionalities. We have shown that we can incorporate organic fluorophores and Gd^{3+} complexes to allow for the potential of optical and MR imaging. We have also shown that we can successfully incorporate a Pt(IV) complex, which upon delivery can be reduced to the active Pt(II) anticancer drug.

6.4 Experimental Details

6.4.1 Materials and Methods

All starting materials were purchased from Aldrich and used without further purification. All solvents were purchased from Fisher. Microwave reactions were carried out in a CEM MARS 5 microwave. Thermogravimetric analysis (TGA) was performed using a Shimadzu TGA-50 equipped with a platinum pan and heated at a rate of 3 °C per minute under air. Powder X-ray diffraction (PXRD) analyses were carried out using a Rigaku Multiflex powder diffractometer using Cu radiation or on a Bruker SMART APEX II diffractometer using Cu radiation. In the latter, the PXRD patterns were processed with the APEX 2 package using phase ID plug-in. A Hitachi 4700 field emission scanning electron microscope (SEM) and a JEM 100CX-II transmission electron microscope (TEM) were used to determine particle size and morphology. A Cressington 108 Auto Sputter Coater equipped with a Au/Pd (80/20) target and an MTM-10 thickness monitor was used to coat the samples with a 5 nm thick conductive layer before taking SEM images. Each SEM sample was prepared by suspending the nanoparticles in ethanol. A drop of the suspension was then placed on a glass slide and the solvent was allowed to evaporate. TEM samples were also prepared from ethanolic particle dispersions on amorphous carbon coated copper grids. A Varian 820-MS Inductively Coupled Plasma-Mass Spectrometer was used to measure Fe, Gd, and Pt concentrations.

6.4.2 NMOF Synthesis

Synthesis of MIL-101 Nanoparticles (6-1). $Fe_3O(DMF)_3Cl(BDC)_3$ nanoparticles (**6-1**) were prepared using microwave heating. 0.0575 g (0.346 mmol) of terephthalic acid

and 0.0935 g (0.346 mmol) of FeCl$_3$·H$_2$O were dissolved in 15 mL of DMF. The solution was placed in a HP500 microwave vessel, and the vessel was sealed. The reaction was then rapidly heated to 150 °C, and was held at this temperature for 10 minutes. After cooling to room temperature, the particles were isolated by centrifuging, and were washed with DMF and ethanol.

Synthesis of 5% amino-MIL Nanoparticles (6-2). Nanoparticles of "5 %" amino BDC (**6-2**) were prepared using a similar procedure as above. 0.1097 g (0.6603 mmol) of terephthalic acid, 0.0063 g (0.0346 mmol) of 2-aminoterephthalic acid, and 0.186 g (0.692 mmol) of FeCl$_3$·H$_2$O were dissolved in 30 mL of DMF. The solution was placed in two HP500 microwave vessels (15 mL each), and the vessels were sealed. The reaction was then rapidly heated to 150 °C, and was held at this temperature for 10 minutes. After cooling to room temperature, the particles were isolated by centrifuging, and were washed with DMF and ethanol.

Synthesis of "10%" amino-MIL Nanoparticles (6-3). Nanoparticles of "10%" amino BDC (**6-3**) were prepared using a similar procedure as above. 0.1035 g (0.6228 mmol) of terephthalic acid, 0.0125 g (0.0692 mmol) of 2-aminoterephthalic acid, and 0.186 g (0.692 mmol) of FeCl$_3$·H$_2$O were dissolved in 30 mL of DMF. The solution was placed in two HP500 microwave vessels (15 mL each), and the vessels were sealed. The reaction was then rapidly heated to 150 °C, and was held at this temperature for 10 minutes. After cooling to room temperature, the particles were isolated by centrifuging, and were washed with DMF and ethanol.

Synthesis of "12.5%" amino-MIL Nanoparticles (6-4). Nanoparticles of "12.5%" amino BDC (**6-4**) were prepared using a similar procedure as above. 0.1976 g (1.189 mmol)

of terephthalic acid, 0.0313 g (0.173 mmol) of 2-aminoterephthalic acid, and 0.374 g (1.384 mmol) of $FeCl_3 \cdot H_2O$ were dissolved in 60 mL of DMF. The solution was placed in four HP500 microwave vessels (15 mL each), and the vessels were sealed. The reaction was then rapidly heated to 150 °C, and was held at this temperature for 10 minutes. After cooling to room temperature, the particles were isolated by centrifuging, and were washed with DMF and ethanol.

Synthesis of "15%" amino-MIL Nanoparticles (6-5). Nanoparticles of "15%" amino BDC (**6-5**) were prepared using a similar procedure as above. 0.1954 g (1.176 mmol) of terephthalic acid, 0.0376 g (0.2076 mmol) of 2-aminoterephthalic acid, and 0.374 g (1.384 mmol) of $FeCl_3 \cdot H_2O$ were dissolved in 60 mL of DMF. The solution was placed in four HP500 microwave vessels (15 mL each), and the vessels were sealed. The reaction was then rapidly heated to 150 °C, and was held at this temperature for 10 minutes. After cooling to room temperature, the particles were isolated by centrifuging, and were washed with DMF and ethanol.

Synthesis of "17.5%" amino-MIL Nanoparticles (6-6). Nanoparticles of "17.5%" amino BDC (**6-6**) were prepared using a similar procedure as above. 0.1897 g (1.142 mmol) of terephthalic acid, 0.0439 g (0.2422 mmol) of 2-aminoterephthalic acid, and 0.374 g (1.384 mmol) of $FeCl_3 \cdot H_2O$ were dissolved in 60 mL of DMF. The solution was placed in four HP500 microwave vessels (15 mL each), and the vessels were sealed. The reaction was then rapidly heated to 150 °C, and was held at this temperature for 10 minutes. After cooling to room temperature, the particles were isolated by centrifuging, and were washed with DMF and ethanol.

Synthesis of "20%" amino-MIL Nanoparticles (6-7).   Nanoparticles of "20%" amino BDC (**6-7**) were prepared using a similar procedure as above. 0.1839 g (1.111 mmol) of terephthalic acid, 0.0503 g (0.2775 mmol) of 2-aminoterephthalic acid, and 0.374 g (1.384 mmol) of FeCl$_3$·H$_2$O were dissolved in 15 mL of DMF. The solution was placed in a HP500 microwave vessel, and the vessel was sealed. The reaction was then rapidly heated to 150 °C, and was held at this temperature for 10 minutes. After cooling to room temperature, the particles were isolated by centrifuging, and were washed with DMF and ethanol.

Synthesis of "50%" amino-MIL Nanoparticles (6-8).   Nanoparticles of "50%" amino BDC (**6-8**) were prepared using a similar procedure as above. 0.1150 g (0.692 mmol) of terephthalic acid, 0.1254 g (0.692 mmol) of 2-aminoterephthalic acid, and 0.374 g (1.384 mmol) of FeCl$_3$·H$_2$O were dissolved in 60 mL of DMF. The solution was placed in four HP500 microwave vessels (15 mL each), and the vessels were sealed. The reaction was then rapidly heated to 150 °C, and was held at this temperature for 10 minutes. After cooling to room temperature, the particles were isolated by centrifuging, and were washed with DMF and ethanol.

Synthesis of 100% amino-MIL Nanoparticles (6-9). Nanoparticles of 100% amino BDC (**6-9**) were prepared using a similar procedure as above. 0.2507 g (1.384 mmol) of 2-aminoterephthalic acid and 0.374 g (1.384 mmol) of FeCl$_3$·H$_2$O were dissolved in 60 mL of DMF. The solution was placed in four HP500 microwave vessels (15 mL each), and the vessels were sealed. The reaction was then rapidly heated to 150 °C, and was held at this temperature for 10 minutes. After cooling to room temperature, the particles were isolated by centrifuging, and were washed with DMF and ethanol.

6.4.3 Synthesis of Fluorophore Standards

Synthesis of BDC-NH-FITC. The molecular compound BDC-NH-FITC was synthesized to use as a standard for determining the amount of fluorescein grafted onto the NMOFs. 1 mg (0.0055 mmol) of 2-aminoterephthalic acid and 2.15 mg (0.0055 mmol) of fluorescein isothiocyanate were dissolved in 1 mL of absolute ethanol. The reaction was then stirred at room temperature, under Ar, overnight. The solvent was then evaporated, and 1.08 mg of the product was dissolved in water after adjusting the pH to 10.1. The sample was diluted to a total volume of 2 mL and this solution was used to construct a calibration curve for quantifying the amount of fluorescein in the digested NMOF samples.

Synthesis of BDC-NH-Rhodamine B. The molecular compound BDC-NH-rhodamine B was synthesized to use as a standard for determining the amount of rhodamine B grafted onto the NMOFs. 20 mg (0.04175 mmol) of rhodamine B was dissolved in 1.5 mL of dry CH_2Cl_2. 5 µL (8.16 mg, 0.0655 mmol) of thionyl chloride was then added, and the reaction was stirred at room temperature, under Ar, overnight. The solvent and excess thionyl chloride were then removed under vacuum. 7.56 mg (0.0417 mmol) of 2-aminoterephthalic acid and 1.2 mL of dry DMF were then added, and the reaction was stirred at room temperature, for two days. The product was then precipitated upon the addition of diethyl ether, isolated by centrifuging, and washed once with additional diethyl ether. Yield: 15.69 mg (0.0245 mmol) 58.8%.

6.4.4 Post-Synthetic Modifications

FITC Functionalized amino-MIL Nanoparticles. 7.5 mg (0.0193 mmol) of fluorescein isothiocyanate was dissolved in 3 mL of absolute ethanol. 10 mg of

Fe$_3$O(DMF)$_3$Cl(NH$_2$-BDC)$_3$ nanoparticles (**6-9**) were added, and the reaction was stirred at room temperature, under Ar, in the dark, for 48 hours. The particles were then isolated by centrifuging, and were washed with ethanol, until a colorless supernatant was observed.

Rhodamine B Functionalized amino-MIL Nanoparticles Method 1. 73.65 mg (0.15375 mmol) of rhodamine B was dissolved in 6 mL of dry CH$_2$Cl$_2$. 12 µL (0.02012 g, 0.1691 mmol) of thionyl chloride was then added, and the reaction was stirred at room temperature, under Ar, overnight. The solvent and excess thionyl chloride were then removed under vacuum. 100 mg of dried amino-MIL particles were then added along with 5 mL of dry DMF, and the reaction was stirred at room temperature, under Ar, for 3 days. The particles were then isolated by centrifuging, and were washed once with DMF, then extensively washed with ethanol. After the supernatant appeared colorless the particles were dried under vacuum.

Rhodamine B Functionalized amino-MIL Nanoparticles Method 2. 14.73 mg (0.03075 mmol) of rhodamine B and 5.98 mg (0.0369 mmol) of 1,1-carbonyldiimidazole were dissolved in 1 mL of anhydrous DMF. The reaction was then heated to 60 °C for 1 hour. After cooling to room temperature 20 mg of **6-9** was added, and the reaction was stirred at room temperature, under Ar, for 3 days. The particles were then isolated by centrifuging and washed extensively with ethanol. After the supernatant appeared colorless the particles were dried under vacuum.

BODIPY Functionalized amino-MIL Nanoparticles. 6.5 mL of a suspension of **6-3** in ethanol was centrifuged to isolate 20.9 mg of particles. The particles were washed once with THF before being redispersed in 5 mL of THF. 4 mg (11.7 µmol) of Br-BODIPY was dissolved in 2 mL of THF and was added to the particle suspension. The reaction was

then stirred at room temperature for 2 days. The particles were then isolated by centrifuging, and were washed with THF until a colorless supernatant was observed. A similar procedure was used to functionalize particles **6-6** with BODIPY.

Gd Loaded amino-MIL Nanoparticles. The amino-MIL particles (**6-9**) were first functionalized with DTPA using the following procedure. 69 mg (0.193 mmol) of diethylenetriaminepentaacetic dianhydride was dissolved in 10 mL of anhydrous DMF. 100 mg of $Fe_3O(DMF)_3Cl(NH_2-BDC)_3$ nanoparticles (**6-9**) were added, and the reaction was stirred at room temperature, under Ar, for 3 days. The particles were then isolated by centrifuging, were washed with DMF, and dried under vacuum.

The Gd was then loaded by first adding 0.775 mL of a 0.2 M $GdCl_3$ solution (0.155 mmol) to 10 mL of distilled water. The pH of the solution was adjusted to 7.0 using dilute NaOH. 80 mg of DTPA functionalized **6-9** particles were then added, and the mixture was stirred at room temperature, overnight. The particles were isolated by centrifuging and then dialyzed against 300 mL of 18 MΩ water for 5 hours to remove any free Gd^{3+}. The particles were then dried under vacuum.

Pt Loaded amino-MIL Nanoparticles. The amino-MIL particles (**6-7**) were first functionalized with succinic acid, using the following procedure. 4.5 mg (0.045 mmol) of succinic anhydride was dissolved in 2 mL of anhydrous DMF. 20 mg of nanoparticles **6-2** were added, and the reaction was stirred at room temperature, under Ar, for 3 days. The particles were then isolated by centrifuging, were washed with DMF and ethanol, and then dried under vacuum.

The Pt was then loaded by first suspending 15.4 mg of succinic acid functionalized amino-MIL particles 2 mL of dry CH_2Cl_2. 5 μL (8.16 mg, 0.069 mmol) of thionyl chloride

was then added, and the reaction was stirred at room temperature, under Ar, for 24 hours. The solvent and excess thionyl chloride were then removed under vacuum. 15 mg (0.041 mmol) of c,c,t-Pt(NH$_3$)$_2$Cl$_2$(OH)(OEt) was then added, along with 3.5 mL of dry DMF. The reaction was then stirred at room temperature, under Ar, for 48 hours. The particles were isolated by centrifuging and were washed twice with DMF. The particles were then dialyzed against 300 mL of 18 MΩ water for 4 hours to remove any free complex. The particles were then dried under vacuum. A similar procedure was used for loading Pt into NMOFs **6-8** and **6-9**.

An alternate method was used to load the Pt(IV) complex in NMOFs **6-3** and **6-6**. This method involved first synthesizing the c,c,t-[Pt(IV)Cl$_2$(NH$_3$)$_2$(OEt)(O$_2$CCH$_2$CH$_2$CO$_2$H)] complex using a previously published procedure.[13] For loading into **6-6**, 22 mg (0.0476 mmol) of c,c,t-[Pt(IV)Cl$_2$(NH$_3$)$_2$(OEt)(O$_2$CCH$_2$CH$_2$CO$_2$H)] was dissolved in 3 mL of anhydrous DMF along with 9.3 mg (0.0574 mmol) of 1,1-carbonyldiimidazole. The reaction was then heated at 60 °C for 1 hour, under Ar. After cooling to room temperature, 85 mg of dried **6-6** was then added and the reaction was stirred at room temperature for 2 days. The product was then isolated by centrifuging, and was washed with DMF and ethanol before being dialyzed against distilled water for 5 hours. A similar procedure was used to load the Pt(IV) complex in **6-3**.

6.5 References

1. Férey, G.; Mellot-Draznieks, C.; Serre, C.; Millange, F.; Dutour, J.; Surblé, S.; Margiolaki, I., A chromium terephthalate–based solid with unusually large pore volumes and surface area. *Science* **2005**, *309* (5743), 2040-2042.

2. Lebedev, O. I.; Millange, F.; Serre, C.; Van Tendeloo, G.; Férey, G., First direct imaging of giant pores of the metal-organic framework MIL-101. *Chem. Mater.* **2005**, *17* (26), 6525-6527.

3. Latroche, M.; Surblé, S.; Serre, C.; Mellot-Draznieks, C.; Llewellyn, P. L.; Lee, J-H.; Chang, J-S.; Jhung, S. H.; Férey, G., Hydrogen storage in the giant-pore metal–organic frameworks MIL-100 and MIL-101. *Angew. Chem. Int. Ed.* **2006**, *45* (48), 8227-8231.

4. Serre, C.; Millange, F.; Thouvenot, C.; Noguès, M.; Marsolier, G.; Louër, D.; Férey, G., Very large breathing effect in the first nanoporous chromium(III)-based solids: MIL-53 or Cr^{III}(OH)·{O$_2$C-C$_6$H$_4$-CO$_2$}·{HO$_2$C-C$_6$H$_4$-CO$_2$H}$_x$·H$_2$O$_y$. *J. Am. Chem. Soc.* **2002**, *124* (45), 13519-13526.

5. Millange, F.; Serre, C.; Férey, G., Synthesis, structure determination and properties of MIL-53as and MIL-53ht: the first Cr^{III} hybrid inorganic–organic microporous solids: Cr^{III}(OH)·{O$_2$C–C$_6$H$_4$–CO$_2$}·{HO$_2$C–C$_6$H$_4$–CO$_2$H}$_x$. *Chem. Commun.* **2002** (8), 822-823.

6. Surblé, S.; Serre, C.; Mellot-Draznieks, C.; Millangea, F.; Férey, G., A new isoreticular class of metal-organic-frameworks with the MIL-88 topology. *Chem. Commun.* **2006** (3), 284-286.

7. Serre, C.; Mellot-Draznieks, C.; Surblé, S.; Audebrand, N.; Filinchuk, Y.; Férey, G., Role of solvent-host interactions that lead to very large swelling of hybrid frameworks. *Science* **2007**, *315* (5820), 1828-1831.

8. Horcajada, P.; Serre, C.; Vallet-Regí, M.; Sebban, M.; Taulelle, F.; Férey, G., Metal–organic frameworks as efficient materials for drug delivery. *Angew. Chem. Int. Ed.* **2006**, *45* (36), 5974-5978.

9. Horcajada, P.; Serre, C.; Maurin, G.; Ramsahye, N. A.; Balas, F.; Vallet-Regí, M.; Sebban, M.; Taulelle, F.; Férey, G., Flexible porous metal-organic frameworks for a controlled drug delivery. *J. Am. Chem. Soc.* **2008**, *130* (21), 6774-6780.

10. Bauer, S.; Serre, C.; Devic, T.; Horcajada, P.; Marrot, J.; Férey, G.; Stock, N., High-throughput assisted rationalization of the formation of metal organic frameworks in the iron(III) aminoterephthalate solvothermal system. *Inorg. Chem.* **2008**, *47* (17), 7568-7576.

11. Kiang, Y-H.; Gardner, G. B.; Lee, S.; Xu, Z.; Lobkovsky, E. B., Variable pore size, variable chemical functionality, and an example of reactivity within porous phenylacetylene silver salts. *J. Am. Chem. Soc.* **1999**, *121* (36), 8204-8215.

12. Seo, J. S.; Whang, D.; Lee, H.; Jun, S. I.; Oh, J.; Jeon, Y. J.; Kim, K., A homochiral metal-organic porous material for enantioselective separation and catalysis. *Nature*. **2000**, *404* (6781), 982-986.

13. Wu, C-D.; Hu, A.; Zhang, L.; Lin, W., A homochiral porous metal-organic framework for highly enantioselective heterogeneous asymmetric catalysis. *J. Am. Chem. Soc.* **2005**, *127* (25), 8940-8941.

14. Wang, Z.; Cohen, S. M., Postsynthetic covalent modification of a neutral metal-organic framework. *J. Am. Chem. Soc.* **2007**, *129* (41), 12368-12369.

15. Feazell, R. P.; Nakayama-Ratchford, N.; Dai, H.; Lippard, S. J., Soluble single-walled carbon nanotubes as longboat delivery systems for platinum(IV) anticancer drug design. *J. Am. Chem. Soc.* **2007**, *129* (27), 8438-8439.

CHAPTER 7

Hybrid Silica Nanoparticles for Bacterial Spore Detection

7.1 Introduction

Bacterial endospores are dormant structures produced by bacterial cells in order to survive harsh conditions. The endospores are resistant to stresses such as heat, radiation, desiccation, and chemical disinfectants, making them difficult to remove.[1] Certain species of endospores are used to check the performance of sterilization techniques, while other species, such as *Bacillus anthracis* have been used as delivery vehicles in anthrax attacks.[2]

Rapid detection of *B. anthracis* spores is a major concern in the event of biological warfare. Inhalation of as few as 10^4 spores can result in death if medical attention is not received within 24-48 hours.[3] Several methods are currently used for detecting the presence of bacterial endospores, including immunoassays,[4-5] polymerase chain reactions (PCR),[6-8] surface-enhanced Raman spectroscopy,[9-11] and Tb(III) luminescence.[1,12-16] Tb(III) luminescence detection has been shown to be a rapid, sensitive, and inexpensive method for endospore detection. The luminescence detection is based on the sensing of dipicolinic acid (DPA) which can account for up to 15% of the dry mass of endospores. Coordination of DPA to Tb(III) results in luminescence after UV excitation at the absorbance maximum of DPA. It has been shown that energy transfer from the ligand (DPA) to the terbium excited states is responsible for the enhanced luminescence when compared to aquated Tb(III) ions.

TbCl$_3$ has been used as a sensor for DPA detection, but has several disadvantages including non-selective binding of other aromatic ligands resulting in false positives; binding of other anions, such as phosphate, which may inhibit DPA binding resulting in false negatives; and finally non-radiative quenching from coordinating water which reduces the quantum yield, and thus the overall sensitivity of the assay. A recent report by Ponce and coworkers discussed the use of a macrocyclic ligand to occupy 6 of the Tb coordination sites,

leaving 3 adjacent sites available for DPA coordination.[15] This prevents water molecules from coordinating to the Tb(III) centers after DPA binding, thus eliminating deleterious quenching by coordinating water molecules to provide a sensitive molecular DPA sensor based on luminescence enhancement.

We have synthesized and evaluated two novel hybrid nanoparticle platforms for DPA detection that involve the immobilization of Tb(III) EDTA complexes onto either silica nanoparticles or silica coated nanoscale metal-organic frameworks (NMOFs). The EDTA ligand serves to occupy 6 of the Tb coordination sites and can also be easily modified to contain one or two triethoxysilane groups to allow for covalent attachment to the silica nanoparticles. The use of a nanoparticle platform for immobilizing the Tb complexes provides a mechanism for incorporating an internal standard in the particle core, which would then eliminate the need for instrument specific calibration curves for quantifying the amount of DPA in an unknown sample.

7.2 Results and Discussion

7.2.1 Synthesis of Nanoparticle Sensors

Three different EDTA based ligands were synthesized for this work. Initially, the EDTA dianhydride was mono-functionalized with aminopropyltriethoxysilane (APTES) to allow for a single point covalent attachment of the complex to the silica particle. After coordination of the Tb ion, this complex (**7-1**) has an overall neutral charge. By reacting the EDTA dianhydride with two equivalents of APTES, the bis functionalized ligand and Tb complex (**7-2**) were then formed. This complex provides two covalent attachment points of the complex to the nanoparticle, and the complex has an overall positive charge. Finally, a

third complex was formed by functionalizing the ETDA dianhydride with two different groups. One side of the dianhydride was first reacted with pentylamine, while the other side was functionalized with APTES. The resulting Tb complex (**7-3**) then had an overall positive charge and one functional group to allow for covalent attachment to the nanoparticle platform (Scheme 7.1).
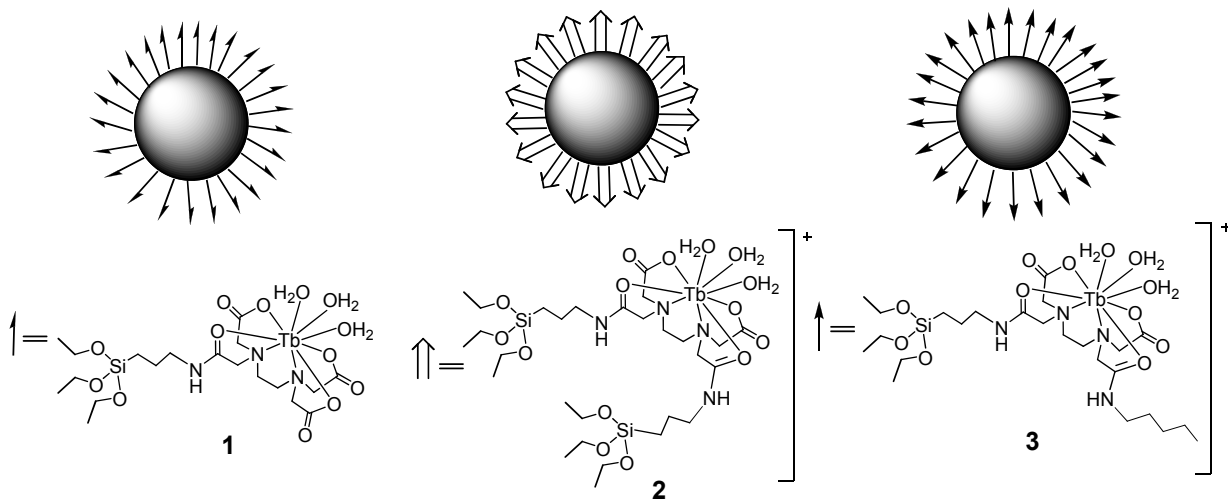
Scheme 7.1. Solid silica nanoparticles coated with three different modified EDTA-Tb complexes.

Two different types of nanoparticle platforms were synthesized for this work. First, solid silica nanoparticles were synthesized from the basic condensation of tetraethylorthosilicate (TEOS) in a water-in-oil microemulsion with a *W*-value of 15. After allowing 24 hours for particle formation, an aliquot of an aqueous solution of the Tb complex was added, and the reaction was continued at room temperature for an additional 18 hours. The particles were then precipitated upon the addition of ethanol, isolated by centrifuging and washed with ethanol and water to remove unreacted starting material and the surfactant. To ensure complete complexation of the immobilized EDTA derivatives, Tb^{3+} was re-loaded by treating the nanoparticles with additional $TbCl_3$ in water at a pH of 9.5. A similar

procedure was used to synthesize silica nanoparticles with a luminescent core. In this case an aqueous solution of $Ru(bpy)_3^{2+}$ was added along with the water and TEOS when forming the initial microemulsion.

The second type of nanoparticle platform used for this work was based on a nanoscale metal-organic framework. Eu-doped Gd NMOFs with the formula $Eu_{0.02}Gd_{0.98}(BDC)_{1.5}(H_2O)_2$ were synthesized using a previously published procedure.[17] The NMOFs were then coated with an organic polymer, polyvinylpyrrolidone (PVP), followed by coating with an 8-9 nm thick silica shell. Tb complex **7-1** was then grafted onto the surface of the silica shell under basic conditions in ethanol.

7.2.2 Characterization

The nanoparticle sensors were characterized by a variety of methods. First, transmission electron microscopy (TEM) was used to determine the particle size and morphology. The solid silica nanoparticles particles obtained are uniform spheres, approximately 37 nm in diameter, while the NMOFs are nanorods approximately 40 nm in diameter and 100 nm in length (Fig. 7.1 and 7.2). No measurable change is seen in the particle size or morphology after immobilization of the Tb complexes (Fig. 7.1). The amount of Tb complex immobilized on the particles was then estimated using thermogravimetric analysis (TGA). TGA of the coated particles shows an initial weight loss for adsorbed solvent molecules, followed by a weight loss from ~250°C to 550°C for the organic portion of the complex (Fig. 7.3). The exact Tb concentration of a suspension of the nanoparticle sensors was then determined through DPA titration.
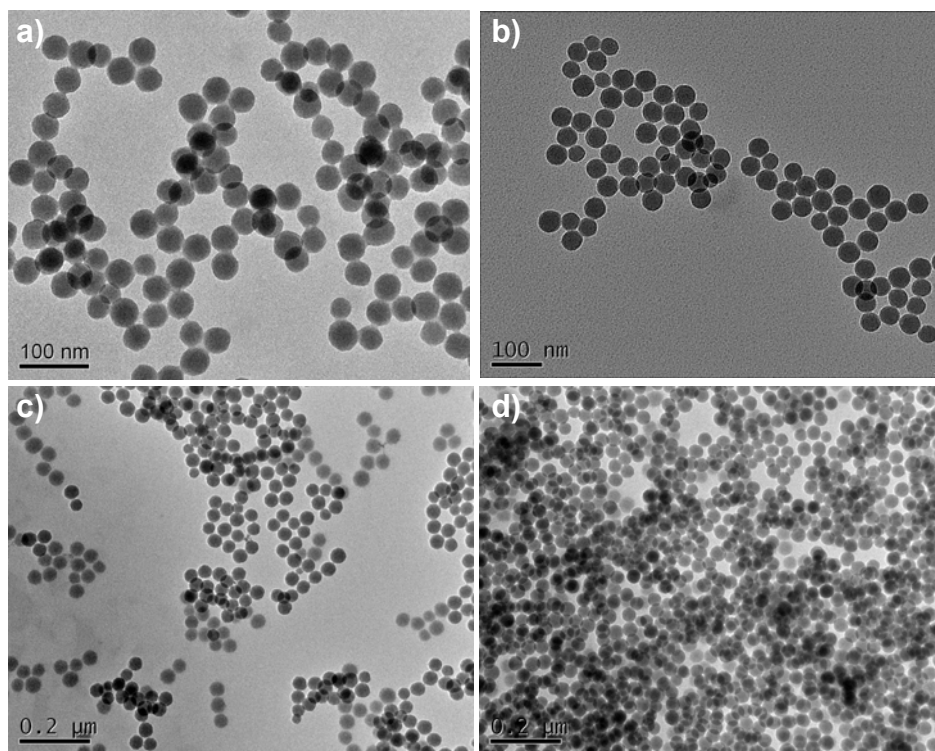
Figure 7.1. TEM images of uncoated silica nanoparticles (a), and silica nanoparticles coated with Tb complexes **7-1** (b), **7-2** (c), and **7-3** (d).
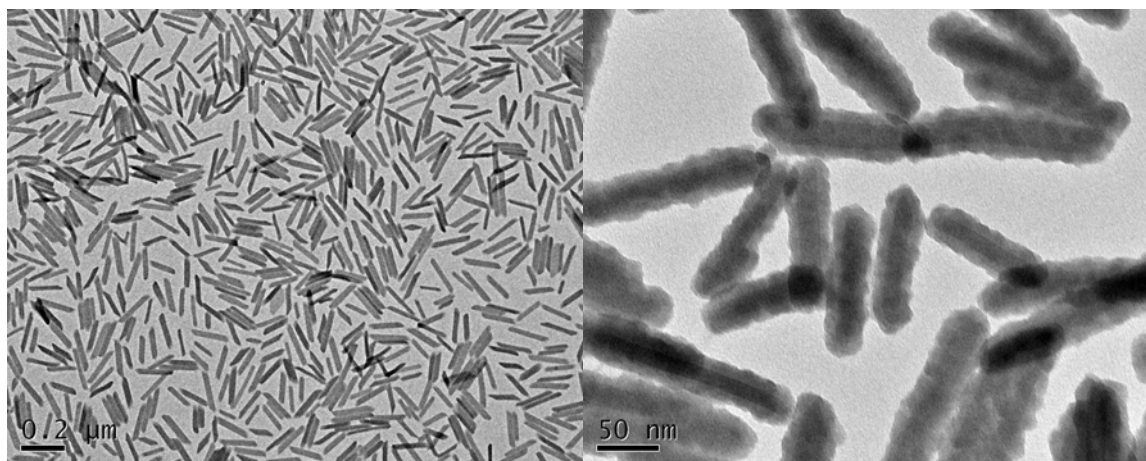
Figure 7.2. TEM images of PVP coated NMOFs (left), and silica coated NMOFs with an 8-9 nm thick silica shell (right).
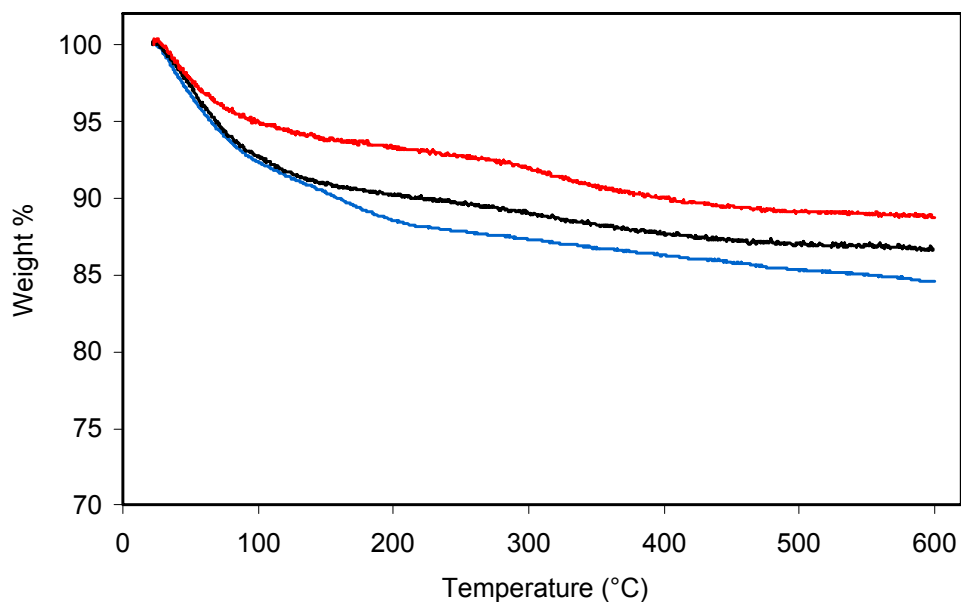
Figure 7.3. TGA of silica nanoparticles coated with complexes **7-1** (black), **7-2** (red), and **7-3** (blue).

7.2.3 DPA Detection Results

As expected, UV excitation of a suspension of the nanoparticle sensors results in no emission. However, upon the addition of the DPA disodium salt, characteristic Tb emission is observed with peaks appearing at 489 nm, 544 nm, and 584 nm (Fig. 7.4 and Scheme 7.2). Titration of a suspension of the nanoparticle sensors with DPA results in a linear increase of emission intensity until all of the Tb complexes have become coordinatively saturated.

Based on the number of available coordination sites, a 1:1 stoichiometry for complex formation with DPA was expected for all three of the Tb complexes. This was however not observed in all cases. The Job's plots revealed that both of the cationic Tb complexes (**7-2** and **7-3**) formed a 1:1 complex with DPA whereas the neutral Tb complex (**7-1**) formed a complex with a 2:3 Tb:DPA ratio (presumably reflecting the influence of charge on DPA coordination to the Tb center) (Fig. 7.5). The Job's plots for the nanoparticles revealed that all three sensors form the expected 1:1 Tb:DPA complex (Fig. 7.6).

Figure 7.4. Emission spectrum of a suspension of silica nanoparticles functionalized with Tb complex **7-2**. The DPA concentration was increased from 0 to 1.5 eq relative to Tb. The peak at 556 nm is a result of second order scattering. Excitation wavelength was 278 nm.

Scheme 7.2. Schematic showing the light-up process for the nanoparticle sensor with immobilized EDTA-Tb complexes (**7-1** to **7-3**) before and after the addition of DPA.

Figure 7.5. Job's plots of Tb complexes **7-1** (black diamonds), **7-2** (red triangles), and **7-3** (blue squares). The curves for complexes **7-2** and **7-3** are offset by 0.2 and 0.4 normalized intensity units, respectively.
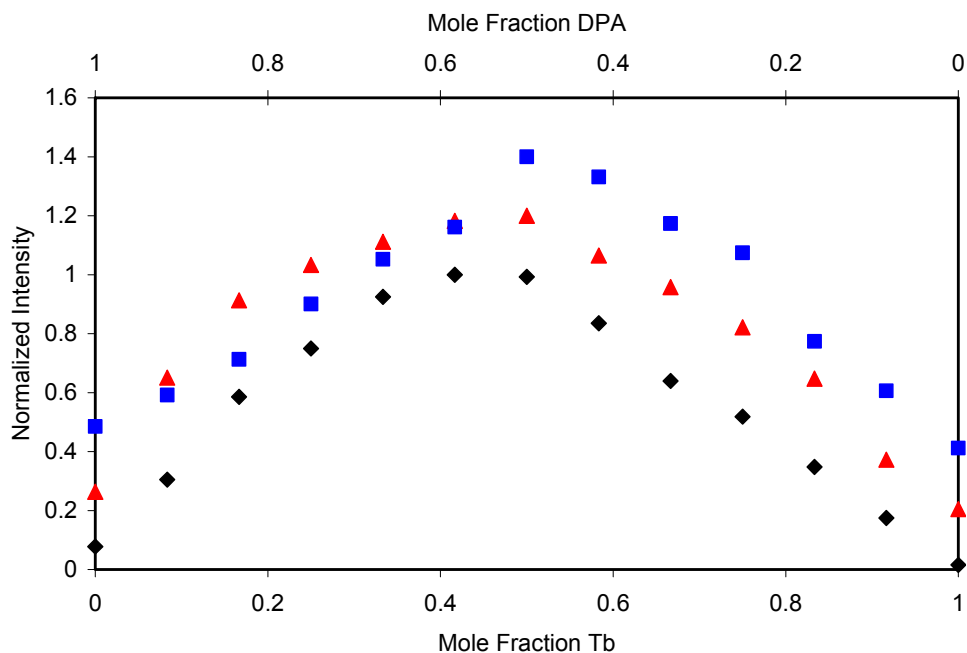
Figure 7.6. Job's plots of nanoparticle sensors functionalized with complexes **7-1** (black diamonds), **7-2** (red triangles), and **7-3** (blue squares). The curves for sensors functionalized with complexes **7-2** and **7-3** are offset by 0.2 and 0.4 normalized intensity units, respectively.

Using the linear response a calibration curve can be constructed, which can then be used to quantitatively determine the amount of DPA in an unknown sample (Fig. 7.7-7.11). The nanoparticle sensors are able to detect low concentrations of DPA. The detection limit for each system was determined using the background intensity plus three standard deviations. The nanoparticles functionalized with Tb complex **7-2** provided the lowest detection limit for all nanoparticle systems. Using the major peak at 544 nm, a detection limit of 10.3 nM was determined. The peak at 489 nm can also be used, resulting in a slightly higher detection limit of 20.3 nM. The nanoparticles functionalized with Tb complexes **7-1** and **7-3** gave slightly higher limits of detection, but all detection limits were below 35 nM.
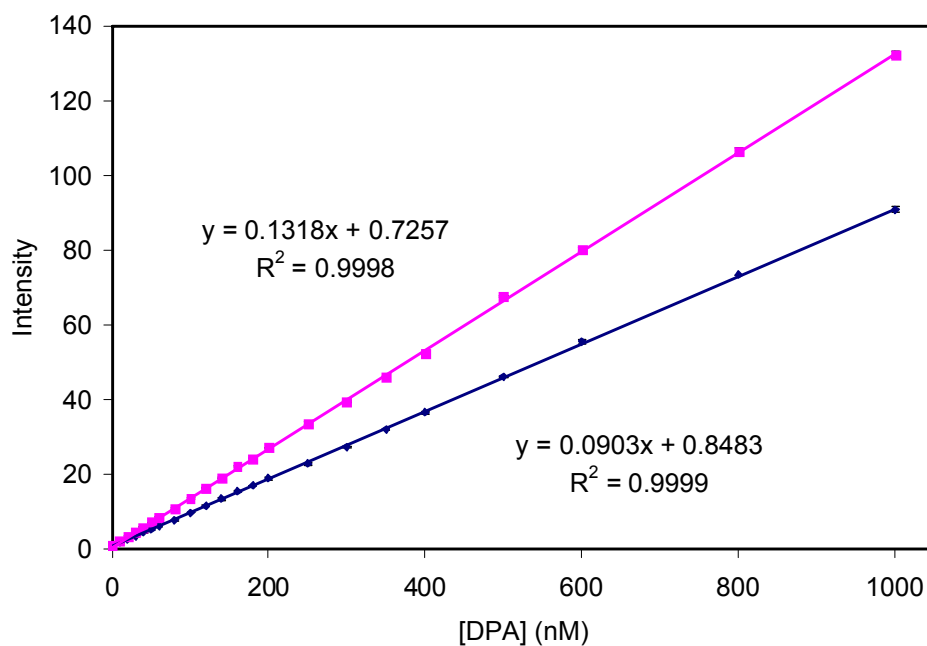
Figure 7.7. Calibration curve for DPA detection using a 10 μM solution of free monoAPS-EDTA-Tb complex (**7-1**) obtained by plotting the intensity at 489 nm (blue) and 544 nm (pink) vs. [DPA]. The detection limit was calculated to be 5.02 nM using the peak at 489 nm and 4.12 nM using the peak at 544 nm.
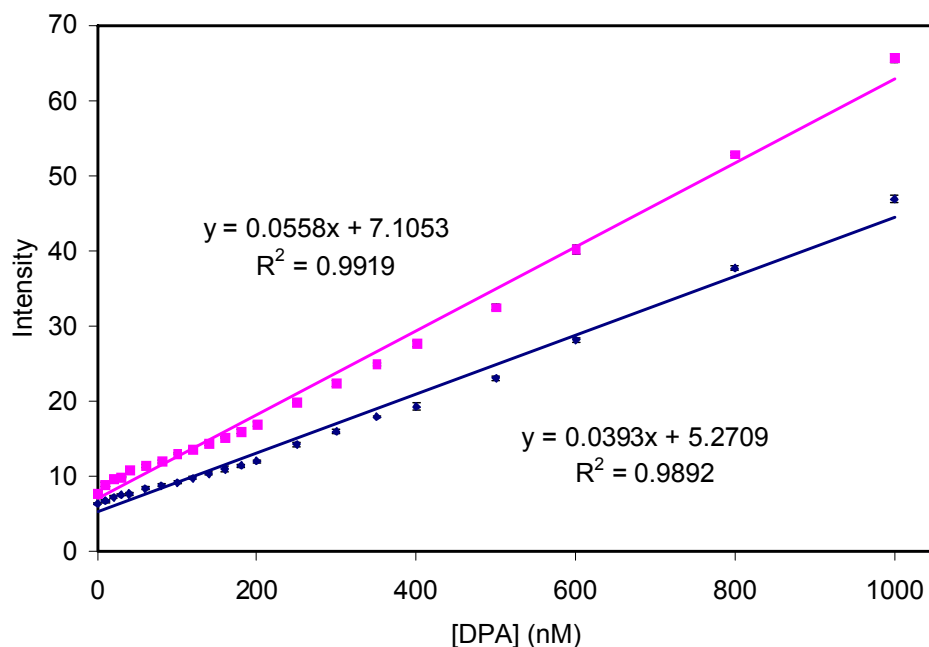
Figure 7.8. Calibration curve for DPA detection using a suspension of monoAPS-EDTA-Tb (**7-1**) coated particles with a Tb concentration of 10 μM obtained by plotting the intensity at 489 nm (blue) and 544 nm (pink) vs. [DPA]. The detection limit was calculated to be 34.6 nM using the peak at 489 nm and 15.7 nM using the peak at 544 nm.
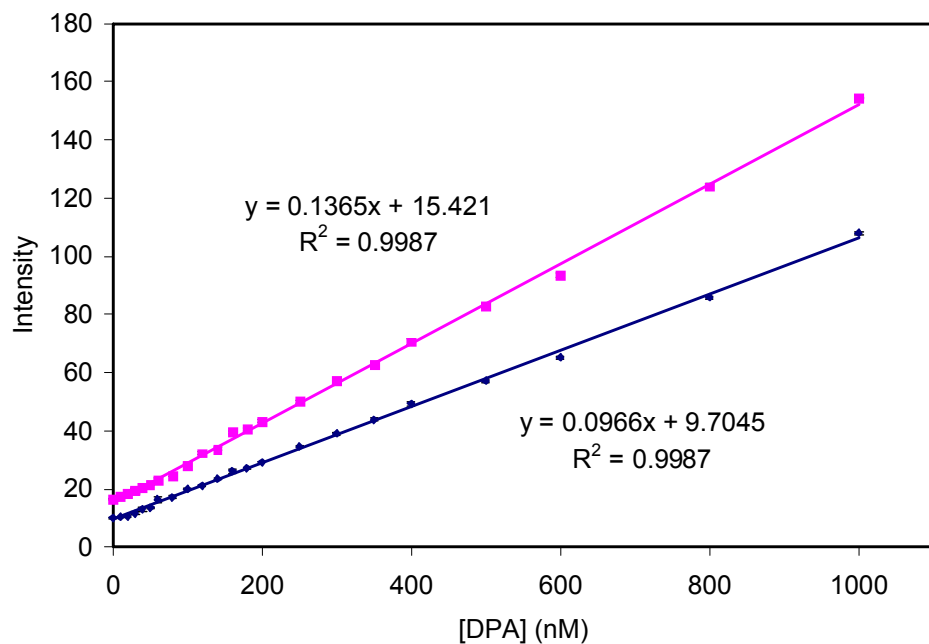
Figure 7.9. Calibration curve for DPA detection using a 10 μM solution of free bisAPS-EDTA-Tb (**7-2**) complex obtained by plotting the intensity at 489 nm (blue) and 544 nm (pink) vs. [DPA]. The detection limit was calculated to be 7.11 nM using the peak at 489 nm and 9.39 nM using the peak at 544 nm.
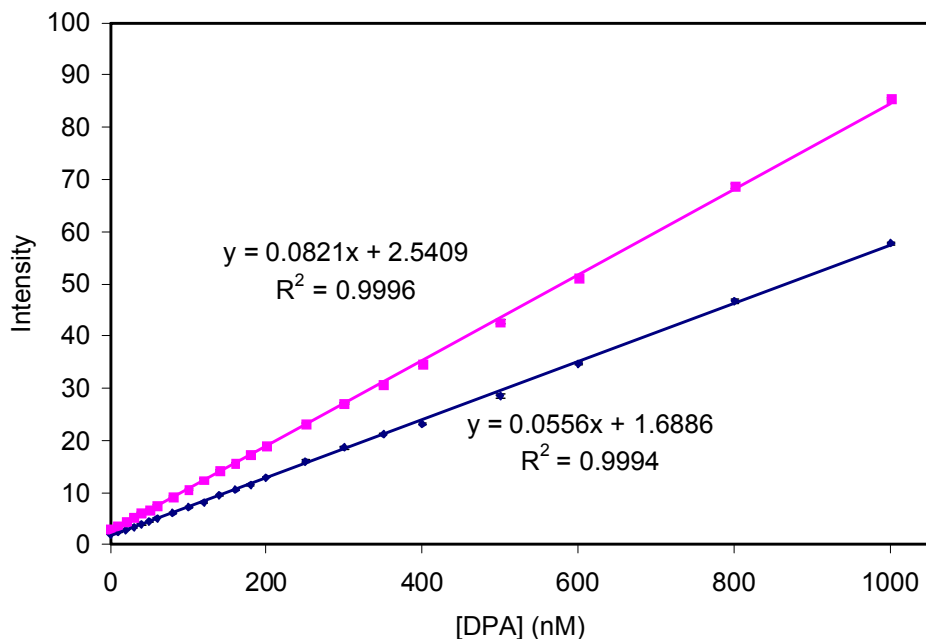
Figure 7.10. Calibration curves for DPA detection using silica nanoparticles functionalized with Tb complex **7-2** using the intensity at 489 nm (blue) and 544 nm (pink). Using this curve detection limits of 20.3 nM and 10.3 nM were calculated using the peaks at 489 nm and 544 nm, respectively.
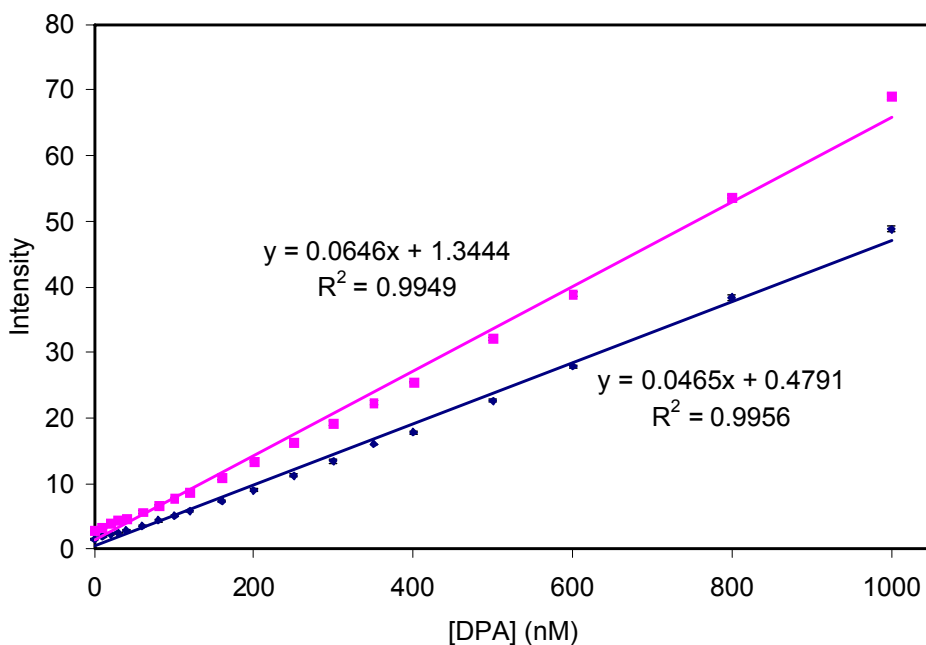
Figure 7.11. Calibration curve for DPA detection using a suspension of pentylamide-APS-EDTA-Tb (**7-3**) coated particles with a Tb concentration of 10 μM obtained by plotting the intensity at 489 nm (blue) and 544 nm (pink) vs. [DPA]. The detection limit was calculated to be 27.2 nM using the peak at 489 nm and 24.1 nM using the peak at 544 nm.

One of the major benefits to using a nanoparticle based sensor is that an internal reference can be incorporated into the nanoparticle to allow for ratiometric detection. This eliminates the need for instrument specific calibration curves, and also alleviates the need of correcting for dilution. Two different types of internal standards were evaluated. First, solid silica nanoparticles were synthesized to contain a luminescent $Ru(bpy)_3^{2+}$ core (Scheme 7.3). Comparison of the Tb emission intensity to the $Ru(bpy)_3^{2+}$ emission allows for the ratiometric detection of DPA. The emission intensity from the $Ru(bpy)_3^{2+}$ remains constant and is independent of the DPA concentration. Because $Ru(bpy)_3^{2+}$ has an absorbance over a wide wavelength range the internal reference can be monitored independently of the Tb luminescence by exciting at a higher wavelength, such as 488 nm (Fig. 7.12). For the NMOFs we were able to use the Eu emission from the particles as an internal standard (Fig. 7.13).
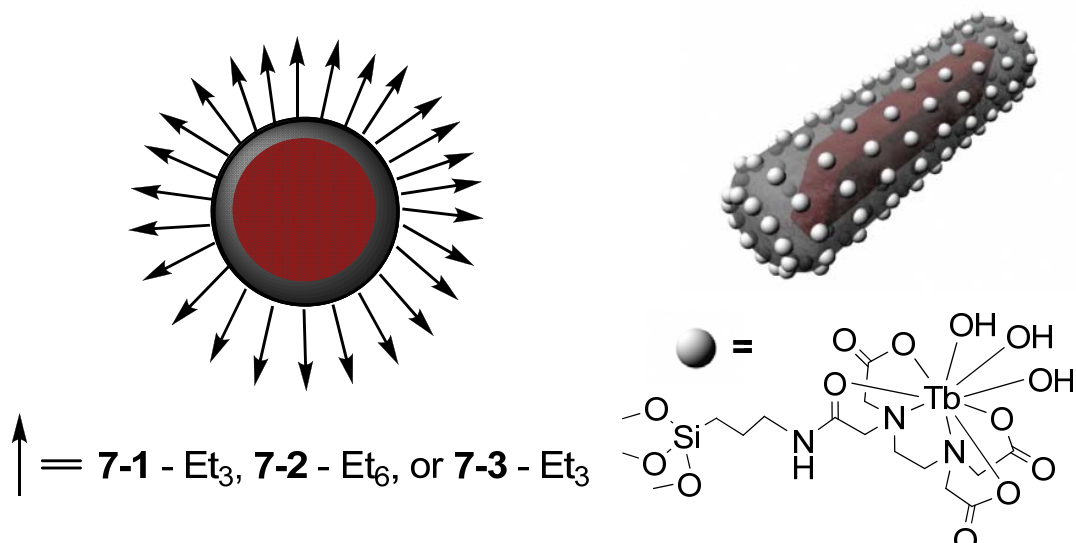
Scheme 7.3. Schematic showing the nanoparticle sensor with a $Ru(bpy)_3Cl_2$ core (left) and the Eu-doped NMOF core (right).
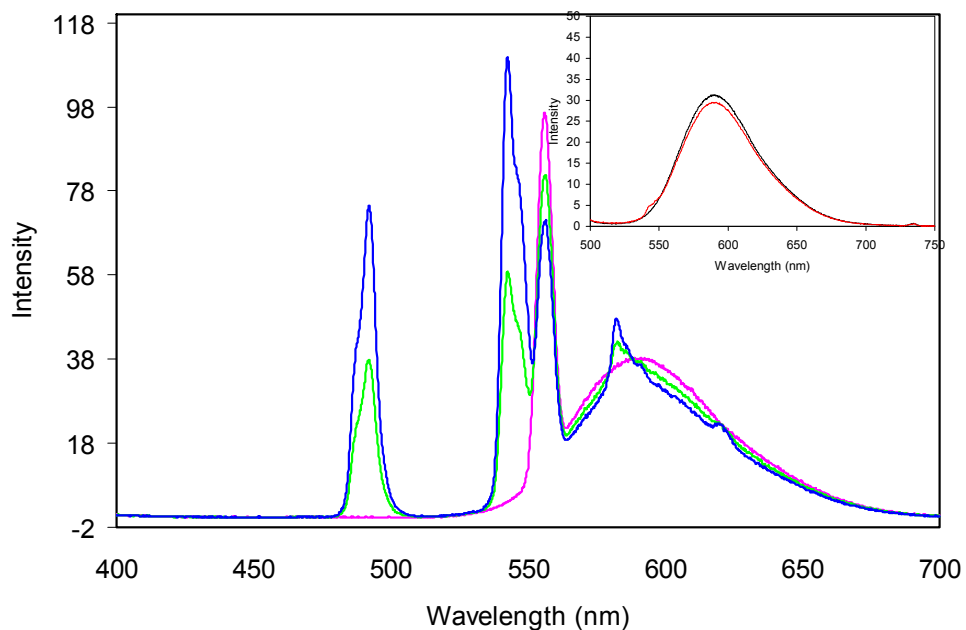
Figure 7.12. Emission spectrum of a suspension of $Ru(bpy)_3Cl_2$ doped silica nanoparticles functionalized with Tb complex **7-2**. The DPA concentration was increased from 0 to 2 equivalents and the emission spectrum was recorded after exciting at 277 nm. The inset shows the emission spectrum after exciting at 488 nm where the only emission observed is that of the $Ru(bpy)_3Cl_2$ internal reference. This emission is independent of DPA concentration (black – 0 eq, red – 2 eq.).
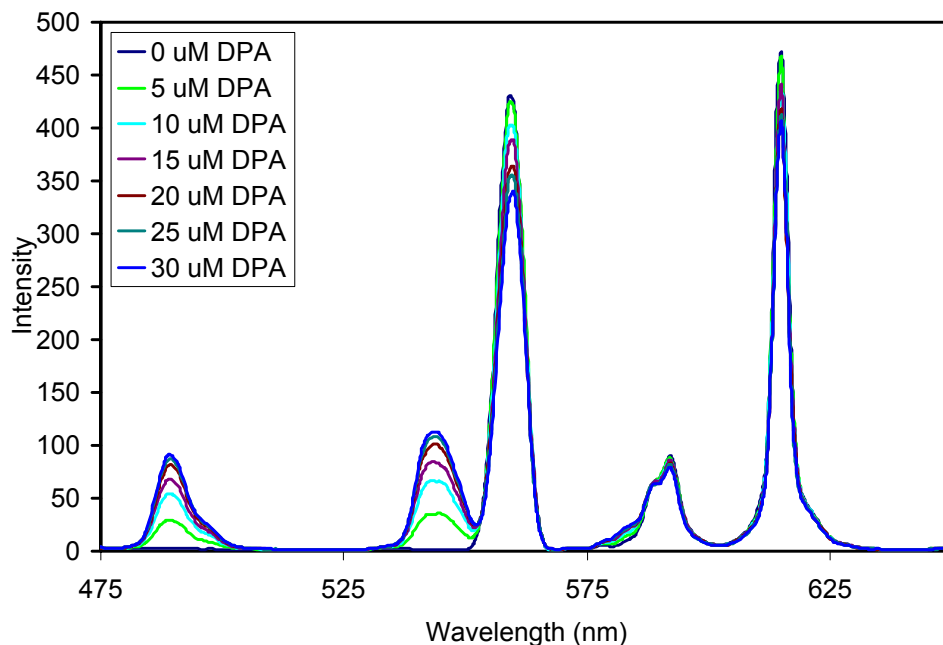
Figure 7.13. Emission spectrum of a suspension of Eu-doped NMOFs functionalized with complex **7-1**. The DPA concentration was increased from 0 to 10 µM and the emission spectrum was recorded after exciting at 278 nm.

In order to evaluate the specificity of this nanoparticle sensor, we have carried out DPA detection experiments in buffered solutions and in the presence of biologically prevalent interferences such as amino acids. Using the Eu doped NMOF sensor, the DPA detection experiment was carried out in a 10 mM Tris buffered solution at pH 7.6, and a similar response was seen compared to the results obtained in an ethanol suspension (Fig. 7.14 and 7.15). The DPA detection limit was calculated to be 56.6 nM in the buffered solution compared to 48 nM in an ethanol suspension.
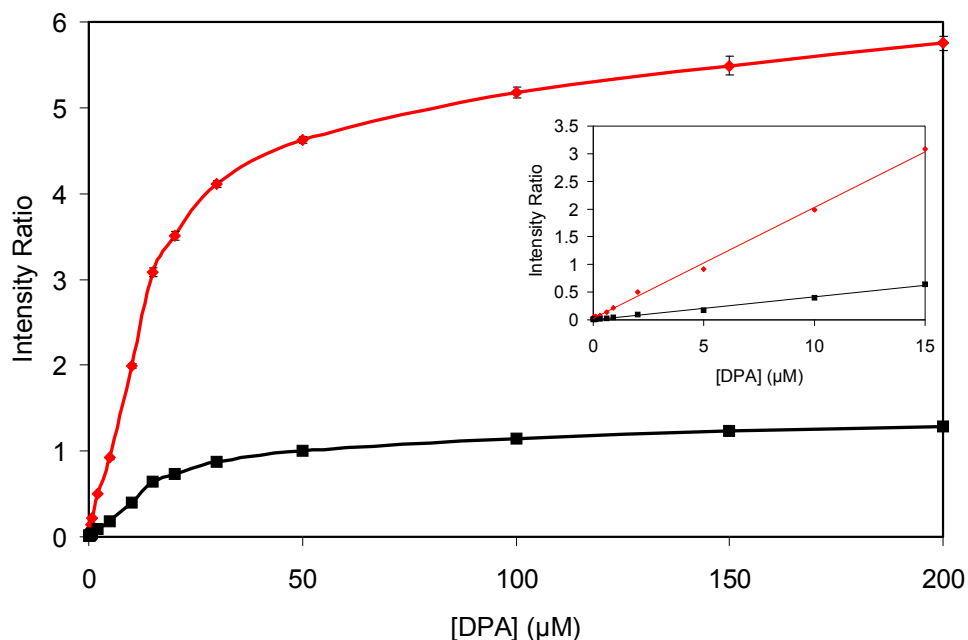
Figure 7.14. Dependence of the ratio of Tb to Eu emission intensities for Eu-doped NMOF sensors (in ethanol) on DPA concentration (red – 544 nm/592 nm, black – 544 nm/615 nm). The inset shows the linear relationship at low [DPA].
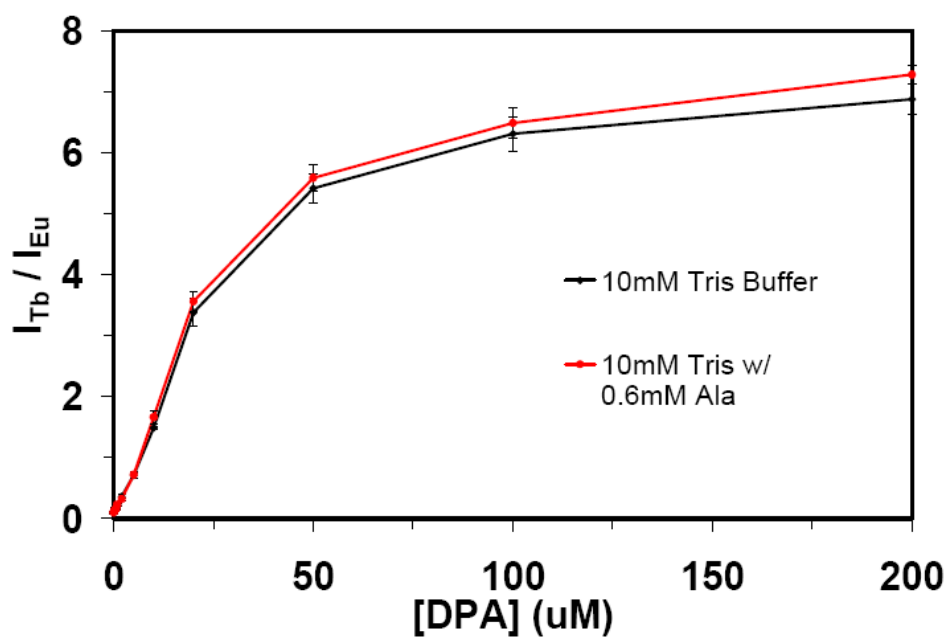
Figure 7.15. Dependence of the ratio of Tb (544 nm) to Eu (592 nm) emission intensities for Eu-doped NMOF sensors on DPA concentration in a 10 mM Tris buffered ethanol in water (1:1) solution (black) and in the presence of 0.6 mM L-alanine (red).

To determine if the Tb-EDTA complex was selective for the detection of DPA against other biologically relevant carboxylic acid-containing molecules, two suspensions of the Eu doped NMOF sensor were made in 10 mM Tris buffered solution at pH 7.6. DPA was then added to both suspensions, one suspension was brought to a [DPA] of 5 µM, while the other was brought to a [DPA] of 150 µM. Aliquots of a 100 mM solution of L-alanine were added to the DPA nanoparticle suspensions to achieve final alanine concentrations of 0.3, 0.6, 0.9, and 1.2 mM. The luminescent intensities were recorded approximately 5 minutes after each addition and the ratio of Tb to Eu luminescent intensities were plotted against the [Ala] (Fig. 7.16). There is a negligible change in the ratios of luminescent intensities even in the presence of over 200 fold excess of alanine.
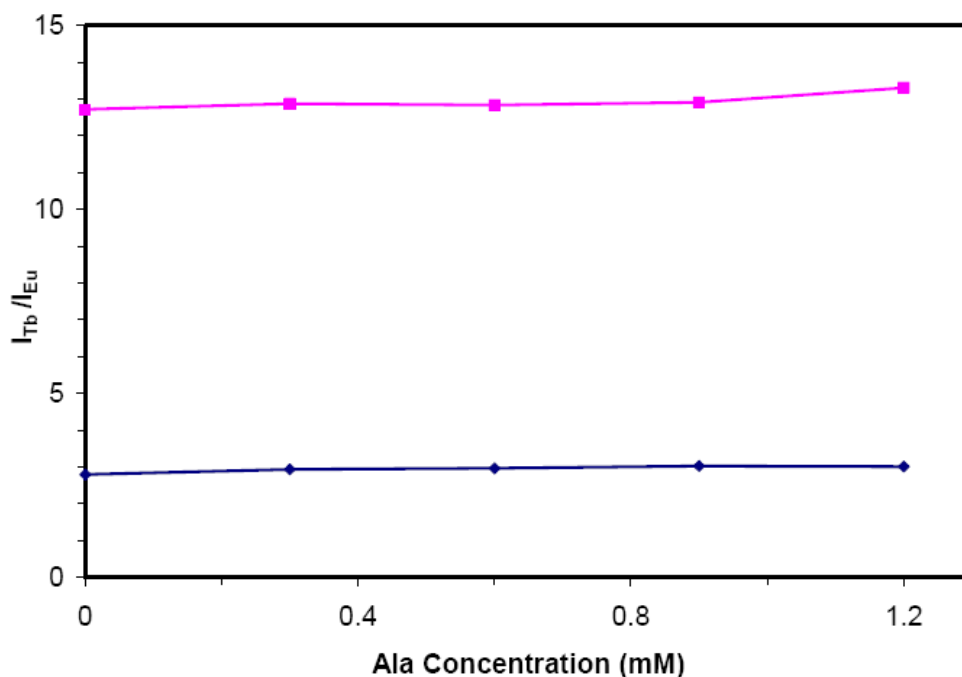
Figure 7.16. Ratio of Tb (544 nm) to Eu (592 nm) signal intensity vs. Ala concentration for a suspension Eu-doped NMOFs functionalized with complex **7-1** in a 10 mM Tris buffered ethanol in water (1:1) solution with 5 µM (blue) and 150 µM (pink) DPA.

7.2.4 Spore Detection Results

The spore detection efficiency of the nanoparticle sensors was also evaluated using *Bacillus subtilis* as a model. *Bacillus subtilis* endospores contain 8.9 % DPA by weight.[10] Lyophilized cells were purchased from Aldrich, and two different methods were employed to extract DPA. The first method involved sonication of the *B. subtilis* cells in 0.02 M nitric acid. A 34% extraction efficiency was reported for this method.[10] Complexes **7-1** to **7-3** and the corresponding silica nanoparticles coated with **7-1** to **7-3** were used to detect DPA from the extracted spore sample. Only the free complex **7-2** resulted in any increase in emission intensity (Fig. 7.17). The calculated DPA concentration based on the emission intensity was approximately 4-8 fold lower than the expected concentration, and a linear increase in emission intensity was not observed (Table 7.1). The pH dependence of the spore detection using complex **7-2** was also evaluated, and a peak intensity was observed at pH 7 (Fig. 7.18).
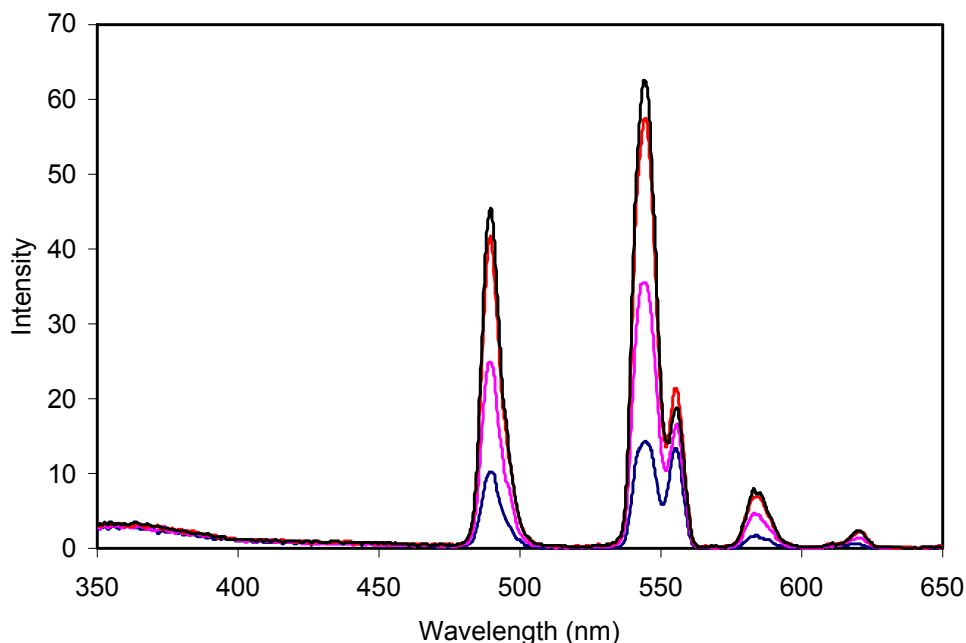
Figure 7.17. Emission spectrum of a 10 μM solution of complex **7-2** before (blue) and after the addition of 1 μL (pink), 3 μL (red), and 5 μL (black) of an extracted spore solution with a calculated [DPA] of 1.12 mM.

Table 7.1. DPA detection from spores extracted with 0.02 M nitric acid, using complex **7-2**.

µL spore soln. added	Calc. [DPA]	Measured [DPA] (489 nm)	Measured [DPA] (544 nm)
0	0 nM	4.2 nM	-8.4 nM
1	560 nM	157 nM	147 nM
3	1680 nM	321 nM	306 nM
5	2800 nM	358 nM	345 nM
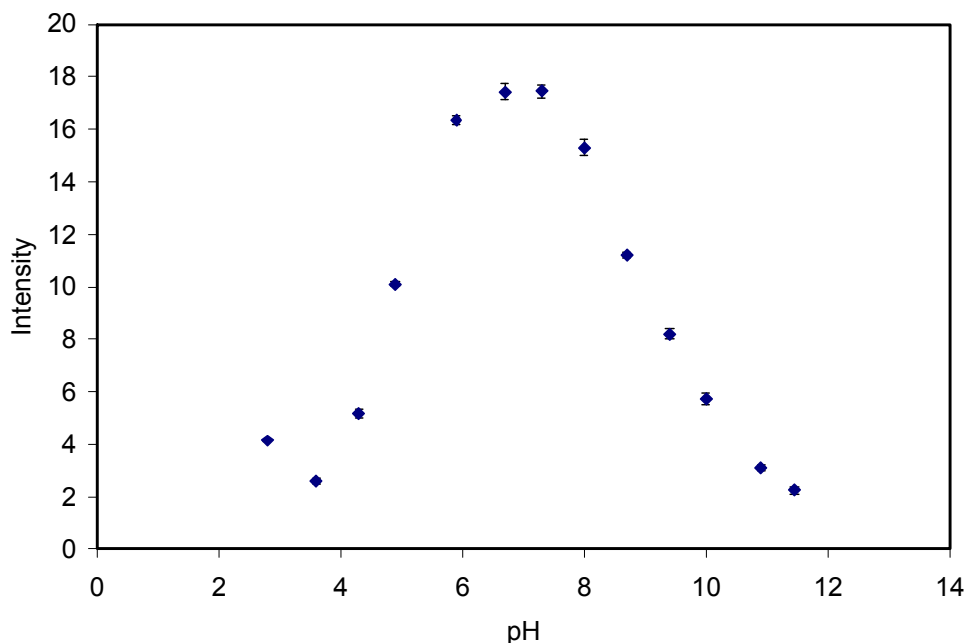
Figure 7.18. Dependence of emission intensity at 544 nM on the pH of a 10 µM solution of complex **7-2** containing 16 µL of an extracted spore solution with a calculated [DPA] of 8.89 µM.

An alternative method was also attempted to extract the DPA. It is known that endospores will release DPA as an initial step of the germination process. This process involves first heat activation by heating a suspension of the lyophilized cells at 70 °C for 30 minutes, followed by the addition of a germinant; in this case L-alanine was used.[1] Similar results were seen as with the nitric acid extraction in that only complex **7-2** showed any response (Fig. 7.19). The concentration determined from the luminescence intensity was approximately 10 fold lower than the expected concentration assuming complete release of DPA (Table 7.2).
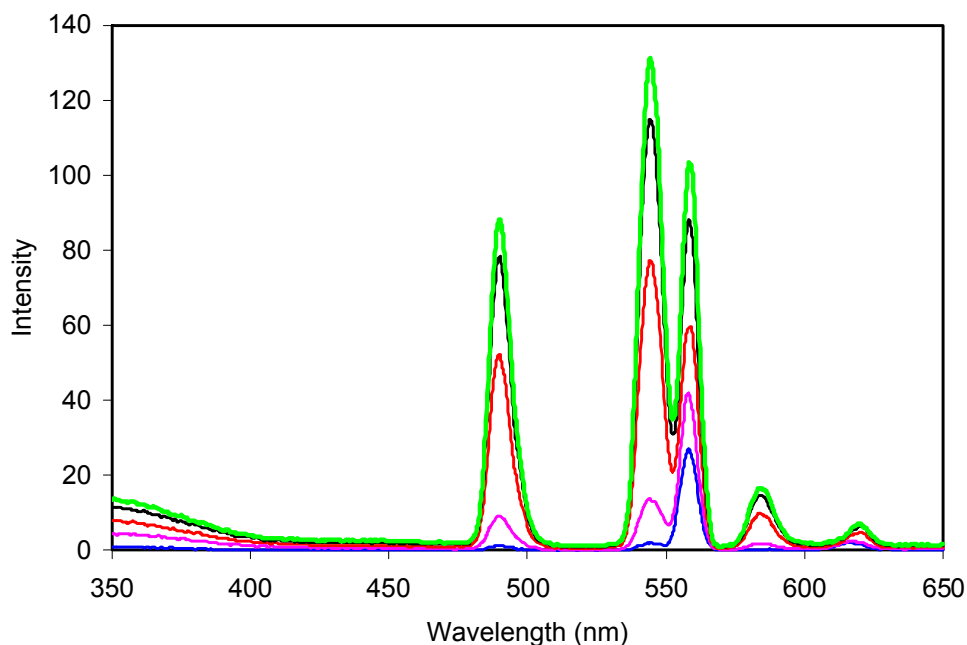
Figure 7.19. Emission spectrum of a 10 μM solution of complex **7-2** before (blue) and after the addition of 1 μL (pink), 3 μL (red), 5 μL (black), and 7 μL (green) of an extracted spore solution with a calculated [DPA] of 2.80 mM.

Table 7.2. DPA detection from spores extracted using the germination method. The DPA was detected using complex **7-2**.

μL spore soln. added	Calc. [DPA]	Measured [DPA] (489 nm)	Measured [DPA] (544 nm)
1	1400 nM	-3.8 nM	-10.8 nM
3	4200 nM	440 nM	452 nM
5	7000 nM	709 nM	728 nM
7	9800 nM	812 nM	847 nM

7.3 Conclusion

We have developed a nanoparticle sensor that allows for quantitative detection of a bacterial spore marker--dipicolinic acid (DPA) at nanomolar concentrations. Immobilization of the Tb complex onto a nanoparticle platform allows for further incorporation of an internal reference to allow for ratiometric detection. We have also shown that the present nanoparticle based luminescent sensors exhibit high selectivity for DPA even in large excess of other potential competing ligands.

7.4 Experimental Details

7.4.1 Materials and Methods

All starting materials and solvents were purchased from Aldrich, Fisher, and Gelest, and were used without further purification. Luminescence data were collected on a Shimadzu RF-5301PC Spectrofluorophotometer. A JEM 100CX-II transmission electron microscope (TEM) was used to determine particle size and morphology. TEM samples were prepared from ethanolic particle dispersions on amorphous carbon-coated copper grids. Tb concentrations of solutions of the complexes were determined using an Applied Research Laboratories (ARL) SpectraSpan 7 Direct Current Plasma (DCP) Spectrometer. The amount of Tb complex immobilized on the particles was determined using thermogravimetric analysis and titration with $Na_2[DPA]$.

7.4.2 Ligand Synthesis

The ligands used in this work were synthesized by reacting 3-aminopropyl-triethoxysilane with suitable EDTA anhydrides. Ethylenediamine tetra(acetic acid) mono anhydride was first synthesized from the dianhydride, following a published procedure.[18]

Ethylenediamine tetra(acetic acid) mono(3-aminopropyltriethoxysilane) (**7-1a**)[16] was synthesized by suspending 0.25 g (0.91 mmol) of EDTA-mono anhydride in 8 mL of anhydrous pyridine. 0.21 mL (0.20 g, 0.90 mmol) of 3-aminopropyltriethoxysilane was then added, and the mixture was stirred at room temperature under N_2 for 16 hours. The product was then precipitated upon the addition of hexanes. The product was collected by centrifuging at 3300 rpm and was washed with additional hexanes to afford pure **7-1a**. Yield: 0.25 g (56%). ^{1}H NMR (DMSO, 300 MHz): δ 3.71 (s, 4H), δ 3.42 (s, 4H), δ 2.79 (t,

J_{H-H} = 6.0 Hz, 2H), δ 2.57 (t, J_{H-H} = 6.0 Hz, 2H). MS (ESI positive ion): m/z 412.1 (412.1 expected for the silanetriol [M+H]$^+$).

Ethylenediamine tetra(acetic acid) bis(3-aminopropyltriethoxysilane) (**7-2a**) was synthesized by reacting 0.10 g (0.39 mmol) of ethylenediamine tetra(acetic acid) dianhydride and 0.19 mL (0.18 g, 0.812 mmol) of 3-aminopropyltriethoxysilane in 2.5 mL of anhydrous pyridine at room temperature and under N_2 for 16 hours. The product was precipitated upon the addition of hexanes, and collected by centrifuging at 3300 rpm. Further washing with additional hexanes afforded the pure product of **7-2a**. Yield: 0.17 g (62.4%). ^{1}H NMR (DMSO, 400 MHz): δ 7.98 (s, 2H), δ 3.72 (q, J_{H-H} = 6.4 Hz, 12H), δ 3.35 (s, 4H), δ 3.19 (s, 4H), δ 3.04 (br., 4H), δ 2.69 (s, 4H), δ 1.44 (m, 4H), δ 1.12 (t, J_{H-H} = 7.0 Hz, 18H), δ 0.51 (t, J_{H-H} = 8.2 Hz, 2H). MS (ESI positive ion): m/z 560.8 (559.2 expected for the silane monoethoxypentatriol [M+H]$^+$).

In order to synthesize ethylenediamine tetra(acetic acid) mono(3-aminopropyl-triethoxysilane) mono(pentylamide) (**7-3a**), EDTA-pentylamide was first synthesized by suspending 1.42 g (5.19 mmol) of a mixture of EDTA mono anhydride and EDTA (50:50 mixture) in 45 mL of anhydrous pyridine. 0.36 mL (0.27 g, 3.10 mmol) of amylamine was then added, and the reaction was stirred at room temperature, under N_2 for 16 hours. The reaction mixture was then centrifuged at 3300 rpm, to separate the pyridine insoluble material which was identified as EDTA and a small amount of EDTA mono anhydride. Hexanes were then added to the supernatant to precipitate the product, which was collected by centrifuging at 3300 rpm. The product was then washed with additional hexanes and dried under vacuum. NMR of the hexane precipitated product shows that this product is a mixture of the desired EDTA-pentylamide, EDTA mono anhydride, and EDTA in a 6.75 :

2.25 : 1 molar ratio. The above procedure was repeated using the isolated product to obtain pure EDTA-pentylamide in ~25% yield. ^{1}H NMR (DMSO, 400 MHz): δ 8.02 (s, 1H), δ 3.35 (s, 4H), δ 3.19 (s, 2H), δ 3.05 (q, J_{H-H} = 6.7 Hz, 2H), δ 2.72 (m, 4H), δ 1.39 (quin., J_{H-H} = 6.9 Hz, 2H), δ 1.24 (m, 4H), δ 0.84 (t, J_{H-H} = 7.0 Hz, 3H).

EDTA-pentylamide-mono anhydride was then synthesized by reacting 0.255 g (0.706 mmol) of EDTA-pentylamide and 150 μL (0.162 g, 1.59 mmol) of acetic anhydride in 1 mL of anhydrous pyridine at 65°C for 20 hours. Hexanes were then added to the reaction mixture to precipitate EDTA-pentylamide-mono anhydride which was washed with hexanes several times to remove the excess acetic anhydride. EDTA-pentylamide-mono anhydride was then redissolved in 6 mL of anhydrous pyridine followed by the addition of 0.2 mL (0.19 g, 0.85 mmol) of 3-aminopropyltriethoxysilane. The reaction mixture was stirred at room temperature for 16 hours. Addition of hexanes and centrifugation at 3300 rpm led to crude product of **7-3a** which was washed with additional hexanes and dried under vacuum. **7-3a** was purified by recrystallization from a mixture of methanol (2 mL) and diethyl ether (~20 mL). Yield: 0.092 g (23.1% based on the amount of pentylamide-EDTA-mono anhydride used). ^{1}H NMR (DMSO, 400 MHz): δ 3.73 (m, 2H), δ 3.58 (br, 2H), δ 3.43 (m, 4H), δ 3.39 (q, J_{H-H} = 7.4 Hz, 6H), δ 3.00 (m, 2H), δ 2.66 (m, 4H), δ 1.40 (m, 2H), δ 1.24 (m, 2H), δ 1.13 (m, 4H), δ 1.09 (t, J_{H-H} = 5.9 Hz, 9H), δ 0.83 (m, 3H), δ 0.57 (m, 2H). MS (ESI positive ion): m/z 475.4 (475.2 expected for the silanetriol).

7.4.3 Tb Complex Synthesis

The corresponding Tb(III) complexes of **7-1a** to **7-3a** (**7-1** to **7-3**) were formed by adding 1 eq of TbCl₃ to an aqueous solution of the deprotonated form of each ligand. The

synthesis of complex **7-1** is shown here as an example. To prepare the terbium complex **7-1**, ligand **7-1a** (0.1 g, 0.2 mmol) was dissolved in 3 eq of NaOH (1.21 mL of a 0.5 M solution) at room temperature with magnetic stirring. One equivalent of $TbCl_3$ (1.35 mL of a 0.15 M solution) was then added dropwise, and the solution was stirred for an additional 30 minutes. Approximately 5 mL of ethanol was then added to the solution to precipitate the complex, which was isolated by centrifuging at 3200 rpm for 10 minutes. The complex was then washed with additional ethanol and dried. Yield: 0.0555 g (39.0%). The complex was dissolved in distilled water, and diluted to a total volume of 5 mL to give a ~ 0.016 M solution.

7.4.4 Nanoparticle Synthesis

The silica nanoparticles were synthesized using a well-established water-in-oil reverse microemulsion procedure. Briefly, to 20 mL of a 0.3 M Triton-X100/1.5 M 1-hexanol/cyclohexane solution was added 1.22 mL of distilled water and 0.20 mL of tetraethylorthosilicate (TEOS). The mixture was stirred for 10 minutes at room temperature to allow for the formation of a microemulsion with a W-value of 15 (W = water/surfactant ratio). 0.4 mL of aqueous ammonia was then added to initiate the hydrolysis. After stirring for 24 hours, an aliquot of an aqueous solution of the Tb complex was added to the reaction mixture, and the reaction was stirred for an additional 18 hours at room temperature. 20 mL of ethanol was added to the reaction to precipitate the particles which were then collected by centrifuging at 13500 rpm for 20 minutes. The particles were then washed twice with ethanol and once with water before being redispersed in 5 mL of distilled water. Using this procedure, uniform spherical particles of approximately 37 nm in diameter were obtained.

A similar procedure was used to synthesize the nanoparticles with a luminescent $Ru(bpy)_3^{2+}$ core. As an example, monoAPS-EDTA-Tb coated, $Ru(bpy)_3^{2+}$ doped, silica nanoparticles were synthesized using a Triton-X100/1-hexanol/cyclohexane/water microemulsion system. To 10 mL of a 0.3 M Triton-X100/1.5 M 1-hexanol/cyclohexane solution was added, 0.57 mL of distilled water, 40 μL of a 0.1 M $Ru(bpy)_3^{2+}$ aqueous solution, and 0.10 mL of tetraethylorthosilicate (TEOS). The mixture was stirred for 10 minutes at room temperature to allow for the formation of a microemulsion with a W-value of 15. 0.2 mL of aqueous ammonia was then added to initiate the hydrolysis. After stirring for 24 hours, 28 μL of a 0.0176 M aqueous solution of monoAPS-EDTA-Tb (**7-1**) was added to the reaction mixture. The reaction was then stirred for an additional 18 hours at room temperature. 10 mL of methanol was added to the reaction to precipitate the particles which were then collected by centrifuging at 13500 rpm for 20 minutes. The particles were then washed twice with ethanol and once with water before being redispersed in 1.5 mL of distilled water.

After synthesis of the nanoparticles and immobilization of complexes **7-1** to **7-3**, Tb was re-loaded to ensure all of the immobilized ligands formed a Tb complex. This was done by adding an aliquot of $TbCl_3$ solution to a suspension of the nanoparticle sensor in water (pH ~ 9.5). The mixture was then stirred at room temperature for 16 hours, after which time the particles were isolated and washed to remove any uncomplexed Tb ions. The amount of $TbCl_3$ added was equal to the initial amount of complex that had been added during the nanoparticle sensor synthesis.

The $Eu_{0.02}Gd_{0.98}(BDC)_{1.5}(H_2O)_2$ NMOFs were synthesized using a cationic cetyltrimethylammonium bromide (CTAB)/1-hexanol/iso-octane/water reverse

microemulsion. Briefly, 441 μL of a 0.05 M GdCl₃ aqueous solution and 9 μL of a 0.05 M Eu(NO₃)₃ aqueous solution were added to a 100 mL aliquot of CTAB (0.05 M) and 1-hexanol (0.5 M) in iso-octane, resulting in the formation of a microemulsion with a *W*-value of 5. To a second 100 mL aliquot of CTAB and 1-hexanol in iso-octane was added 450 μL of a 0.067 M solution of di(methylammonium)-benzenedicarboxylate forming a second microemulsion with a *W*-value of 5. After the two separate microemulsions had formed they were combined and stirred at room temperature for 2 hours. 1.35 mL of a 5 mM aqueous solution of polyvinylpyrrolidone (PVP, MW = 40,000) was then added and the reaction was stirred for an additional 12 hours. The particles were then isolated by centrifuging, and were washed with ethanol.

The PVP coated NMOFs were then coated with a silica shell using sol-gel techniques. Briefly, an aliquot of a suspension of the PVP coated NMOFs in ethanol was diluted with additional ethanol to reach a final particle concentration of 0.2 mg/mL. An aliquot corresponding to 4% by volume (of ethanol) of aqueous NH₄OH was then added, followed by tetraethylorthosilicate (TEOS, 5 μL per mg of NMOF). The reaction was then stirred at room temperature for 2 hours, after which time an additional aliquot of TEOS (5 μL per mg of NMOF) was added. The reaction was then continued for 7 hours at room temperature. The particles were then isolated by centrifuging and were washed with ethanol. The resulting particles had a silica shell of approximately 8-9 nm in thickness.

The Tb complex **7-1** was then immobilized on the surface of the silica coated NMOFs using the following procedure. An aliquot of silica coated NMOFs containing 8.8 mg of particles was diluted to a total volume of 4 mL. The pH of the suspension was adjusted to approximately 10 with the dropwise addition of aqueous NH₄OH. 42 μL of a 0.016 M

solution of **7-1** was then added, and the reaction was stirred at room temperature for 16 hours. The particles were then isolated by centrifuging, and were washed with water and ethanol before being redispersed in 2 mL of ethanol.

7.4.5 DPA Detection

The optimal stoichiometry for complex formation with dipicolinic acid (DPA) was determined using Job's method of continuous variation. 13 solutions were made by inversely varying the concentration of Tb and DPA from 0 to 12 μM. The samples were then excited at 277 nm, and the emission intensity at 545 nm was measured.

Calibration curves were made by adding varying amounts of DPA to a nanoparticle suspension with a Tb concentration of 10 μM. After exciting at 277 nm, the intensities at 489 nm and 544 nm were measured. The detection limit was determined using the background intensity plus three standard deviations.

7.4.6 Extraction of DPA from Bacillus subtilis

Method 1 – 6.2 mg of lyophilized *B. subtilis* cells were added to 1 mL of 0.02 M nitric acid and the suspension was sonicated for 15 minutes. The suspension was then centrifuged at 3000 rpm to separate the insoluble material, and the supernatant was transferred to another tube. The estimated [DPA] of the supernatant was determined as follows:

6.2 mg of cells * 8.9 wt% DPA = 0.55 mg DPA

34% reported extraction efficiency: 0.55 mg * 34% = 0.188 mg DPA = $1.12*10^{-6}$ mol/0.001L

= 1.12 mM

Method 2 – 10.5 mg of lyophilized *B. subtilis* cells were added to 2 mL of distilled water. The suspension was heated to 70°C for 30 minutes. After cooling to room temperature, 40 µL of a 0.5 M L-alanine solution was added. The mixture was then stirred at room temperature for 2 hours. The mixture was then centrifuged at 3000 rpm to remove the insoluble material. The [DPA] of the supernatant was calculated to be 2.8 mM, assuming a 100% extraction efficiency.

7.5 References

1. Pellegrino, P. M.; Fell Jr., N. F.; and Gillespie, J. B., Enhanced spore detection using dipicolinate extraction techniques. *Analytica Chimica Acta*, **2002**, *455* (2), 167-177.

2. Enserink, M., Bioterrorism: This time it was real: Knowledge of Anthrax put to the test. *Science* **2001**, *294* (5542), 490-491.

3. Walt, D. R. and Franz, D. R., Peer Reviewed: Biological Warfare Detection. *Anal. Chem.* **2000**, *72* (23), 738A-746A.

4. Yolken, R. H. and Wee, S-B., Enzyme immunoassays in which biotinillated β-lactamase is used for the detection of microbial antigens. *J. Clin. Microbiol.* **1984**, *19* (3), 356-360.

5. King, D.; Luna, V.; Cannons, A.; Cattani, J.; and Amuso, P., Performance assessment of three commercial assays for direct detection of *Bacillus anthracis* spores. *J. Clin. Microbiol.* **2003**, *41* (7), 3454-3455.

6. De Wit, M. Y.; Faber, W. R.; Krieg, S. R.; Douglas, J. T.; Lucas, S. B.; and Hartskeerl, R. A., Application of a polymerase chain reaction for the detection of mycobacterium leprae in skin tissues. *J. Clin. Microbiol.* **1991**, *29* (5), 906-910.

7. Hurtle, W.; Bode, E.; Kulesh, D. A.; Kaplan, R. S.; Garrison, J.; Bridge, D.; House, M.; Frye, M. S.; Loveless, B.; Norwood, D., Detection of the *Bacillus anthracis gyrA* gene by using a minor groove binder probe. *J. Clin. Microbiol.* **2004**, *42* (1), 179-185.

8. Fasanella, A.; Losito, S.; Adone, R.; Ciuchini, F.; Trotta, T.; Altamura, S. A.; Chiocco, D.; Ippolito, G., PCR assay to detect *Bacillus anthracis* spores in heat-treated specimens. *J. Clin. Microbiol*. **2003**, *41* (2), 896-899.

9. Farquharson, S.; Gift, A. D.; Maksymiuk, P.; and Inscore, F. E., Rapid dipicolinic acid extraction from Bacillus spores detected by surface-enhanced Raman spectroscopy. *Appl. Spectrosc.* **2004**, *58* (3), 351-354.

10. Zhang, X.; Young, M. A.; Lyandres, O.; and Van Duyne, R. P., Rapid detection of an anthrax biomarker by surface-enhanced Raman spectroscopy *J. Am. Chem. Soc.* **2005**, *127* (12), 4484-4489.

11. Bell, S. E. J.; Mackle, J. N.; and Sirimuthu, N. M. S., Quantitative surface-enhanced Raman spectroscopy of dipicolinic acid—towards rapid anthrax endospore detection. *Analyst* **2005**, *130* (4), 545-549.

12. Rosen, D. L.; Sharpless, C.; and McGown, L. B., Bacterial spore detection and determination by use of terbium dipicolinate photoluminescence. *Anal. Chem.* **1997**, *69* (6), 1082-1085.

13. Pellegrino, P. M.; Fell, Jr., N. F.; Rosen, D. L.; and Gillespie, J. B., Bacterial endospore detection using terbium dipicolinate photoluminescence in the presence of chemical and biological materials. *Anal. Chem.* **1998**, *70* (9), 1755-1760.

14. Hindle, A. A. and Hall, E. A. H., Dipicolinic acid (DPA) assay revisited and appraised for spore detection. *Analyst* **1999**, *124* (11), 1599-1604.

15. Cable, M. L.; Kirby, J. P.; Sorasaenee, K.; Gray, H. B.; and Ponce, A., Bacterial spore detection by [Tb^{3+}(macrocycle)(dipicolinate)] luminescence. *J. Am.Chem. Soc.* **2007**, *129* (6), 1474-1475.

16. Rieter, W. J.; Taylor, K. M. L.; and Lin, W., Surface modification and functionalization of nanoscale metal-organic frameworks for controlled release and luminescence sensing. *J. Am. Chem. Soc.* **2007**, *129* (32), 9852-9853.

17. Rieter, W. J.; Taylor, K. M. L.; An, H.; Lin, W.; and Lin, W., Nanoscale metal−organic frameworks as potential multimodal contrast enhancing agents. *J. Am. Chem. Soc.* **2006**, *128* (28), 9024-9025.

18. Ebright, Y. W.; Chen, Y.; Ludescher, R. D.; and Ebright, R. H., N-(Iodoacetyl)-p-phenylenediamine-EDTA: A reagent for high-efficiency incorporation of an EDTA-metal complex at a rationally selected site within a protein. *Bioconjugate Chem.* **1993**, *4* (3), 219-225.